Université Libre de Bruxelles
Faculté des Sciences

Contribution to the study of the central tracking system of the CMS detector, at the future proton collider LHC

Dissertation présentée en vue
de l'obtention du titre
de Docteur en Sciences

Pascal VANLAER

Septembre 1998

Cette thèse de doctorat a été réalisée avec le soutien du Fonds pour la Formation à la Recherche dans l'Industrie et l'Agriculture (F.R.I.A.) et du Fonds National de la Recherche Scientifique (F.N.R.S.).

Contents

Chapter 1

Introduction

At the beginning of the twenty-first century, the new proton-proton collider of CERN, the LHC, will enter in function. This accelerator will permit the study of proton collisions at the unprecedented energy of 14 TeV in the centre of mass of the interaction. The LHC will allow to tackle several fundamental questions still open to date in particle physics: what is the origin of particle masses, are there other forms of matter besides the known quarks and leptons, as foreseen in some models like supersymmetry, do all interactions unite at very high energies and if yes, what is the adequate theory of the unified force?

The phenomena that will be searched for at the LHC are expected to have a very small probability of occurence per proton collision. This is why the LHC luminosity must be as high as possible. However this imposes harsh conditions of operation on most of the detectors that will be installed at the LHC. Proton bunches will cross every 25 nanoseconds, emitting of the order of 1000 charged particles into the detectors at every crossing. The central track detectors are among the most exposed, as they are located near the beam pipe.

The role of a tracking system is to measure the coordinates of a set of points along the track of charged particles and permit the reconstruction of the particle trajectories. Track detectors have been the subject of extensive research and development in order to reach the level of performance required at the LHC. This thesis is a contribution to the study of the central tracker of the Compact Muon Solenoid (CMS), one of the two general purpose experiments to be built at the LHC. We have first participated to the development of the Micro-Strip Gas Counter (MSGC). This relatively novel gas detector, introduced in 1988, takes advantage of the microelectronics technology for its fabrication. The precision of microelectronics processes permits the production of detectors with very small detection cells, allowing to cope with the counting rates expected at the LHC. With its low price per surface unit, about five times cheaper than solid state detectors, the MSGC constitutes an adequate technology for the construction of large detection surfaces at high rate experiments. In CMS, MSGC's are foreseen to equip the outer layers of the central tracking system.

One of the important issues for these counters is that of robustness under sustained irradiation at LHC rates. Large gain variations due to detector ageing have been observed, sometimes after irradiation doses equivalent to less than one year of operation at the LHC. Discharges that can damage the MSGC electrodes also appear at relatively low gains. A possible way of improving the stability of operation of MSGC's resides in the choice of the gas filling. Gas mixtures providing a high detection efficiency for minimum ionizing particles across a large range of working voltages are favoured. They allow operation at voltages much lower than the breakdown limit, which reduces the occurence of sparks. In addition full detection efficiency should be reached at low voltage, in order to limit the energy released in case of a spark. Mixtures of neon and dimethylether (DME) were thought to be good candidates, as they lead to

stable operation at high gas gains. However there were doubts that a high detection efficiency for minimum ionizing particles could be achieved with a gas of such a low ionization yield as neon. With the help of a cosmic ray hodoscope installed in Brussels we could study the response of MSGC's filled with Ne-DME mixtures to minimum ionizing particles. The results of these measurements were then reproduced and studied further by means of a Monte Carlo simulation of the MSGC response.

Another challenge is the design and construction of a very large MSGC tracker. The CMS MSGC system will be composed of about 15000 counters of typically 10×10 cm^2, arranged in detection layers so as to provide on average seven measurement points along the tracks of high momentum particles. In the Belgian CMS community we have thought that this would be best done with modules composed of several counters placed side by side in a common gas volume. This layout minimizes the dead areas between counters and the amount of material in the tracker. The questions of the stability of operation and uniformity of the response of multicounter modules have been addressed with a dedicated prototype tested in the cosmic ray hodoscope.

The second part of this thesis is dedicated to the analysis of track reconstruction with the CMS tracker. Track reconstruction consists in grouping the hits generated by the same particle and fitting a trajectory through these points in order to estimate the particle kinematical parameters (momentum, direction and impact parameters). As it is difficult to disentangle the intrinsic limitations of the detector from the imperfections of the reconstruction program, we have first studied and improved one of the possible track finding and fitting algorithms, based on the Kalman filter. We have then investigated some of the factors that affect the track finding efficiency and the accuracy of the track parameter measurement: efficiency and spatial resolution of the detector elements, density of background hits, amount of material inside the tracker, type of the particle to be measured. This work was performed with a detailed simulation of the CMS tracker, including the simulation of particle signals on the electrodes of the detector elements. In the case of MSGC's, the simulation relies on the same Monte Carlo program as the one used in the study of MSGC's filled with Ne-DME mixtures.

Eventually, we have studied the possibility to identify jets produced by b-quarks with the CMS tracker. Jets from b-quarks are expected to be a clear experimental signature through which supersymmetric processes could be searched for. The b-tagging method studied relies on the measurement of the impact parameter with respect to the interaction vertex of particles produced in the beauty hadron decay chain. The performance of the tagging algorithm is analysed in relation with the results of the track reconstruction study.

The LHC project and the CMS detector are described in chapter 2. Some of the principles of particle detection with gaseous detectors are presented at the beginning of chapter 3. This material will help to understand the principles of operation of micro-strip gas counters and the factors influencing their performance, described later in the chapter. The experimental study of MSGC prototypes in the cosmic ray hodoscope will then be detailed in chapter 4, together with the Monte Carlo study of the MSGC response. Chapter 5 is dedicated to the analysis of the CMS tracker performance. In chapter 6 the study of the tracker b-tagging capability is described. Eventually, we shall summarize the results and conclusions of the different studies.

Chapter 2

The Compact Muon Solenoid at the Large Hadron Collider

2.1 The Large Hadron Collider project

2.1.1 Description of the Large Hadron Collider

The Large Hadron Collider (LHC) is the new proton-proton collider that will be built at CERN, the laboratory of the European Organization for Nuclear Research, near Geneva [1]. This accelerator will allow the study of proton collisions at the energy of 14 TeV in the centre of mass of the interaction, about eight times higher than at the $p\overline{p}$ collider of Fermilab, in the USA. The partons, i.e. the quarks and gluons inside the protons, will interact at an energy up to 1 TeV, far beyond the reach of present accelerators. The LHC project was conceived in the mid eigthies, during the construction of the electron-positron collider LEP, and was finally approved in 1994 by the CERN council.

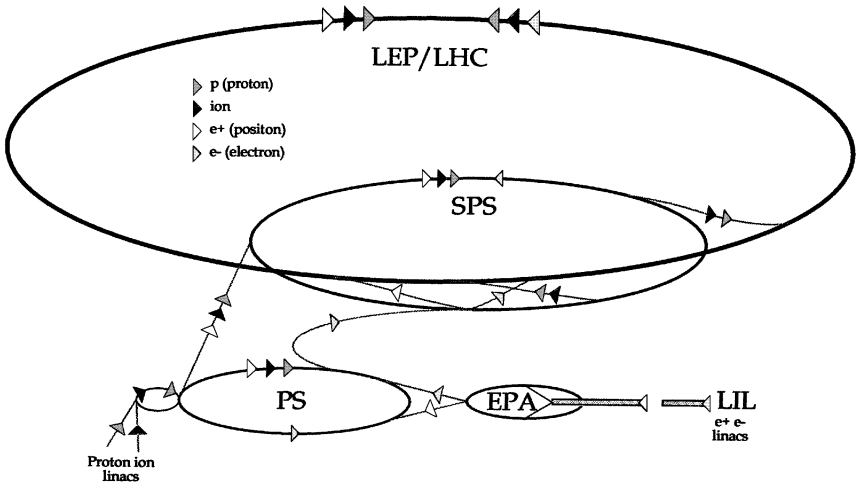

Figure 2.1: The CERN accelerator network as injection chain for the LHC.

The construction of the LHC is scheduled between 2001 and 2004. It will be followed by one or two years of running at a reduced beam intensity, during which an already rich physics

programme will be conducted, in particular in the study of the heavy quarks b and t. Then the running period at full beam intensity will start, with the study of the electroweak symmetry breaking and discovery of the Higgs boson as a main objective. The LHC will benefit from the existing CERN facilities:

- it will be installed in the LEP tunnel, 27 km long, located between 50 and 170 m underground;
- the particles will be injected in the LHC thanks to the existing accelerator chain of CERN, as illustrated in figure 2.1. The protons are first accelerated in a linear accelerator (LINAC) and in the PS booster, up to a kinetic energy of 1.4 GeV. Then the Proton Synchrotron PS and the Super Proton Synchrotron SPS bring the proton beams to an energy of 450 GeV, before final acceleration up to 7 TeV per beam in the LHC ring.

The CERN accelerator network renders the installation of the LHC cost-effective, and also permits other modes of operation in addition to the p-p mode. Lead ion collisions will be produced at an energy of 1150 TeV in the centre of mass, about thirty times higher than at the Relativistic Heavy Ion Collider (RHIC) under construction at the Brookhaven Laboratory.

The performance of a collider can essentially be characterized by two parameters: the energy in the centre of mass of the particle collision, and the luminosity L. The luminosity relates the cross section σ of a certain process to its rate of occurence r: $r = L\sigma$. It depends on the number of particles per bunch in the two colliding beams, N_1 and N_2, on the bunch crossing frequency f, and on the cross-sectional area of each particle bunch. If the particle distribution in the bunches is Gaussian, the luminosity can be expressed as:

$$L = \frac{1}{4\pi} \frac{N_1 N_2 f}{\sigma_x \sigma_y}, \tag{2.1}$$

where σ_x and σ_y are the R.M.S. of the distribution in the directions transverse to the beam, x and y. The LHC design luminosity, also called high luminosity, is equal to 10^{34} cm^{-2}s^{-1} and will be achieved with a bunch crossing frequency of 40 MHz, a particle density of 10^{11} protons per bunch, and beam transverse dimensions of 15 μm R.M.S. at the interaction point. An integrated luminosity of 5×10^5 pb^{-1} is expected over ten years of operation, corresponding to 5×10^7 seconds of running at high luminosity. An integrated luminosity of 3×10^4 pb^{-1} will be accumulated during the low luminosity start-up phase.

The LHC beams will circulate in two separate vacuum pipes. A magnetic field of 8.4 Tesla is required in order to incurve the trajectory of 7 TeV protons along the LEP tunnel. It will be created by superconducting coils, cooled at 1.9 K by superfluid helium. Two antiparallel fields are needed to bend the two counter-rotating proton beams along the same circular path. The solution minimizing the cost of the magnets is a single iron yoke and cryostat shared by the two coils. The beams cross and pass from one vacuum pipe to the other at four points. This is where the experiments are located. The transverse dimensions of the beams at the intersections are reduced by additional focusing magnets, in order to achieve the luminosity values required by each experiment. ATLAS and CMS, the two general purpose detectors of the LHC, are designed for physics studies at the highest LHC luminosity. ALICE, a detector conceived for the study of heavy ion collisions, and LHC-B, an experiment dedicated to B physics, will occupy the other intersection points (see figure 2.2).

We shall now describe selected topics of the physics programme that will be made possible with the LHC. We shall concentrate on the studies that will be performed with ATLAS and CMS in the p-p mode of operation of the collider, and focus on the analyses that set the most stringent constraints on the detector performance.

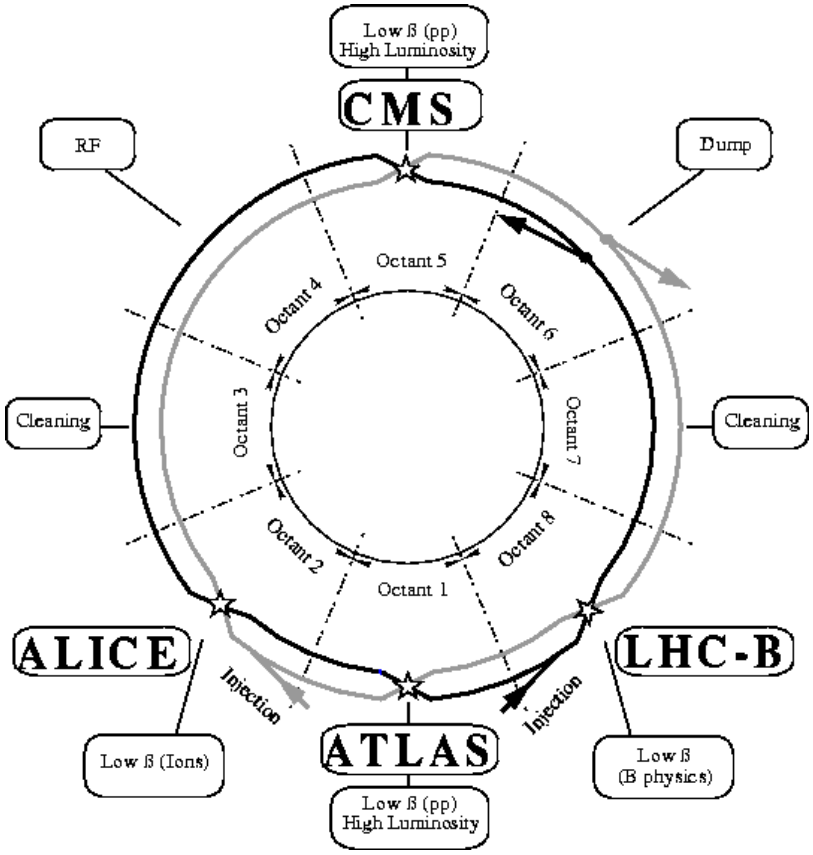

Figure 2.2: Schematic layout of the LHC. The figure shows the location of the experiments and the sections of the ring dedicated to beam injection, acceleration (RF), cleaning and dumping.

2.1.2 Physics at high luminosity

Figure 2.3 shows the cross-sections of various characteristic processes as a function of the proton collision centre of mass energy $\sqrt{s}$. The values expected at a centre of mass energy of 14 TeV are Standard Model predictions extrapolated from data obtained at lower energies in previous experiments. Typical cross-sections expected at the LHC are about 1 pb for Higgs production if the mass of the Higgs boson is around 500 GeV, about 1 nb for $t\bar{t}$ pair production, and above 100 μb for $b\bar{b}$ pair production. The corresponding event rates at a luminosity of 10^{34} cm^{-2}s^{-1} are 10^{-2} Hz for Higgs production, 10 Hz for $t\bar{t}$ creation and more than 10^{6} Hz for $b\bar{b}$ production.

The total p-p collision cross-section at the LHC is estimated to about 100 millibarns [3], and the total event rate at a luminosity of 10^{34} cm^{-2}s^{-1} will be one gigahertz. The highest luminosity possible is required to permit the study of rare events, like the production of the Higgs boson, and to increase the potential of the LHC for the study of processes involving heavy particles (t-quarks, Higgs, supersymmetric particles,...). The disadvantage is that on average 25 soft proton-proton interactions, called "minimum bias" events, will be superimposed on top of every hard event. The interactions will be distributed along the beam axis with a standard deviation of 5.3 cm, so it will be possible to separate the primary vertices with detectors of moderate resolution in z, the coordinate along the beam axis. However the high interaction rate does not only complicate the event analysis but also imposes stringent constraints on the detectors and their readout electronics. We shall elaborate more on that subject in the next sections.

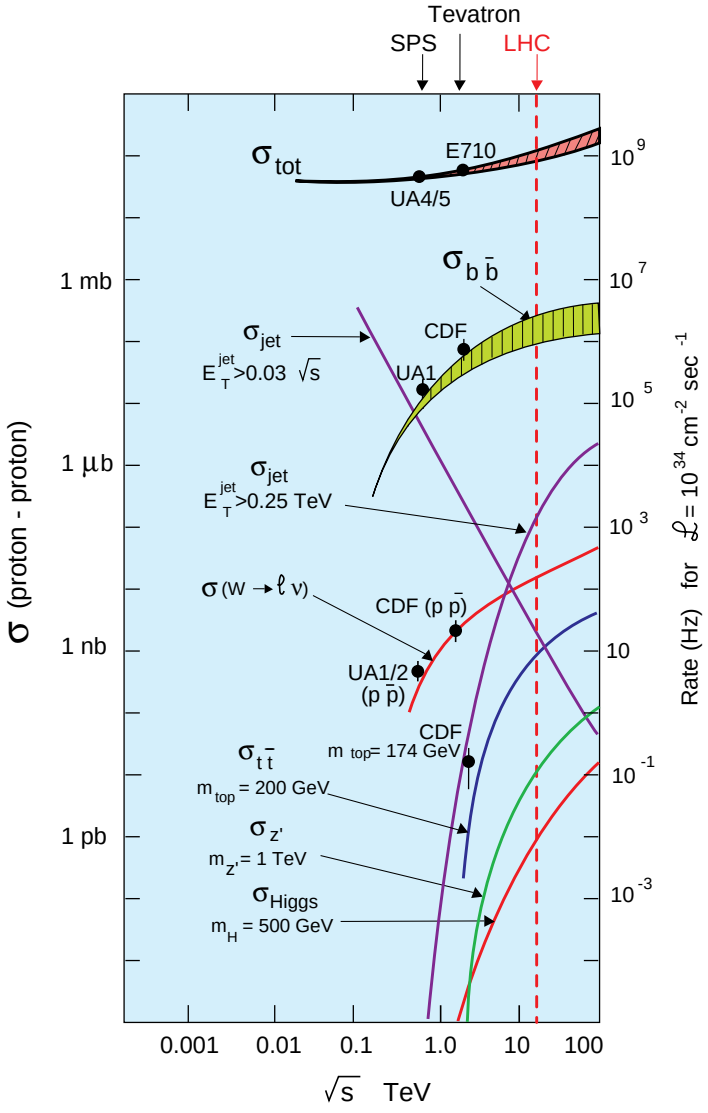

Figure 2.3: Cross-section and event rate of various processes at a luminosity of 10^{34} cm^{-2}s^{-1}, as a function of the proton collision centre of mass energy. [2]

The momentum distribution of the secondary particles follows simple laws [4]. Let us introduce the pseudorapidity η, defined as:

$$\eta = \frac{1}{2} \ln \left(\frac{p + p_z}{p - p_z} \right) = -\ln \tan \left(\frac{\theta}{2} \right) . \tag{2.2}$$

Here θ is the angle of emission of the particle with respect to the beam axis, and $p_z = p \cos \theta$ is the z-component of the particle momentum. The distribution of the number of particles $dN/d\eta$ is roughly constant with the pseudorapidity, at least in the range $|\eta| \leq 5$ corresponding to angles from 1° to 179°. Of the order of 1000 charged particles will be emitted per bunch crossing in this pseudorapidity interval.

In the plane transverse to the beam, the transverse momentum distribution dN/dp_T^2 approximates an exponential in p_T, and at the LHC the average transverse momentum will be 0.5 GeV/c [2]. As the experiments will be looking for processes which produce particles of high transverse momentum in the final state, particles of transverse momentum below 0.7 - 1 GeV/c do not have to be considered in the event analysis.

Search for the Higgs of the Standard Model

Our present understanding of the elementary particles is based on the Standard Model, a theoretical framework which combines the Glashow-Salam-Weinberg model of electroweak interactions, the quark model and quantum chromodynamics (QCD). The Standard Model has been very successful in describing the particles and their interactions at energies up to a few hundreds of GeV, i.e. the range accessible with the present accelerators. No experimental result in contradiction with the Standard Model has been observed to date.

One of the main problems that remain to be understood in the Standard Model is that of gauge symmetry breaking in the electroweak interaction. In the absence of the Higgs field, gauge invariance of the electroweak Lagrangian would require all gauge bosons to be massless. While the photon, the exchange boson of the electromagnetic interaction, is indeed massless, the weak exchange bosons W and Z are very heavy, 80 and 91 GeV/c^2 respectively. A theoretical solution to this problem was proposed independently by F. Englert and R. Brout [5] and by P. Higgs in 1964 [6]. They introduced a new field, the Higgs field, with the characteristic property that the state with minimal energy (vacuum) is attained at a non-zero expectation value of the field. The equations of motion of the exchange bosons in vacuum are then modified by the interaction with the Higgs field as though they had a mass.

Breaking the gauge symmetry in the way prescribed by the Higgs mechanism also preserves a fundamental property of gauge theories, called renormalizability. This ensures that all divergences that would be encountered in calculations of physical quantities can be absorbed in a finite number of free parameters of the theory. In addition, fermion masses may be created by introducing an interaction term between fermions and the Higgs field. However there is at present no experimental evidence of such a Higgs particle. The study of electroweak symmetry breaking at the LHC is therefore of fundamental importance, as it would allow to find out what the origin of the particle masses really is.

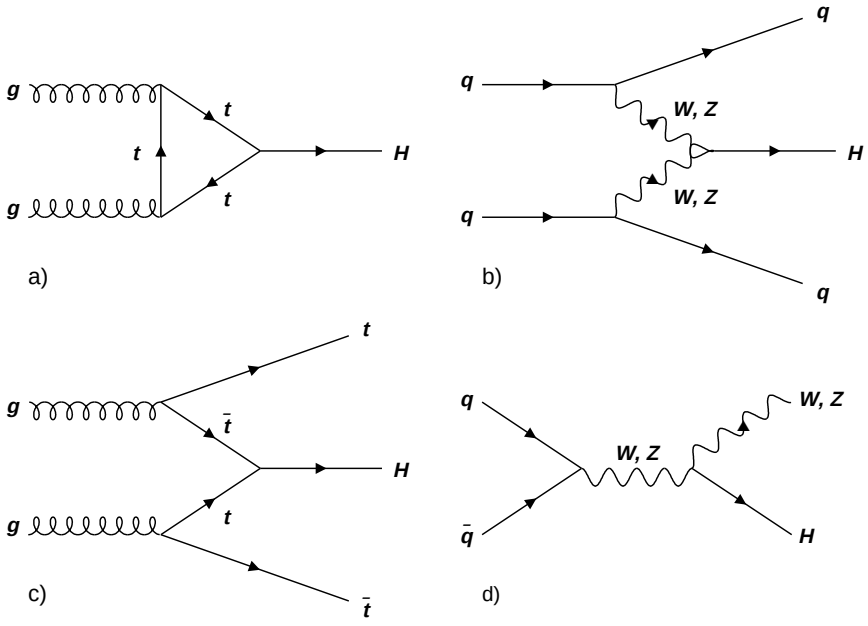

Figure 2.4: Dominant Higgs production mechanisms at hadron colliders: a) gluon-gluon fusion, b) WW or ZZ fusion, c) $t\bar{t}$ fusion, d) W or Z bremsstrahlung.

The search for the Higgs boson largely constraints the design of the general purpose exper-

iments at the LHC. The main Higgs production and decay mechanisms should thus be kept in mind during the description of the CMS detector in section 2.2. First of all, finding the Higgs is rendered difficult by the fact that its mass cannot be predicted accurately from present experimental data. Indirect searches based on LEP data collected until 1997 combined with the measurement of the top quark mass from the CDF experiment indicate that the mass of the Standard Model Higgs should be less than 250 GeV/c^2 at 95% confidence level [7]. Direct searches exclude masses below 77.5 GeV/c^2 at 95% confidence level [8]. The lower bound will be pushed up to about 95 GeV/c^2 at the end of the high energy phase of LEP.

The Higgs field couples to the elementary particles with a strength proportional to their mass. The dominant Higgs production mechanisms will thus involve weak exchange bosons or top quarks, which are much heavier than the other quarks and leptons. The dominant diagrams are shown in figure 2.4. The Higgs production rates expected at the LHC are reasonably large, from 10^6 to 10^4 events per year at a luminosity of 10^{34} cm^{-2}s^{-1} for Higgs masses varying from 0.1 to 1 TeV/c^2. Unfortunately the decay channels which provide the best experimental signature have small branching ratios, of the order of 10^{-3}. Statistics will thus be the limiting factor, and the highest luminosity is mandatory.

The upper plot of figure 2.5 shows the total decay width of the Higgs boson as a function of its mass. In the mass range below 200 GeV/c^2 the decay width is smaller than 2 GeV/c^2. The experimental mass resolution will thus play an important role in detecting a significant Higgs signal in this mass range.[1] At $m_H = 1$ TeV/c^2, the Higgs width reaches 0.5 TeV/c^2 and the Higgs signal dissolves into the background.

The lower plot of figure 2.5 shows the branching ratios of the dominant Higgs decay modes as a function of the Higgs mass. Below 100 GeV/c^2 the most important mode is $H \rightarrow b\bar{b}$, but it cannot be exploited experimentally since it is overwhelmed by the enormous rate of direct $b\bar{b}$ pair production. The most favourable channel in the low mass range is $H \rightarrow \gamma\gamma$, leading in the final state to two isolated energetic photons[2] pointing to the same vertex. The most important sources of background are

- prompt diphoton production during proton-proton collisions. This irreducible background originates from quark annihilation, gluon fusion or bremsstrahlung;
- jets leaving a large amount of energy in the electromagnetic calorimeter. These deposits can be due to the decay of neutral hadrons inside the jets or to bremsstrahlung. This contamination can be reduced by the combination of isolation and π^0 rejection cuts.

Detection of this signal requires an experimental mass resolution of about 1 GeV/c^2. The need for a good distinction between photons and π^0's leads to a high calorimeter granularity, to permit the separation of the two photons from a π^0 decay.

In the mass range 120 GeV/$c^2 \leq m_H \leq 2m_Z$ best experimental signature is obtained in the channel $H \rightarrow ZZ^* \rightarrow l^+l^-l^+l^-$. The branching ratio of this channel is only about 1.2 10^{-3}, but it provides a clean signal by the presence of four isolated energetic leptons. The backgrounds to be considered arise from direct production of ZZ^* pairs, and from $t\bar{t}$ and $Zb\bar{b}$ events leading to a final state with four leptons. The first source is irreducible. The contamination from $t\bar{t}$ pair

[1] The definition of signal significance used here is the ratio $S/\sqrt{B}$ of the number of signal events counted in a mass window of a few times the experimental resolution Γ_{exp} around the mass peak, to the square root of the number of background events expected in the same mass window. It corresponds to a certain probability that the observed signal is due to a statistical fluctuation of the background. The signal significance would be proportional to $1/\sqrt{\Gamma_{exp}}$ if the background spectrum were flat.

[2] A particle is said to be isolated if no other particle is detected in a cone of a certain aperture around the particle direction.

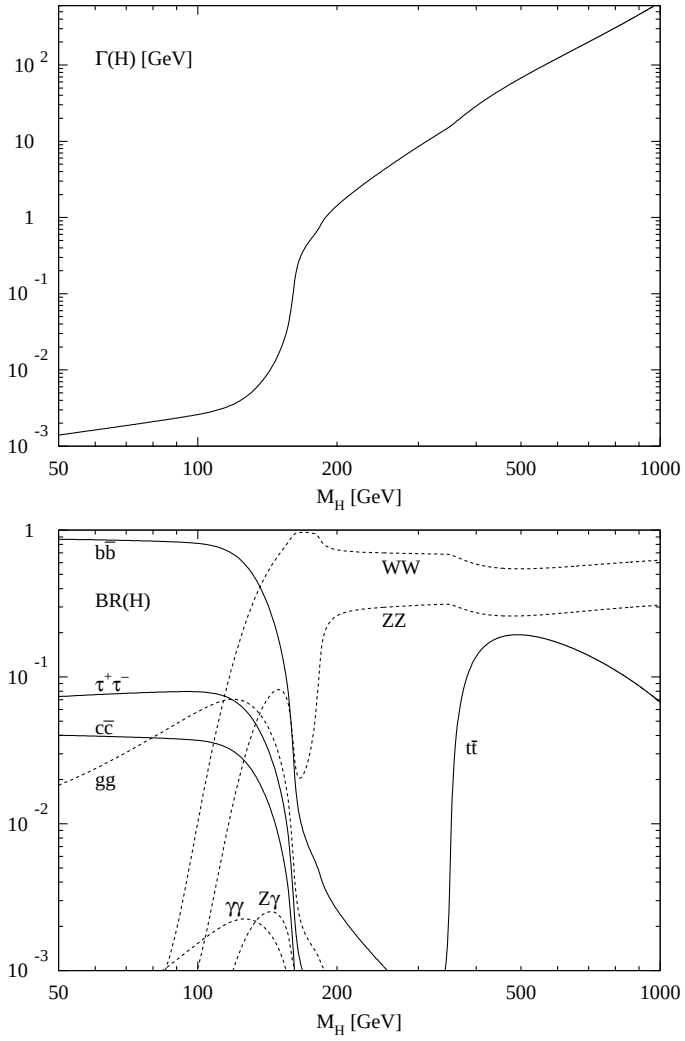

Figure 2.5: Total decay width Γ and branching ratios of the dominant decay modes of the Standard Model Higgs. [9]

production can be suppressed by requiring that the reconstructed mass of one of the lepton pairs be compatible with the Z mass. Lepton isolation cuts and b-jet identification help in reducing both background sources.

Above 180 GeV/c^2 both Z's can be on-shell, and additional background rejection can be achieved by requiring two lepton pairs of invariant mass compatible with m_Z. However the Higgs production cross-section decreases rapidly at large values of m_H. In the range $m_H \geq 500$ GeV/c^2 decay processes of larger branching ratios as compared to the four lepton channel must be considered. One then relies on the processes $H \rightarrow ZZ \rightarrow l^+l^-\nu\overline{\nu}$ or $H \rightarrow W^+W^- \rightarrow l\nu + 2$ jets. A summary of the most favourable Higgs discovery channels and the corresponding mass ranges is given in table 2.1.

The reconstruction of the Higgs mass in the multilepton final state requires a large detector acceptance and a high track finding efficiency in order to reconstruct all leptons. The leptons from a Higgs decay are biased to low pseudorapidity, and full acceptance is reached with a coverage up to $|\eta| = 5$. In addition good lepton identification and precise energy or momentum measurement are needed to permit the use of a Z mass cut. The coverage of the tracking

Final state	Mass interval
$H \to \gamma\gamma$	80 GeV/$c^2 \leq m_H \leq$ 150 GeV/c^2
$H \to ZZ^* \to 4l^\pm$	120 GeV/$c^2 \leq m_H \leq$ 180 GeV/c^2
$H \to ZZ \to 4l^\pm$	180 GeV/$c^2 \leq m_H \leq$ 650 GeV/c^2
$H \to ZZ \to 2l^\pm 2\nu$	500 GeV/$c^2 \leq m_H \leq$ 1 TeV/c^2
$H \to W^+W^- \to l\nu jj$	$m_H \sim$ 1 TeV/c^2
$H \to ZZ \to 2l^\pm 2\nu$	

Table 2.1: Most favourable discovery channels of the Standard Model Higgs and corresponding mass intervals.

system, electromagnetic calorimeter and muon chambers should thus match. However, as the particle flux and irradiation dose increase with the pseudorapidity, the use of particle track detectors beyond $|\eta| \simeq 2.5$ is excluded.

ATLAS and CMS have been designed to measure electrons and muons up to $|\eta| \simeq 2.5$, corresponding to a geometrical acceptance of about 95% per lepton from a Higgs decay [10, 11]. A track reconstruction efficiency above 95% is required for isolated leptons in the rapidity range covered by the tracking system. Hermeticity is ensured by radiation hard, low resolution calorimeters covering the range $2.5 \leq |\eta| \leq 5$. Good tracking inside jets is also desireable at the LHC. Isolation cuts are effective only if most of the tracks from jets are reconstructed. The desired track finding efficiency in jets is 90%. The reconstruction of b-jets leads to a few other requirements that will be discussed in section 2.1.3.

Higgs bosons in the Minimal SuperSymmetric Model

In the absence of experimental data in contradiction with theoretical expectations, the Standard Model remains a valid model. However there are extensions of this theory that are equally consistent with the data, and that predict the existence of new particles at energies below 1 TeV. Among these extensions, the Minimal SuperSymmetric Model is attractive, as it provides a means of incorporating gravity into the quantum theory of particle interactions and allows the unification of all interactions at very high energies. The MSSM introduces an additionnal symmetry between fermions and bosons. It associates every particle of the Standard Model to a supersymmetric partner with a spin different by half a spin unit. This model leads to five physical Higgs fields:

- 2 neutral scalar fields, denoted h and H,
- 1 neutral pseudoscalar field, denoted A,
- 2 charged vector bosons, $H^\pm$.

The lightest of these particles, h, is likely to have a mass below 135 GeV/c^2 [12].

The identification of b-jets is of great importance in the search for supersymmetric Higgs bosons, as most of the discovery channels involve b-quarks. For example the lightest supersymmetric Higgs can be produced in cascade decays of supersymmetric particles, and here the channel $h \to b\bar{b}$ can be exploited thanks to the additional event signature provided by the presence of stable neutral particles in the final state [12]. The neutral Higgses can also be produced in association with a $b\bar{b}$ pair in a mechanism similar to the one shown in figure 2.4 c). In top decay, the process $t \to H^+ b$ enters in competition with $t \to W^+ b$. As the Higgs bosons decay

preferentially into heavy particles, this process would show up as a number of $t \to \tau^+ \nu_\tau b$ events in contradiction with the constant branching ratio into leptons expected if only W decays were at play [12].

2.1.3 Physics at low luminosity

The study of beauty hadrons is the main topic of the low luminosity programme at the LHC. The disintegration of B hadrons can be exploited to measure a large number of parameters of the Cabbibo-Kobayashi-Maskawa quark mixing matrix. Of particular interest are the parameters which lead to the violation of the CP symmetry in weak interactions. C and P are transformations of the particle system wave function which correspond respectively to the exchange of the particles by their antiparticles (Charge conjugation) and to the reversal of the space coordinates (Parity). We will not enter in the details of the theory. We shall instead try to find out which are the properties of B hadrons that permit their identification, and show briefly how these properties arise in the framework of the Standard Model.

Quark families and the CKM matrix

The six different types of quarks are listed in table 2.2 together with their mass range. They are grouped in three families, also called flavours, because a quark from a given family can transform into the other quark from the same family by emitting a W boson. However, it was experimentally observed that transitions between families are also possible in weak interactions, although less probable. The weak eigenstates q' are thus not identical to the flavour eigenstates q.

u 2 - 8 MeV/c^2	d 5 - 15 MeV/c^2
c 1.0 - 1.6 GeV/c^2	s 100 - 300 MeV/c^2
t $\simeq$ 175 GeV/c^2	b 4.1 - 4.5 GeV/c^2

Table 2.2: The quarks and their mass ranges [13, 14].

The relation between the two sets of eigenstates is given by the Cabbibo-Kobayashi-Maskawa (CKM) quark mixing matrix:

$$\begin{pmatrix} d' \\ s' \\ b' \end{pmatrix} = V_{\mathrm{CKM}} \begin{pmatrix} d \\ s \\ b \end{pmatrix} = \begin{pmatrix} V_{ud} & V_{us} & V_{ub} \\ V_{cd} & V_{cs} & V_{cb} \\ V_{td} & V_{ts} & V_{tb} \end{pmatrix} \begin{pmatrix} d \\ s \\ b \end{pmatrix}. \tag{2.3}$$

The CKM matrix is complex and unitary. By convention we have

$$\begin{pmatrix} u' \\ c' \\ t' \end{pmatrix} = \begin{pmatrix} u \\ c \\ t \end{pmatrix}. \tag{2.4}$$

A commonly used parametrization of the CKM matrix is [15]

$$V_{CKM} = \begin{pmatrix} 1-\frac{\lambda^2}{2} & \lambda & A\lambda^3 re^{i\delta} \\ -\lambda & 1-\frac{\lambda^2}{2} & A\lambda^2 \\ A\lambda^3(1-re^{i\delta}) & -A\lambda^2 & 1 \end{pmatrix} + \mathcal{O}(\lambda^4), \tag{2.5}$$

where the parameters λ, A, r and δ are real. The measured values of λ and A are 0.22 and 0.8 ± 0.04 [13]. The matrix elements of flavour transitions involve the corresponding elements of the CKM matrix, and thus a hierarchy appears in the probability amplitudes of quark transitions:

$$\begin{aligned} A(d \to u) &\sim V_{ud} \sim 1 \\ A(s \to u) &\sim V_{us} \sim \lambda \\ A(b \to c) &\sim V_{cb} \sim \lambda^2, \text{ etc.} \end{aligned}$$

It must be noted that a non-zero value of the phase δ gives rise to CP violation.

Properties of b-quarks useful in b-jet identification

The characteristics that distinguish the b-quark from the other quarks are its large mass and the fact that its decay modes are strongly suppressed due to the small value of the corresponding elements of the CKM matrix. Hadrons containing a b-quark are thus heavy and of noticeable lifetime, of the order of the picosecond.[3] Table 2.3 gives the masses and mean lifetimes of a few experimentally observed beauty hadrons.

Hadron	Mass (MeV/c^2)	τ (ps)	cτ (μm)
B^+	5278,9 $\pm$ 1,8	1,62 $\pm$ 0,06	486
B_d^0	5279,2 $\pm$ 1,8	1,56 $\pm$ 0,06	468
B_s^0	5369,3 $\pm$ 2,0	1,61 $\pm^{0,10}_{0,09}$	483
Λ_b^0	5641 $\pm$ 50	1,14 $\pm$ 0,08	342

Table 2.3: Masses and lifetimes of a few experimentally observed beauty hadrons. [13]

A first possible selection procedure could thus rely on the large transverse momentum of the beauty hadron decay products. Semi-leptonic decay chains lead to a high momentum lepton in the final state, a clear event signature in an environment dominated by QCD processes. However this technique suffers from the small branching ratio of beauty hadrons into leptons (BR($b \to l$) $\sim$ 18%). It can only be used in the study of frequent processes like the ones at play in B-physics.

The second method takes advantage of the lifetime of beauty hadrons. Their lifetime is such that they travel up to a few millimeters in the beam pipe before decay, giving rise to a secondary vertex displaced with respect to the vertex of the primary proton collision. The beauty hadron is thus identified by the presence of tracks not compatible with the primary vertex inside the jet. Such tracks are characterized by a non-zero impact parameter with respect to the primary vertex, i.e. a distance of closest approach to the primary vertex not compatible with zero. In addition beauty hadrons decay mostly into charmed particles with a lifetime also of the order

[3] The top quark is much heavier than the b-quark, but it decays immediately into a W boson and a b-quark and has no time to hadronize.

of the picosecond. These produce a few more tracks with an impact parameter with respect to the primary vertex, which helps the selection. For the same reason direct charm production constitutes the largest source of mistags.

The identification of b-jets with the impact parameter method is the subject of chapter 6 of this thesis. We will see that a much higher b-tagging efficiency can be reached as compared to the lepton tag technique. This method is thus more adequate for the study of rare processes and events with several b-jets in the final state. Tagging b-jets of transverse energy of several tens of GeV/c^2 requires a powerful tracking system. Of the order of 10 tracks must be reconstructed per jet, with a separation of only a few degrees between the tracks. In addition the impact parameter of the beauty hadron decay products with respect to the primary vertex is only a few hundreds of micrometres. The precision of the impact parameter measurement must thus be better than 100 μm.

2.2 The Compact Muon Solenoid

The Compact Muon Solenoid (CMS) is a detector designed for discoveries at the highest luminosity available in proton collisions at the LHC. Like most of modern collider experiments it comprises several subdetectors of complementary functions: muon chambers, calorimeters, and tracking system. Figure 2.6 shows a three-dimensional view of the CMS detector. The detector has a cylindrical shape, with an approximate symmetry in the azimuthal angle ϕ. Its overall dimensions are 15 m in diameter and 21 m in length. It will be built around a superconducting solenoid generating a uniform magnetic field of 4 Tesla inside the coil. The magnetic flux is returned through a thick saturated iron yoke instrumented with muon chambers. The iron of the yoke serves as an absorber, permitting muon identification.

Thanks to the large coil dimensions, 13 m in length and 3 m in radius, both tracking system and calorimetry can be accomodated inside the magnet coil. This prevents the performance of the calorimeters from being affected by the coil material. An electromagnetic calorimeter of excellent energy resolution is indeed required in order to permit the discovery of the Higgs in the two photon channel. The main task of the inner tracker is to measure accurately the momentum of charged particles. The tracker constitutes a substantial amount of material in front of the electromagnetic calorimeter, which renders the measurement of photons and electrons difficult. The reason for this thick tracker is the high particle rate expected at the LHC, which can only be handled with a large number of small detection cells.

Online event selection is needed in order to reduce the event rate from 10^9 Hz down to less than 100 Hz, which is the maximum rate that can be archived for offline analysis. This selection, called "triggering", is one of the key problems at the LHC, as it determines the whole subsequent analysis. The 10^7 rate reduction factor is achieved with a staged trigger system selecting potentially interesting events with a clear signature (high p_T leptons and photons, high p_T jets, imbalance in transverse energy,...). This selection is performed on the basis of a subset of the detector data. A pipelined data flow is necessary to avoid dead time during the trigger decision.

2.2.1 The muon system

The muon system [16] is composed of four muon stations interleaved with the flux return yoke plates. It is divided into a central part ($|\eta| \leq 1.2$) and a forward part ($0.9 \leq |\eta| \leq 2.4$) as can be seen in figure 2.6. The muon detector should fulfill three basic tasks: muon identification, trigger, and momentum measurement. Muon identification relies on the fact that, in contrast

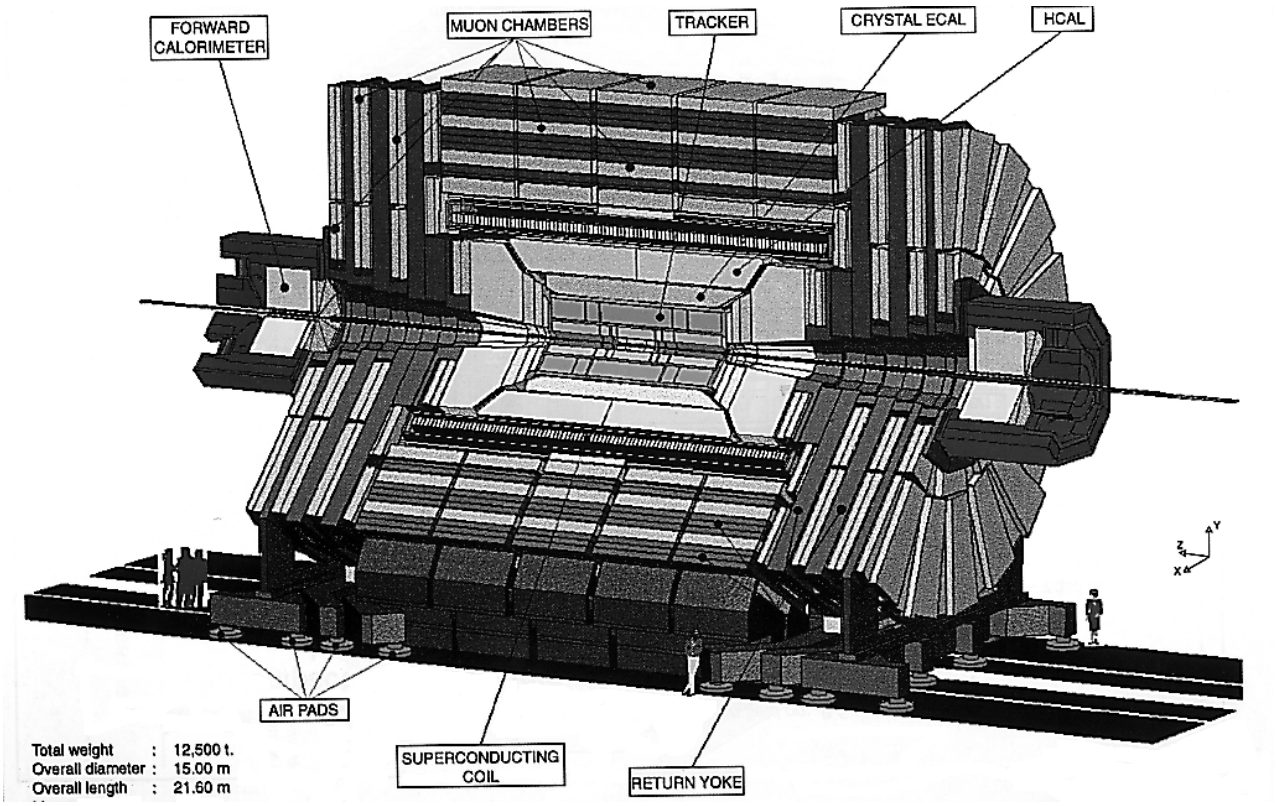

Figure 2.6: A three-dimensional view of the CMS detector.

with most charged particles, muons do not interact much with matter. The muon detector can be placed outside the magnet coil, after the calorimeters, which reduces the hadron background. Furthermore the total thickness of absorber before the last muon station amounts to 16 nuclear interaction lengths, so that only muons can reach it.

As part of the new physics shows up by the presence of muons of high transverse momentum in the final state, the muon detector has to take part in the trigger decision. It must therefore be composed of fast detectors, delivering a signal that can be associated to a single bunch crossing, and capable of providing a fast estimation of the muon transverse momentum in order to allow p_T cuts at the trigger level.

The CMS muon system is requested to measure the transverse momentum with an accuracy between 8 and 40% for muons of p_T between 10 and 1000 GeV/c. This can be done in two ways. As the muon track gets curved by the magnetic field in the return yoke, a sagitta measurement allows to determine the muon transverse momentum. The second way is to measure the muon direction in the transverse plane just after the magnet coil. For muons originating from the beam crossing point the angle of the track with respect to the radial direction is directly related to the transverse momentum. We shall now briefly describe the three technologies chosen for the muon detector in CMS.

Drift tubes

The drift tubes (DT) used in CMS are drift chambers of 4×1.1 cm^2 section filled with an Ar-CO_2 gas mixture. The use of drift tubes is limited to the barrel part of the muon system. In this region the particle rate is expected to be below 10 Hz/cm^2, allowing a response time of

the order of 400 ns with a cell occupancy below 1%. This response time matches the maximum electron drift time measured in the DT's. In addition the magnetic field between the barrel iron yoke plates is almost zero, which prevents the electron drift lines from being distorted.

Each barrel muon station comprises twelve layers of drift tubes grouped four by four. Two groups measure the coordinates of the muon crossing point in the (R, ϕ) plane and the third group measures the coordinate along the beam. The spatial resolution of each layer is better than 250 μm. The 23 cm lever arm between the $R\phi$ groups allows to measure the muon direction in the transverse plane with an accuracy of about 1 mrad. The time resolution of the drift tubes is about 5 ns when averaging the drift time measured in the four layers of a group.

Cathode strip chambers

The forward muon spectrometer is composed of cathode strip chambers (CSC). These counters are well suited to the conditions met in the forward part of the muon system (rates up to 1 kHz/cm^2 and a high magnetic field between the yoke plates). The chambers have a trapezoidal shape and are filled with an Ar-CO_2-CF_4 gas mixture. The cathode strips are radial. In these conditions spatial resolutions of about 75 μm in the $R\phi$ coordinate have been reached. The anode wires are strung perpendicularly to the mid cathode. They are read out to measure the radial coordinate and to provide bunch crossing identification. Each forward muon station comprises six CSC layers.

Resistive plate chambers

The muon trigger system also requires detectors capable of reacting in less than 1 LHC bunch crossing interval. This is achieved with resistive plate chambers (RPC), of which the time resolution is better than 3 nanoseconds. The RPC's cover the rapidity range $|\eta| < 2.1$ with 160000 cells projective in ϕ. In the barrel muon detector, two layers of RPC's are accomodated per muon station in the first two stations, and one layer per station in the two outer stations. This arrangement allows to trigger on low p_T muons. The minimum transverse momentum required to reach the first (second) muon station is indeed 2.5 GeV/c (8 GeV/c). In the forward muon detector one layer of RPC is foreseen per muon station.

2.2.2 The electromagnetic calorimeter

The principle of the electromagnetic calorimeter (ECAL) is to absorb the energy of photons and electrons and to deliver a signal proportional to the deposited energy. The electromagnetic calorimeter plays a very important role in the study of the $H \rightarrow \gamma\gamma$ channel as well as in the measurement of electrons from W and Z decays in the $H \rightarrow WW, ZZ$ channels. The energy resolution of the calorimeter must be excellent, which leads to the choice of an homogeneous crystal calorimeter. The crystals should also have a fast response as the ECAL information must be available at the trigger level.

The CMS electromagnetic calorimeter [17] is divided into a central part covering the pseudorapidity range $|\eta| < 1.48$, and a forward part in the range $1.48 < |\eta| < 2.6$. Crystals will also be placed in the region between 2.6 and 3 in pseudorapidity to improve hermeticity. The relative energy resolution σ/E can be parametrized as:

$$\left(\frac{\sigma}{E}\right)^2 = \left(\frac{a}{\sqrt{E}}\right)^2 + \left(\frac{\sigma_n}{E}\right)^2 + c^2, \tag{2.6}$$

where $a/\sqrt{E}$, σ_n/E and c are the stochastic, noise and constant terms. At high luminosity the contributions of the different terms are expected to be $a = 2.7\%$, $\sigma_n = 210$ MeV, $c = 0.55\%$ for

the barrel part, and $a = 5.7\%$, $\sigma_n = 915$ MeV, $c = 0.55\%$ for the endcaps, E being expressed in GeV in formula 2.6. The difference in performance between the central and forward parts is mainly due to the presence of a preshower detector in front of the forward crystals (see later in the text) and to the increase of the pile-up noise at large η.

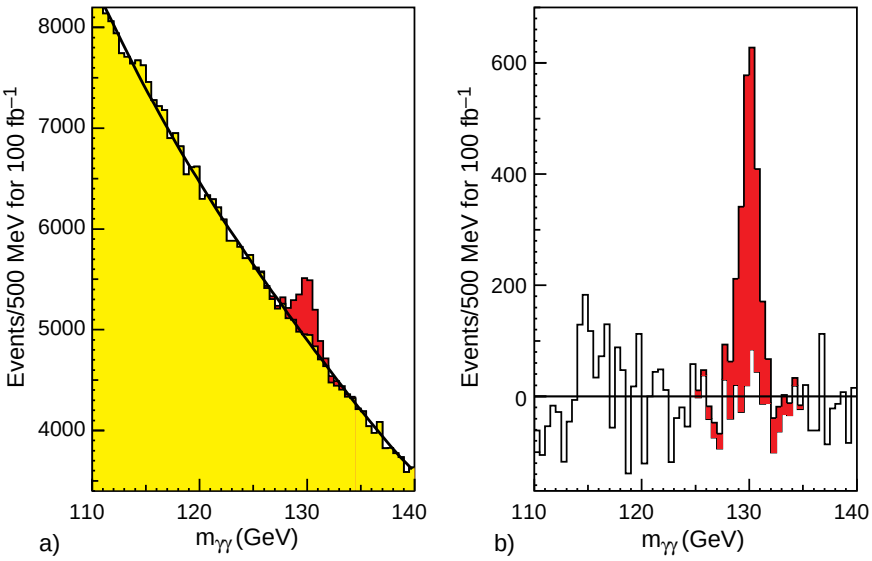

Figure 2.7: Higgs signal in the channel $H \rightarrow \gamma\gamma$ for $m_H = 130$ GeV/c^2 after an integrated luminosity of 10^5 pb^{-1}, (a) before, and (b) after background subtraction. [17]

Figure 2.7 illustrates the performance of the CMS electromagnetic calorimeter in reconstructing the mass of a Higgs of 130 GeV/c^2 in the two photon channel, after an integrated luminosity of 10^5 pb^{-1}. The mass resolution is around 650 MeV/c^2 and the signal significance is above 12. After an integrated luminosity of 10^5 pb^{-1} the Higgs should be discovered in the two photon channel in the mass range from 85 to 150 GeV/c^2 with a significance above 5.

Crystals

Lead tungstate ($PbWO_4$) has been chosen as an active material for the CMS electromagnetic calorimeter because of its short radiation length and small Molière radius, and the existence of production plants capable of delivering the 83000 crystals needed in due time. The radiation length and Molière radius of $PbWO_4$ are respectively 0.89 cm and 2.19 cm. The crystals are arranged in a projective way in η and ϕ. The dimensions of the crystal front face are typically 2.2×2.2 cm^2, matching the Molière radius of $PbWO_4$. The corresponding granularity in $\Delta\eta \times \Delta\phi$ is 0.0175×0.0175 in the barrel region and up to 0.05×0.05 in the forward region. The length of the crystals is equivalent to 26 radiation lengths. This absorber thickness is necessary in order to limit the longitudinal shower leakage to an acceptable level.

Preshower

In the endcaps, above $|\eta| = 1.65$, the calorimeter granularity is not sufficient to distinguish a single photon from the two photons from a π^0 meson decay. To improve on π^0/γ separation, a preshower composed of two silicon strip planes alternating with lead converters will be installed in front of the crystals in the rapidity range $1.65 < |\eta| < 2.6$. A π^0 rejection factor of 2 - 3 can be achieved with this setup.

2.2.3 The hadron and very forward calorimeters

The main goal of the hadron calorimeter (HCAL) is to measure the energy and direction of hadron jets [18]. The requirements are the following. A fine segmentation is needed in order to separate nearby jets, like in the process $H \rightarrow W^+W^- \rightarrow l\nu + 2$ jets, and to measure the jet direction with sufficient precision. A good hermeticity is necessary in order to detect and measure an imbalance in transverse energy. Missing E_T would indeed be, together with b-jets, one of the clearest signatures of supersymmetry. The granularity chosen is $\Delta\eta \times \Delta\phi = 0.087 \times 0.087$. The HCAL covers the rapidity range $|\eta| \leq 3$, and a very forward calorimeter extending up to $|\eta| = 5$ completes the coverage. A moderate energy resolution of square root of $(100\%/\sqrt{E})^2 + (4.5\%)^2$ is adequate.

An absorber thickness of 7 nuclear interaction lengths is required in order to contain 95% of the energy of a hadronic shower [13]. The absorber chosen for the CMS hadron calorimeter is copper, as it is non-magnetic and has a short interaction length (15 cm). Copper layers will be interleaved with plastic scintillator tiles read out by wavelength shifting fibers. In the barrel part of the hadron calorimeter, the amount of absorber that can be accomodated inside the magnet coil is only 5.15λ. To ensure adequate sampling depth for the entire rapidity coverage, the first plates of the magnet return yoke will be instrumented with scintillator tiles to form an outer hadron calorimeter.

2.2.4 The central tracking system

The purpose of the central tracking system is to reconstruct the trajectory of charged particles. In particular, the tracker allows to measure the momentum and direction of charged particles at their production vertex.

In vacuum, in a uniform magnetic field, charged particles describe a helicoidal trajectory around the field axis. The curvature of the track is directly related to the component of the momentum in the plane transverse to the field:

$$p_T = qBR_c, \tag{2.7}$$

where q is the particle charge, B is the magnetic field intensity, and R_c is the radius of curvature. In a practical unit system this expression reads

$$p_T[\mathrm{GeV}/c] = 0.3\ B[\mathrm{T}]\ R_c[\mathrm{m}]. \tag{2.8}$$

for a particle of charge e. Thus in principle the transverse momentum can be determined by measuring the (x, y) or (R, ϕ) coordinates of a set of points along the track in the plane transverse to the magnetic field, and by fitting a circle through the measured points. In practice the situation is more complicated, since the particles lose energy and are scattered in the tracker material. Energy loss and multiple scattering are not negligible in position sensitive detectors like the ones that will be used at the LHC, as will be shown later.

The particle momentum is computed as

$$p = p_T / \sin\theta, \tag{2.9}$$

where θ is the angle of the particle direction with respect to the field axis. The value of θ is calculated from the z-coordinates of the measured points.

Momentum resolution

The above formulas show that the momentum resolution has contributions from the errors on the track curvature and on the polar angle. Each of these errors has in turn two contributions, one from the spatial resolutions of the detectors and one from multiple scattering in the material traversed by the particle. The expressions of the different contributions to the momentum resolution can be found in references [19, 20]. We discuss here the behaviour of the dominant terms.

As the errors on p_T and θ are practically independent, the momentum resolution can be written as:

$$\left(\frac{\Delta p}{p}\right)^2 = \left(\frac{\Delta p_T}{p_T}\right)^2 + \left(\frac{\cos\theta}{\sin\theta}\Delta\theta\right)^2. \tag{2.10}$$

If the scattering errors are neglected, the second term turns out to be

$$\left(\frac{\Delta p}{p}\right)_\theta = f_n \cos\theta \sin\theta \frac{\sigma_z}{L_T}, \tag{2.11}$$

where σ_z is the z-resolution of the position sensitive detectors and L_T is the length of the particle path projected onto the transverse plane. The factor f_n depends on the number of measurement points and on their distribution along the track. For n uniformly spaced points it is given by

$$f_n \simeq \sqrt{\frac{12(n-1)}{n(n+1)}} \quad \text{for } n > 10. \tag{2.12}$$

With a typical z-resolution of 1 mm and a tracker radius of 1 m, the contribution of the error on the polar angle is below 10^{-3} and can be neglected as compared to the other contributions.

The error on p_T due to the spatial resolution of the detectors is referred to as the intrinsic momentum error. It can be written as

$$\left(\frac{\Delta p_T}{p_T}\right)_{R\phi} = \frac{a_n \sigma_{R\phi}}{0.3 B L_T^2} p_T, \tag{2.13}$$

where $\sigma_{R\phi}$ is the spatial resolution of the detector elements in $R\phi$. The variables are expressed in the same units as in formula 2.8. The factor a_n can be computed as

$$a_n \simeq \sqrt{\frac{720}{n+4}} \quad \text{for } n > 10 \tag{2.14}$$

in the case of uniformly spaced points. The intrinsic momentum error is thus an increasing function of the particle transverse momentum. At the LHC, in order to determine the charge of the most energetic particles ($p_T \simeq 2$ TeV/c), the experiments must combine a large tracking system, a high magnetic field and detectors of very good spatial resolution. The goal in CMS is to reach an intrinsic momentum resolution around $10^{-4} p_T$ (p_T in GeV/c). The CMS tracker is imbedded in the 4 T magnetic field and has a radius of 1.2 m. It will measure on average 12 points along the particle path. An average $R\phi$-resolution of about 25 μm per point is thus required.

Multiple scattering in the tracker material sets a lower limit to the momentum resolution. This limit can be expressed as a function of the thickness of material traversed by the particle. In the approximation of an homogeneous material distribution it reads:

$$\left(\frac{\Delta p}{p}\right)_{m.s.} = \frac{0.06 \text{ [Tm]}}{\beta B L_T} \sqrt{\frac{L}{X_0}}, \tag{2.15}$$

where L is the track length inside the tracker, X_0 is the average radiation length of the material traversed and $\beta = v/c$ is the particle velocity. This expression shows that the contribution of multiple scattering to the momentum resolution is independent of the particle momentum (β is close to 1 for all particles of interest).

Consequently, the intrinsic momentum resolution is the dominant error for particles of high transverse momentum, while at low transverse momentum the tracker performance is spoiled by multiple scattering. In the CMS tracker, the amount of material encountered by the particles is relatively large, between 0.2 and $0.6X_0$ depending on the pseudorapidity. The momentum resolution is thus limited to 0.5 - 1% for particles of p_T below 10 - 20 GeV/c. The intrinsic resolution dominates only at transverse momenta above 50 - 100 GeV/c.

Requirements

The CMS tracker must be able to reconstruct most of the tracks of charged particles down to the lowest transverse momentum possible (1 GeV/c at high luminosity). The required reconstruction efficiency is 95% for isolated tracks and 90% for tracks in jets. The desired momentum resolution for high p_T particles is $\Delta p/p \simeq 0.1 p_T$ (p_T in TeV/c). These performance requirements lead to the choice of tracking elements with a very high detection efficiency, close to 100%, and a very good spatial resolution, 25 μm on average.

The event rate and particle flux at the LHC also impose

- that the detectors be very fast, with response time below 50 ns;
- that the detection cells be very small, in order to keep the occupancy of the readout channels to the level of a few percent. This leads to a number of channels close to 10^8;
- that the technologies chosen be radiation resistent.

In addition, the amount of material inside the central tracking system should be reduced as much as possible. The main reason is that any absorber in front of the electromagnetic calorimeter causes bremsstrahlung and photon conversions, and thus deteriorates the measurement of electrons and photons in the calorimeter. A light tracker also performs better in measuring low momentum charged particles, as explained in the previous section.

Description of the tracker

Figure 2.8 shows a longitudinal section of the CMS tracker. This layout corresponds to the version V3 of the tracker design [21], which is the version studied in this thesis. The tracker is composed of silicon pixel detectors, located close to the beam pipe at distances between 7.5 and 15 cm, silicon strip detectors at radii between 20 and 52 cm, and micro-strip gas counters at radii between 60 and 120 cm. Solid state technologies were chosen for the innermost detection layers, as they permit small cell sizes coping with the high particle rate close to the beam, and high spatial resolution for precise vertex reconstruction. Micro-strip gas counters, of larger detection cells and worse resolution but also lower cost, were preferred for the outer layers.

Each subdetector is divided into a barrel part, composed of cylindrical detection layers, and a forward part, made of disk shaped detection plates. The barrel counters measure the $R\phi$ and z-coordinates of the particle crossing points, while the R-coordinate is determined by the radius of the detection layers. The forward counters measure $R\phi$ and R, and the position of the forward disks along the beam pipe gives the z-coordinate. The detector elements are arranged in such a way that each detection layer presents a complete coverage in ϕ and η. Particles of transverse momentum above 1 GeV/c emitted at the primary vertex traverse on average 12 - 13

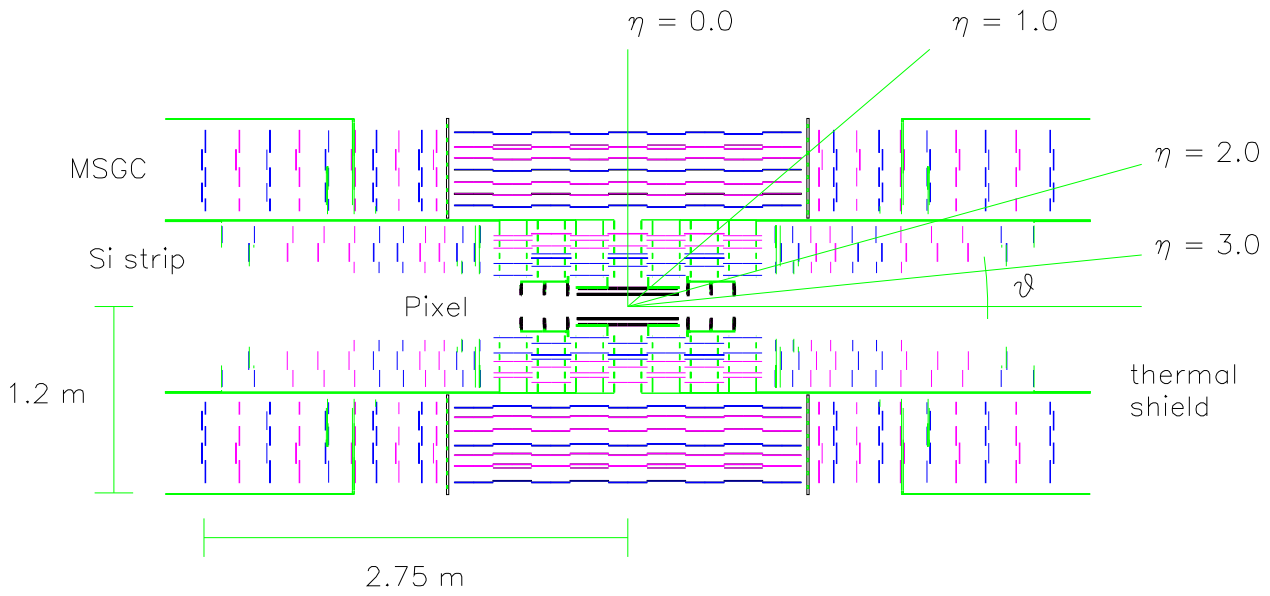

Figure 2.8: Longitudinal section of the CMS tracker version V3.

detection layers in the rapidity range $|\eta| \leq 2.6$. Table 2.4 summarizes the number of channels, cell sizes and spatial resolutions of the different detector types.

Detector	Cell size	$R\phi$ resolution	z or R resolution
Pixel barrel	125 μm $\times$ 125 μm	15 μm	15 μm
Pixel forward	50 μm $\times$ 300 μm	15 μm	90 μm
Number of channels	7.7×10^7		
Si strip single sided	100 μm $\times$ L	15 μm	$L/\sqrt{12}$
Si strip double sided	67 μm / 200 μm $\times$ L	15 μm	1 mm
Number of channels	3.5×10^6		
MSGC single sided	200 μm $\times$ L	40 μm	$L/\sqrt{12}$
MSGC double sided	200 μm / 400 μm $\times$ L	40 μm	2 mm
Number of channels	7.5×10^6		

Table 2.4: Cell sizes, intrinsic resolutions and number of channels of the different tracker elements. Here L stands for the detector striplength.

Pixel counters allow to measure simultaneously two coordinates with high precision. The pixel tracker comprises two barrel layers and six endcap disks, three on each side. Its main goals are to improve the determination of the charged particle impact parameter in order to permit the identification of b-jets, and to allow vertex reconstruction in three dimensions thanks to the good resolution in both coordinates measured (see table 2.4).

The silicon strip tracker is composed of four barrel layers and twenty-two forward disks, eleven on each side. It extends up to 2.65 m in z in order to provide precise $R\phi$ measurements in the rapidity range above 2.2. The barrel counters are inclined by 7^o with respect to the radial direction in order to compensate for the effect of the magnetic field on the drift direction of the charge carriers. No such tilt is required in the endcaps as the magnetic field is parallel

to the drift direction. Half the detection layers are double sided. The strips of the single sided detectors are parallel to the beam in the barrel counters and radial in the forward counters, in order to measure $R\phi$ with high precision (15 μm). In double sided detectors, the strips of the second readout side run at an angle of 60 mrad with respect to the $R\phi$ strips. The combination of the two readout sides allows to measure the second coordinate with an accuracy of about 1 mm.

The outer layers of the CMS tracker will be composed of detectors of a recent type, called micro-strip gas counters (MSGC). Since its introduction by A. Oed in 1988 [22], the qualities of the MSGC have been demonstrated in many respects. Because of its low price per surface unit, about five times cheaper than solid state detectors, the MSGC is an adequate technology to equip large detection surfaces in high luminosity experiments. The MSGC tracker consists of seven barrel layers and ten endcap wheels on each side. The Belgian experimental high energy physics groups contribute to the design and construction of the endcap MSGC wheels. They have proposed an assembly scheme in which trapezoidal detectors are mounted side by side in ring-shaped gas volumes without gas tight wall between them, as illustrated in figure 2.9. This design minimizes the dead space between counters and the amount of material inside the tracker. The present thesis is a study of the CMS tracker, with a focus on the forward MSGC modules. A detailed description of micro-strip gas counters can be found in chapter 3.

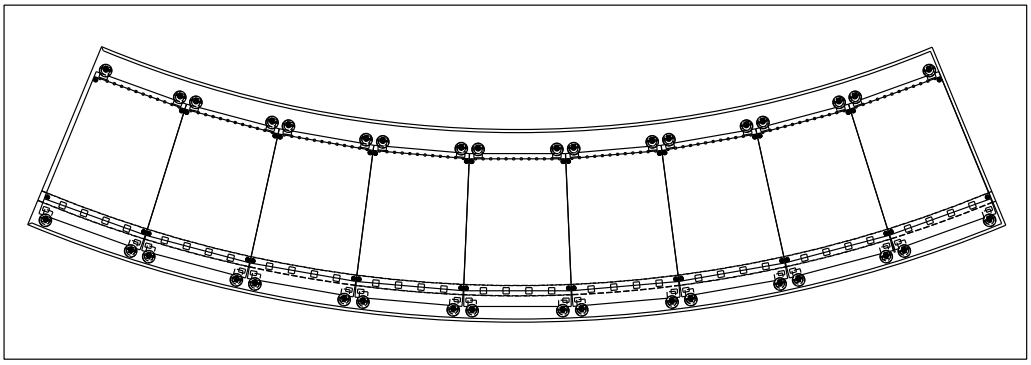

Figure 2.9: Nine forward MSGC counters mounted side by side in a ring-shaped gas volume.

The MSGC strip layout is similar to the one of the silicon strip tracker, with $R\phi$ strips in single sided modules and $R\phi$ plus small angle stereo strips in double sided modules. The stereo angle is 50 mrad, allowing to measure the second coordinate with a precision better than 2 mm. In the forward counters, the striplength is varied from 14 to 8 cm from the outermost to the innermost ring, to cope with the increase of particle rate with decreasing distance to the beam. The intrinsic resolution of the CMS MSGC's is 30 - 40 μm in $R\phi$ for particles of transverse momentum above 10 GeV/c. In the barrel counters this resolution is achieved by tilting the detectors by 14^o to compensate for the effect of the magnetic field. To account for mechanical misalingments between counters, the target resolution per layer in $R\phi$ is 50 μm.

Amount of material

Figure 2.10 (left plot) shows the amount of material inside the tracker, expressed in fractions of radiation length, as a function of the pseudorapidity. It ranges between 0.2 and 0.6 with a maximum in the forward region. Electrons emitted at $\eta = 2$ will on average lose 45% of their energy by bremsstrahlung before reaching the electromagnetic calorimeter. In the case

of photons, the probability of conversion before the calorimeter at $\eta = 2$ is as high as 37%. The tracker thus significantly affects the measurement of electrons and photons. Moreover, a fraction of the hadron flux is also absorbed in the tracker. Figure 2.10 (right) shows the equivalent tracker thickness in nuclear interaction lengths. On average 20% of the hadronic projectiles will experience strong interactions in the detector material.

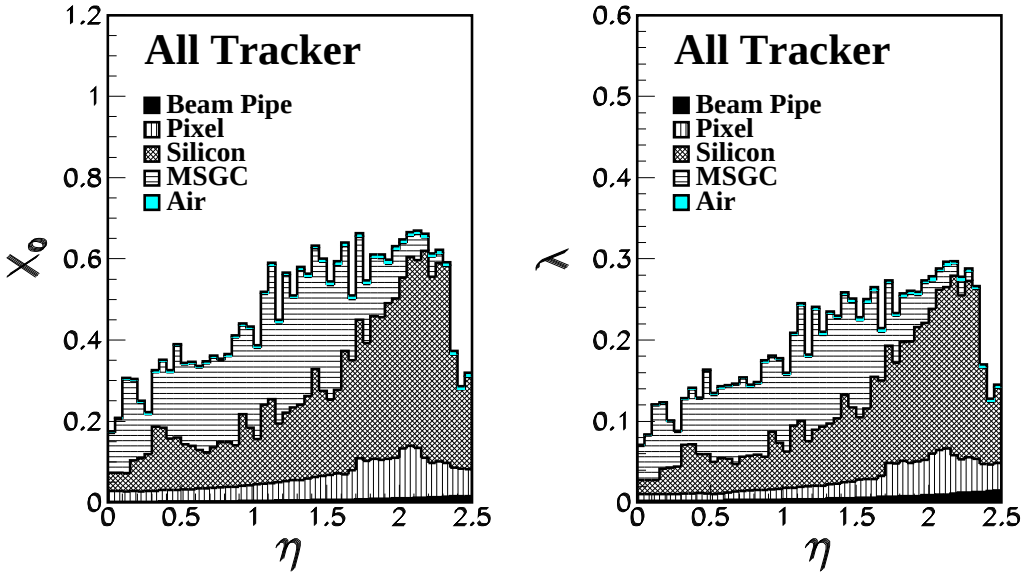

Figure 2.10: Thickness of the CMS tracker as a function of the pseudorapidity, in radiation lengths (left) and interaction lengths (right).

Radiation environment

The most critical issue for the CMS tracker is the long term behaviour of the detector elements and their readout electronics under heavy irradiation. The tracking system must be designed to guarantee stable operating conditions for several years of running at the highest LHC luminosity. The irradiation originates from two main sources: a direct particle flux emerging from the interaction region, and the backscattering of neutrons produced in nuclear reactions in the material of the electromagnetic calorimeter.

Figure 2.11 gives the radiation dose, neutron and charged hadron fluences in the tracker as a function of z, at various distances to the beam R, for an integrated luminosity corresponding to ten years of LHC operation. The charged particle flux is approximately constant with z and decreases roughly as $1/R^2$, as expected from calculations based on a constant η distribution of secondary particles. It ranges between 10^{15} cm^{-2} at the innermost pixel layer and 3×10^{12} cm^{-2} at the outermost MSGC layer. The neutron flux instead rises when approaching the endcap calorimeter, and the drop of the direct neutron flux at large radii is partly cancelled by neutron albedo from the barrel calorimeter.

A detailed description of the radiation damage suffered by silicon devices can be found in [23]. Radiation hard processes (DMILL, Harris, Honeywell) are currently investigated for the production of the tracker front-end electronics, which in the case of the pixel detectors must be qualified up to 100 Mrad (10^6 Gy) of radiation dose. In silicon detectors the most critical effect is the change of doping concentration in the bulk of the substrate material. This leads to an increase of the depletion voltage, which can eventually exceed the breakdown limit of the

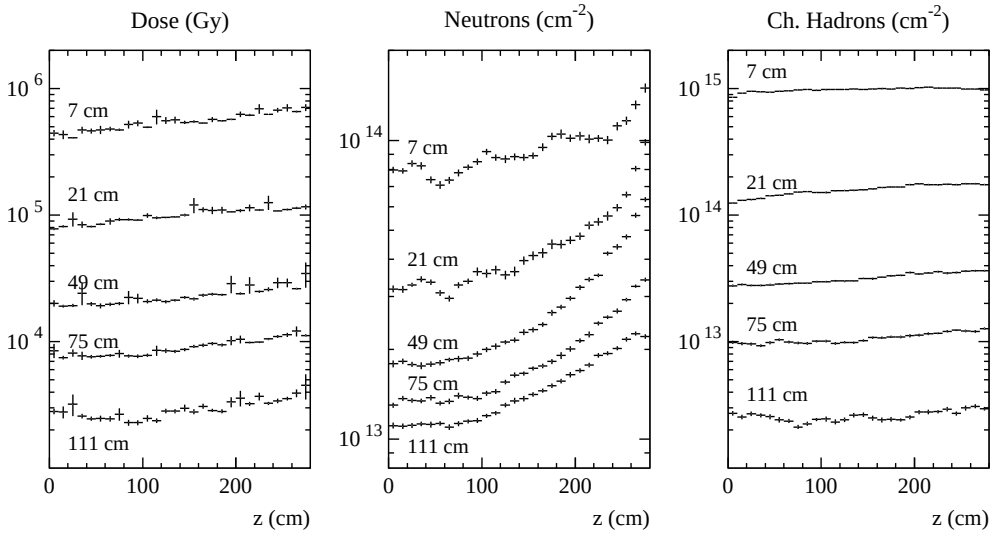

Figure 2.11: Radiation dose, neutron and charged hadron fluences in the CMS tracker as a function of z and R, after an integrated luminosity of 5×10^5 pb^{-1}. [23]

material. In order to survive to several years of running, the CMS solid state detectors will be kept at low temperature. A thermal shield will separate the silicon strip and pixel counters operated at -10^oC from the MSGC's operated at room temperature. Long term stability of MSGC's at the LHC is also a major issue. This problem will be discussed in detail in the next chapter.

Chapter 3

The Micro-Strip Gas Counter

The Micro-Strip Gas Counter (MSGC) is a relatively novel development of gaseous detectors, similar to the multi-wire proportional chamber, but with greatly improved characteristics thanks to the use of microelectronics technology for its fabrication. This chapter discusses the use of the micro-strip gas counter as a high energy particle track detector. As a good knowledge of gaseous counters is required in order to understand the experimental results shown here and in the next chapters, the basic principles of charged particle detection with gaseous detectors are first presented. The MSGC's are then described in detail, and the MSGC performance in various conditions is discussed. The current best choice of MSGC parameters and working conditions for use in the central tracker of the CMS detector is highlighted. In the last section, alternative gas detectors also produced with microelectronics techniques are briefly described.

3.1 Gaseous detectors

The detection and identification of particles is based on their interaction with matter. The incoming particle loses part or all of its energy inside the material that constitutes the active medium of the detector. In the case of gas filled detectors, the active material is a gas, and the lost energy is transferred into excitation and/or ionization of the gas atoms or molecules. This excitation or ionization is in turn amplified and converted into an electric signal.

As an illustration let us consider the cylindrical proportional counter of figure 3.1. It consists of a gas filled cylindrical volume, with a thin wire in its middle. The wire is set to a high positive voltage with respect to the outer cylindre. First the incident particle ionizes the atoms or molecules of the gas inside the detector. Then, the released electrons drift towards the anode wire under the action of the electric field which reigns inside the counter. The electric field intensity rises as the inverse of the distance to the counter axis and, in the neighbourhood of the wire, the electrons are accelerated up to energies high enough to ionize other gas molecules, in a process called "avalanche". The motion of the ions and electrons generated in the avalanche towards the electrodes induces an electric signal that can be measured. In this section, we shall first discuss the interaction of particles with matter. We shall then describe the drift and diffusion of the charges inside the gas under the action of the detector electric field. In the next paragraph we will say a few words on the gas amplification process. Finally the signal induction on the electrodes will be studied.

3.1.1 Interaction of particles with matter

Two different types of interaction must be considered for particle detection, i.e. electromagnetic and nuclear interactions. In gaseous detectors, the electromagnetic interaction is the most

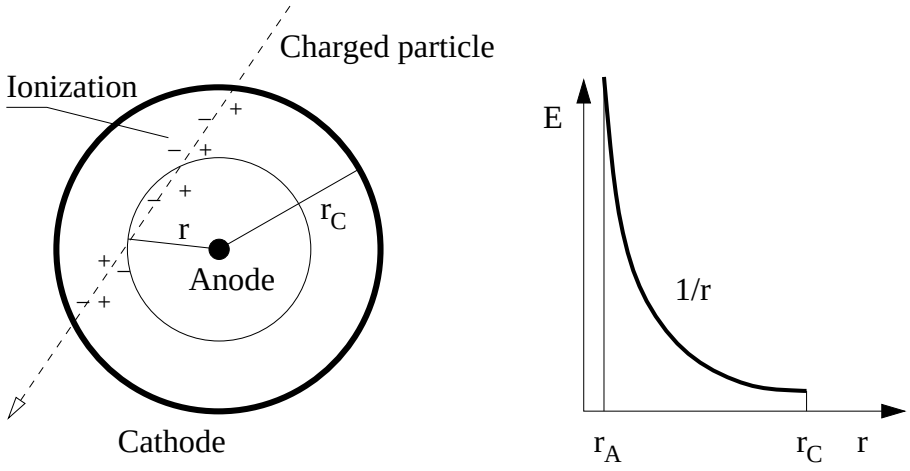

Figure 3.1: Transverse section of a cylindrical proportional counter. The plot to the right shows the intensity of the electric field E as a function of the distance to the counter axis r, between the surface of the anode wire ($r = r_A$) and the outer cathode ($r = r_C$).

important in terms of energy loss, and will therefore be described in detail. Nuclear interactions are less probable and will not be discussed much here. For this work it is enough to remember that a nuclear reaction between the incoming hadron and a nucleus of the matter causes the production of ionizing secondary particles, induced by a nuclear reaction between the incoming hadron and a nucleus of the matter.

For charged particles, the following electromagnetic processes are possible:

- collisions with atomic electrons, creating excited atoms or electron-ion pairs. For relativistic particles heavier than the electron this is the primary source of energy loss. This process will be discussed extensively, as it governs the signal development in gaseous detectors.
- emission of bremsstrahlung photons in the Coulomb field of the nuclei and of the atomic electrons. The energy loss due to these processes is proportional to the ratio between the particle energy and the inverse of its mass squared, and will therefore become large at energies depending very much on the particle mass. For electrons, in materials such as lead, it already dominates the ionization loss at energies of the order of 10 MeV, while for muons and pions this transition happens at several hundreds of GeV.
- elastic scattering on the nuclei and on the atomic electrons, being responsible for modifications in the particle trajectory.

For photons, three electromagnetic phenomena are of importance:

- the photoelectric effect, in which the photon energy is absorbed by an atomic electron;
- the Compton effect, which corresponds to the diffusion of the photon by an atomic electron;
- the conversion of the photon into an electron-positron pair, in the Coulomb field of a nucleus or of an atomic electron.

Although the first two effects play an important role in X-ray detection with gaseous detectors, we shall only discuss pair creation, as it is the only relevant process in the framework of tracking at high energy.

Electromagnetic loss of charged relativistic particles in matter

Relativistic charged particles heavier than the electron lose energy essentially by collisions with the electrons of the medium traversed, creating excited or ionized atoms. The first quantum-mechanical formulation of this problem is due to Bethe, in 1930. He related the electromagnetic loss to the differential momentum transfer cross section between the incident particle and the atomic electrons. The mean energy loss per unit length of traversed material, normalized to the density of the medium, is given by the Bethe-Bloch formula:

$$-\frac{dE}{\rho dx} = \frac{Kz^2Z}{A\beta^2}\left[\frac{1}{2}\ln\frac{2m_ec^2\beta^2\gamma^2T_{max}}{I^2} - \beta^2 - \frac{\delta}{2}\right]. \tag{3.1}$$

Here ρ, A and Z denote the density, atomic weight and atomic number of the medium, m_e is the electron mass, and ze, $\beta = v/c$, $\gamma = (1-\beta^2)^{-1/2}$ are the charge, velocity and Lorentz factor of the incident particle. Here T_{max} is the maximum kinetic energy that can be transferred to a free electron in a single collision. For a point-like charged particle it is equal to:

$$T_{max} = \frac{2m_ec^2\beta^2\gamma^2}{1 + 2\gamma m_e/M + (m_e/M)^2}, \tag{3.2}$$

where M is the mass of the incident particle. T_{max} is about 100 MeV for 1 GeV muons. The numerical value of K is 0.307 MeV g^{-1} cm^2. The quantity I is an effective excitation potential averaged over all electrons, and is approximately equal to $10Z$ electron-Volts. The term $\delta/2$ is a correction due to the polarization of the medium and will be discussed below.

The Bethe-Bloch function is shown in figure 3.2, for various materials. In all practical cases, the ionization loss in a given medium is a function only of the velocity β of the incoming particle, and does not depend on its mass.[1] Except for hydrogen it also only slightly depends on the chemical composition of the medium, the ratio Z/A decreasing slowly with increasing Z. At low energy, the ionization loss drops steeply with increasing β, then reaches a broad minimum at $\beta\gamma = 3-4$. At relativistic energies ($\beta \simeq 1, \gamma \gg 1$), a logarithmic increase is seen, arising from two causes. The first cause is that the transverse component of the electric field due to the incident particle, when transformed into the laboratory frame, acquires a relativistic factor γ. Thus the field due to the particle extends to greater distances from the trajectory, and more distant collisions become important. The second cause is the increase of the maximum transferable energy T_{max}, which rises as γ^2.

At ultra-relativistic speeds, the measurable ionization loss levels off to reach a constant value, the Fermi plateau. The canceling of the relativistic rise has two origins. On the one hand, the electric field of the incident particle polarizes the medium, which leads to a screening effect limiting the field extension. On the other hand, high energy knock-on electrons will escape from the detection medium, so that the contribution of collisions with energy transfers between a certain value T_{cut} and T_{max} will not be measured. There is less than a factor two between the minimum energy loss and the Fermi plateau. Most of the particles produced in today's high energy physics experiments have an ionization loss close to the minimum, and are therefore called Minimum Ionizing Particles or MIP's.

In many applications it is also important to know the fluctuations of the energy loss. Landau [24], in 1944, was the first to derive the distribution $F(x,\Delta)$ of the energy loss Δ in a material layer of thickness x. He considered the atomic electrons as free, and used Rutherford scattering

[1] A minor dependence on M is introduced through T_{max}, but it only becomes sizeable at the highest energies, about 100 GeV for pions.

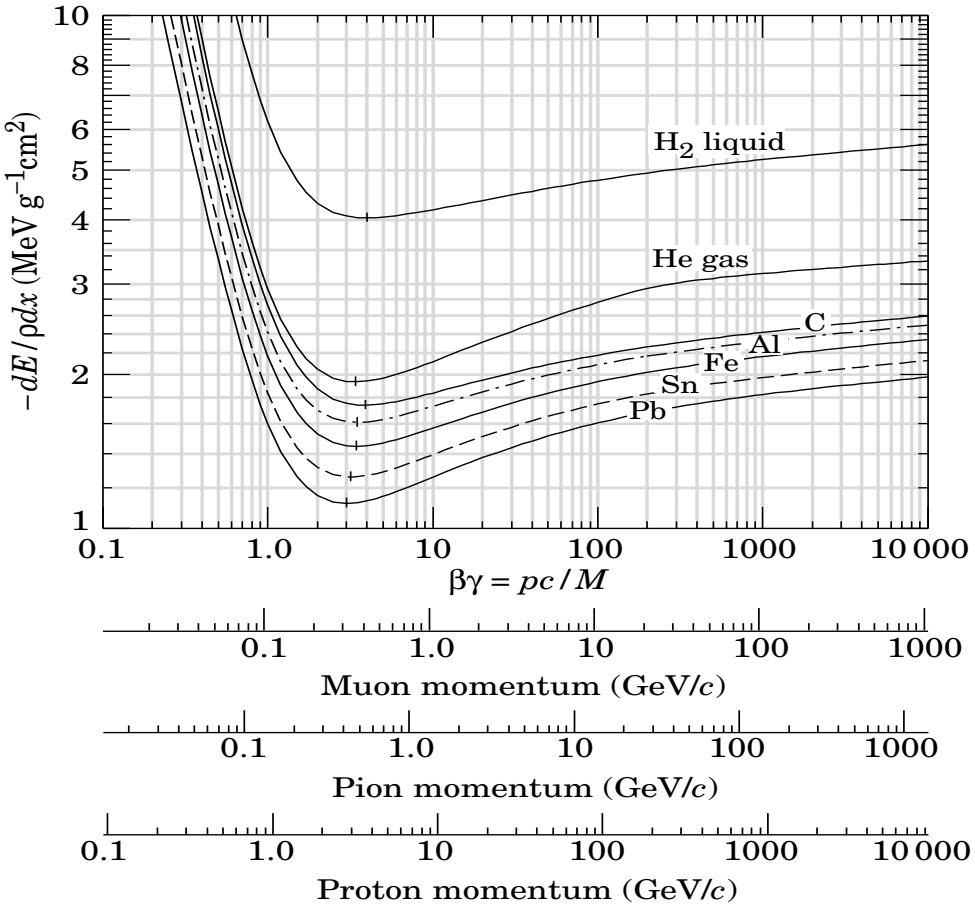

Figure 3.2: Specific electromagnetic energy loss as a function of the particle momentum, for muons, pions and protons, in various materials.

to describe the interaction between the incident particle and the atomic electrons. He obtained an universal function ϕ of only one reduced variable λ:

$$F(x,\Delta)d\Delta = \phi(\lambda)d(\lambda), \qquad \text{with } \lambda = \left(\frac{\Delta - \Delta_0}{\xi}\right). \tag{3.3}$$

The parameters Δ_0 and ξ are respectively the most probable energy loss and a scaling factor, which theoretical expressions derive both from Landau's theory. The expression of ξ as a function of the thickness x is:

$$\xi = \frac{K}{2}\frac{Z}{A}\frac{\rho x}{\beta^2}, \tag{3.4}$$

where K is the same constant as in equation 3.1.

The Landau theory only holds when the energy loss fluctuations are dominated by the contribution of collisions in which the electrons can actually be considered as free, i.e. in which the energy transferred to the electron is large as compared to its binding energy. In other terms, collisions with small energy transfers should be so frequent that their sum does not fluctuate anymore. This can be expressed by the condition $\xi \gg I$, which in gases at

atmospheric pressure is satisfied only for a thickness $x \gg 10$ cm. It was only in the seventies that models including the contribution of low energy transfers to the energy loss fluctuations were worked out [25, 26, 27]. Figure 3.3 shows the energy loss distributions for 3 GeV π^- in 1.5 cm of Ar at atmospheric pressure as predicted by the Landau theory and by the model of Cobb et al., compared to experimental data. The distribution foreseen by Landau has a smaller width than the experimental distribution, while the model of Cobb et al. is closer to reality.

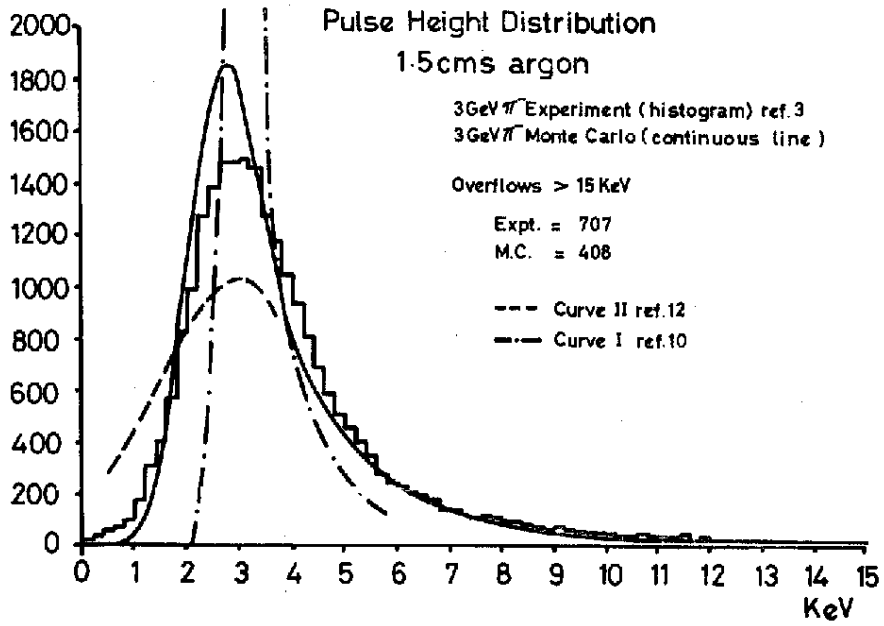

Figure 3.3: Comparison of the experimental energy loss distribution of 3 GeV π^- in a 1.5 cm thick Ar layer at standard temperature and pressure (histogram) with the Landau function (dash-dotted line) and the model of J.H. Cobb et al. (full line) [27].

Primary and secondary ionizations

In some collisions, the amount of energy transferred to the struck electron exceeds its binding energy. The electron is thus emitted, with a kinetic energy equal to the energy lost by the incident particle minus the atomic binding energy. Such electrons are called primary electrons or δ-rays. The primary ionizations are distributed along the particle track, spaced in average by a distance λ. That distance is the inverse of the primary ionization density n_P, defined as the average number of primary electrons released by the incident particle per centimeter of gas traversed. The number k of primary electrons released in a path of length x is Poisson-distributed, with an average number equal to $n_P x$:

$$P(k) = \frac{(n_P x)^k}{k!} \exp(-n_P x). \tag{3.5}$$

The inefficiency of a perfect detector of thickness x would thus be equal to the probability of having no primary electron inside the detector, i.e. $P(0) = exp(-n_P x)$.

Most of the ionization, however, comes from atoms not encountered directly by the incident particle. So-called secondary electrons can be emitted in collisions between the primary

electrons and the atoms:

$$e^- + A \rightarrow e^- + A^+ + e^-.$$

or through intermediate excited states, induced either by the incoming particle or by primary electrons:

$$\begin{aligned} \pi^\pm + A \rightarrow \pi^\pm + A^* \quad \text{or} \quad e^- + A \rightarrow e^- + A^*, \\ A^* + B \quad \rightarrow \quad A + B^+ + e^-. \end{aligned}$$

In the second mechanism, the excitation energy of A is transferred to the atom B, which ionization energy is lower than the excitation energy of A. This effect is known as the Penning effect and depends very much on the gas composition. The amplitude of the detector signal is proportional to the total number of electrons released in the detector, and thus to the total ionization density n_T.

High detection efficiency and large signal amplitude for MIP's are thus ensured by choosing a gas with high primary and total ionization densities. The values of n_P and n_T for particles at the minimum of ionization are given in table 3.1, for some components commonly used in gaseous detectors, at normal conditions of temperature and pressure (N.T.P.). High Z noble gases are not considered because they lead to detector instabilities, as will be explained in section 3.1.4. Organic gases like isobutane and dimethylether (DME) are favoured choices, as well as mixtures of organic compounds and light noble gases.

Gas	n_P (cm^{-1})	n_T (cm^{-1})	W_I (eV)	I_1 (eV)	U_1 (eV)
He	3.3	7.6	42.3	24.6	19.8
Ne	10.9	39.9	36.4	21.6	16.5
Ar	24.8	96.6	26.3	15.8	11.5
Kr	33.0	197.5	24.0	14.0	-
Xe	44.8	313.3	21.9	12.13	-
Ne + 0.5% Ar	-	57.4	25.3	-	-
CO_2	33.6	100.0	32.8	13.8	-
CH_4	24.8	59.3	27.1	12.7	-
iso-C_4H_10	83.6	232.8	23.2	10.5	-
DME	55	160 (?)	-	10.0	-

Table 3.1: Characteristics of some gases commonly used in gaseous detectors: n_P, n_T are the primary and total ionization densities at standard temperature and pressure for particles at the minimum of ionization, W_I is the mean energy of electron-ion pair creation, I_1 and U_1 are the first ionization and excitation potentials [28, 29]. For DME the total ionization density was never mentioned.

An instructive parameter is W_I, the average energy to be lost by the ionizing particle before an electron-ion pair is created. It is defined by $-dE/dx = n_T * W_I$. In a Penning mixture like Ne + 0.5% Ar, the total energy loss is practically the same as in pure Ne, but the excitation energy of Ne atoms is converted into ionization of Ar atoms. This results in an increase of n_T, or equivalently a decrease of W_I, as illustrated in table 3.1.

Each primary electron travels a certain range inside the gas, and releases a few secondary electrons on its way. The energy of the primary electron and the direction of emission with respect to the incident particle trajectory are kinematically related. Low energy δ-rays, the

most probable ones, are emitted almost perpendicularly to the particle track. The range of the δ-rays can be parametrized by the empirical formula [20]:

$$R(E) = aE\left(1 - \frac{b}{1+cE}\right) \tag{3.6}$$

with $a = 5.3710^{-4}$ g cm^{-2} keV^{-1}, $b = 0.9815$, and $c = 3.123010^{-3}$ keV^{-1}. As an illustration, in argon N.T.P., δ-rays of 1 keV are stopped in about 30 μm.

The small ionization cloud created along the path of a δ-ray is often called a primary cluster. The distribution $w(n)$ of the number n of electrons inside a cluster is directly related to the distribution of the energy E transferred by the ionizing particle to the primary electron, as on average we have $E = nW_I$. In the approximation of free charged particles, Rutherford's theory prescribes:

$$w(n) = w(1)n^{-\kappa}, \qquad \text{for } n \geq 2, \tag{3.7}$$

with $\kappa = 2$. The above approximation holds only for large energy transfers as compared to the atomic binding energies, which are not very likely to occur. However the formula can be used as a two-parameter fit to the low energy part of the experimental spectrum. The values of $w(1)$ and κ obtained are around 0.70 and 2.0 for most gases [30].

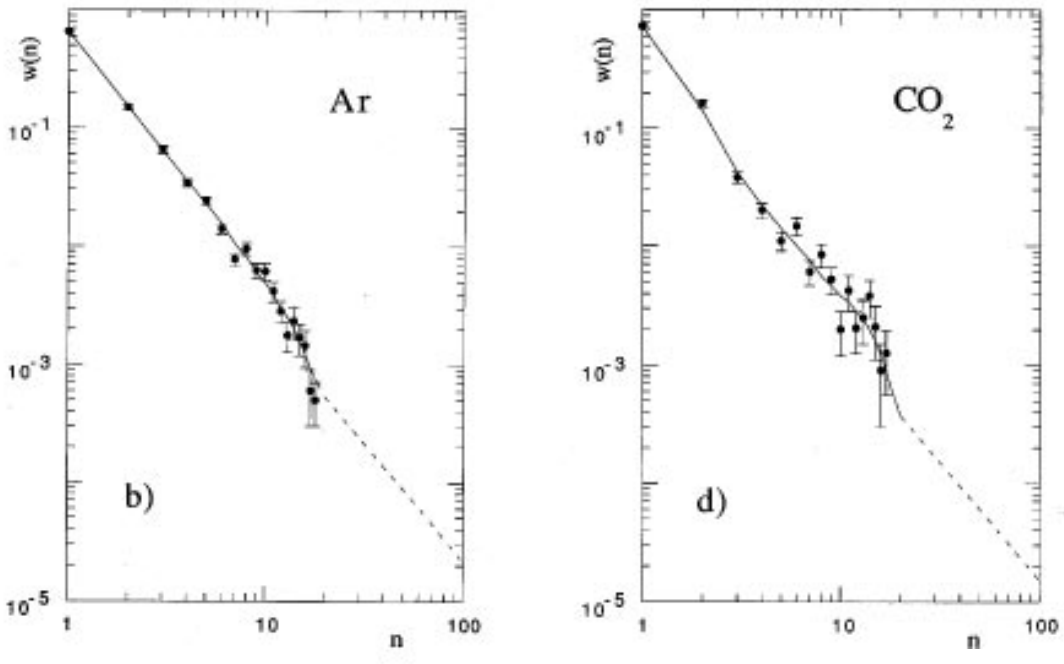

Figure 3.4: Probability $w(n)$ of having n electrons in a primary cluster, in Ar and CO_2, from measurements by Fischle et al. [30].

The experimentally measured values of $w(n)$ are shown in figure 3.4 for argon and CO_2. These results indicate that the emission of energetic δ-rays by MIP's is very rare in gases at atmospheric pressure: in argon, less than 1% of the primary electrons lead to a cluster of more than 20 electrons, which corresponds to a δ-ray energy of about 500 eV and a range of about 20 μm. Therefore the measurement of the crossing point of a MIP inside a detector filled with a gas at atmospheric pressure will not be distorted much by the δ-rays emitted in the gas.

Formulas 3.5, 3.6 and 3.7 can easily be implemented in a Monte Carlo algorithm to simulate the ionization of gases by charged particles. Such an algorithm is used in the CMS collaboration to simulate the response of micro-strip gas counters to ionizing particles. The Monte Carlo study of micro-strip gas counters described in chapter 4 is also based on these formulas.

Bremsstrahlung

High energy electrons lose their kinetic energy essentially by the emission of bremsstrahlung photons, in the Coulomb field of the nuclei and electrons of the traversed medium. The electrons can lose up to the totality of their energy in one radiative collision. Bremsstrahlung increases the photon background in the calorimeters. It also renders difficult the reconstruction of electron trajectories in the tracker, because of the discontinuitites of curvature at the emission points of bremsstrahlung photons. It is convenient to measure the thickness of the detector material in units of radiation length X_0. This is the distance over which a high energy electron loses all but a fraction $1/e$ of its energy by bremsstrahlung.

A compact formula fitting the experimental data is given by [13]:

$$X_0 = \frac{716.4A}{Z(Z+1)\ln(287/\sqrt{Z})} \text{ g cm}^{-2}. \tag{3.8}$$

The term in Z^2 originates from bremsstrahlung in the field of the nucleus, and the term in Z is the contribution of the atomic electrons. To give an order of magnitude, the radiation length of aluminium is 10 cm. In CMS, the detection layers of the tracker with their support structure and cabling have a thickness of about 5% of radiation length each. A high energy electron will on average lose 5% of its energy per detection layer by bremsstrahlung.

Multiple scattering

A charged particle traversing a medium is deflected by many small-angle scatters. Most of this deflection is due to Coulomb scattering by the nuclei and the electrons of the material. However, for hadronic projectiles, strong interactions also contribute to multiple scattering. The standard deviation of the total deflection angle due to multiple Coulomb scattering, projected onto a plane parallel to the direction of the incident particle, can be expressed as [13]:

$$\theta_0 = \frac{13.6 \text{ MeV}}{\beta cp} z\sqrt{x/X_0}\,[1 + 0.038\ln(x/X_0)]\,, \tag{3.9}$$

where p is the particle momentum and z its charge number. The distribution of the multiple scattering angle is Gaussian for small deflection angles, i.e. the central 98% of the distribution. At large angles it behaves like Rutherford scattering, having larger tails than does a Gaussian distribution.

As an example, multiple scattering will cause a deflection of 0.3 milliradians R.M.S. in tracks of 10 GeV/c particles at each detection layer of the CMS tracker. At the next detection layer, about 10 cm further, the R.M.S. of the particle impact coordinates will be of the order of 30 μm, which is comparable to the spatial resolution of the detector elements. This confirms that the tracker performance is limited by multiple scattering for charged particles of momentum below 10 GeV/c, as already discussed in chapter 2. In addition, this indicates that multiple scattering must be accounted for in track reconstruction in CMS. We will see in chapter 5 how this is done.

Attenuation of photons in matter

The different processes relevant for the attenuation of photons in matter have different relative importances depending on the photon energy. Above 10 MeV, the most important process is the conversion of the photon into a e^+e^- pair. Pair creation renders the identification of photons difficult and degrades the measurement of the photon energy in the electromagnetic calorimeter. This process also increases the background of charged particles inside the tracker.

Creation of pairs and bremsstrahlung are closely related processes. The conversion length C_0 of high energy photons is defined as the distance after which a photon beam is attenuated by a factor $1/e$ by creation of e^+e^- pairs. For energies higher than 1 GeV, C_0 is equal to $9/7X_0$ with an accuracy of a few percent.

3.1.2 Drift and diffusion of electrons in gases

Drift and diffusion in gases affect several aspects of the performance of gas filled detectors. The electron drift velocity determines the ionization collection time and thus affects the speed of the detector response. Diffusion causes a spread of the ionization inside the detector and thus blurs the measurement of the particle crossing point. How they act exactly will be explained later when we will discuss the choice of the appropriate gas for the micro-strip gas counters in CMS. In this paragraph we shall try to get a global understanding of the phenomena at play.

The electrons released in the detector by the incident particle drift towards the electrodes at positive potential. Their microscopic motion can be seen as a succession of short free travels, during which they gain kinetic energy from the electric field, and collisions with gas atoms or molecules, in which they lose a fraction of their kinetic energy. This results in a macroscopic drift, which proceeds at an average speed u called the drift velocity. In CMS, a drift velocity well in excess of 50 μm/ns is requested in order to get a fast enough response from the MSGC's.

The collisions with the gas molecules also cause a random diffusion of the electrons. After a drift over a distance x, an initially point-like cloud of electrons would exhibit a Gaussian spread of standard deviation equal to $\sqrt{2Dt}$, where D is the diffusion coefficient and $t = x/u$, the drift time. In the presence of an electric field, the diffusion in the direction of the field differs from the transverse diffusion, hence the introduction of D_L and D_T, the longitudinal and transverse diffusion coefficients. A transverse diffusion coefficient in the range 100 - 200 $\mu\mathrm{m}/\sqrt{\mathrm{cm}}$ is adequate in CMS, and allows to reach an MSGC spatial accuracy of about 40 μm.

In the presence of a magnetic field, the moving electrons will be subject to the Lorentz force which will make them spiral around the magnetic field direction. As a consequence the drift direction will in general not be aligned with the electric field. The angle between the electric field and the drift direction is called the Lorentz angle α_L. Another consequence is the reduction of the diffusion in the direction perpendicular to the magnetic field.

An additional process that can occur during the drift is electron attachment by a gas atom or molecule, which means that the captured electron is lost for detection. This happens more frequently in electronegative gases like O_2 or CF_4. As the drift distance is small in the gas counters studied here, typically a few millimeters, gas contamination with electronegative compounds is not a major concern. However CF_4, sometimes used to raise the electron drift velocity of a gas mixture, is ruled out because of its too short attenuation length at the high drift fields used in MSGC's at the LHC [31].

Drift velocity and Lorentz angle from a macroscopic model of the electron motion

The motion of charged particles under the influence of electric and magnetic fields, $\mathbf{E}$ and $\mathbf{B}$, can be understood in terms of an equation of motion with friction:

$$m\frac{d\mathbf{u}}{dt} = e\mathbf{E} + e[\mathbf{u} \times \mathbf{B}] - K\mathbf{u}, \tag{3.10}$$

where m and e are the mass and the charge of the particle, $\mathbf{u}$ is its velocity, and $K\mathbf{u}$ is a frictional force caused by the collisions of the particle with the gas molecules. The drift velocity is the solution of the steady state equation ($d\mathbf{u}/dt = 0$):

$$\frac{\mathbf{u}}{\tau} = \frac{e}{m}[\mathbf{E} + \mathbf{u} \times \mathbf{B}], \tag{3.11}$$

where $\tau = m/K$ has the dimension of a time, and depends on the gas through the parameter K. The right hand side of equation 3.11 is the acceleration of the charged particle between two collisions due to the electromagnetic force, and thus τ can be seen as the average time interval between two collisions, during which the particle acquires an average speed $\mathbf{u}$.

Equation 3.11 is linear in $\mathbf{u}$. Denoting $(e/m)\mathbf{E} = \boldsymbol{\varepsilon} = (\varepsilon_x, \varepsilon_y, \varepsilon_z)$, and $(e/m)\mathbf{B} = \boldsymbol{\omega} = (\omega_x, \omega_y, \omega_z)$, we obtain the linear system:

$$\begin{aligned} M\mathbf{u} &= \boldsymbol{\varepsilon}, \\ \text{with } M &= \begin{bmatrix} 1/\tau & -\omega_z & \omega_y \\ \omega_z & 1/\tau & -\omega_x \\ -\omega_y & \omega_x & 1/\tau \end{bmatrix}. \end{aligned} \tag{3.12}$$

Solving for $\mathbf{u}$ yields:

$$\begin{aligned} \mathbf{u} &= M^{-1}\boldsymbol{\varepsilon}, \\ \text{with } M^{-1} &= \frac{\tau}{1+\omega^2\tau^2} \begin{bmatrix} 1+\omega_x^2\tau^2 & \omega_z\tau + \omega_x\omega_y\tau^2 & -\omega_y\tau + \omega_x\omega_z\tau^2 \\ -\omega_z\tau + \omega_x\omega_y\tau^2 & 1+\omega_y^2\tau^2 & \omega_x\tau + \omega_y\omega_z\tau^2 \\ \omega_y\tau + \omega_x\omega_z\tau^2 & -\omega_x\tau + \omega_y\omega_z\tau^2 & 1+\omega_z^2\tau^2 \end{bmatrix}. \end{aligned} \tag{3.13}$$

case $\mathbf{E}$ *perpendicular to* $\mathbf{B}$*:* Choosing $\mathbf{B} = (0, 0, B)$ and $\mathbf{E} = (E, 0, 0)$, we get:

$$\begin{aligned} u &= \sqrt{u_x^2 + u_y^2} \\ &= \frac{\varepsilon\tau}{\sqrt{1+\omega^2\tau^2}}, \end{aligned} \tag{3.14}$$

$$\begin{aligned} \alpha_L &= \frac{u_y}{u_x} \\ &= -\omega\tau. \end{aligned} \tag{3.15}$$

Thus the drift velocity in the presence of perpendicular electric and magnetic fields is reduced by a factor $1/\sqrt{1+\omega^2\tau^2}$ as compared to the situation without magnetic field. Moreover, the drift direction acquires a component perpendicular to $\mathbf{E}$ and $\mathbf{B}$. The deviation angle α_L with respect to the direction of the electric field is proportional to the magnetic field intensity, but also depends on the gas through τ. In the 4 Tesla magnetic field of CMS, in MSGC's filled with DME-based gas mixtures, α_L is typically around 14^o. The reduction of drift velocity due to the magnetic field is only 3%.

case $\mathbf{E}$ *parallel to* $\mathbf{B}$*:* In the case of parallel electric and magnetic fields, the drift speed and drift direction are not modified by the presence of the magnetic field. The diffusion is still affected, as will be seen later.

Drift and diffusion from a microscopic model of the electron motion

A simple classical model relates the macroscopic transport parameters and the variables describing the microscopic motion of the drifting electron. This model provides a theoretical understanding of the behaviour of the electron drift velocity and diffusion in gas mixtures as a function of the electric field intensity.

In the absence of any external field, the electron is in thermal equilibrium with the gas. Its average kinetic energy is equal to $\varepsilon_v = \frac{3}{2}kT$, where T is the absolute gas temperature and k, the Boltzmann constant (at room temperature $kT \simeq 1/40$ eV). In the presence of an electric field, the average kinetic energy increases:

$$\varepsilon_v = \frac{1}{2}mv^2 = \varepsilon_E + \frac{3}{2}kT. \tag{3.16}$$

Here ε_E is the contribution of the electric field to the average kinetic energy. At drift fields used in gaseous detectors and in most gases, ε_E amounts to a few eV, so the thermal energy can be neglected. The electric field also causes a net drift at speed $u \ll v$. In a time interval τ between two collisions with the gas molecules, the drift speed communicated by the electric field E can be written as:

$$u = \frac{eE}{m}\tau = \mu_e E, \tag{3.17}$$

where μ_e is the electron mobility.

In every collision with a gas molecule, the electron loses on average a fraction δ of the energy ε_E communicated by the field, so that there is a balance between the losses in collisions and the acceleration due to the field. Over a travel dx in the direction of the field, the number of collisions is equal to the drift time dx/u divided by τ, so the energy balance reads:

$$\frac{dx}{u\tau}\delta\varepsilon_E = eEdx. \tag{3.18}$$

The average time interval between two collisions can be expressed as a function of the nonmotive velocity v, the collision cross-section σ and the molecular density N:

$$\frac{1}{\tau} = N\sigma v. \tag{3.19}$$

Neglecting the thermal motion, the expressions of the equilibrium velocities can thus be written as:

$$u^2 = \frac{eE}{mN\sigma}\sqrt{\frac{\delta}{2}}, \tag{3.20}$$

$$v^2 = \frac{eE}{mN\sigma}\sqrt{\frac{2}{\delta}}. \tag{3.21}$$

The diffusion coefficient is related to the velocity v, or to the kinetic energy ε_v, of the electron. The mean squared displacement in a given direction $\mathbf{y}$ after a large number of collisions n can be computed as:

$$\sigma_y^2 = \sum_{i=1}^{n} y_i^2 = n < y^2 >, \tag{3.22}$$

where $< y^2 >$ is the mean squared displacement in the direction **y** between two collisions. The free path l between two collisions is distributed as a decreasing exponential, and because $u \ll v$, the direction of motion can be considered as isotropic in first approximation. Therefore

$$\begin{aligned} < y^2 > &= \int_0^{+\infty} \frac{dl}{L} \int_{-1}^{+1} \frac{d\cos\theta}{2} (l\cos\theta)^2 e^{-l/L} \\ &= \frac{2}{3} L^2, \end{aligned} \tag{3.23}$$

where $L = v\tau$ is the mean free path between two collisions. The expression of the diffusion coefficient D is thus:

$$D = \frac{\sigma_y^2}{2t} = \frac{2}{3}\frac{\varepsilon_v}{m}\tau, \tag{3.24}$$

obtained by replacing the drift time t by $n\tau$.

Very often, an empirical quantity ε_K, called the characteristic energy, is defined as:

$$\varepsilon_K = \frac{eD}{\mu_e}. \tag{3.25}$$

Using the expression of the electron mobility in 3.25, it appears that ε_K equals 2/3 of the average kinetic energy ε_v. The diffusion is also often given in centimeters per unit of drift distance:

$$D' = \frac{\sigma_y}{\sqrt{x}}. \tag{3.26}$$

The calculation yields $D' = \sqrt{2D/u} = \sqrt{2\varepsilon_K/eE}$, and so the size of the electron cloud turns out to be proportional to the square root of the drift distance.

Therefore, in order to understand the behaviour of the drift velocity and diffusion coefficient with the drift field intensity in a given gas, one has to look at the curves of the average kinetic energy (or of the characteristic energy) as a function of E, and at the dependence of the parameters σ and δ on the electron energy. These curves are shown in figure 3.5. As an example, in pure argon, the characteristic energy ε_K is slowly rising from 3 to 10 eV in the range of electric fields between 100 and 3000 V/cm. At these energies, the collision cross-section is close to its maximum value of 10^{-15} cm^2. The fractional energy loss is constant and very small, because the only possible collisions below the excitation thresholds of Ar are elastic, with energy losses of the order of $m_e/m_{Ar} \simeq 10^{-5}$. Thus, the drift velocity is low and rising more or less as $\sqrt{E}$, as shown in the lowest curve of figure 3.6 a).

Adding a small fraction of methane to argon causes a very large increase of drift velocity as compared to pure argon, because it affects both σ and δ of the gas mixture. Polyatomic molecules have rotation and vibration levels, which can be excited in collisions with low energy electrons. This is the origin of the very large value of δ in CH_4, as compared to Ar. Inelastic collisions also reduce the average kinetic energy of the electrons, and maintain it in the range from 0.1 to 1 eV, where the collision cross-sections are small. At high electric fields, when the electron kinetic energy exceeds 1 eV, the fractional energy loss of CH_4 drops, and the collision cross sections rise. Thus, the drift velocity levels off or even decreases.

Thermal limit

In some gases, among which CO_2, isobutane and DME, the electron kinetic energy remains constant around $\frac{3}{2}kT$ in a large range of electric fields, up to $\simeq$ 1000 V/cm. Therefore v and τ do not depend on E, so the diffusion coefficient and the electron mobility are constant, and the drift velocity rises linearly with E. Often, such gases are added to a mixture in order to decrease the diffusion and permit a better localization accuracy.

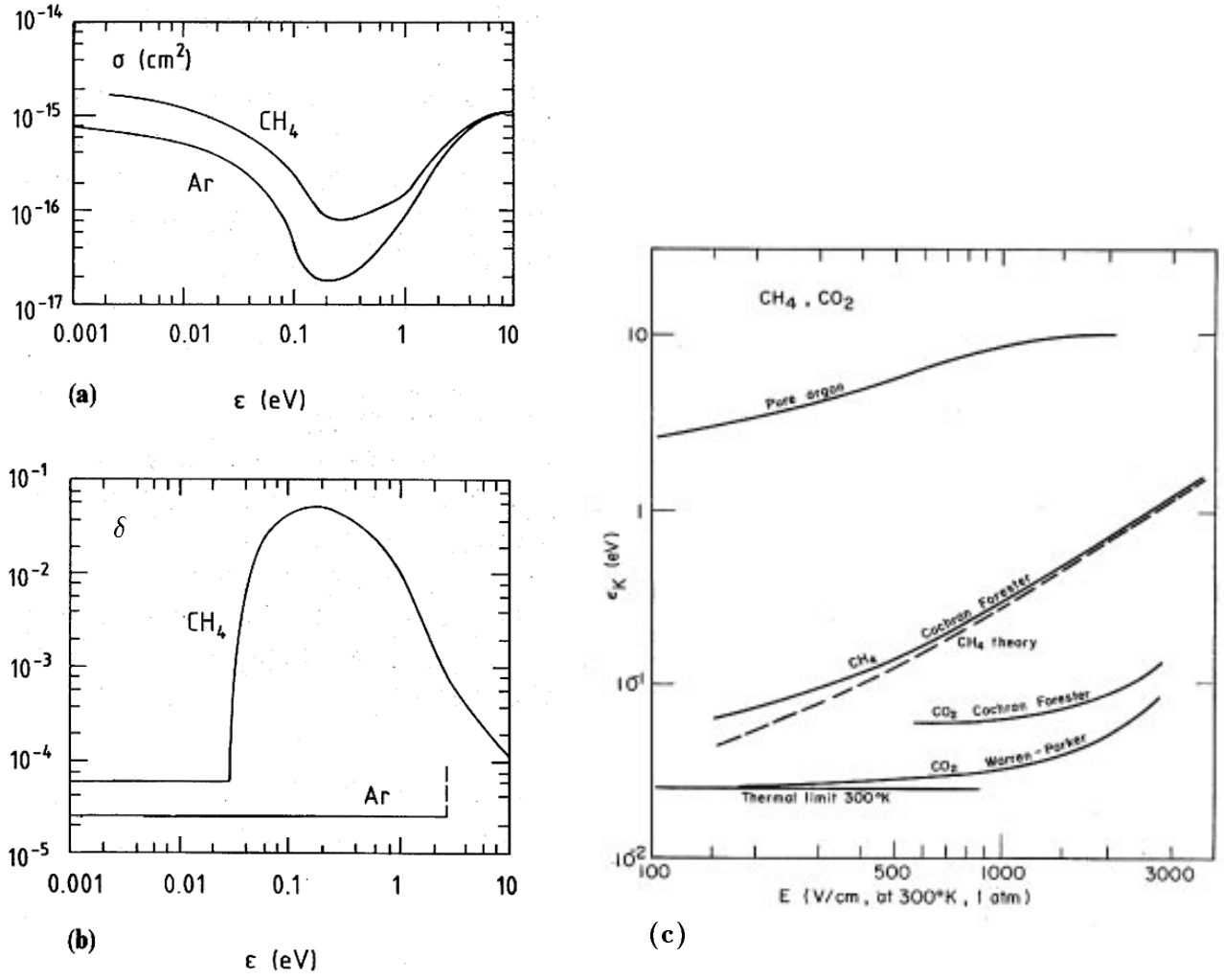

Figure 3.5: Collision cross-section (a) and fractional energy loss (b) in Ar and CH_4 [20]. (c) Characteristic energy as a function of the drift field intensity, in various gases [32].

Transverse and longitudinal diffusion

Since the experiments of Wagner et al. in 1967 [33] it is known that the diffusion is not isotropic in the presence of an electric field. In 1969 this phenomenon was explained theoretically by a difference in mobility of the electrons in the leading and trailing edge of the electron cloud [34], which results in a longitudinal diffusion coefficient D_L different from the transverse diffusion coefficient D_T. A compilation of experimental data on longitudinal and transverse diffusion can be found in [35].

In the presence of a magnetic field, the diffusion coefficient is reduced in the direction perpendicular to **B**, due to the incurved trajectory of the electrons. The calculation shows that the mean squared displacement in the direction transverse to **B** gets a reduction factor of $1/(1+\omega^2\tau^2)$, i.e. 0.94 in MSGC's in CMS conditions. The diffusion in the direction parallel to the magnetic field is not affected.

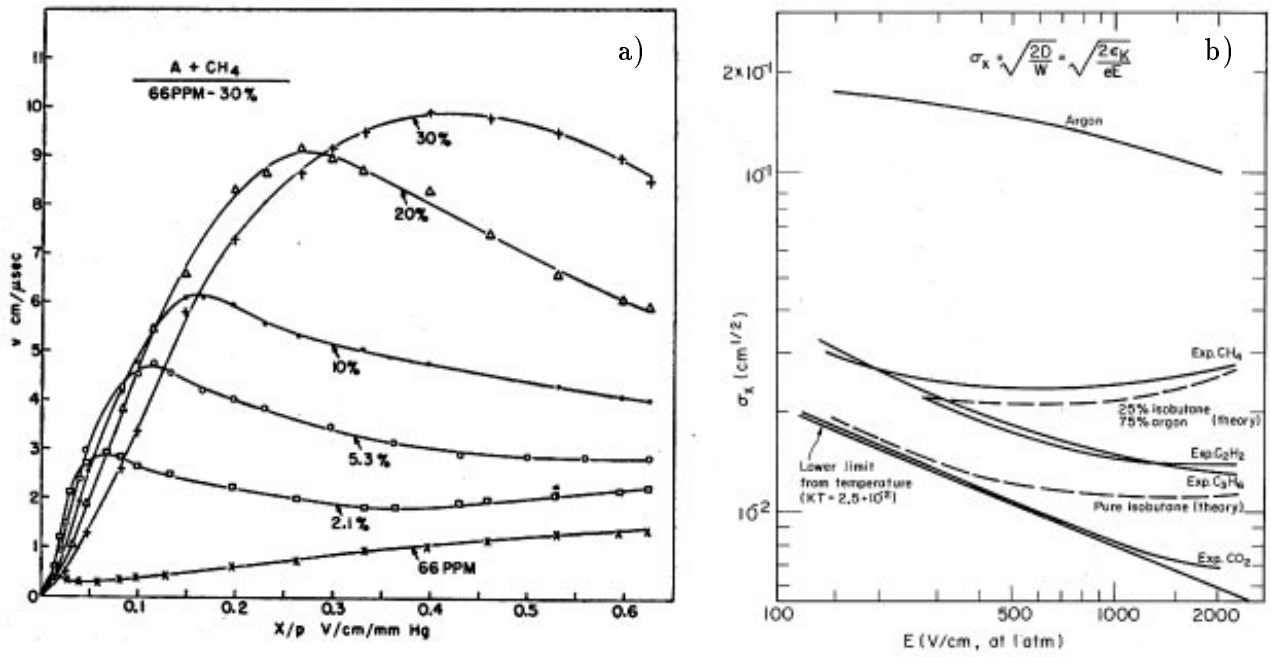

Figure 3.6: a) Drift velocity in Ar-based mixtures as a function of the reduced electric field E/p, for various contents of CH_4. b) Diffusion as a function of the drift field intensity, in various gases at atmospheric pressure [32].

3.1.3 Drift of ions

In gas proportional counters, the detection of the ionizing particles relies on the electric signal induced by the motion of the charges, created in the avalanche, drifting towards the electrodes. As will be seen in section 3.1.5, the contribution of ions to the induced signal is much larger than that of electrons. Therefore, the ion drift speed determines the time development of the avalanche signal.

As their mass is large, comparable to the mass of the gas molecules, ions travel at much smaller speed and are much less subject to diffusion than electrons. They lose much more energy in elastic collisions with gas molecules than electrons, and remain thermal up to high electric fields. Therefore, up to relatively high fields, the ion mobility μ_i is constant, and the relation between the ion drift velocity and the field intensity is linear. A typical value of μ_i is 1 cm/s per V/cm, 10^4 smaller than typical electron mobilities [20]. The order of magnitude of the ion diffusion coefficient is $D = \mu_i kT/e$, about 250 smaller than usual values for electrons, and the Lorentz angle $\alpha_L = \omega\tau = B\mu_i$ is reduced by a factor 10^4 as compared to electrons. In good approximation, ions can thus be considered as travelling along the electric field lines. At electric fields where the ion kinetic energy departs from the thermal limit, the ion drift speed rises as $E^{1/2}$, with a form very similar to 3.20.

3.1.4 Gas amplification

When the drifting electrons reach the region of high electric field around the anodes, they acquire enough energy from the field to ionize other gas molecules. The newly released electrons are in turn accelerated, causing further ionizations in a process called "avalanche". Depending on the gas filling and the field intensity and configuration, the avalanche can evolve in different ways, corresponding to different modes of operation of the gas counter. In the proportional

mode, in which MSGC's are operated, the number of electron-ion pairs created in the avalanche is on average proportional to the amount of ionization left in the counter by the incident particle.

The avalanche exhibits a drop-like shape, with a cloud of fast electrons heading for the anode, and a trail of ions almost immobile at the time scale of the avalanche development. The formation of an avalanche involves numerous and complex processes, similar to the reactions occuring in plasma chemistry: excitation and ionization of the gas molecules by collisions with electrons, radiative desexcitation, photoionization, transfer of charge or excitation energy in collisions between gas molecules, recombination of the electrons and ions, molecular dissociation or polymer formation, interaction between the electrode metals and the species formed in the avalanche, etc. These reactions will not be described here, but will be mentioned when their role is important.

Gas gain

The charge amplification factor in the avalanche is called the gas gain, noted G. It can be derived from the first Townsend coefficient α. This coefficient describes the increase in the number of free electrons over a path of length ds:

$$\frac{dN}{N} = \alpha ds. \tag{3.27}$$

The coefficient α is determined by the cross sections of several of the processes involved in the avalanche, which depend in a complicated manner on the electron energy distribution. Therefore no fundamental expression of α can be given. To determine the total gain, the first Townsend coefficient has to be measured for a wide range of electric fields, and integrated along the path of the electrons in the field geometry of the detector [32]:

$$\begin{aligned} G = \frac{N}{N_0} &= \exp\left[\int_{s_a}^{s_0} \alpha(s) ds\right] \\ &= \exp\left[\int_{E_a}^{E_0} \frac{\alpha(E)}{dE/ds} dE\right], \end{aligned} \tag{3.28}$$

where s_0 is the point at which the electric field intensity E_0 becomes high enough to create new ionizations and s_a is the position of the anode.

Figure 3.7 shows the behaviour of $\eta = \alpha/E$ for some noble gases, as a function of the reduced field E/p, where p is the gas pressure. It can be seen that α rises steeply with E up to very high fields. In Ar at atmospheric pressure, $\alpha \simeq 10$ e$^-$/cm at a field of 10 kV/cm, and $\simeq 2000$ e$^-$/cm at 100 kV/cm. Therefore, a given gain value can either be obtained in a small volume of high field or in an extended volume of low field. A few curves are also given for mixtures composed of Ne with small additions of Ar. They show the very large increase in gas amplification at low fields due to the Penning effect. At very high fields, thus very high electron kinetic energy, the cross-section of ionizing collisions between the electrons and the gas molecules decreases, hence the reduction of η.

Limitations to the gas gain in proportional mode

The gas gain cannot be increased at will. On one hand, at high gains, the counter departs from the proportional mode because of space charge deformation of the electric field in the neighbourhood of the avalanche. On another hand, secondary processes like photon emission induce the generation of avalanches spread all over the detector. These phenomena eventually

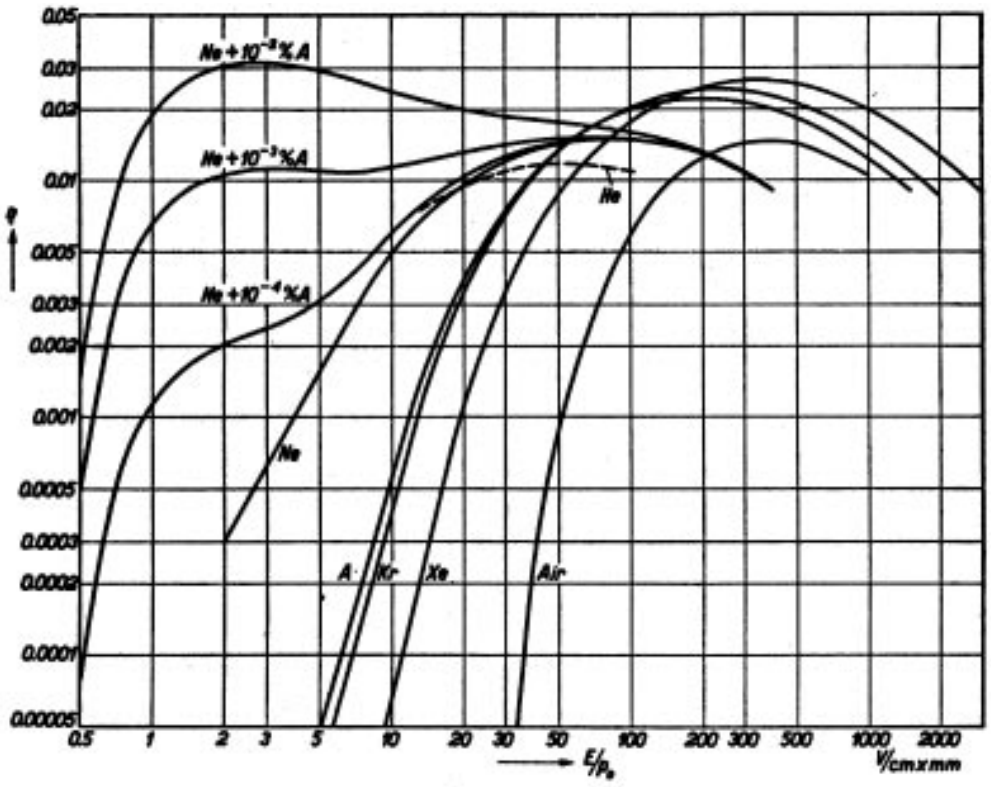

Figure 3.7: Amplification coefficient $\eta = \alpha/E$ in V^{-1} as a function of the reduced electric field, in various noble gases and in mixtures of Ne with a small addition of Ar [36].

result in spark breakdown. An upper gain limit in proportional mode is 10^6. Two breakdown mechanisms of particular importance in the study of MSGC's are described below.

Secondary emission of electrons: The first source of breakdown, sometimes called "photon feedback", results from emission of secondary electrons ejected from the cathodes. This emission can be provoked by photons emanating from the avalanche, releasing electrons by photoelectric effect. It also happens that ions neutralizing at the cathode release their excitation energy by extracting an electron. When the amount of secondary electrons is large enough to create an avalanche of same size as the initial one, the counter enters a self-sustained regime of discharge.

Photon emission is particularly present in high Z noble gases, like argon. These gases are used in gas counters because they provide high gains. However they present low energy excitation levels, which can only return to the ground state by radiative transition. In Ar, the minimum energy of the emitted photon is 11.6 eV, well above the ionization potential of any cathode metal (7.7 eV for copper). To prevent photon feedback, a fraction of polyatomic, often organic gas is added to the gas filling. Such gases, named "quenchers", present non-radiative excited states, like molecular vibrations and rotations, which allow efficient absorbtion of photons in a wide energy range. They can also dissipate energy by dissociating into simpler radicals. Because quenchers usually have a low ionization potential, Penning effect and transfer of charge take place in collisions between the molecules of the quencher and the other species, such that only ions of the quencher reach the cathode. CO_2, methane, isobutane and DME are among the most widely used quenchers.

The main drawback of organic additives is that they are likely to form insulating polymer deposits on the electrodes. This phenomenon is called "ageing". Polymer formation is initiated by free radicals created in the avalanche. The accumulation of charges on the insulating layer covering the electrodes causes a variation of field strength and gas gain. On the cathodes, it also happens that the dipole field created in the insulating layer due to the accumulation of positive ions is high enough to cause electron extraction from the electrode (Malter effect). The ageing rate appears to be very sensitive to the presence of trace pollutants, which can be released in the gas by the materials used to build the counter. A review of the ageing properties of gases and construction materials used in gas filled detectors can be found in [37]. It can be noted that pure DME is not expected to polymerize [38].

Streamer development: The second source of breakdown goes through the formation of a streamer. As the avalanche increases in size, the space-charge fields of the clouds of electrons and positive ions become important, so that the total electric field is sharply enhanced at the head and tail of the avalanche. On the side of the avalanche, instead, the dipole field created between the clouds of electrons and ions reduce the external field. In this situation, electrons released at the tips of the avalanche by photoionization or Penning effect are amplified in the high field created by the avalanche itself, and quickly evolve into new avalanches merging with the primary one. Breakdown occurs when the streamer grows up to the cathode.

The streamer can also quench by itself if the space-charge field at its tail does not compensate the decrease of the external field. Some counters are operated in this mode, called self-quenching or limited streamer mode. It provides signals two orders of magnitude larger than the proportional mode. In MSGC's, streamer development should be avoided, because the streamer current is large enough to damage the MSGC electrodes. This limits the maximum gain in MSGC's to a rather low value, around 10^4. To prevent streamers, the detector field geometry should be such that the field intensity drops quickly with increasing distance to the anode.

Gain fluctuations

Since the amplification is a stochastic process, variations are to be expected in the total amplification factor between individual events. Assuming that the probability of ionization per unit path length of an electron depends only upon the field strength and does not depend on the history of the electron, the distribution of the amplification factor should be of exponential form:

$$p\left(\frac{K}{\bar{K}}\right) = p(z) = e^{-z}, \tag{3.29}$$

where $\bar{K}$ is the average gain and K is the gain of a single avalanche. Experimentally the avalanche size distribution appears to have a clear maximum, and can be described in cylindrical proportional counters by the Curran distribution [39]:

$$p(z) = 3(\tfrac{3}{2}/\pi)^{\frac{1}{2}} z^{\frac{1}{2}} \exp(-\tfrac{3}{2}z). \tag{3.30}$$

The failure of equation 3.29 comes from the hypothesis that the probability of ionization is independent of the electron history. In the model proposed by Byrne [40] and Lansiart and Morucci [41], the probability $a(K)$ for an electron to ionize depends on the total number of electrons already produced in the avalanche as:

$$a(K) = \alpha(1 + \mu/K), \tag{3.31}$$

where α is the first Townsend coefficient and μ is an empirically defined parameter. They arrived at the Polya distribution for the gas gain:

$$p(z) = \frac{m^m}{\Gamma(m)} z^{m-1} e^{-mz}, \tag{3.32}$$

with $m = 1 + \mu$. In the particular case, that $m = 3/2$, this distribution is equal to the experimentally found Curran distribution. The variance σ_z^2 of the Polya distribution is equal to $1/m$.

In the work of Alkhazov [42, 43], it is shown that the gain variance in uniform fields is a decreasing function of the parameter $\kappa = \alpha(E)W_I/E = \eta(E)W_I$, where W_I is the energy required for the creation of an electron-ion pair. As $\eta(E)$ rises with E in a large range of electric fields (see figure 3.7), smaller gain fluctuations are reached when operating at higher fields. This argument can be generalized to non-uniform fields, in which the total amplification can be seen as small successive avalanches in constant field. It can be concluded that, for a given gain, smaller fluctuations will be recorded when the avalanche develops in a small region of high field, as compared to configurations with an extended region of low field. This is illustrated in figure 3.8, which shows the gain distributions in three detectors of increasing field confinement, respectively a cylindrical proportional counter, a micro-strip gas chamber and a micro-gap chamber. The histograms are obtained with a Monte Carlo simulation of the avalanche development. The curves are Polya distributions of parameter $m = 1.5$, 2 and 2.5 respectively [44].

3.1.5 Signal generation

Electrons and positive ions created in the avalanche drift towards the positive and negative electrodes, where they are eventually collected. The motion of the charges induces electric currents on the electrodes, which can be amplified and measured. Current integrating amplifiers deliver an output voltage proportional to the charge collected on the electrodes. After full charge collection, the anode of a cylindrical proportional counter will have received a charge $Q = neG$ on average, with n the number of electrons released in the counter by the ionizing particle. In the presence of several electrodes the situation is more complicated, because of capacitive coupling between the electrodes. The time development of the signal must also be considered, in order to choose the appropriate signal shaping. This timing does not only depend on the charge motion, but also on the RC time constant of the electrode response. These aspects will be discussed here in some details.

Signal induction on the electrodes

The calculation of the signal induced by a moving charge on a set of electrodes is a delicate problem. We consider here the case where each electrode is perfectly conductive, at fixed potential and connected to an infinite reservoir of charge. This happens in practice when the impedances of the electrode and of the connection to the power supply are small, so that the corresponding RC time constants are much smaller than the signal rise time. For instance, MSGC anode strips made of aluminium have typically a resistance of a few hundred Ω and a capacitance to ground of a few pF. Connected to ground through low input impedance amplifiers, their response time is of the order of 1 ns.

The potential $\Phi(\mathbf{r})$, solution of the electrostatic problem with the charge q at point $\mathbf{r}_1$ and with boundary conditions determined by the electrode potentials V_i, is the sum of the solutions $\{\Phi_k(\mathbf{r}), k = 0, 1, 2...\}$ of the following problems:

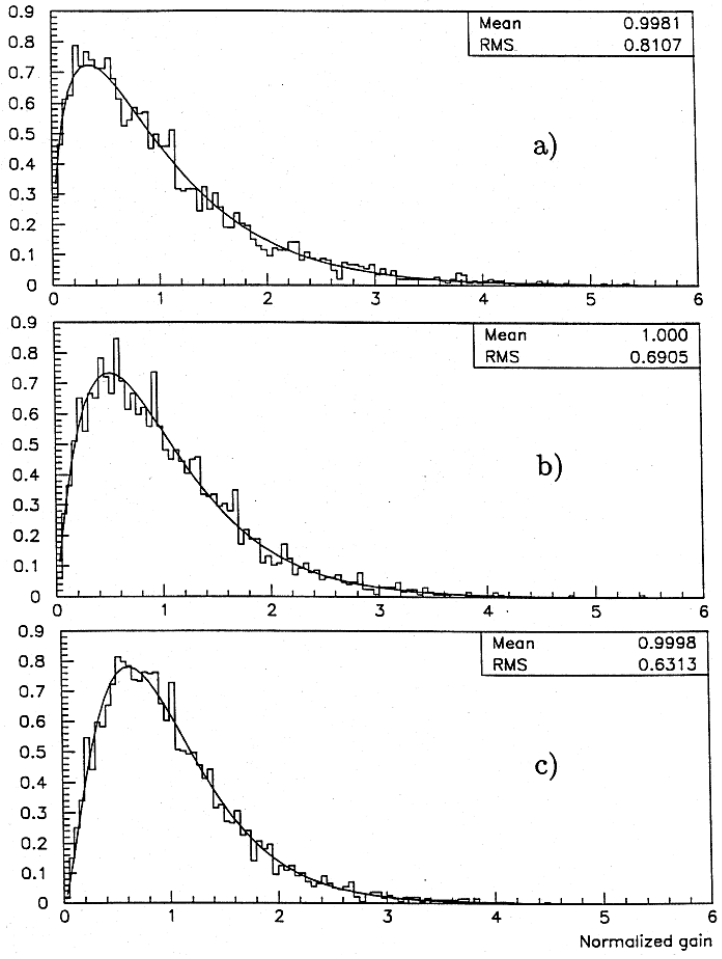

Figure 3.8: Gain fluctuations in a cylindrical proportional counter (a), a micro-strip gas chamber (b) and a micro-gap chamber (c), from a Monte Carlo simulation of the avalanche development. The curves are Polya distributions of parameter $m = 1.5$, 2 and 2.5 respectively [44].

- $\{\Phi_i, i = 1, 2...\}$ all electrodes grounded but the i^{th} electrode at potential V_i, without charge q, and
- Φ_0 with all electrodes grounded and the charge q at point $\mathbf{r}_1$.

Green's second identity states that for every i,

$$\int_V \left(\Phi \nabla^2 \Phi_i - \Phi_i \nabla^2 \Phi\right) dV = \int_S \left(\Phi \nabla \Phi_i - \Phi_i \nabla \Phi\right) . \mathbf{n} dS. \tag{3.33}$$

Here V is the detector volume, delimited by a well-chosen closed surface S, and $\mathbf{n}$ is the unit vector normal to S and outgoing from V. S encloses each electrode j and the charge q in the way depicted in figure 3.9.[2] The righthand side of equation 3.33 reduces to the sum of the integrals on the electrode surfaces S_j and on the little sphere containing the charge q, while the contributions of the other surface elements cancel each other.

[2] We suppose for simplicity that electrode 1 encloses the detector volume completely.

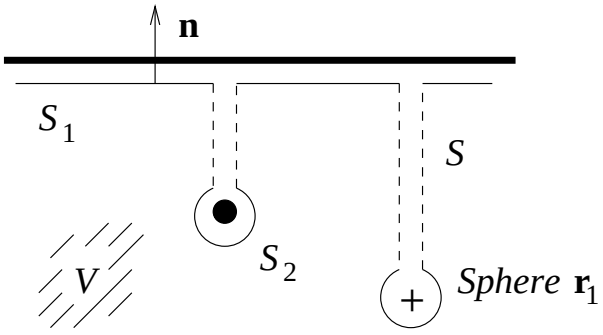

Figure 3.9: Definition of the integration surface S, delimiting the detector volume V and enclosing the electrodes and the moving charge.

In the absence of electric charges in the volume V, $\nabla^2\Phi_k = \nabla^2\Phi = 0$, such that the volume integral vanishes. The surface terms can be evaluated thanks to Gauss's theorem:

$$\int_{S_j} \nabla\Phi.\mathbf{n}dS = \int_{S_j} \mathbf{E}.(-\mathbf{n})dS = \frac{\mathcal{Q}_j}{\epsilon_0}, \tag{3.34}$$

where $\mathcal{Q}_j$ is the charge enclosed in the surface delimiting electrode j, $(-\mathbf{n})$ is the normal vector outgoing from the electrode volume and ϵ_0 is the permittivity of free space. In a similar way one obtains:

$$\int_{S_j} \nabla\Phi_i.\mathbf{n}dS = \frac{\mathcal{Q}_j^i}{\epsilon_0}, \tag{3.35}$$

$$\int_{Sphere\ \mathbf{r}_1} \nabla\Phi.\mathbf{n}dS = \frac{q}{\epsilon_0}, \tag{3.36}$$

$$\int_{Sphere\ \mathbf{r}_1} \nabla\Phi_i.\mathbf{n}dS = 0, \tag{3.37}$$

where $\mathcal{Q}_j^i$ is the charge induced on electrode j by the potential of electrode i alone. Equation 3.33 becomes:

$$0 = \sum_j V_j\mathcal{Q}_j^i - q\Phi_i(\mathbf{r}_1) - V_i\mathcal{Q}_i. \tag{3.38}$$

The first term is constant in time, and the current induced in electrode i by the moving charge can eventually be expressed as:

$$\begin{aligned} \frac{d\mathcal{Q}_i}{dt} = I_i &= \frac{-q}{V_i}\frac{d}{dt}\Phi_i(\mathbf{r}_1) \\ &= \frac{-q}{V_i}\frac{d\mathbf{r}_1}{dt}.\nabla\Phi_i(\mathbf{r}_1) \\ &= q\frac{\mathbf{v}.\mathbf{E}_i(\mathbf{r}_1)}{V_i}. \end{aligned} \tag{3.39}$$

This result is known as Ramo's theorem. $\mathbf{E}_i(\mathbf{r}_1)$ is the electric field from solution i at the point where the free charge is located, and $\mathbf{v}$ is the drift speed of the charge, function of the total electric field at this point. $\mathbf{E}_i/V_i$ and Φ_i/V_i are called respectively the weighting field and weighting potential of electrode i. A weighting potential is dimensionless, and the corresponding

electrode is at weighting potential 1, while all other electrodes are at 0. The charge induced on electrode i between time $t = t_1$ and time $t = t_2$ by the moving charge q is:

$$\Delta \mathcal{Q}_i = \int_{t_1}^{t_2} I_i(t)dt = \frac{-q}{V_i} \left[\Phi_i \left(\mathbf{r}_1 \left(t_2 \right) \right) - \Phi_i \left(\mathbf{r}_1 \left(t_1 \right) \right) \right]. \tag{3.40}$$

In practice, the calculation of the current induced on electrode i requires:

1. the calculation of the electric field in the detector, created by the electrodes at working potential,
2. the calculation of the weighting field of electrode i,
3. the calculation of the position $\mathbf{r}_1(t)$ and the drift speed $\mathbf{v}(t)$ of the moving charge.

The field calculations are usually performed using commercial programs solving the Laplace equation under given boundary conditions. The solution of the charge equations of motion requires the knowledge of the drift velocity as a function of the electric field intensity, in the detector working gas. For ions, a linear relation can be used in first approximation, with a value of the ion mobility equal to 1 $\mathrm{cm^2 V^{-1} s^{-1}}$.

Figure 3.10 shows the equipotential lines of the anode weighting field in an MSGC counter. The lines are separated by a weighting potential difference of 0.1. The anode is at $\Phi_{anode}/V_{anode} = 1$, while the cathode is at 0. Two detector field lines are also drawn. The little arrows indicate the position of drifting ions at time intervals of 10 ns. Equation 3.40 shows that an ion drifting away from the anode where the avalanche has occured induces on it a positive charge, equal to a fraction $k, 0 < k < 1$ of its charge q. k is equal to the weighting potential difference crossed during the ion drift. As indicated by the little arrows, most of the ion signal is induced within a few tens of nanoseconds.

A positive current is thus drawn from the power supply or from the amplifier connected to the anode, i.e. a negative current is injected in the power supply or in the amplifier. A signal of same polarity but much lower amplitude is generated by the electrons drifting towards the anode. Indeed, as the avalanche occurs very close to the anode, the weighting potential difference traversed by the electrons before being collected is very small. Because of their much faster drift velocity, the signal induced by the electrons is much faster. In MSGC's, about 10% of the avalanche signal is induced by the electrons in less than 1 ns time, and 90% of the signal is created by the ions in a few tens of nanoseconds. It must however be noted that the time development of ionizing particle signals is not determined by a single avalanche, but by the successive amplifications of primary electrons grouped in clusters. The spread and drift time of the primary electrons must thus be considered as well.

In the presence of several electrodes, the calculation shows that all electrodes but the anode where the avalanche has occured carry a signal of opposite sign. This effect is known as "crosstalk". Those signals can also be used for particle detection, but by charge conservation they are of smaller amplitude than the signal on the main anode.

Front-end electronics

The choice of the adequate preamplifier for a given application depends on several factors: amplitude and duration of the detector signals, readout rate, etc. In the case of MSGC's, the signal induced on the electrodes by a relativistic particle is about 25000 - 50000 electrons. It needs amplification with a dedicated low-noise amplifier. At the LHC, the signals will be generated at the proton bunch crossing frequency of 40 MHz. This requires fast amplifiers and

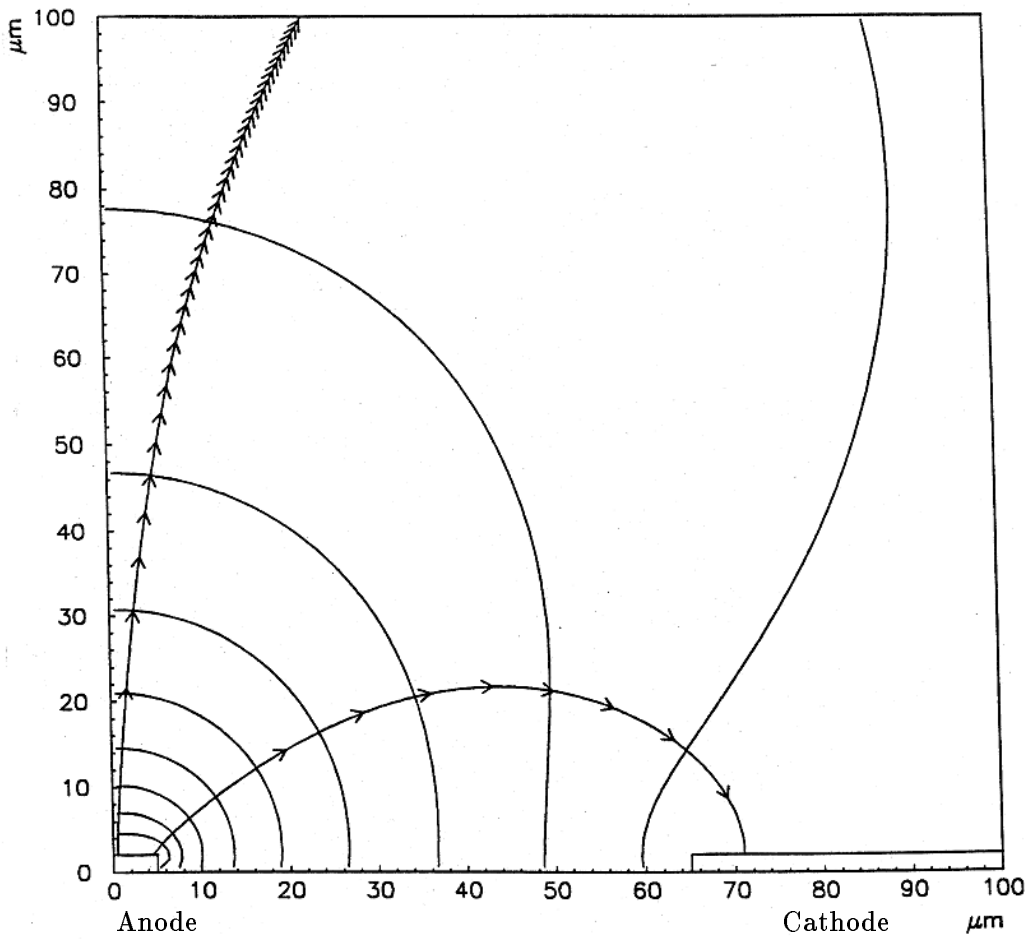

Figure 3.10: Equipotentials of the anode weighting field and detector field lines in an MSGC. The equipotentials are 0.1 weighting potential units apart. The arrows denote the position of drifting ions every 10 ns [44].

a shaping of the signals into short pulses, in order to reduce the channel deadtime and to allow the association of detector signals to a bunch crossing.

Gaseous detectors are usually equipped with charge amplifiers like the one shown in figure 3.11. If the gain of the operational amplifier is very high (usual values are 10^4 - 10^6), it is easy to show that the output voltage V_o is proportional to the input charge Q as:

$$V_o = \frac{-Q}{C_f}, \tag{3.41}$$

where C_f is the value of the amplifier feedback capacitance. The feedback circuit also contains a resistor R_f which serves to reset the amplifier and to shape the signal. Integrated amplifiers are now commonly used, as they allow to read out a large number of channels at low cost. Such amplifiers have been developed for silicon strip detectors, and are in most cases also suited for MSGC's because of the similar signal amplitude and detector capacitance. Table 3.2 presents some characteristics of two integrated amplifiers.

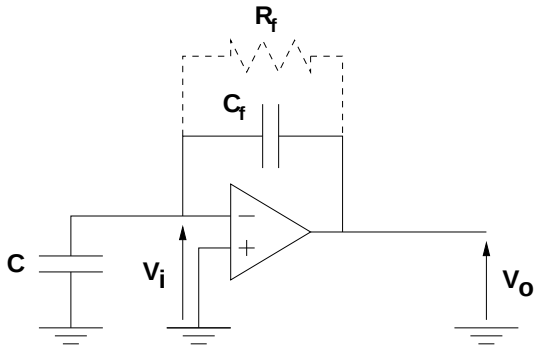

Figure 3.11: Principle of the charge amplifier. V_i and V_o are the voltages at the input and output of the amplifier, C is the capacitance of the electrode connected to it, C_f and R_f are the feedback capacitance and resistance.

	APC	APV6
Clock frequency (MHz)	10	40
Shaping time (ns)	tunable	45
Noise (electrons E.N.C.)	675 + 28/pF	1000 + 46/pF

Table 3.2: Some characteristics of integrated amplifiers used for the readout of MSGC anodes [45, 46].

The APC chip [45], developed for the silicon vertex detector of the H1 experiment at HERA, equips some of the MSGC prototypes tested in Brussels, and will be described in chapter 4. In CMS, radiation hard amplifiers of the family of the APV are foreseen to equip both silicon strip and microstrip gas detectors [46]. The APV6 chip consists of 128 amplifiers and a multiplexer for serial readout. Each channel comprises a charge amplifier and shaper of 45 ns $RC-CR$ shaping time, and a switched capacitance pipeline which samples the output of the amplifier at the LHC bunch crossing frequency of 40 MHz. The pipeline is 160 cells deep to accomodate the latency of the level 1 trigger of CMS. When a trigger is received, the channel output is computed as a weighted sum of three samples. The values of the weights are determined on the basis of the $RC-CR$ impulse reponse of the amplifier. This technique, called "deconvolution", was shown to be effective in achieving a short pulse shape limited to 1 LHC bunch crossing interval (25 ns) in the case of silicon strip detectors.

Two figures of merit are of particular importance for an MSGC amplifier at the LHC: the noise and the ballistic deficit. The noise is the random fluctuation of the amplifier output voltage in the absence of a particle signal. An unavoidable noise source is the thermal motion of the electrons inside the resistor constituted by the electrode connected to the amplifier:

$$V_{noise} = \sqrt{4kTRB}, \tag{3.42}$$

where V_{noise} is the noise voltage R.M.S., R is the input resistance and B is the preamplifier bandwidth. The thermal noise thus increases with the input resistance and with the amplifier response speed. At room temperature, it amounts already to 25 μV for an amplifier of 40 MHz bandwidth connected to an electrode of 1 kΩ resistance. The noise is usually expressed as the Equivalent Noise Charge (E.N.C.) at the input of the amplifier. The E.N.C. is equal to the noise voltage R.M.S. times the capacitance of the detector. In the above example, for a typical

electrode capacitance of 10 pF, it amounts to 1500 electrons. The noise of the detector is thus an increasing function of the detector capacitance.

The ballistic deficit is the signal reduction factor due to a mismatch between the signal duration and the amplifier shaping time. If the shaping time $R_f C_f$ is of the same magnitude or smaller than the signal rise time, the amplifier feedback capacitor starts to discharge before the whole charge has been amplified. This results in a decrease of the output signal. Noise and ballistic deficit affect the counter detection efficiency: a particle signal can only be detected if its amplitude exceeds significantly the amplitude of noise pulses. Because of the relatively low operating gains in MSGC's, around 10^3, the noise and the ballistic deficit of the front-end amplifier should be small to permit efficient MIP detection.

The MSGC signals differ from those of silicon detectors in two main respects: the collection time of the electrons is longer, typically 50 ns instead of a few nanoseconds in solid state detectors, and the signal fluctuations are larger due to the small number of primary electrons released in the gas. Because of the long electron collection time, MSGC's equipped with the APV electronics suffer from a ballistic deficit of 0.7 [47]. A shaping time as short as 45 ns seems however not necessary for MSGC's in CMS, as the counting rate per channel is expected to be well below 10^6 Hz. With a 100 ns time constant the channel occupancy would still be reasonable, a few percent. This number would be even lower after signal processing (deconvolution, or double correlated sampling, as implemented in the APC chip). On the other hand, signal fluctuations will cause a 50 ns uncertainty in the determination of the ionizing particle crossing time. It means that part of the hits from the previous and subsequent bunch crossings will be attributed to the triggered event, doubling the number of MSGC signals to be considered at the track reconstruction stage [48].

We can now estimate the minimum number of primary electrons that should be deposited by a minimum ionizing particle in an MSGC in order to be detected. At a typical gas gain of 2000, with an equivalent noise charge of 1500 e^-, a ballistic deficit of 0.7 and a threshold set at three times the noise, that number amounts to about 3 electrons, as compared to 1 for an ideal detector.

3.2 Description of the Micro-Strip Gas Chamber and Micro-Gap Chamber

3.2.1 Introduction: the Multi-Wire Proportional Chamber

The Micro-Strip Gas Chamber and the Micro-Gap Chamber (MGC) are modern developments of the Multi-Wire Proportional Chamber (MWPC) well known from the work of G. Charpak [49]. As these detectors are based on similar principles, the MWPC will be described first as an introduction. The outline of a MWPC is shown in figure 3.12: thin wires of typically 20 to 70 μm diameter are strung parallel in a gas volume, closed by conducting planes. The anode wires are set to a high positive voltage, a few thousand volts, and the cathode planes are on a negative voltage. When a particle crosses the active volume of a MWPC, it ionises gas molecules on its way. The electrostatic force makes the liberated electrons move towards the anodes, and the positive ions to the cathode planes. In the neighbourhood of the anode wires, the electrons experience avalanche multiplication. The amplitude of the signals induced on the electrodes allows to determine the particle crossing point.

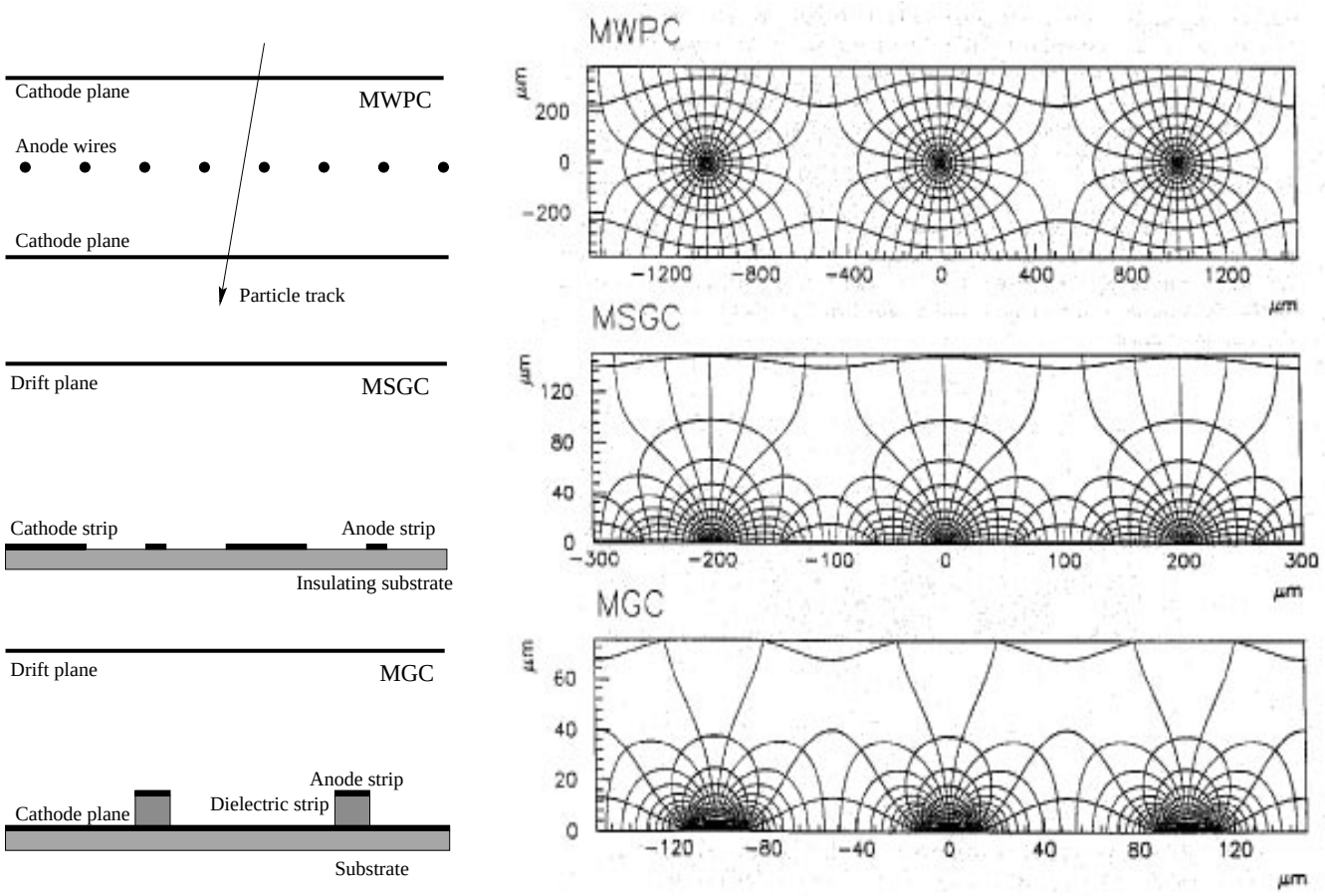

Figure 3.12: Outline of the MWPC, the MSGC and the MGC and the corresponding field configurations [44]. The drawings on the left are not at scale.

The main limitation of the MWPC is that the distance between the wires cannot be made much smaller than 1 mm, to limit the electrostatic force between adjacent wires. The granularity, i.e. the number of detection cells per surface unit, is therefore limited. With a detector response of a few hundreds of nanoseconds duration, the counting rate of the MWPC cannot exceed 10^4 charged particles per cm^2 per second.

3.2.2 The Micro-Strip Gas Chamber and the Micro-Gap Chamber

The micro-strip gas chamber and the micro-gap chamber result from the attempts to built highly granular multiwire chambers. In 1988, A. Oed proposed a detector where the wires were replaced by conducting strips, printed on an insulating surface by a photolithographic process like the ones used in microelectronics [22]. This detector, later called micro-strip gas counter, is schematically drawn on figure 3.13. It consists of an insulating plate on which narrow anode strips are interleaved with broader cathode strips to shape the electric field. Typical strip widths are 10 μm for the anodes and 100 μm for the cathodes. The back of the insulating substrate is sometimes also metallized and biased for further field shaping. The plate is positioned in a gas volume which acts as active medium: passing particles ionise molecules in this gas volume, and the liberated electrons are pushed towards the anode strips by the negatively charged drift plane placed a few millimeters above the substrate. Avalanche multiplication takes place in the very high electric field ($>$ 100 kV/cm) which develops at small distance ($\leq$ 50μm) from the anodes. Gas gains of the order of 10^3 - 10^4 can be obtained, which correspond to signals of a few times 10000 electrons for minimum ionizing particles.

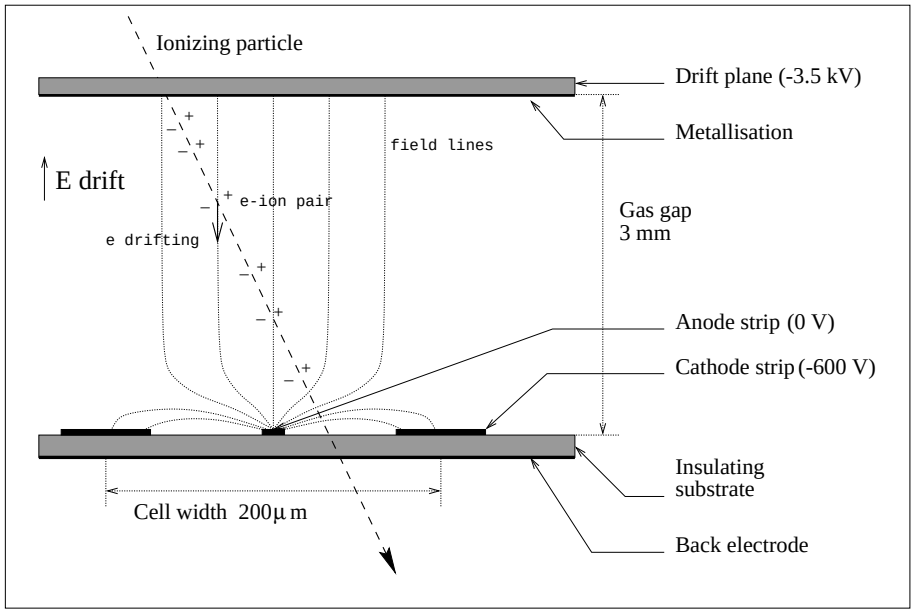

Figure 3.13: Principle of the micro-strip gas counter. Typical dimensions and voltages are indicated on the figure.

The MSGC shows a number of advantages over the classical wire chamber:

- Having strips fixed all along on a rigid plate allows much smaller electrode spacing than in MWPC, with typical anode interdistances of 200 μm. There is no need of a strong frame to take the tension of the wires, which makes the counter lighter. The small strip interdistance is also rendered possible thanks to the submicron precision of the strip patterning.
- The avalanche space charge is quickly removed from the region of high field around the anode strips, thanks to the presence of the nearby cathode strips and to the possibility of operating at high drift fields ($\simeq$ 10 kV/cm). The electric field configuration is such that the signal induction is faster in MSGC's than in MWPC's. A typical risetime value is 50 ns for an avalanche originating from a single electron.

- The highly granular, fast MSGC can operate at particle fluences in excess of 10^6 Hz/mm^2.
- The crossing point of the incident particle is accurately determined thanks to the small electrode spacing. The spatial resolution can be as good as 30 μm for particles of normal incidence with respect to the substrate, when calculating the barycentre of the signals collected on the hit strips. Such a position accuracy can also be reached with multiwire chambers used in drift mode, but at much lower counting rates than with MSGC's.
- Smaller gain fluctuations can be reached with MSGC's than with MWPC's thanks to the highly concentrated amplification field.

It has also been shown that the MSGC can sustain high radiation doses, up to 100 mC of accumulated charge per centimeter of strip. This value is a conservative estimate of the charge collected by the anodes in 10 years of LHC operation at 50 cm from the beam pipe. The MSGC is therefore an adequate detector element for tracking at high luminosity. As compared to solid state detectors, which allow better position resolution ($\leq 10\mu$m) and shorter signal risetime ($\leq$ 10 ns), MSGC substrates have the main advantage of being a factor 5 cheaper per surface unit. The main drawbacks of the MSGC are related to the insulating substrate which carries the strip pattern. Substrate polarization and charging due to the accumulation of ions on the insulating surface causes modifications in the amplification field and therefore in gas gain. The interaction between the subtrate and gas pollutants or chemical species produced during the avalanche are not well understood and lead in some cases to fast detector ageing.

To solve the problems caused by the presence of an insulating substrate, the micro-gap counter was introduced by the group of R. Bellazzini [50]. In this detector, the anode strips sit on top of thin dielectric strips, a few micrometers high, lying on a full cathode plane, as shown on figure 3.12. Only the sides of the insulating strips are left exposed to the gas. Such counters have been operated successfully at gains above 10^4 and counting rates above 10^7 Hz/mm^2. The MGC also shows some additional features over the MSGC:

- Because of the very small distance between the anode and cathode, the signal induction is very fast ($\simeq$ 10 ns risetime for a single avalanche). It should be noted that for MIP detection this is not a very big advantage, as the ionization collection time is typically 50 ns for counters with a 3 mm gas volume at atmospheric pressure.
- Even less gain fluctuations are obtained in MGC's than in MSGC's, due to the higher field confinment.
- Two-dimensional readout can be implemented easily by patterning the MGC cathode plane. Such a 2D readout can also be obtained with MSGC's, by metallizing the back of the substrate and etching a strip pattern in the back electrode. However the signal amplitude induced on the back electrode decreases with the insulator thickness: substrates thinner than 100 μm are required, or a multilayer support must be used. Moreover highly resistive substrates must be chosen in order not to shield the back electrode, which is not adequate for high rate applications.

MGC's are considered as a possible technique for building the double sided gas counters of the CMS tracker. However this technology is less mature than the MSGC, and shows no fundamental advantage over MSGC's in terms of long-term stability, which is one of the main issues to be solved for use at the LHC.

MSGC's and MGC's have already found a very wide range of applications. They have been used as tracking elements in several high-energy physics detectors. In the NA12 experiment

at CERN, 8 MSGC plates were assembled as an upgrade of the beam magnetic spectrometer [51]. Thanks to the high spatial resolution of the counters as compared to the precision of the former spectrometer MWPC's, the accuracy of the momentum measurement of the 450 GeV/c proton beam was improved from 7 GeV/c to 1.2 GeV/c. At the fixed target experiment SMC, also at CERN, 16 MSGC's of 10×10 cm^2 active area were successfully installed, improving the determination of particles scattered from the beam at small deviation angles [52]. The vertex detector of the HERMES experiment at HERA consists of 12 MSGC's of up to 15×20 cm^2 size [53]. The choice of MSGC's was dictated by the wide detection area to be covered and the low amount of material tolerable in front of the calorimeters. Apart from high-energy physics, MSGC's/MGC's have been successfully used or are proposed for synchrotron radiation experiments like in the DUBBLE beam line in Grenoble [54], in X-ray astronomy [55] and in medical radiology [56], among other applications.

3.2.3 Factors influencing the performance of MSGC's and MGC's

Since the Oed paper, the various aspects of the MSGC/MGC performance were studied by many groups around the world. To co-ordinate the research conducted in several laboratoria, many of them working on tracking devices for the LHC experiments, the RD-28 collaboration was created at CERN in 1992. After completion of most of its program the collaboration published its final status report in february 1996 [57]. The research program covered by the RD-28 collaboration and other MSGC groups consists in generic research and development as well as specific developments related to the LHC experiments. We shall review some of these aspects, focusing on LHC-related topics:

- Development of substrates suitable for MSGC manufacturing, with the proper characteristics in order to ensure long term stable operation under a high particle flux. An additionnal requirement for tracking at LHC is that the substrate material must be obtainable in large ($\sim 10 \times 10$ cm^2), thin (~ 200 μm) samples;
- Optimization of the detector geometry and gas filling in order to achieve the highest stable gain, detection efficiency and spatial resolution;
- Choice of operating gases and construction materials, compatible with obtaining an acceptable lifetime of MSGC's under sustained irradiation;
- Behaviour in intense magnetic field;
- Stability under irradiation with Heavily Ionizing Particles (HIP's) and neutrons;
- Two-dimensional readout;
- Signal time development.

The above aspects are linked and will therefore not be described separately. Possible choices of detector geometry and construction materials will be presented instead, with a discussion of their influence on the MSGC performance.

Substrate

Almost any insulator with high dielectric strength and adequate surface quality for photolithography can be used as an MSGC substrate. One of the most commonly used material is the high resistivity ($10^{15}\Omega$cm) DESAG D-263 glass. It presents a very good surface quality and

can be obtained in samples of size and thickness suited for high energy physics applications. It is adequate for moderate rate experiments like SMC at CERN or HERMES at HERA. Still, the study of the ageing of counters made with D-263 glass substrates has revealed important performance degradation after an accumulated charge of 100 mC/cm of strip, i.e. gain drops of more than 40% and severe deterioration of the energy resolution. The detectors seem however to recover after a few days without irradiation. This phenomenon was observed by several groups and is not well understood yet [58, 59, 60].

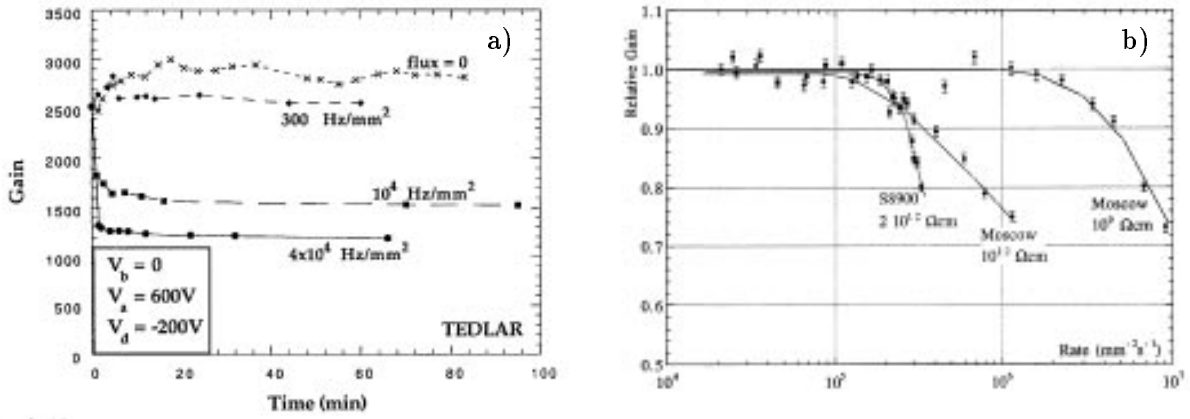

Figure 3.14: Rate behaviour of MSGC's. a) Gain as a function of time, at various irradiation rates with 5.9 keV X-rays, for an MSGC made with a Tedlar plastic substrate of resistivity $10^{14}\Omega$cm [61]. b) Rate dependence of gain for MSGC's manufactured on several semi-conducting glass plates, having a bulk resistivity between 10^9 and $10^{12}\Omega$cm [62].

In general, detectors built with highly resistive substrates suffer from the accumulation of ions or electrons on the strip support. The space charge field created by the deposited charges modifies the electric field around the electrodes and causes gain variations. At detector switching on, the gain changes rapidly as the substrate charges up, then an equilibrium is reached when charge conduction inside the support balances charge deposition. The regime gain is rate dependent, as illustrated in the left plot of figure 3.14, showing the gas gain as a function of time for various irradiation rates with 5.9 keV X-rays [61]. The use of a substrate of moderate bulk or surface resistivity solves the charging problem up to very high rates. With a bulk resistivity in the range 10^9 - $10^{12}\Omega$cm or a surface resistivity in the range 10^{14} - $10^{16}\Omega/\Box$, counting rates up to 10^6 Hz/mm^2 have been reached without significant gain drop (see right plot of figure 3.14) [62]. MGC detectors, offering almost no insulating surface to charge up, exhibit the highest rate capabilities, up to and above 10^7 Hz/mm^2 [50]. It should be noted that, with DESAG D-263, the rate capability is already 10^4 Hz/mm^2, a value about equal to the LHC particle flux at 50 cm from the beam intersect.

In addition to high rate capability, it has been experimentally demonstrated that supports with moderate resistivity also yield the best results in terms of ageing. With custom-made or commercial glasses (Moscow, Pestov or Schott S-8900), MSGC detectors could sustain doses up to 100 mC/cm of strip, equivalent to more than 10 years of LHC operation at 50 cm from the beam pipe, without degradation of gain or energy resolution [62, 59], as shown in figure 3.15 a) for the Schott S-8900 glass. The main disadvantage of these materials is that they contain heavy elements and have therefore a short radiation length. They are thus not very adequate for tracking, unless they can be produced in very thin layers ($\leq 150\mu$m).

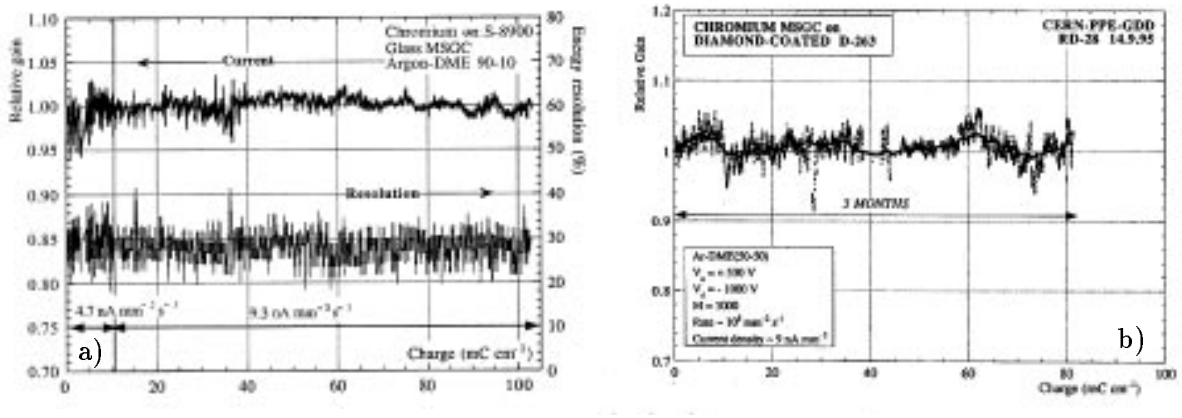

Figure 3.15: Ageing of MSGC's made on low resistivity substrates. a) Relative gain and energy resolution as a function of the charge accumulated per cm of strip, for an MSGC made with S-8900 glass and chromium strips [62]. b) Relative gain as a function of the cumulative charge for an MSGC made on diamond-coated DESAG D-263 glass [63].

Several techniques have been tried in order to grow thin slightly conductive layers on light insulating supports. Among the most promising methods is the chemical vapour deposition of diamond-like layers, used industrially for the hardening of mechanical components. The CERN group was the first to investigate the production of thin ($\sim$ 150 nm) diamond-like layers of sufficiently uniform resistivity on large (10" $\times$ 10") supports. The layer resistivity, obtained by a doping technology, is very stable in time [63]. Detectors made with diamond-like coated substrates have demonstrated very good ageing properties, showing no gain drop up to 80 mC/cm of strip, as shown in figure 3.15 b). An alternative solution is the sputtering of a thin layer of low resistivity glass. This technique provides better control of the surface smoothness than diamond-like coatings, allowing better quality of the metallization. As good performance as with bulk S-8900 was observed with a 800 nm thick S-8900 layer deposited on a high resistivity glass [59]. Substrates with slightly conductive layers deposited on top of an existing strip pattern have been tested as well. In this design the semiconductive layer is more exposed to damages during the avalanche process. Still, over-coated detectors could be operated up to 50 mC/cm of accumulated charge [64].

In view of developing light non-brittle substrates, the production of MSGC's on plastic foils was investigated. Plastics have some disadvantages over glass: surface smoothness and metal adhesion are poorer, plastics absorb trace impurities which are likely to interact with the operating gas, and plastics resistivity is naturally high. However polymer films can be made very thin, which can provide inexpensive 2D detectors. Ion implantation was successfully tried in order to reduce the surface resistivity of plastics substrates [65]. The long term behaviour of such counters is still under investigation. The best performance published reports tolerance to a few mC/cm before breakdown [65]. Some of the gases commonly used in MSGC's, like DME, act as solvants for plastics, which can jeopardize the mechanical stability of the counters.

The main disadvantages of using low resistivity layers are that a higher voltage must be applied on the strips to reach the same gain as with an insulating substrate, and that the probability of streamer development is increased. Figure 3.16 a) shows the gain curves measured with substrates of surface resistivities $10^{17}\Omega/\Box$ and $10^{13}\Omega/\Box$. An anode-cathode voltage 50 V higher must be applied to the MSGC with the low resistivity substrate to reach the same gas gain as with the high resistivity substrate. Figure 3.16 b) shows the electric field intensity at

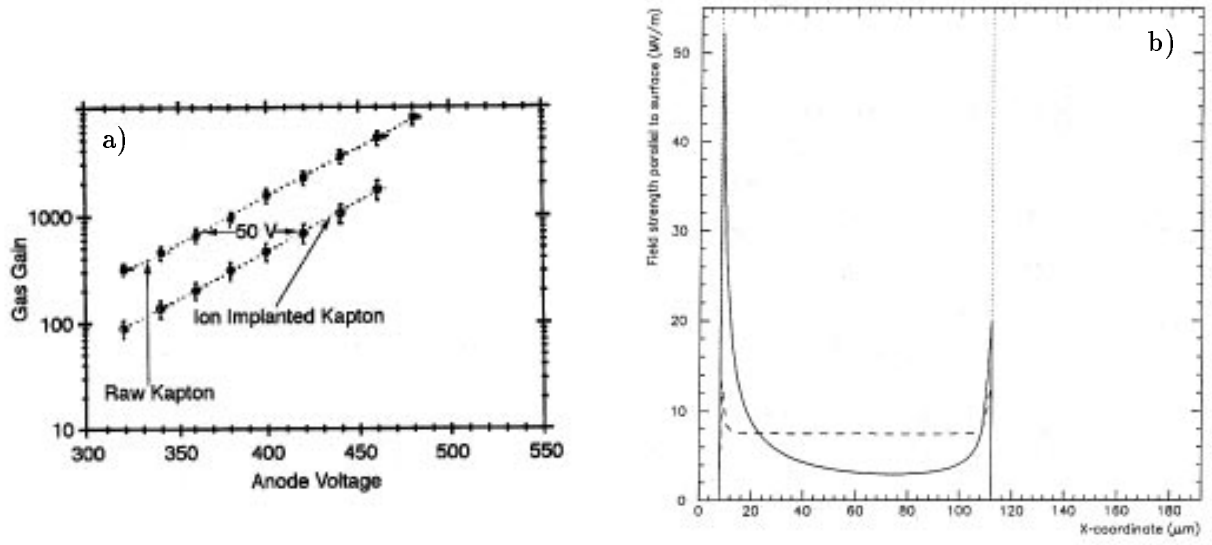

Figure 3.16: a) Gain as a function of the voltage difference between the anode and cathode strips, in MSGC's made with substrates of surface resistivity $10^{17}\Omega/\Box$ (raw Kapton) and $10^{13}\Omega/\Box$ (ion implanted Kapton) [65]. b) Electric field strength parallel to the substrate as a function of the distance to the anode, for a chamber with uniform support of resistivity $10^{14}\Omega$cm (solid line) and for a chamber having a 4 μm thick $10^{11}\Omega$cm resistivity layer on top of the support (dashed line) [66].

the dielectric surface, in the presence and in the absence of conductive layer [66]. The field was computed at strip voltages adjusted to give the same gas gain in both cases. On one hand, the field peak value at the anode is reduced by a factor 3 in the presence of conductive layer. This explains the gain reduction at fixed cathode voltage. On the other hand, a high uniform field ($\sim$ 100 kV/cm) is created in the anode-cathode gap. This field geometry favours the development of unquenched streamers between the electrodes [67].

In MSGC's, unquenched streamers must be avoided because the energy released in a spark is large enough to damage the strip pattern. Sparks are not likely to occur when using MSGC's at gains around 2.10^3 for MIP detection. However, streamers can be triggered by the space charge field of large avalanches produced by Highly Ionizing Particles (HIP's). A HIP like an α-particle, a slow proton or an activation gamma, released for instance by the interaction of a hadron with the detector construction materials, can release 100 times more ionization in the detector than a MIP. At the LHC the neutron fluence at 50 cm from the beam crossing point will be about 10^3 - 10^4 Hz/mm^2, which generates a rate of HIP's estimated to 0.1 - 1 Hz/cm^2 in the detectors. Figure 3.17 a) shows the maximum stable gas gain in a diamond coated chamber, in the presence of α-particles from a ^{220}Rn source (curve B), as compared to the maximum gain in the presence of 8 keV X-rays (curve A) and in the absence of radiation. The surface of the chamber is scanned in groups of 16 strips. The maximum gain that can be reached in the whole chamber is 3500, less than a factor 2 above the gain required for efficient MIP detection. This safety margin is not satisfactory for long-term operation of a large MSGC system at the LHC [68].

Therefore the protection of the MSGC counters against streamer-induced discharges has become a subject of concern. The group of R. Bellazzini has introduced the "advanced passivation" technique, in which the edges of the cathode strips are covered by narrow dielectric

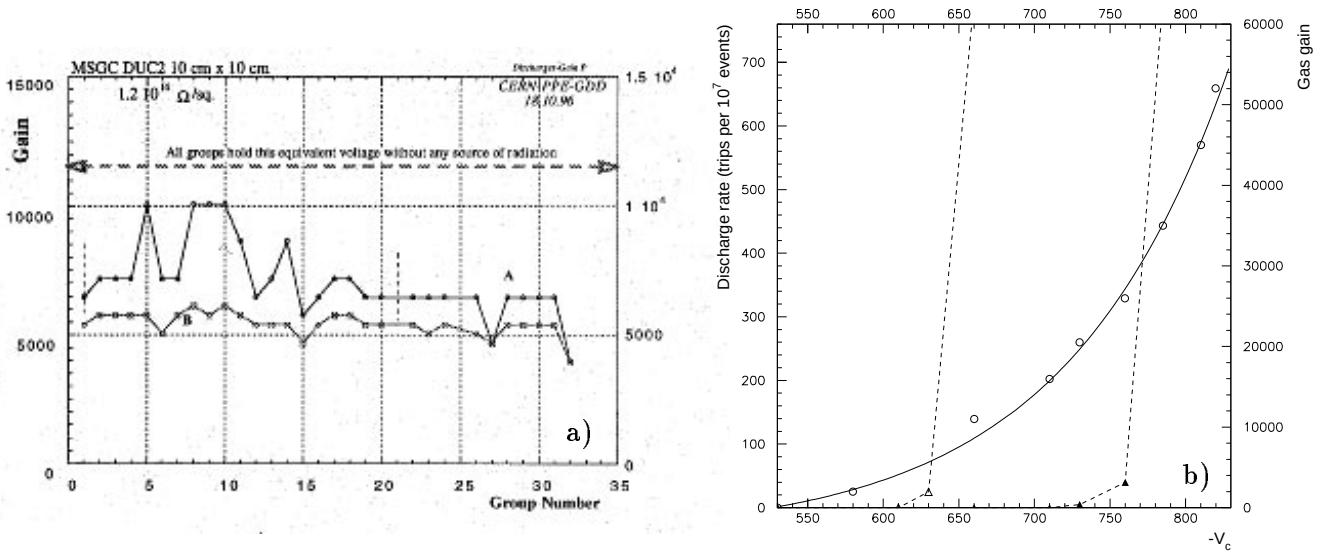

Figure 3.17: a) Maximum gains in the presence of 8 keV X-rays (curve A) and α-particles from a ^{220}Rn source (curve B), across a diamond coated substrate. The detector surface is scanned by groups of 16 strips [68]. b) Gain (circles) and discharge rates as a function of the cathode strip voltage, in diamond coated chambers irradiated with α's, with and without advanced passivation (closed and open triangles respectively) [69].

strips in order to suppress the electric field at the cathode edges [69]. Figure 3.17 b) shows the gain and rate of discharges in the presence of α-particles, for diamond coated MSGC's with and without advanced passivation. It can be seen that the range of cathode voltages before breakdown is increased by more than 100 V in passivated detectors. Detectors built with Pestov glass coatings of resistivity 10^{15} - $10^{16}\Omega/\Box$ and protected by advanced passivation sustained a high intensity beam of 5×10^3 pions/mm^{2}s during 170 hours without spark-induced damage [70]. Tests have been performed with detectors of identical specifications in a neutron beam equivalent to 2000 times the combined MIP and HIP flux of LHC during 10 hours [71]. The counter gas box and electronics were assembled with similar materials as the ones that will be used for the construction of the MSGC modules for the CMS tracker, so that the activity induced by neutrons is comparable to what will be encountered at LHC. The results are encouraging, as no strip in the area irradiated by the neutron beam broke during the test.

Micro-gap counters could sustain radiation doses comparable to the best performance obtained with MSGC's [72]. The signals induced on the cathode plane and on the anode strips are of comparable amplitudes, which makes the implementation of 2D readout possible by segmenting the cathode plane. An amplitude of 80% of the anode signal was recorded on the cathode plane of an MGC made on a glass substrate [72]. Behaviour under HIP's is still under investigation. Destructive sparks have been noticed in 2D MGC's, due to the discharge of the decoupling capacitors connected between the cathode plane segments, at high voltage, and their readout electronics, at ground potential.

In conclusion, MSGC substrates coated with semiconducting materials (diamond-like or semiconducting glass coatings) with advanced passivation meet the stability and lifetime requirements of high luminosity experiments like CMS. In applications where long term stability under a high rate of ionizing particles is not a concern, several choices of substrates exist, from glass to plastics. Strip patterning is easier on glass but the flexibility and the use of thin layers opens a wider range of applications for plastic substrates. Rate capability up to and above

10^6 Hz/mm^2 can either be obtained with low resistivity substrates or with MGC's. Two-sided readout can either be realized with thin ($\leq 100\mu$m) MSGC substrates or with MGC's.

Strip metal

Several materials have been tried as strip metallization. Among the aspects to be considered are the quality and cost of the etching process, the influence of the metal on the ageing rate and the metal resistivity. Aluminium is easy to process by wet etching, but has always led to fast ageing. Gold is a favoured choice, as it is known to allow long detector lifetimes, but is more difficult to process. Figure 3.18 a) shows the relative gain as a function of the cumulative charge, with strips made of aluminium and gold grown on a nickel adhesion layer. While aluminium provoked a 10% gain drop after less than 1 mC/cm of accumulated charge, gold strips sustained an irradiation dose equivalent to several years of operation at LHC [73]. Nickel seems a promising candidate, as it has yielded as good results as gold in comparable conditions, but needs further investigations because the LHC requirements could not be met yet [74].

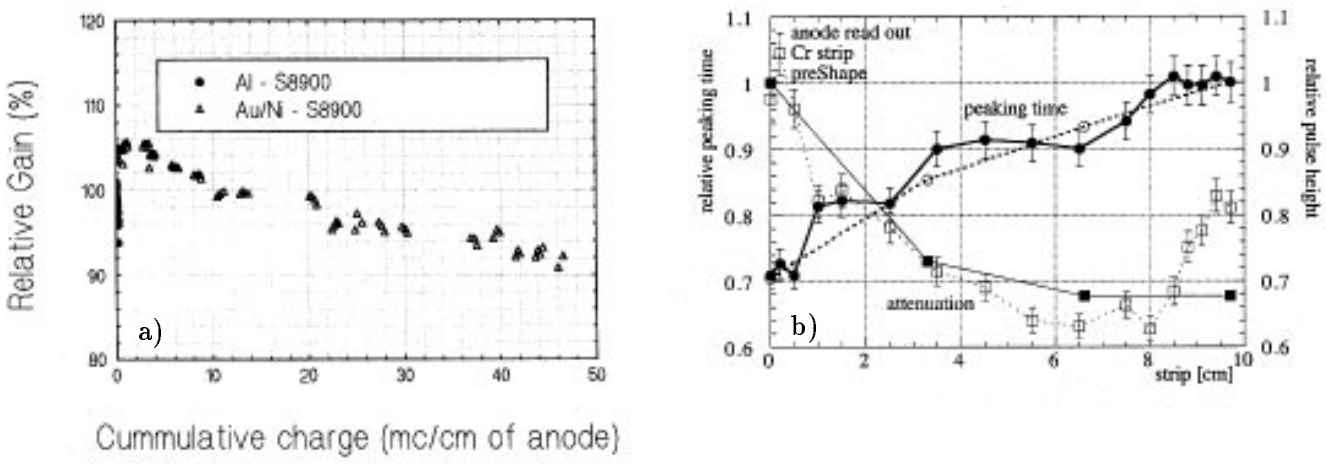

Figure 3.18: Choice of the strip metal. a) Relative gain as a function of the cumulative dose, with aluminium and gold strips, on a Schott S-8900 substrate [73]. b) Relative pulse height and peaking time as a function of the distance along chromium anode strips. The points with error bars are measurements and the other points are simulation results obtained with a model of the microstrip counter using an equivalent electric circuit [75].

Lifetimes adequate for LHC have also been reached with chromium, as shown in figure 3.15 a). Chromium provides artwork of excellent quality at low costs. However the striplength is limited to a few cm, because of the high resistivity of this metal. Figure 3.18 b) shows the relative signal amplitude and peaking time as a function of the anode length between the irradiation spot and the amplifier. The resistance of the 7 μm wide anodes is 2 kΩ/cm. A 30% signal attenuation and a 30% increase in signal risetime is recorded at a striplength of 6 cm [75]. The thermal noise also increases with the strip resistance, but as demonstrated in [75] the RC circuit formed by the strip acts as a filter, and the noise measured at the output of the amplifier is smaller than expected from formula 3.42.

Detector, electrodes and field geometry

The optimization of the MSGC geometrical parameters is very application-specific. We shall focus on the use of MSGC's for tracking in CMS, which requires counters designed for high detection efficiency (above 95%), stable operation, good localization accuracy (better than 40 μm), high signal speed (about 50 ns peaking time) and low occupancy (at the level of a few percent per channel).

Particle signals are detected only if they exceed the noise of the electronics. The detector field configuration should therefore allow the highest stable gas gains. The optimal field, highly concentrated around the anode strips, is obtained with the narrowest anodes and the widest cathodes possible. However the fragility of the metallization sets a lower limit of about 5 μm to the anode width, and the discharge rate is increased with very close anode and cathode edges. The largest stable gain is reached with cathodes of about 90 μm, for an anode pitch of 200 μm (see figure 3.19) [76].

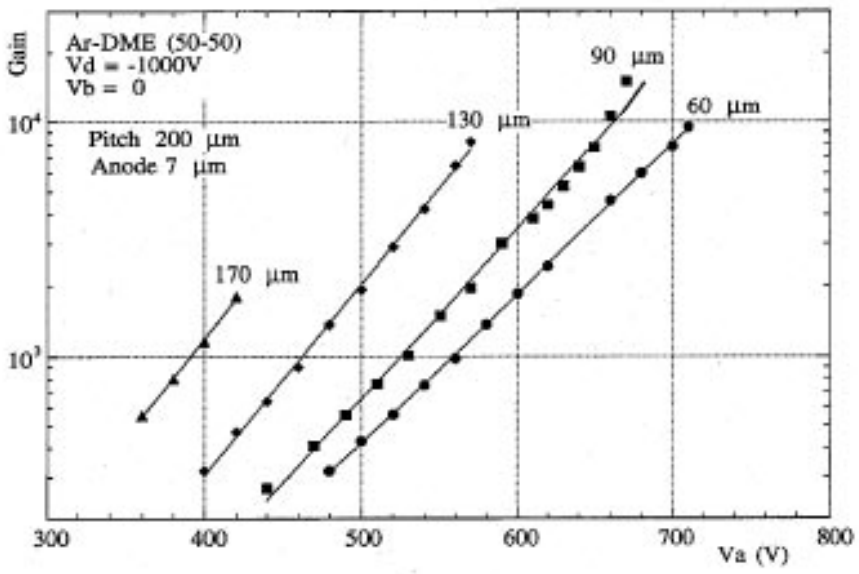

Figure 3.19: Gain as a function of the voltage difference between the anode and cathode strips, for various cathode widths. The anode pitch is 200 μm, and the anode width, 7 μm. The curves stop when the bias current from the power supply exceeds 20 μA due to the appearance of discharges [76].

Although it is not desireable to have amplification inside the drift space, operation at high drift field is preferable. A higher drift field allows to reach a given gain value with a reduced voltage between anodes and cathodes, hence reducing the chance of discharge. Apart from better detector stability, it also yields high electron drift velocity, thus fast charge collection, and low electron mobility, thus small Lorentz angle (cf. section 3.2.3). In CMS, the drift field recommended when using DME-based gas mixtures is $\sim$ 10 kV/cm.

The theoretical detection efficiency directly determines the minimal thickness of the gas volume. In usual gas mixtures at atmospheric pressure, the average number of primary electrons released in 1 mm gas is between 3 and 5, so the probability of releasing at least 1 electron in 1 mm is between 95% and 99%. The minimum thickness of an ideal counter filled with a gas at atmospheric pressure is thus 1 mm. This value increases to about 2 mm when considering that the minimum number of primary electrons that can be detected clearly above the noise

is rather 3 primary electrons. The electron drift velocity determines the maximal useful gas thickness. With practical drift speeds limited to about 60 - 70 μm/ns, the gas gap should not exceed 3 mm, if all the primary ionization is to be collected within the 45 ns shaping time of the APV electronics.

Some of the factors affecting the detector spatial resolution are related to the detector geometry, like the interdistance of the read-out electrodes and the thickness of the gas gap, whereas others depend on the choice of the gas mixture. In the work of J. Schmitz [77], their effect has been evaluated by studying the distribution of the ionization reaching the strip support. In the case where the ionizing particle crosses the detector at normal incidence, the R.M.S. of the electron distribution on the substrate is approximately:

$$\Delta x \simeq \frac{1}{2}\sigma_T\sqrt{L}, \tag{3.43}$$

where σ_T is the transverse diffusion coefficient and L is the thickness of the gas volume. Measuring the position of each of the N electrons reaching the substrate would allow to localize the incident particle with an accuracy equal to:

$$\Delta x_N \simeq \frac{1}{2\sqrt{N}}\sigma_T\sqrt{L} \simeq \frac{\sigma_T}{2\sqrt{n_T}}, \tag{3.44}$$

where n_T denotes the total ionization density.

This formula shows that the ultimate spatial resolution is directly related to the transverse diffusion coefficient and to the ionization density in the gas mixture. It also indicates that the position accuracy for normal incidence tracks is in first approximation not affected by the gas gap. The increase of the electron spread with L is compensated by the larger ionization statistics. In practice, however, N fluctuates statistically from event to event, and the ionization is not spread uniformly along the track. Formula 3.44 is only valid if N is large, i.e. if $L \geq 5$ mm. For thinner gas gaps, Δx_N is larger than equation 3.44 would suggest.

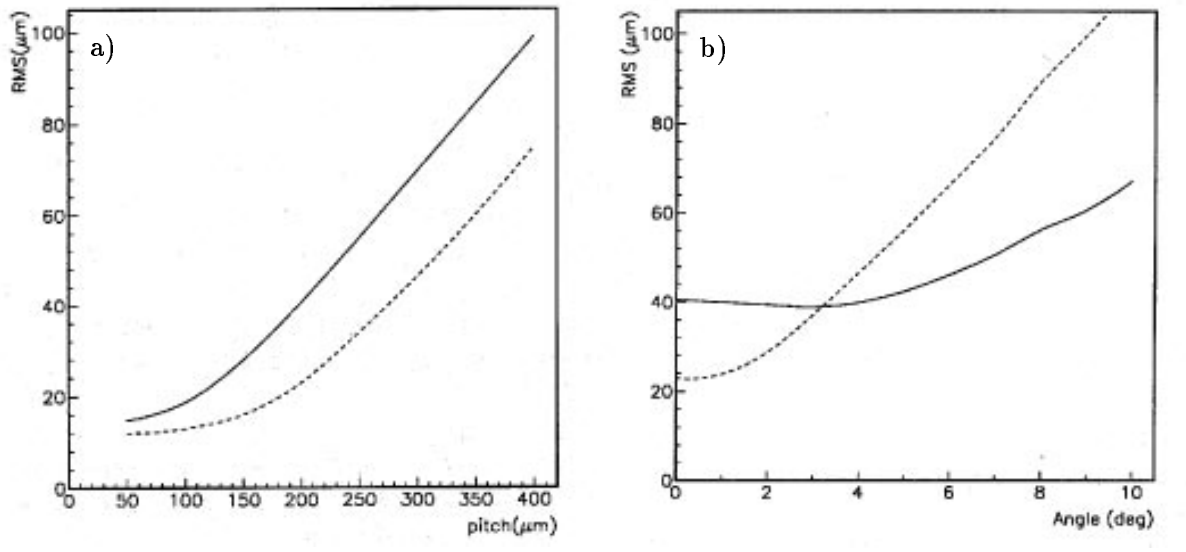

Figure 3.20: Position resolution of an MSGC, a) as a function of the anode pitch for tracks with normal incidence and b) as a function of the incident angle for a pitch of 200 μm, for a gas gap of 2 mm (full line) and 5 mm (dashed line) [77].

The readout pitch p affects the resolution in the sense that, when it is much smaller than Δx, the electron distribution is effectively sampled and optimal performance is reached. When $p \gg \Delta x$, generally only one anode gives a signal when a particle crosses, and the resolution is given by $p/\sqrt{12}$. Figure 3.20 shows the behaviour of the position resolution as a function of the readout pitch, for two values of the gas thickness (2 and 5 mm), in DME-CO_2 60%-40%, as predicted from the simulation study of J. Schmitz. In this gas mixture, at drift fields around 10 kV/cm, the diffusion coefficient is about 60 μm/$\sqrt{\text{mm}}$, and hence the optimal resolution is obtained with a readout pitch of a few tens of μm. However 40 μm accuracy as required in CMS can be acheived with 2 mm thick counters and 200 μm readout pitch.

Another aspect to be considered when choosing the detector thickness is the increase of the strip occupancy and the degradation of the position accuracy with increasing particle incident angle. Particle tracks that traverse the counter at a certain angle in the projection plane perpendicular to the strips will generate signals on several anodes. The number of strips hit and so the occupancy from inclined tracks rises with the gas thickness. Simulations and experimental tests have shown that the MSGC position resolution degrades with the incident angle, and that this deterioration is faster with a thicker gas gap (see figure 3.20) [77, 11]. Therefore the smallest gas gap providing sufficient detection efficiency should be preferred.

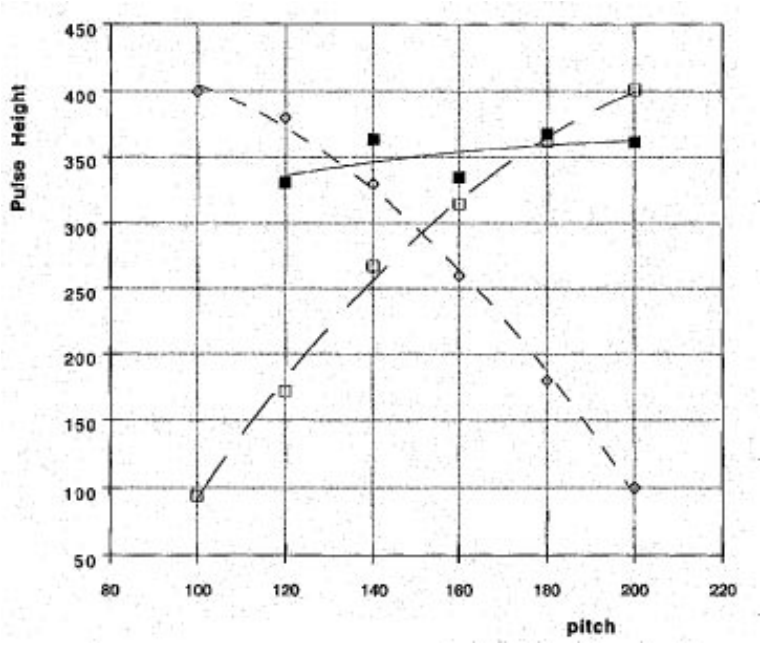

Figure 3.21: Pulse height as a function of the anode strip pitch, in three different strip configurations. Open squares: fixed anode width and gap between anode and cathode strips, open diamonds: fixed anode and cathode widths, closed squares: fixed anode width, cathode width and gap varied according to rule 3.45 [78].

The anode pitch also affects the gas gain. Fixing the anode width and the gap between the anode and cathode leads to an increase of gain as a function of increasing pitch, as shown by the open squares in figure 3.21. More drift field lines are collected per anode in the case of a large anode pitch, which results in an increase of the total amplification field around the anodes and an increase of gas gain. Fixing the anode and cathode widths leads to a decrease of the field in the gap between the anodes and cathodes and thus to a gain drop when the pitch increases, as shown by the open diamonds. These effects can be compensated by varying both

gap and cathode width. Using the scaling law [78]

$$g = p/8 + 20\mu\text{m}, \tag{3.45}$$

one is able to construct an MSGC plate with varying pitch and constant gain (closed squares on the figure). This rule is used to desing the trapezoidal counters of the forward part of the CMS tracker, which have their strips radially pointing to the beam pipe.

Once the pitch is fixed, the strip length is chosen so as to maintain the occupancy due to ionizing particles to the level of 1%. In CMS, this is acheived with a striplength of 12.5 cm in the barrel part of the tracker, and with lengths varying from 8 to 14 cm in the forward part, coping with the increase of particle rate with the pseudorapidity.

Gas filling

Several detector performance requirements affect the choice of the gas mixture: detection efficiency, spatial resolution, signal speed, Lorentz angle, long term stability and safety. These requirements translate into the following gas characteristics: high primary and total ionization, high stable gain, low transverse diffusion, high drift velocity, small mobility, good quenching and ageing properties.

In very thin detectors with relatively low gain limit, like MSGC's in CMS, the primary ionization density of the operating gas is of essential importance in order to reach a good efficiency. A primary statistics of more than 30 e^-/cm is desireable, which restricts the choice to mixtures with a high content of DME, CO_2, organic or heavy noble gases (see table 3.1). Because of photon feedback, heavy noble gases like Xe or Kr cannot be used in large proportions, except in combination with strong quenchers. Organic compounds like methane or isobutane lead to fast detector degradation due to polymer deposition on the strips [79, 73], while long-term tests have been successfully performed with DME-based mixtures (see figure 3.15). The primary ionization density of CO_2 is still poor. Therefore the use of DME as main component is a quite natural option.

Figure 3.22 shows the drift velocity and the diffusion coefficients in pure DME as a function of the drift field [31, 80]. The drift velocity levels off at a relatively low value of 50 μm/ns, barely sufficient to meet the speed demands in CMS. This low value is reached only at high drift fields, above 10 kV/cm. The transverse diffusion is low, around 120 $\mu\text{m}/\sqrt{\text{cm}}$, which provides good position accuracy as shown in formula 3.44. Another disadvantage of using pure DME is that a high electric field is needed to get gas amplification, which increases the energy released and the risk of damage in case of discharges.

For the above reasons, mixtures of DME and some other gases are preferred. Among the best candidates, mixtures of DME and CO_2 provide high drift velocity ($u = 70$ μm/ns in DME-CO_2 60%-40% at a drift field $E = 10$ kV/cm [31]) and low diffusion ($\sigma_T \simeq 100$ $\mu\text{m}/\sqrt{\text{cm}}$ in the same conditions). Still, DME and CO_2 are quenchers, and a high electric field is required to obtain gas amplification. When this work started, first experimental evidence was reported that MGC's filled with Ne-DME mixtures could be operated at high stable gains [81]. There was however a concern that the detection efficiency could be diminished because of the low primary ionization in Ne. We were the first group to perform measurements of detection efficiency in MSGC's filled with Ne-DME gas mixtures, with the help of the cosmic ray hodoscope installed in Brussels [82]. This work is described in chapter 4.

In the 4 Tesla solenoidal field of CMS, the barrel MSGC's must be tilted in order to compensate for the Lorentz deviation of the electron drift. The modules are inclined by α_L, the Lorentz angle, so that the spread of the electrons collected on the substrate is minimal for high p_T particles which emerge radially from the beam intersection point (see figure 3.23). This tilt

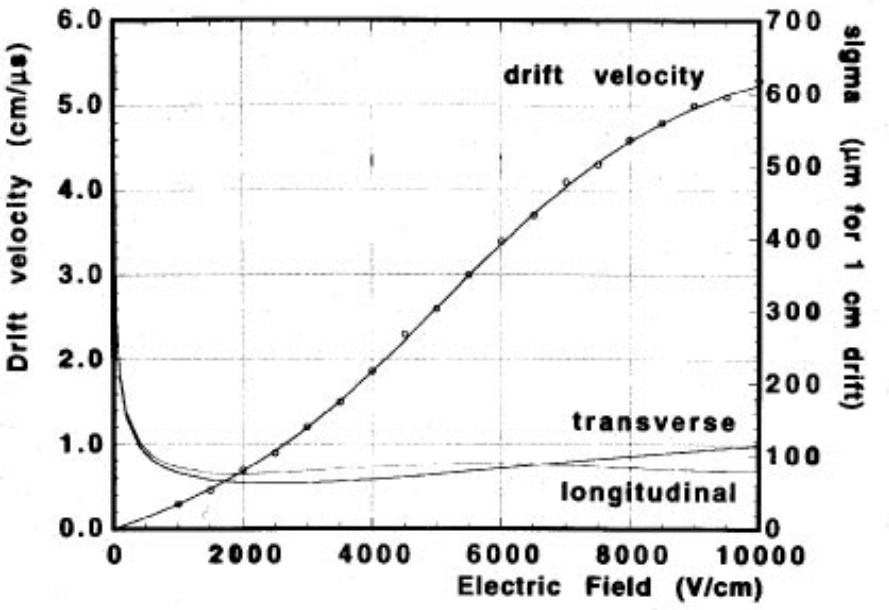

Figure 3.22: Drift velocity and diffusion coefficients in pure DME. The circles are experimental data and the full lines are simulation results [31, 80].

increases the radial space required for each detection layer, and might introduce an asymmetry in the reconstruction of positively and negatively charged particles. The Lorentz angle can be minimized when working at high drift fields. Indeed, α_L is proportional to the magnetic field intensity and to the electron mobility $\mu_e = u/E$. Operation at high drift fields, where the drift velocity is saturated, allows simultaneously high drift speed and low Lorentz angle. Figure 3.23 shows that, in DME-based gas mixtures and at drift fields of about 1 kV/mm, α_L is around 4^o/Tesla [83].

3.3 Other detector developments using the microelectronics technology

Since the MSGC has been introduced, a new class of gas detectors relying on the microelectronics technology has appeared. Among the recent developments, the Gas Electron Multiplier (GEM) developed at CERN by the group of F. Sauli [68] and the MICRO-MEsh GAseous Structure (MICROMEGAS) developed at Saclay [84] are of particular interest for high rate experiments. These detectors are expected to yield comparable performance as MSGC's in terms of detection efficiency, spatial resolution and counting rate, but do not suffer from the same gain limitations.

3.3.1 The Gas Electron Multiplier

The GEM consists of a thin polymer foil about 50 μm thick, metal-clad on both sides and perforated by a regular matrix of holes of typically 200 μm spacing. By applying a potential difference of a few hundred volts between the two sides of the foil, a high field of up to 100 kV/cm is created in the holes. When the GEM foil is inserted in the gas volume of a gaseous detector,

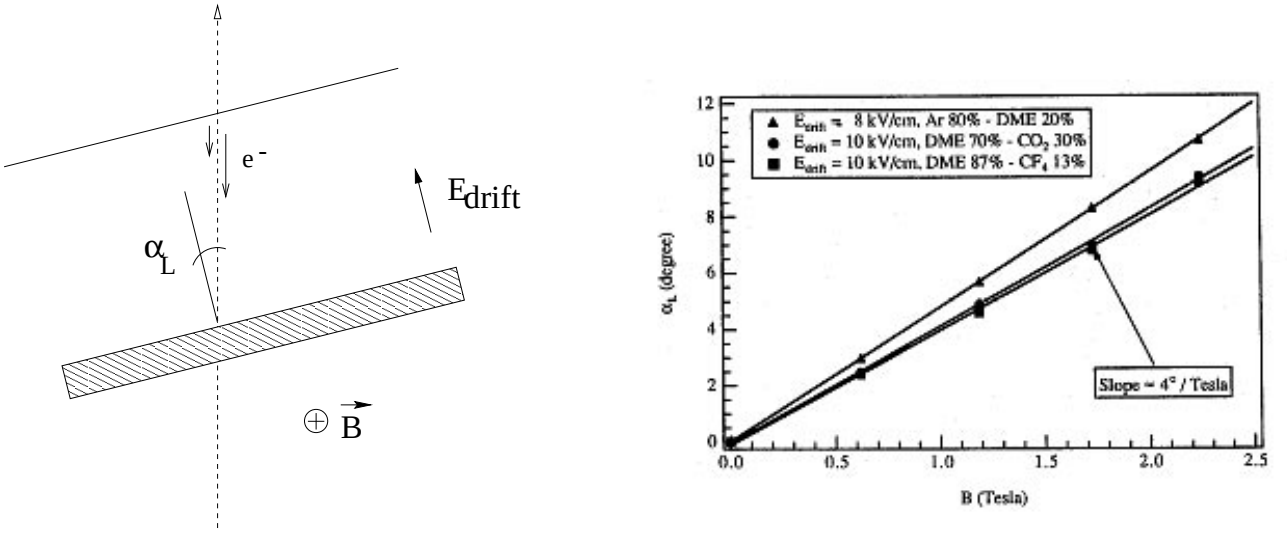

Figure 3.23: Left: inclination of the MSGC's with respect to the radial direction, in the barrel part of the CMS tracker. Right: Dependence of the Lorentz angle on the magnetic field intensity, for a few gas mixtures and drift fields [83].

it provides a pre-amplification of the electrons released by the ionizing particle and drifting through the open channels. Figure 3.24 shows such a GEM grid placed inside the drift volume of an MSGC detector.

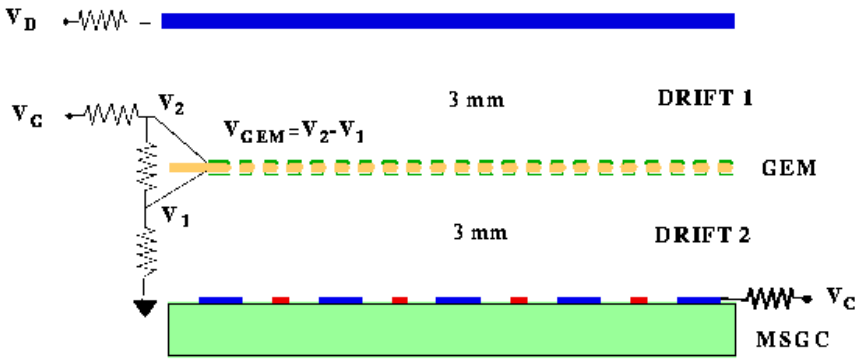

Figure 3.24: GEM foil placed in the middle of the drift volume of an MSGC [68].

Using a GEM in combination with an MSGC allows to reduce the voltage applied between the cathode and anode strips by up to 200 V while reaching the same total gain. The GEM provides a gain of about 100, and only a factor 10 to 100 must be provided by the MSGC, which can be acheived at low cathode strip voltage (around 400 V). The safety margin before breakdown on the substrate is therefore greatly improved. A problem that remains to be studied is that high electron transmission through the GEM grid requires a low electric field above the GEM as compared to the field underneath the GEM. This would result in slow collection of the ionization and large Lorentz angle with the gas mixtures presently studied.

3.3.2 The MICRO-MEsh GAseous Structure

The MICROMEGAS is a two-stage parallel plate detector, composed of a conversion region of about 3 mm and an amplification region of about 100 μm thickness, separated by a micromesh. The mesh consists in a metallic grid of 25 μm cell size and 3 μm thickness, produced by an electroforming technique. When applying a low drift field (1 - 10 kV/cm) across the conversion region and a high amplification field (100 kV/cm) across the multiplication region, the ionization left by the incident particle in the conversion gap is transmitted through the micromesh and avalanche multiplication takes place in the high uniform field below the mesh (see figure 3.25). Most of the ions generated in the avalanche are quickly collected onto the mesh, which prevents space charge buildup in the conversion region and makes the induced signals very fast. The signals are read out by pick-up electrodes at ground potential. Gains close to 10^5, signal risetimes below 100 ns and counting rates up to 10^6 Hz/mm^2 have been obtained with such devices. The electron transmission through the mesh was measured to be above 80%, and the fraction of ions from the avalanche reaching the conversion gap was estimated to 10%, for a ratio of 10 between the amplication and the drift fields [84].

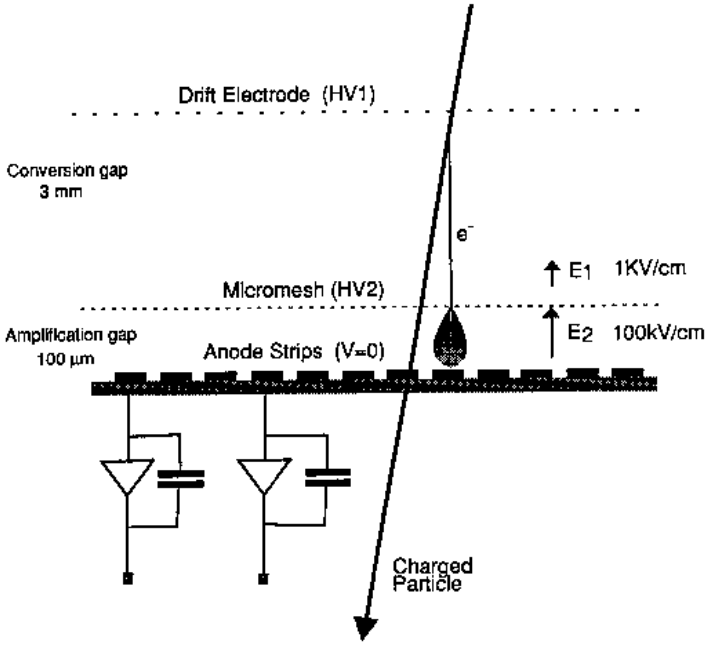

Figure 3.25: Principle of the MICROMEGAS [84].

Stable gains in parallel plate mode are achieved when operating at very high reduced fields E/p, where the first Townsend coefficient saturates. Indeed, at such fields, the gas amplification is not sensitive anymore to a small change of amplification field or gas pressure. This can be obtained at low pressure, or at high electric fields like in MICROMEGAS. In this case, the amplification gap must be small, in order to obtain gains below the breakdown limit, and of well controlled thickness, in order to have a good gain uniformity across the counter. The group of Saclay proposed to use a photoresist film, which thickness is accurate to 1 μm, patterned to form small pillars of 100 μm diameter, supporting the micromesh every 1 mm. The other critical piece is the micromesh itself. In order to have a sufficiently uniform amplification field, the mesh cell size must be small as compared to the thickness of the amplification gap. This is

achieved thanks to the precision of the electroforming technique.

The fabrication of a micromesh should be less critical than the production of a microstrip pattern. Moreover the pick-up electrodes can be very wide, as they do not contribute to the gas amplification, and a simple and robust printed circuit board can be used as a readout plane. At the gain values reached in MICROMEGAS, single electron detection can be achieved, and the conversion gap could therefore be reduced to 1 mm. Detectors operating in parallel plate mode are thought to be less prone to ageing than wire or microstrip counters. Although still in the development stage, this new detector technique seems thus a promising alternative to microstrip counters for high rate experiments. However the front-end electronics equipping a MICROMEGAS should be carefully protected against discharges. Due to the large detector capacitance, about 2 nF, the spark energy is large enough to destroy most of commonly used integrated amplifiers.

3.4 Conclusions

The micro-strip gas counter has been the subject of extensive research and development since its invention. It has reached the level of maturity which makes it an adequate detection technique for high rate experiments like at the LHC. The weak points of the MSGC are still the fragility of the strip pattern under sparks and the loss of performance at large irradiation doses. Although sparking and ageing are under control in laboratorium tests, the reliability of large MSGC systems during several years of operation in the high particle flux expected at the LHC has not been completely proven yet. Large scale prototypes are currently being built and tested by the CMS community in order to study these aspects.

Some parameters can still be optimized in order to improve the performance of the detectors in high rate experiments. In chapter 4 we shall describe the studies performed in Brussels concerning two problems specific to the use of MSGC's in CMS. We shall first discuss the possibility of mounting several MSGC's side by side in a common gas volume, as foreseen in the design of the endcap tracker of CMS. We will then describe our contribution to the study of gas mixtures suited for MSGC operation at the LHC. Our goal is to identify a gas mixture providing high gains at low cathode strip voltages and a high detection efficiency for minimum ionizing particles, together with a good stability of operation of the detectors.

The microelectronics technology has opened a new range of applications for gaseous detectors. Several amplification structures have been proposed which could solve some of the limitations of the MSGC, i.e. low gain limit and long term stability. Still, more development is required to bring these techniques to the level of maturity of the MSGC.

Chapter 4

Experimental study of MSGC's for the forward tracker of CMS

4.1 Introduction

In the design of the forward MSGC tracker, it is foreseen to place several MSGC substrates side by side in a common gas volume. This layout permits a coverage of the detection surface without detector overlaps in ϕ and with less than 1% dead space. Endcap MSGC disks built according to this design should thus be light and highly efficient, as required for good track reconstruction. However the stability of operation and the uniformity of the response of multisubstrate modules still remained to be checked. We have thus measured the length of the efficiency plateau for minimum ionizing particles, and the detection efficiency across the surface of such a module. The measurements were performed in a cosmic ray hodoscope defining the track of the cosmic particles traversing the counters.

As outlined in chapter 3, no gas mixture has been found yet which fulfills all the requirements for MSGC's in CMS. When this work started, the best mixture identified was DME-CO_2. It exhibits most of the properties required (high ionization yield, high drift velocity and low diffusion), except that a high electric field is needed in order to get gas amplification. Operation at high voltage increases the risk of a destructive spark. Mixtures of DME and neon have the attractive property of providing high gains at low voltage. However, in Ne-rich mixtures, the efficiency could be reduced because of the low amount of primary ionization. Thanks to the cosmic ray hodoscope, the influence of the gas gain and primary ionization on the MSGC detection efficiency could be studied experimentally. The results have also been reproduced and further analysed with the help of a Monte Carlo simulation of the detector response.

We first describe the experimental setup, in section 4.2. The analysis of the hodoscope and MSGC data is then explained in section 4.3. The stability of multisubstrate modules and the uniformity of their response are studied in section 4.4. The analysis of the performance of Ne-DME mixtures is presented in section 4.5, followed by the Monte Carlo study of the counter response with such gas mixtures, in section 4.6. We also discuss recent results of detection efficiency and drift velocity measurements in triple mixtures of DME, Ne and CO_2. These results complete our study and allow to choose the best operating gas currently available for MSGC's in CMS, taking all relevant parameters into account.

4.2 Experimental setup

In order to study the MSGC response to MIP's, a cosmic ray hodoscope has been installed in Brussels. It allows to select cosmic muons of energy above the minimum of ionization, and to reconstruct their track through the detectors to be tested thanks to a set of twelve drift chambers. This apparatus was previously used to test the forward muon chambers of the DELPHI detector [85]. The data acquisition system had however to be rebuilt.

In the middle of the hodoscope, a stack of MSGC counters has been installed. The tests have started with two prototypes, one with a substrate cut in two pieces used to study the behaviour of multisubstrate modules, and a second one with an uncut substrate, placed below, used as a reference counter. Later on, a third counter, identical to the first reference chamber, was added on top of the others. The particle tracks could then be defined with a high accuracy in the two reference chambers in order to study the counter in the middle.

4.2.1 Cosmic ray hodoscope

A schematic view of the hodoscope is shown in figure 4.1. Cosmic muons of momentum above 300 MeV/c are selected by a coincidence of two scintillator plates, 40 $\times$ 40 cm^2 large, with a layer of 10 cm lead in between. The muon tracks are reconstructed using twelve drift chambers of 20 cm $\times$ 40 cm, grouped three by three. In each group, the third chamber is staggered over the two others placed side by side, to solve left-right ambiguities. The groups are disposed so as to provide four points along the track in two orthogonal projections.

The drift chambers are operated in proportional mode with an Ar-CH_4 90%-10% gas mixture. The drift voltage applied to the chambers is -3.5 kV so as to create a drift field of $\sim$ 350 V/cm. The corresponding electron drift velocity is $\sim$ 45 mm/μs. The anode wire voltage is +2.2 kV. Charge amplifiers are used to amplify the anode signals up to typical pulse heights of 100 mV on a 50 Ω impedance. More details can be found in [86].

4.2.2 MSGC prototypes

The three prototypes tested have very similar designs. The two reference MSGC's are identical to the counters built at NIKHEF, Amsterdam, for the SMC collaboration [52]. These are 93 $\times$ 99 mm^2 counters with 512 parallel anode strips. The substrate is made of DESAG D-263 glass of 300 μm thickness. It is glued onto a printed circuit board frame, which also supports the front-end electronics and the high voltage bus. The strips are made of aluminium, 1 μm thick. The anodes are 7 μm wide and the cathodes, 90 μm. The anode pitch is 200 μm. The anode strips are connected to the preamplifiers by wire bonding. A pitch adaptor brings the 200 μm strip pitch down to the 50 μm pitch of the readout chips. The input of the front-end electronics is protected by 740 Ω resistors connected in series between the strips and the pitch adaptor. The resistors are made of short NiCr strips, 5 nm thick. In case of spark, they limit the current at the input of the preamplifier to less than 1 ampere.

The high voltage is distributed to the cathode strips by a HV bus on the support board. The cathodes are connected to the bus in groups of 16, by a discrete resistor of 4.7 MΩ. The capacitance of a cathode group is about 100 pF. In case of spark, only one group is discharged, which limits the energy released to about 20 μJ.

The drift electrode consists of 300 μm thick aluminized glass, mounted on four spacers placed at each corner of the chamber. The glass plate is squeezed in slits made in the side of the spacers, allowing easy dismounting and access to the substrate to repair shorts. The gas

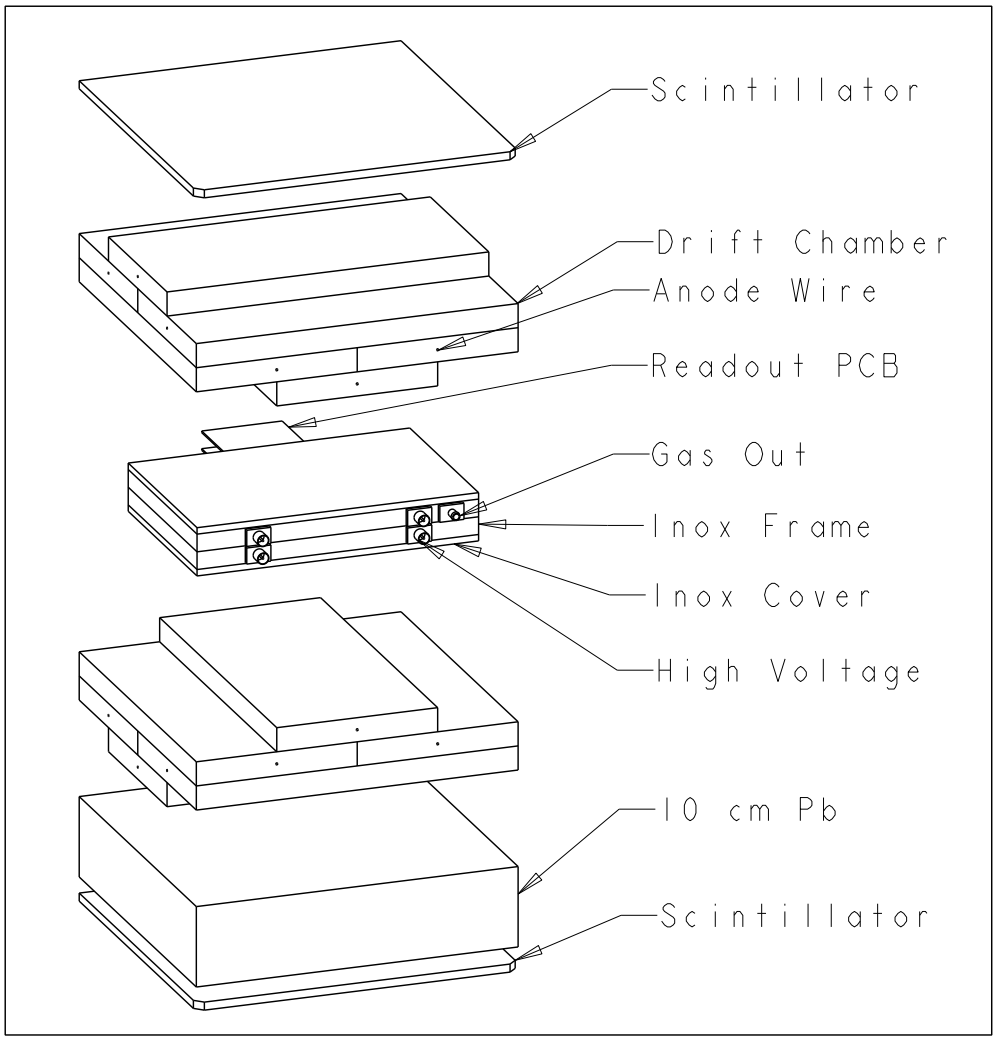

Figure 4.1: The cosmic ray hodoscope and the MSGC gas box.

gaps of the reference chambers are 2.7 mm for the lower chamber and 3.3 mm for the upper one.

The third MSGC is similar to the other ones except for the strip support, which is made of two pieces of glass glued side by side on the same PCB frame at a distance of ~ 70 μm. The two glass pieces were obtained by cutting away 3 cathode blocks (48 channels) from the middle of an SMC substrate. The edges are terminated by a cathode strip. The interanode distance across the substrate separation amounts to (400 ± 5) μm, two times the nominal pitch. This detector is called the ϕ-crack prototype, as it reproduces the disposition of the detectors on the endcap disks of the CMS tracker, with a small spacing in ϕ between them. The layout of the prototype is detailed in figure 4.2. One of the two substrate pieces is glued on two sides only, and therefore sags along the strips. The sagitta in the middle of the strips is ~ 200 μm. This prototype has a gas gap of 3 mm. The MSGC's are mechanically aligned under a microscope in such a way that the strips of each chamber are parallel to the edges of the gas box. The parallelism is better 0.5 mrad.

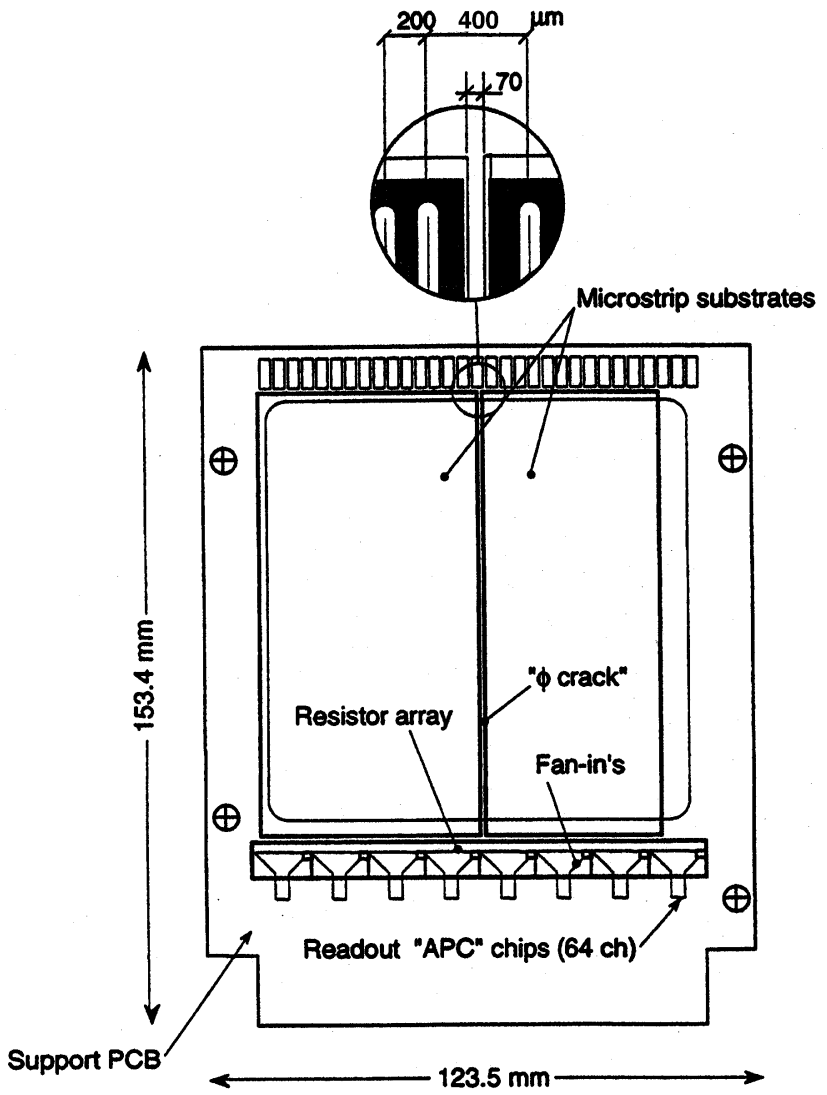

Figure 4.2: Prototype of MSGC with a substrate made of two pieces of glass mounted side by side at 70 μm distance.

4.2.3 Gas and high voltage systems

The MSGC gas box was designed in such a way that several aspects of the MSGC behaviour could be studied. Staggering of the counters was foreseen in order to study the angular dependence of the MSGC response. The gas enclosure is made of individual frames, one per chamber, which comprise several rows of screwholes allowing assembly in a staggered configuration. The frames are 2 cm thick. Slits made in the side of the frames allow the connection of the chambers to the data acquisition system. This connection is realized by feedthrough printed circuit boards. Figure 4.3 shows one of the chambers mounted in its inox frame. The gas volume is closed by two 50 μm aluminium foils to minimize multiple scattering.

Care was also taken to avoid plastic materials, to prevent gas pollution. The gas box and tubing are made of stainless steel. Gas tightness is ensured by indium seals, squeezed in grooves milled in the frames. Various gas mixtures can be studied, thanks to a gas mixer built in the Mons university. It comprises four gas entries equipped with massflow meters, calibrated for the following components: noble gases, DME, CO_2 and isobutane. The desired mixture is delivered

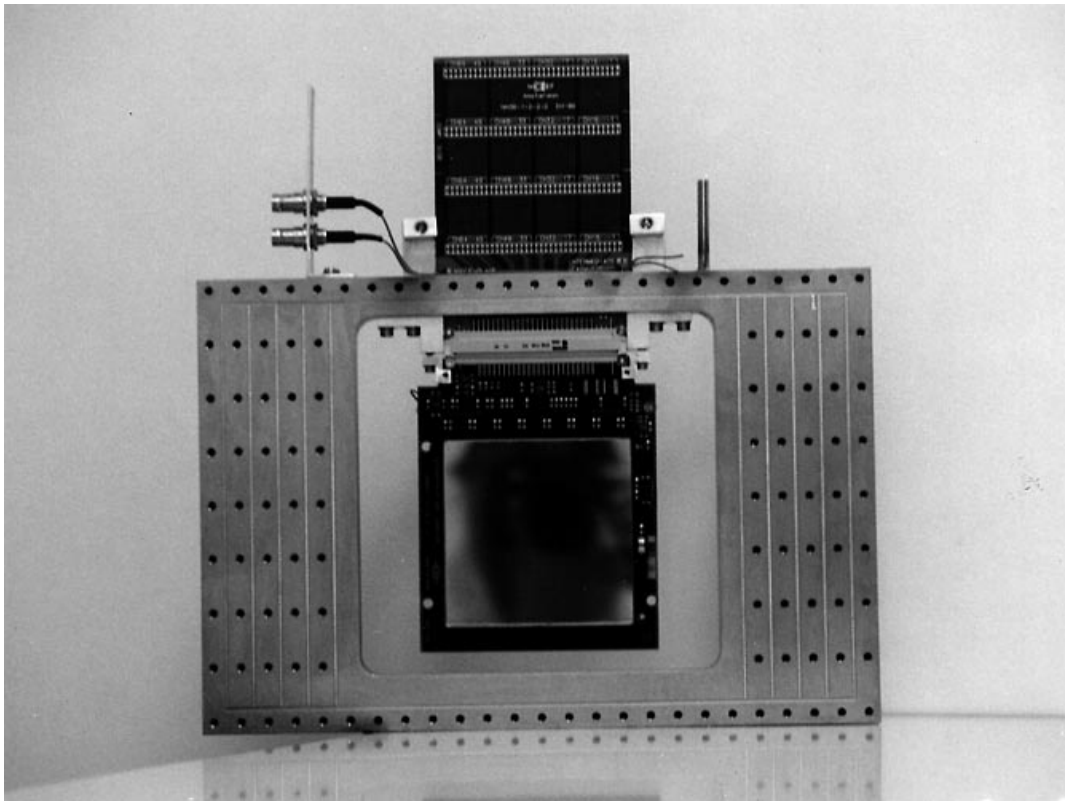

Figure 4.3: MSGC counter, 10×10 cm^2 large, mounted in a stainless steel frame.

to the chambers through one of the four gas outputs available.

The high voltage applied on the drift planes and on the cathode strips is provided by CAEN power supplies. The cathode strip voltage is typically between -500 V and -650 V. The drift voltage ranges from -1000 V to -3000 V. The anodes are grounded through the readout chips. The current drawn by the substrates is monitored by opto-coupled electrometers which accept input voltages up to 10 kV. Their sensitivity can be set to 10, 100 or 1000 nA. The cathode strips are disconnected from the power supply when the current exceeds a tunable threshold. This protects the detectors against sustained discharges. In our counters the leakage current at nominal voltage was below 10 nA and the threshold was set to 80 nA.

4.2.4 Data acquisition

Hodoscope readout

The data acquisition system is based on a Macintosh II-ci computer interfaced with a CAMAC (Computer Automated Measurement And Control) instrumentation bus. The drift time in the twelve drift chambers of the hodoscope is measured in two CAMAC 12-bit Time-to-Digital Converters (TDC's). These modules contain 8 channels measuring the time elapsed since a common start pulse has been received. Their range is set to 2 μs. The common start is given by the coincidence of the hodoscope scintillator signals. The stop pulses are generated by the anode signals of the drift chambers. Because the minimum time interval measureable by the TDC's is 50 ns, the drift chamber signals are delayed by 100 ns thanks to 20 m long cables.

MSGC readout

The MSGC readout system is composed of integrated electronics mounted on the counters, a controller module driving the readout, and a Flash Analog-to-Digital Converter (F-ADC) digitizing the strip signals in series. The signals of up to four chambers of 512 channels are handled by one controller and one F-ADC, thanks to a multiplexer module to which the chambers are connected.

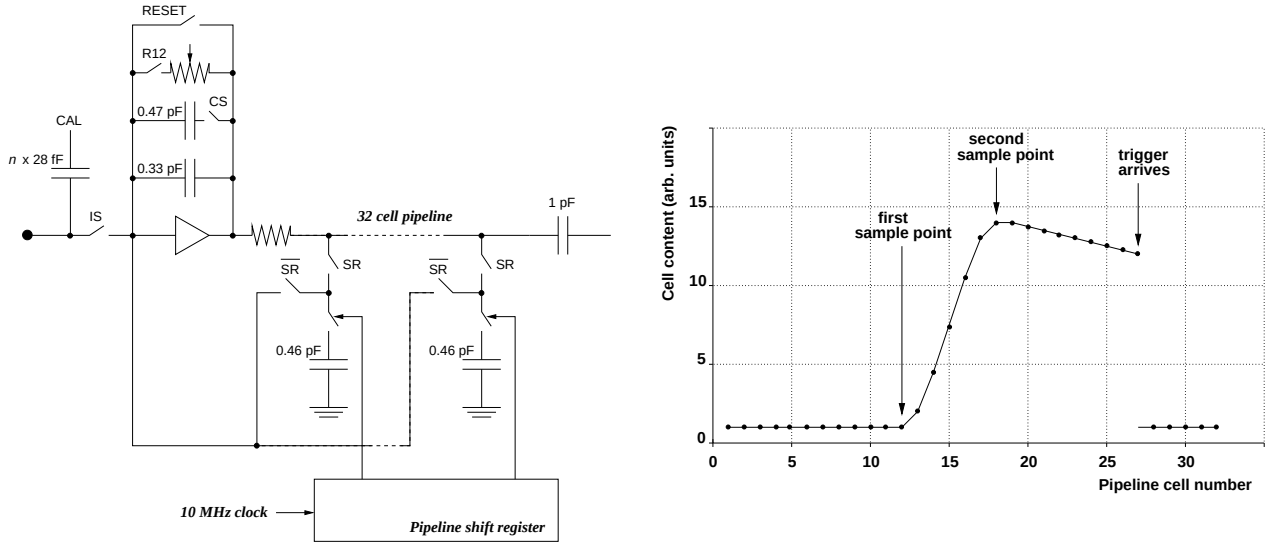

Figure 4.4: Principle of the APC chip.

As a front-end amplifier the 64-channel Analog Pipeline Chip (APC) is used [45]. Each channel is composed of two elements: a preamplifier mounted as a current integrator, and a 32-cell switched capacitor pipeline sampling the output of the preamplifier every 100 ns. Using double correlated sampling, only the difference between the signal level at a sample before and after the event is sequentially read out. The basic concept of the chip is illustrated in figure 4.4. In the first phase of the readout, the incoming charge from one anode strip is integrated and stored on the 0.33 pF feedback capacitor within 85 ns, the rise time of the preamplifier. The capacitor is gradually discharged by a feedback resistor which is enabled by the switch R12. Sequentially, the output voltage of the preamplifier is stored into each of the 32 pipeline capacitors of 0.46 pF. The pipeline shift register contains 32 bits which control 32 capacitor switches, and shifts one position every 100 ns.

The second phase starts when an external trigger is received. The anode strips are disconnected from the preamp inputs by signal $\overline{\text{IS}}$, while the pipeline capacitors are disconnected from the preamp outputs to memorize the past 3.2 μs by signal $\overline{\text{SR}}$. Meanwhile the feedback capacitor is discharged through the RESET switch. The pipeline pointer is shifted to the cell corresponding to the instant just before the rising edge of the anode signal, called the first sample point. The charge contained on that cell is re-read through the preamplifier and stored into the latch capacitor of 1 pF. Then, the preamp feedback capacitor is discharged again. The pipeline pointer is shifted to another position, called the second sample point, which corresponds to the maximum of the anode signal. The corresponding pipeline cell is discharged through the preamp, and the difference of the signals of the two sample points is stored into the latch capacitor. In the last phase, the signals of all channels are sequentially read out.

The signal shape can be adjusted by tuning the value of the feedback resistor. A high value is

preferred, as it reduces the ballistic deficit and increases the signal decay time, which renders the positioning of the second sample point less critical. An additionnal feedback capacitor can also be enabled by switch CS to increase the dynamic range of the integrator. In calibration runs, a known charge can be injected at the input of the preamplifiers by a capacitor of $n \times 28$ fF, n running from 1 to 4, integrated in the chip. The correct position of the sample points is determined by maximizing the signal amplitude. With our setting of the feedback resistor the signal decay time is about 2 μs. The width of the interval between the samples is thus not critical, but it should be larger than the sum of the signal peaking time ($\leq$ 200 ns) and the APC trigger jitter (100 ns). The optimum delay between the samples is found to be 600 ns. To improve the S/N ratio, we read two neighbouring capacitors instead of one for each sample point.

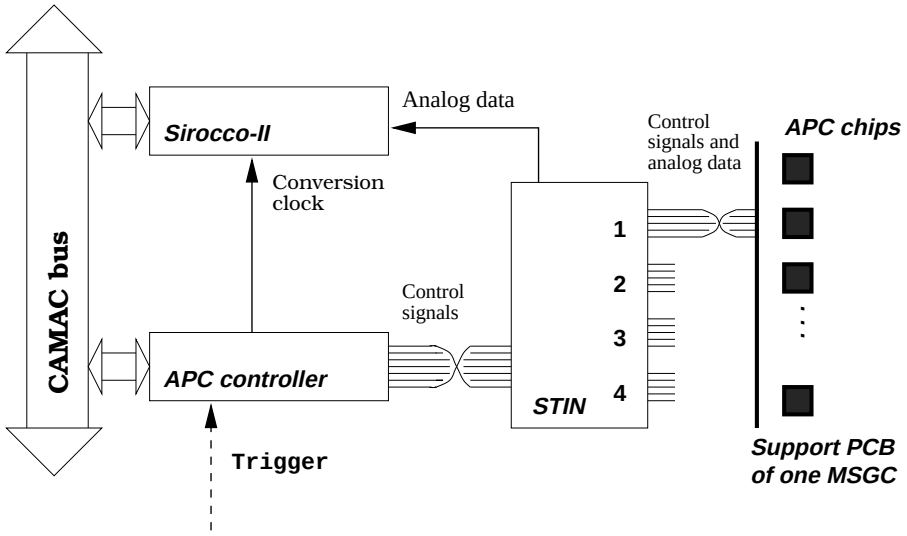

Figure 4.5: Principle of the MSGC readout system.

The MSGC readout system is depicted in figure 4.5. The control signals are provided by the APC controller, housed in a CAMAC module [87]. The controller is triggered externally by a NIM signal. Three programmable registers control most of the system settings: number of chips to read out, values of the preamp feedback resistor and capacitor, position of the sample points, etc. Most of the control signals are logic balanced TTL pulses, except for the analog levels controlling the preamp feedback resistor and the amplitude of the calibration pulses. The control signals are distributed to the chambers by the STation INterface (STIN). This module also groups the chamber data onto one channel, connected to the F-ADC by a shielded bipolar LEMO cable. The connection between the STIN and the chambers is done with flat twisted pair cables, made short to prevent noise pickup on the analog data lines. The APC controller and the STIN were designed in NIKHEF.

The digitization of the analog data is performed in series by a 10 bit F-ADC: the CAMAC Sirocco-II [88]. The conversion is commanded by a clock signal synchronized with the data, generated in the APC controller. The Sirocco-II can be loaded with 2048 pedestal values and one threshold level in order to perform zero suppression online. In our case, zero suppression is done offline to permit common mode correction. The last bit of the pedestal registers is a stop bit which allows to define the number of analog signals to be converted.

Trigger system

Data readout is triggered by the passage of a particle through the two hodoscope scintillators. Immediately after a coincidence of the scintillator signals has been detected, further triggers are disabled during 2 ms in order to let the data acquisition system react. During this time, the TDC's receive the stop signals from the drift chambers, and the computer detects the presence of data in the TDC's. The computer then activates a long veto signal, reads the TDC's and tries to reconstruct a straight track with the hodoscope drift chambers. If such a track is found and crosses the MSGC gas box, the Sirocco-II is read and the event is written on file. This takes about 1 s, after which the computer veto is removed. The rate of events written on file is about hundred per hour.

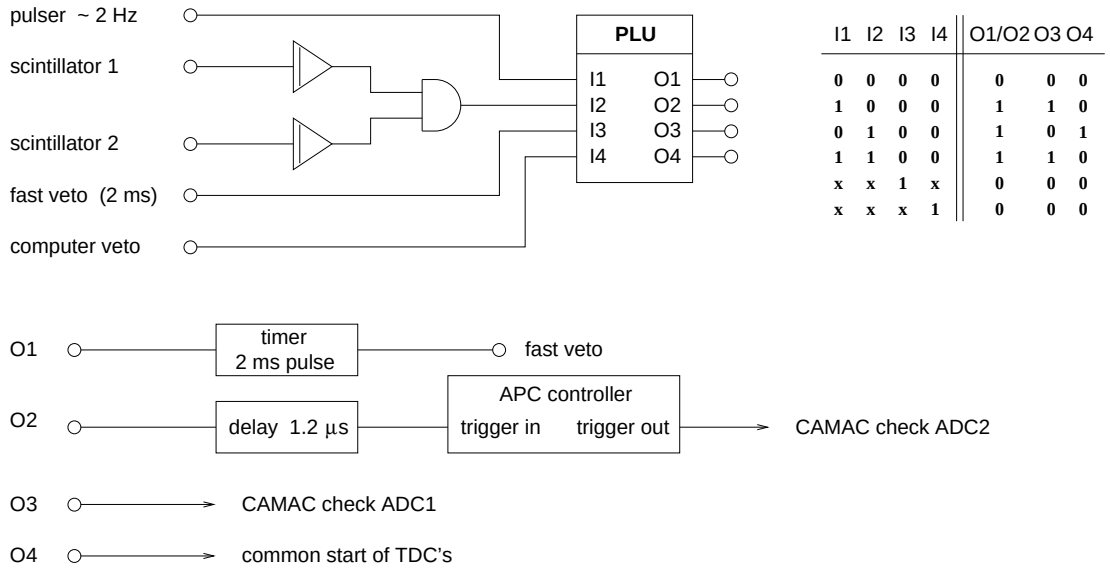

Figure 4.6: Principle of the trigger system. The truth table of the Programmable Logic Unit (PLU) is also shown.

Figure 4.6 gives a more detailed overview of the trigger system. The analog signals of the scintillators are first converted into logic NIM pulses by means of discriminators. The logic AND of the scintillator pulses is sent to a 4-channel Programmable Logic Unit (PLU). This unit receives all trigger and veto signals and generates the pulses required by the various CAMAC modules. The fast veto of 2 ms duration is generated by a NIM timer started after every trigger. The computer veto is set thanks to a CAMAC output register. An additional start signal of $\sim$ 2 Hz frequency is required in order to reset the APC chips at regular intervals. This reset pulse is also used as a trigger for calibration and pedestal measurements. Scintillator triggers and reset pulses are sent to the APC controller (output O2 of the PLU). They are delayed by 1.2 μs to allow integration and sampling of the anode signals in the chips. The TDC common start signal is provided by output O4 of the PLU, which is high when only the scintillator coincidence signal is high.

Output O3 of the PLU transmits the reset pulses that are not veto-ed to the gate of a CAMAC ADC. This module is checked by the computer in order to distinguish real triggers from reset pulses. Finally, the APC controller provides a "trigger out" signal, which is high when the trigger received by the controller has actually been transmitted to the chips. The presence of the "trigger out" signal is checked in a second CAMAC ADC.

Data acquisition program

The data acquisition is controlled by a program conceived for tests of MSGC's in the cosmic ray hodoscope. The program is written in Fortran in the MacUA1 environment [89]. MacUA1 is a Macintosh-based development system for data acquisition, control and monitoring applications. It includes Fortran libraries which support graphics, histogramming and CAMAC operations. It also supports access to the Macintosh dialog facilities by Fortran-callable routines.

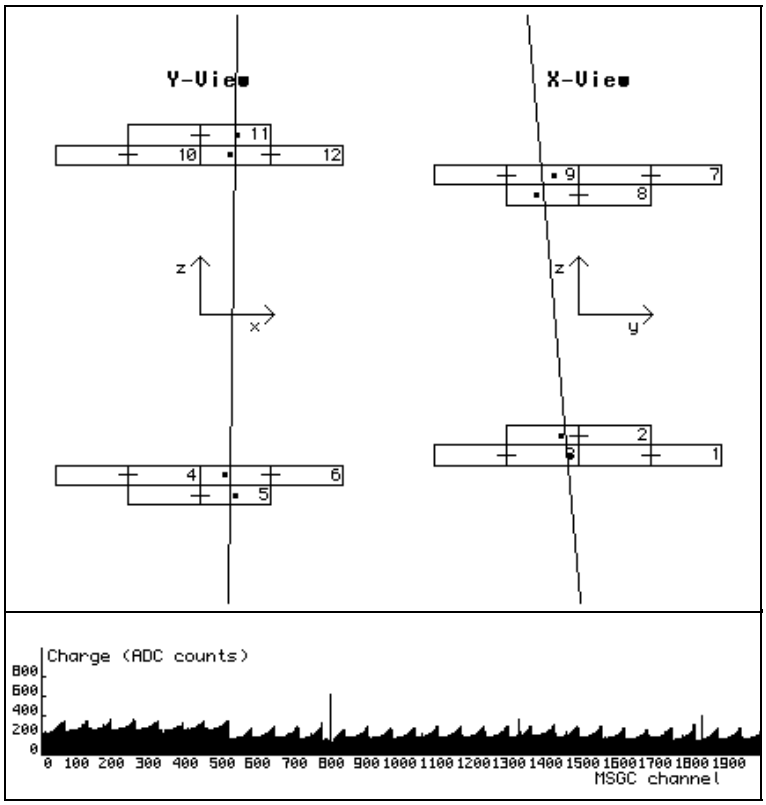

Figure 4.7: Hodoscope and MSGC event displays. The hodoscope coordinate system is shown, with the x-axis running parallel to the MSGC strips and the y-axis perpendicular to them. The signals recorded on the successive MSGC channels exhibit the typical APC pedestal shape (see later in the text) plus three particle hits around channels 800, 1300 and 1800. Here four 512-channel chambers were tested simultaneously.

The data acquisition control screen consists of an event display and a menu bar for user interactions. The event display comprises one window showing the hodoscope and the particle track reconstructed in the drift chambers, one window showing the data of the MSGC strips, one window with information relative to the last events and the Fortran default input/output window. The hodoscope and MSGC data windows are shown on figure 4.7. The menu bar offers two pull-down menus for initialization and program steering. In the initialisation menu, several item boxes can be opened, in which the run parameters can be defined: number of events, position of the counters to be tested, online zero suppression active or not, etc. The user can also enter the location of the modules in the CAMAC crate and program the registers of the APC controller. This menu is disabled during run. In the program steering menu, the user can start the run, stop or pause it, activate/disactivate the event display, and ask to show monitoring histograms.

The program logic is the following. At initialization, the CAMAC crate and modules are cleared, the APC controller registers are loaded, and 50 events triggered by the reset pulses are accumulated in order to compute the pedestal and noise of the MSGC channels. If online zero suppression is required, the Sirocco-II pedestal memory is loaded, and the threshold level is set to three times the noise averaged over all channels. Once the run is started, the computer waits for data to show up in the TDC's during 1 ms, performs the appropriate actions if TDC data appear, checks the mouse for a user request, and loops so until the required amount of events is written on disk. Every hour, the run interrupts itself to update the pedestals and threshold, and restarts automatically.

When TDC data are present, the computer blocks the triggers by writing a 1 into the output register, and tries to reconstruct a track in the hodoscope. It first reads the TDC's and checks that a signal was detected in the four layers of drift chambers in each projection. If so, it is practically certain that a particle has traversed the setup. The hit coordinates are calculated with an accuracy of 2 mm using an approximate time-distance relation for the drift chambers. Events with a hit closer than 1.5 cm from an anode wire are rejected, because in this region the drift velocity is not constant, and therefore a precise offline reconstruction is difficult [86]. A straight line fit is performed in each projection. The particle crossing point in the hodoscope mid plane is computed, and only tracks traversing a certain zone of interest are kept. This zone is usually chosen so as to cover the MSGC active area plus a margin of 1 or 2 cm on all sides.

Then, before reading out the MSGC data, the test ADC modules are checked. Events without a "trigger out" signal from the controller are rejected, as well as events in which a reset signal is detected. About 20% of the triggers sent to the APC controller are not transmitted to the chips, because of a conflict inside the controller logic. In the remaining accepted events, TDC and Sirocco-II data are written on file for further analysis, and the event is displayed if requested. Update of the event display is slow, about 2 s per event. By default it is disabled to reduce deadtime. Eventually, the CAMAC modules are cleared, and the computer veto is removed to accept the next event.

Calibration and tests of the MSGC readout

The functionality of the MSGC readout can be tested by means of calibration signals sent at the input of the APC chips. The SMC counters provide two calibration modes. The first mode makes use of the calibration capacitors integrated in the chips. This mode allows to detect dead preamplifier channels, and in principle permits the absolute calibration of the electronics chain. Figure 4.8 a) shows the response of one chip. The polarity of calibration signals is negative, opposite to particle signals. One step corresponds to an input charge of 28 fF $\times$ 200 mV = 35000 e^-, a typical MIP signal amplitude. Because of an unknown problem in our setup, the calibration signals were attenuated by a factor ~ 4. We therefore relied on the calibration of identical counters performed in NIKHEF, and estimated the conversion factor to 250 e^-/ADC count with a precision of 15%.

The second calibration mode consists in sending a pulse on a line running in the PCB under the cathode strip HV lines. This pulse is transmitted to the anode strips by capacitive coupling. The amount of charge received by the amplifier is proportional to the active length of the strip. By this way interrupted or disconnected anodes can be identified, and the number of damaged strips can be monitored (see figure 4.8 b). The number of broken or disconnected anodes was 23 and 18 respectively in the lower reference and in the ϕ-crack prototypes. The upper reference chamber had a concentration of 20 damaged strips around channel 400, due to a scratch in the substrate. As the central part of this counter was operational, it could still be used to test the ϕ-crack region of the middle counter.

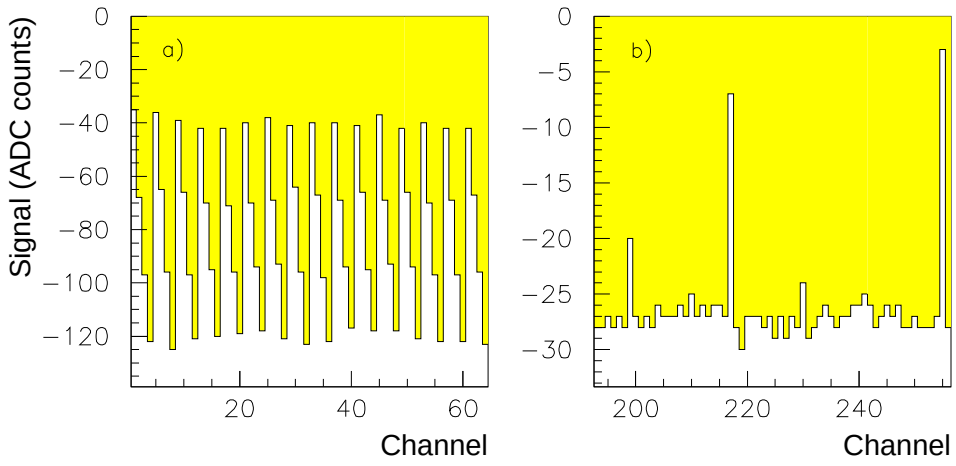

Figure 4.8: Calibration signals: a) from the APC internal calibration capacitors, and b) from a charge induced on the anode strips.

4.3 Data analysis

4.3.1 Track reconstruction with the hodoscope

The purpose of the hodoscope is to define the cosmic muon tracks independently of the MSGC's to be tested. In each event, the track is reconstructed in the two projections by performing a linear fit to the points measured in the drift chambers. The coordinates of the fitted points are given by the vertical position of the drift chamber anode wires and by the drift distances measured in the chambers. In chamber k, the drift distance is given by

$$d_k = v_k t_k + d_k^0, \tag{4.1}$$

where v_k, d_k^0 are the drift velocity and delay parameter of that chamber and t_k is the drift time measured in the corresponding TDC channel.

The parameters v_k and d_k^0 are not known with a good precision *a priori*. They are estimated with the help of a constrainted χ^2 fit technique using Lagrange multipliers. The procedure is described in detail in [90]. The constraints are set by the hodoscope geometry:

- in each projection, the particle incident angle is the same in the upper and lower groups of drift chambers.
- the incident angle is related to the drift distances and to the vertical and horizontal spacing of the anode wires as described in figure 4.9.

Iterations are required, as the constraint equations do not only involve the drift parameters, but also the particle incident angles. These in turn depend on the drift parameters in a non-explicit way. Convergence is reached in two or three iterations.

The quality of the track reconstruction after calibration is shown in figure 4.10. The left plot shows a typical distribution of the residuals in one of the drift chambers. The R.M.S. of the Gaussian curve adjusted to the experimental data is 400 μm. The resolution of the drift chambers derived from the residuals is about 600 μm, in agreement with previous results obtained with these chambers [85]. The centre plot shows the χ^2 distribution for the projection

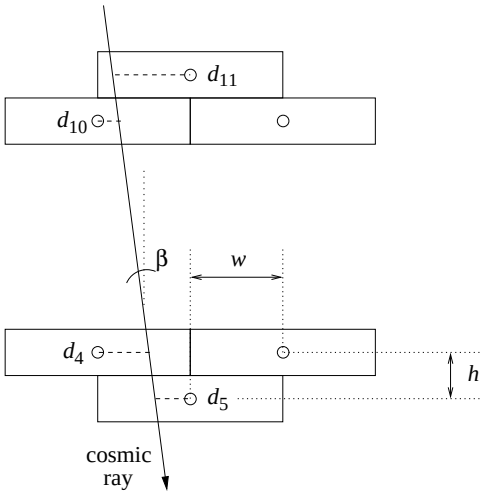

Figure 4.9: Illustration of the constraint equations used in the calibration of the hodoscope. The drift distances d_k measured in drift chambers 4, 5, 10, 11 are related to the cosmic ray incident angle β and to the horizontal and vertical spacing between the anode wires, w and h.

parallel to the MSGC strips. It is in agreement with the expected χ^2 distribution with 2 degrees of freedom. The plot on the right shows the distribution of the χ^2 upper tail probability. It is uniform between 0 and 1, except for 20% of the tracks which are not compatible with straight lines. This is attributed to multiple scattering in the setup, as will be discussed later. In the projection perpendicular to the MSGC strips, one of the drift chambers was malfunctioning, likely because one of the field grading electrodes was disconnected. The results are thus worse. A loose χ^2 cut ($\chi^2 \leq 100$) is applied in the two projections in order to keep most of the statistics. In most of our tests, such a track quality is sufficient.

The distribution of the cosmic ray impact point is uniform on the ground surface. The angular distribution has some spread around vertical incidence: it behaves as $\cos^2\theta$, θ being the polar angle. Due to acceptance effects, the distributions of the tracks reconstructed by the hodoscope differ notably from those of the incoming particles. The distribution of the fitted track impact point in the hodoscope mid plane is shown in figure 4.11 a). The coordinate system is placed in the centre of the hodoscope, with the x-axis parallel to the MSGC strips and the y-axis perpendicular to them. It can be seen that the coverage is not uniform. This is the combined effect of the accepted angular range and the rejection of tracks passing in the vicinity of an anode wire. The rate is maximum around $|x|$, $|y| = 0$, because the angular acceptance is the widest in this region. However no vertical tracks are accepted in this region, because such tracks would cross the drift chambers close to an anode wire.

The accuracy of the hodoscope in y can be checked thanks to the MSGC chambers. The distribution of the difference between the y-coordinates predicted by the hodoscope and reconstructed in one of the MSGC's is shown in figure 4.12 a). Tracks crossing the damaged drift chamber are excluded from the plot. The curve superimposed on the histogram is the result of a fit with the sum of two Gaussian functions. The standard deviation of the narrow Gaussian is 370 μm, comparable to the expected hodoscope accuracy of 300 μm. The standard deviation of the broad Gaussian is about 1800 μm. This value is compatible with multiple scattering in the 3 mm thick drift chamber walls and in the 8 mm thick aluminium support plate on which the MSGC gas box is fixed. The imprecision due to multiple scattering in the support plate alone, estimated from formula 3.9 for cosmic muons of 1 GeV/c most probable momentum, is

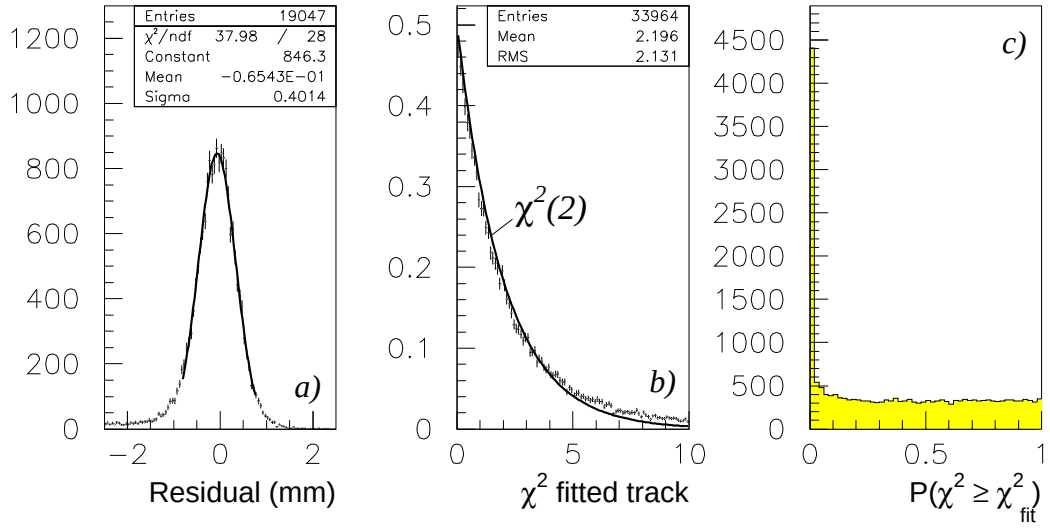

Figure 4.10: a) Distribution of the residuals in one of the drift chambers. b) χ^2 distribution of the fitted tracks in the projection parallel to the MSGC strips. c) Distribution of the χ^2 upper tail probability.

1 mm.

The angles with respect to vertical incidence, denoted α and β respectively in the projections perpendicular and parallel to the MSGC strips, are measured with an accuracy of 0.1^o. The acceptance is $[-20^o, 20^o]$ in α and $[-15^o, 15^o]$ in β. Figure 4.11 b) shows the distribution of $\tan(\alpha)$. It exhibits two dips, due to the rejection of tracks passing close to an anode wire. The dashed line shows the angular distribution of the simulated events, generated for the Monte Carlo study of the MSGC response described in section 4.6.

4.3.2 Impact point reconstruction in the MSGC's

The ionizing particle generates charges on one or several consecutive strips, depending on the track inclination and on the diffusion of the electrons in the gas. The reconstruction of the particle impact point consists in grouping these strips into clusters and calculating the position of the crossing point from the strip signals.

Pedestal analysis

In the absence of a particle signal, the pulse height read on each channel has a Gaussian distribution. The average value of this distribution is called the channel pedestal. The fluctuations around the pedestal are due to noise. The R.M.S. of the distribution is often referred to as the channel "noise". Expressed in electrons at the input of the front-end amplifier, it is called the Equivalent Noise Charge (E.N.C.).

The first step thus consists in subtracting the pedestals from the strip signals. The channel pedestal is computed for each run as the average pulse height recorded in the first 300 events. It is done in two iterations, in order to minimize the bias introduced by the presence of cosmic particle signals in a few events for each channel. A first estimation of the pedestal and noise R.M.S. is computed, and in the second iteration, signals further than three times the R.M.S. away from the pedestals are not used. In some events, all channels of a chip exhibit a common

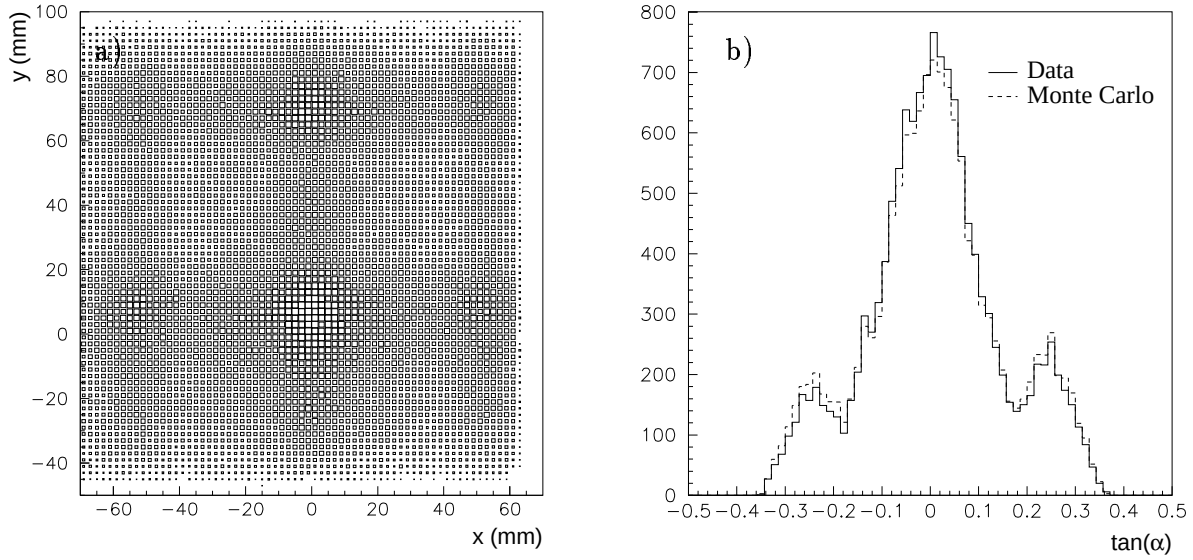

Figure 4.11: a) Distribution of the track crossing point in the hodoscope mid plane, for all accepted tracks. b) Angular acceptance in the projection perpendicular to the MSGC strips.

pedestal shift. This common mode fluctuation is computed and subtracted for each chip, event per event. The noise after common mode correction amounts to 4.6 ADC counts, which corresponds to an E.N.C. of 1200 electrons. The strip signal is considered as significant if it exceeds 14 ADC counts, about three times the noise. On average 3 strips remain above that threshold per chamber per event.

Figure 4.13 a) shows the 512 pedestal values in one counter. As seen on the plot, the pedestals increase from the first to the last channel of each chip. This is a known default of the version of the APC chip that we used. It results in an increase of the noise counts on the channels located at the chip ends, as shown in figure 4.13 b). It appears that the noise pulses on these channels are correlated: in each run, in 7 to 10% of the events, all chip ends exhibit a signal above threshold simultaneously. These events, referred to as "noisy", are handled in two different ways. In the study of the multisubstrate prototype, the noisy events are rejected by requiring less than 15 strips above threshold per chamber. The purpose of this study is indeed the detection of a localized loss of efficiency in the prototype, and we want to avoid losing sensitivity in some regions because of a local increase of noise. In the study of Ne-DME gas mixtures all events are kept. In both cases the detection efficiency is corrected for the contribution of noise as described in section 4.3.3.

Clustering algorithm

A two-threshold clustering algorithm is applied to the strip data. First, a strip threshold of 14 ADC counts, common for all strips, is applied. Then, consecutive strips above threshold are grouped into clusters, and a cut on the cluster charge is applied for further noise rejection. To allow for broken or dead strips, the presence of one channel without signal between two strips over threshold is tolerated in a cluster.

The total cluster charge is proportional to the energy lost in the detector by the ionizing particle. Figure 4.14 shows the cluster charge distribution for cosmic rays in a Ne-DME 50%-50% gas mixture, at -540 V cathode strip voltage and -2200 V drift voltage. It exhibits

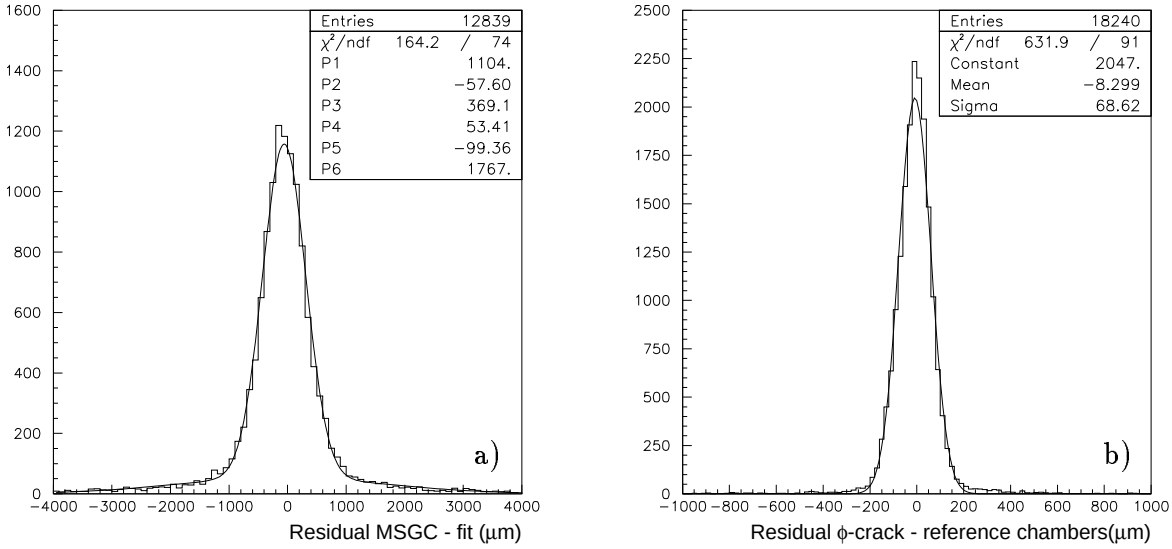

Figure 4.12: a) Distribution of the residuals between the point predicted by the hodoscope and reconstructed in one of the MSGC's. b) Distribution of the residuals between the point predicted by the reference chambers and reconstructed in the ϕ-crack chamber for tracks with $|\alpha| \leq 4^o$.

a Landau-like shape, with a broad peak and a long tail. The noise spectrum shows up at small cluster charges and can clearly be separated from the MIP signals. In the experimental conditions illustrated on the figure, a cluster threshold of 22 ADC counts suppresses most of the noise clusters.

The position of the impact point is reconstructed by computing the barycentre of the cluster:

$$y_{cluster} = \frac{\sum_i Q_i y_i}{\sum_i Q_i}, \tag{4.2}$$

where y_i, Q_i are the y-coordinate and charge of the i-th strip of the cluster.

4.3.3 Estimation of the detection efficiency

The detection efficiency of the tested prototypes is computed as the fraction of reconstructed tracks, traversing the counter sensitive area, that lead to a cluster compatible with the impact point predicted by the hodoscope. The cluster which is the closest to the predicted impact, in a window of 10 mm on each side of the prediction, is associated to the hodoscope track. The window is chosen so wide in order to retain signals from particles scattered in the setup. To ensure that the sensitive area was crossed, tracks passing through the counter border are not used. The width of the excluded border is also 10 mm.

The contribution of the noise hit rate r_n to the measured efficiency ϵ_m is given by the combined probability of having no particle signal in the detector and finding a noise hit inside the window:

$$\epsilon_m = \epsilon_r + (1 - \epsilon_r) r_n; \tag{4.3}$$

where ϵ_r is the real detection efficiency. The noise hit rate is measured in events in which the reconstructed track does not cross the MSGC surface. A randomly placed window of 20 mm

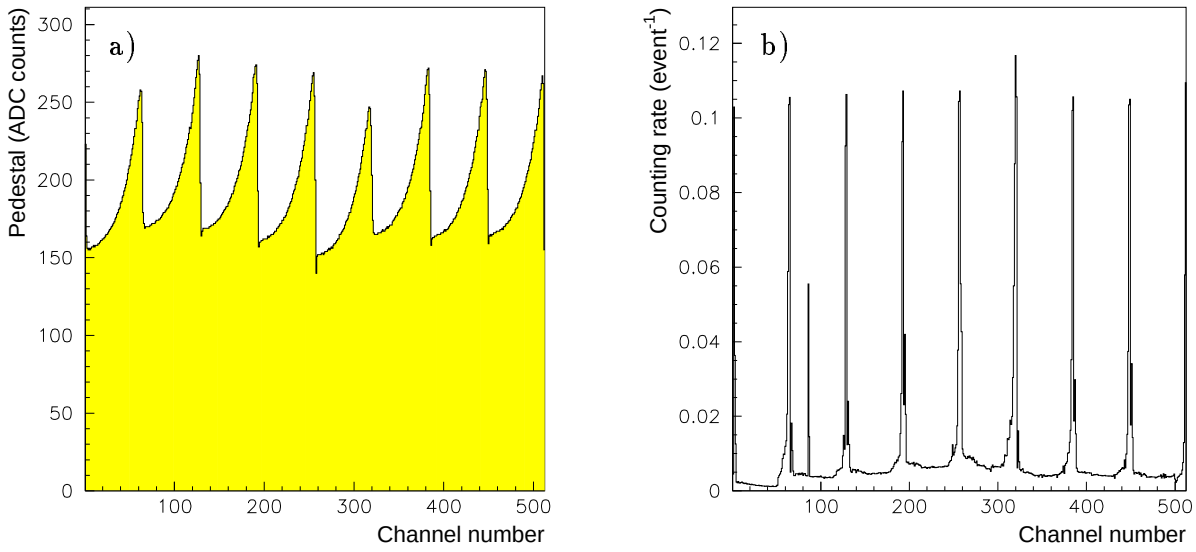

Figure 4.13: a) Pedestals in one of the MSGC prototypes. b) Channel counting rate.

width is opened, and r_n is computed as the fraction of events in which a noise cluster is found inside the window. It is evaluated to 7% on average, all events included. The actual efficiency is then calculated from equation 4.3.

In the study of the ϕ-crack chamber, better tracking than allowed with the hodoscope is desireable, in order to detect a possible localized loss of efficiency in the region of the substrate separation. This is achieved by using the two reference MSGC's to define the cosmic ray track. The procedure is explained in the next section.

4.4 Study of the performance of two substrates mounted side by side

In this section we describe the performance of the ϕ-crack prototype used to test the possibility of operating several MSGC substrates side by side in a single gas volume. The stability of operation of the prototype is evaluated by measuring the length of the efficiency plateau for cosmic rays. The detection efficiency and the plateau length obtained are compared to the performance of a reference MSGC with a substrate in one piece. The detection efficiency is measured with a particular care across the substrate separation of the ϕ-crack prototype, to find out if the counter response is degraded in this region.

4.4.1 Stability of operation and global performance

The reference and ϕ-crack chambers were operated with a Ne-DME 50%-50% gas mixture, at a drift voltage of -2200 V. The upper plot of figure 4.15 shows the average cluster charge for cosmic rays accepted in the hodoscope for the two chambers, as a function of the cathode strip voltage. The signal in the ϕ-crack prototype is 15% smaller than in the reference chamber. This can partly be explained by the larger gas gap, 3 mm in the ϕ-crack prototype as compared to 2.7 mm in the reference chamber. Indeed, although the amount of primary ionization is 10% larger, the drift field is 10% smaller. Such a reduction of drift field accounts for about

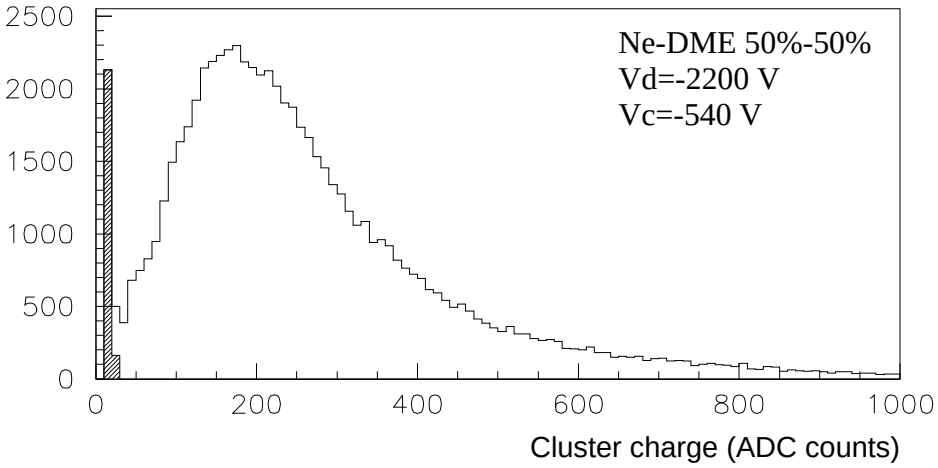

Figure 4.14: Cluster charge distribution in Ne-DME 50%-50% at a cathode strip voltage of -540 V and a drift voltage of -2200 V before application of the cluster threshold. The shaded histogram shows the clusters rejected by a cluster threshold of 22 ADC counts.

15% gain difference, as could be checked experimentally by increasing the drift voltage in the ϕ-crack chamber. The remaining loss is compatible with variations seen from one substrate to another. These are attributed to changes in the etching process, which can make the strips a bit wider or a bit narrower.

The detection efficiency is shown in the lower plot as a function of the cathode strip voltage. Efficiency values above 98% are reached in both prototypes. The range of cathode voltages, in which maximal detection efficiency is measured, is larger than 60 V. The length of the efficiency plateau is the parameter which best characterizes the detector stability: the lower the operation voltage as compared to the plateau end, the lower the breakdown rate. The operation voltage is thus chosen at the beginning of the efficiency plateau, in our case with a margin of 60 V before breakdown.

The measurements are stopped when repeated current excursions are recorded by the cathode strip HV electrometers, i.e. 3 trips above 80 nA in 24 hours. This occurs 5 to 10 V lower in the ϕ-crack prototype, a small reduction as compared to the plateau length. The detection efficiency is 1 to 2% higher in the ϕ-crack chamber, which can probably be attributed to the presence of dead channels in the reference counter.

4.4.2 Uniformity of the detection efficiency

The idea of the ϕ-crack design comes from the observation that no loss of detection efficiency could be noticed in detectors comprising several broken anodes. The electrostatic field lines from the drift space above a missing anode gather on the neighbouring anode strips. The ionization released in this region by an incoming particle would thus be collected and amplified on the nearest active anodes, permitting the detection. The ϕ-crack prototype was built in such a way that the distance between the consecutive anodes at the substrate separation is two times the nominal pitch, like in the case of a missing strip. Therefore no loss of detection efficiency is expected.

This hypothesis is tested by measuring the detection efficiency across the ϕ-crack chamber, for particles with small angle of incidence ($|\alpha| \leq 4^o$). With this angular selection, the ionization

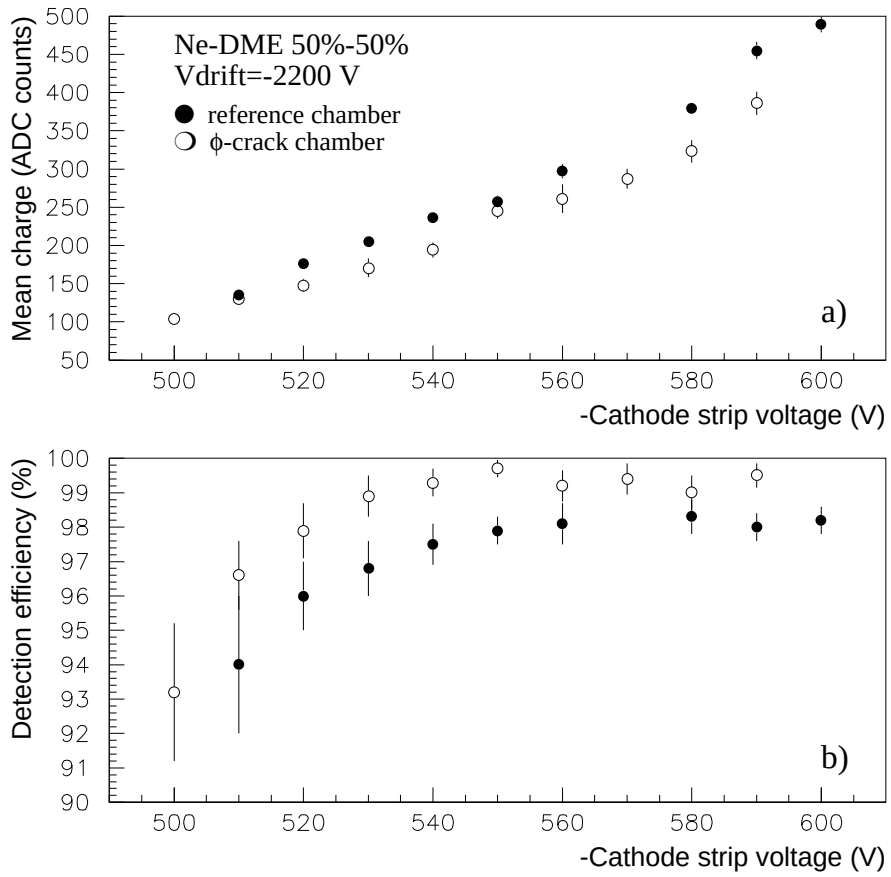

Figure 4.15: Average cluster charge (upper plot) and detection efficiency with respect to the hodoscope (lower plot) as a function of the cathode strip voltage, in the reference and ϕ-crack chambers. The gas mixture used is Ne-DME 50%-50%. The chambers are operated at a drift voltage of -2200 V. The gas volume is 2.7 mm in the reference chamber and 3 mm in the ϕ-crack prototype.

left by the incident particle is deposited in a gas column narrower than 200 μm. In this analysis, the two reference MSGC's on top and below the ϕ-crack prototype are used to define the cosmic ray track. Figure 4.12 b) shows the distribution of the residuals between the impact point reconstructed in the ϕ-crack chamber and the point interpolated from the positions of the clusters reconstructed in the reference chambers. The R.M.S. of the Gaussian curve fitted to the residuals is 70 μm. This value is still large as compared to the precision expected with perfectly aligned chambers (about 50 μm for three counters of 40 μm spatial resolution), but sufficient for the present analysis.

The prediction of the crossing point is thus about six times more precise than when using the hodoscope. The particles are also less affected by multiple scattering within the MSGC stack, as seen from the tails of the residual distribution. A window of 1 mm on both sides of the predicted impact allows to retain all particle signals. This reduces by a factor 10 the probability of finding a random noise hit inside the window as compared to analyses using the hodoscope. Correlated noise is suppressed by rejecting events in which more than 15 strips are hit in the

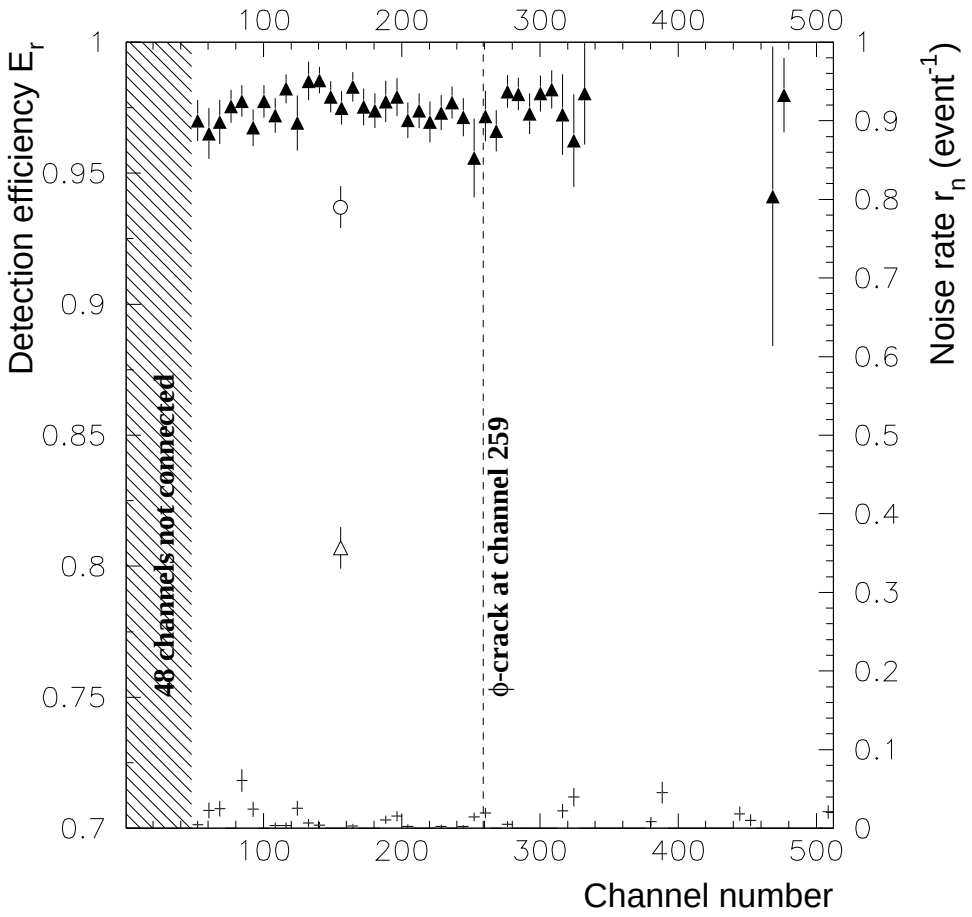

Figure 4.16: Detection efficiency for tracks with $|\alpha| \leq 4^o$ (left scale, full triangles) and noise hit rate (right scale, crosses) in the ϕ-crack chamber. The channels are grouped in bins of 8 strips. The open circle and triangle show the efficiency expected in a bin containing respectively one and two consecutive dead channels.

ϕ-crack chamber. The remaining noise rate r_n amounts to 0.5% on average. Eventually, care is taken not to build artificial tracks out of noise hits. Signals from the first and last two channels of each chip are thus not used in the reference chambers.

Figure 4.16 shows the detection efficiency versus the channel number in the ϕ-crack chamber. The measurements were taken at cathode strip voltage $V_c = -540$ V and drift voltage $V_d = -2200$ V. The chamber is divided in bins of 8 strips. The average number of events is 300 per bin. The statistical error on the detection efficiency is about 1% in each bin. The substrate separation is physically located in front of an unconnected preamplifier input, at channel 259. A uniform efficiency of 97.5% is measured. No significant efficiency decrease is seen at the substrate separation. Channels 320 to 460 are located in the centre of the hodoscope, where no tracks of small incident angle are accepted, hence the lack of data in this zone.

The sensitivity of our measurement was checked by canceling the signals of a few consecutive channels out of the crack region before running the analysis program. A dead zone of two consecutive channels shows up as a 16% efficiency drop in the bin where the dead channels are located, whereas a single dead strip causes a 4% drop (open marks in the figure). Therefore our results are compatible with no efficiency loss at all at the crack, but by lack of statistics

the measurement is sensitive to dead zones wider than 200 μm only. The corresponding dead space, of maximum 0.2% of the detection surface, is however very small and will not impair track reconstruction in CMS. The noise hit rate across the chamber was also measured in order to verify that a local loss of efficiency was not compensated by a local increase in the number of noise hits. As shown by the crosses in figure 4.16, the noise rate remains below 5% everywhere in the chamber, contributing to the efficiency by less than 0.1%.

4.4.3 Conclusions

The prototype of MSGC made with two pieces of glass mounted side by side was operated successfully under cosmic rays. It is as stable and efficient as any counter made with a uniform strip support. No significant loss of detection efficiency was seen at the substrate separation. These tests validate the design of the CMS forward MSGC modules, in which several counters will be mounted side by side in ring-shaped gas volumes.

The experimental study of the ϕ-crack prototype was followed by a Monte Carlo study, performed by D^r T. Todorov from IReS, Strasbourg. The study consists in a simulation of the microscopic motion of the electrons, in the electric field created by an electrode pattern with one missing anode strip. It is estimated that about 20% of the primary electrons, released in the gas column above the missing strip, drift to the substrate between the neighbouring active strips and are not amplified. However, as more drift field lines are focusing on the neighbouring anodes, the gas gain predicted by the simulation is slightly larger on these strips. The average signal amplitude is the same for tracks passing inside or outside the ϕ-crack, but larger fluctuations are foreseen in the ϕ-crack region [91]. Still, the expected loss of efficiency is negligible.

Some aspects of the operation of counters mounted in a ϕ-crack geometry remain to be studied. Contrary to the design of the MSGC modules, the ϕ-crack prototype had an uncut drift plane covering the two pieces of substrate. Moreover, some stability problems, due for example to charge accumulation on the insulating substrate, only appear at high counting rates (10^4 mm^{-2}s^{-1}), while the present tests were performed in cosmic rays at very low rate (10^2 m^{-2}s^{-1}). Eventually, the possible degradation of the spatial resolution at the substrate junctions has still to be investigated. These studies are planned for future beam tests.

4.5 Study of Ne-DME gas mixtures

This study aims to measure the signal amplitude and the detection efficiency of MSGC's filled with Ne-DME mixtures. Mixtures of Ne and DME lead to stabler operation and higher gas gains as compared to gases commonly used in high-energy physics applications, like DME-CO_2. Several explanations have been proposed for this behaviour, based on the fact that Ne has very high excitation and ionization potentials, 17 and 21 eV respectively, as compared to the ionization potential of DME, about 10 eV. Ne would therefore act as an inert dilutant, and adding Ne would be equivalent to low pressure operation with pure DME [81]. As the first Townsend coefficient rises steeply with the reduced field E/p, a gain increase is expected when reducing the partial pressure of DME in the mixture. The Penning effect exhibited by these mixtures is also in favour of safe operation: high gains can be reached at low voltages, which reduces the electrostatic energy stored in the counter and the damage to the strips in case of sparks.

However, because of the low primary ionization density in Ne, high gains might not translate directly into high detection efficiency. We consider here both maximum signal before breakdown

and range of stable operation at maximal efficiency. The measurements are performed with the lower reference counter, using the hodoscope as external tracking system. To disentangle the performance of the gas mixture from the detector quality, tracks passing in zones of the chamber containing several broken anodes are not used. When including these zones, the overall detection efficiency drops by about 2%. The noise contribution is corrected for as described in section 4.3.3.

4.5.1 Signal amplitude

Figure 4.17 shows the cluster charge distribution for cosmic rays, in Ne-DME 40%-60% (left plot) and CO_2-DME 40%-60% (right plot). The drift voltage applied across the 2.7 mm gas gap is -2200 V. The cathode strip voltage is $V_c = -560$ V in Ne-DME 40%-60% and -625 V in CO_2-DME 40%-60%. In both gases, the distribution is well above the cluster threshold of 22 ADC counts. The average cluster charge is however 1.8 larger in Ne-DME 40%-60% than in CO_2-DME 40%-60%, although the cathode strip voltage is 65 V lower.

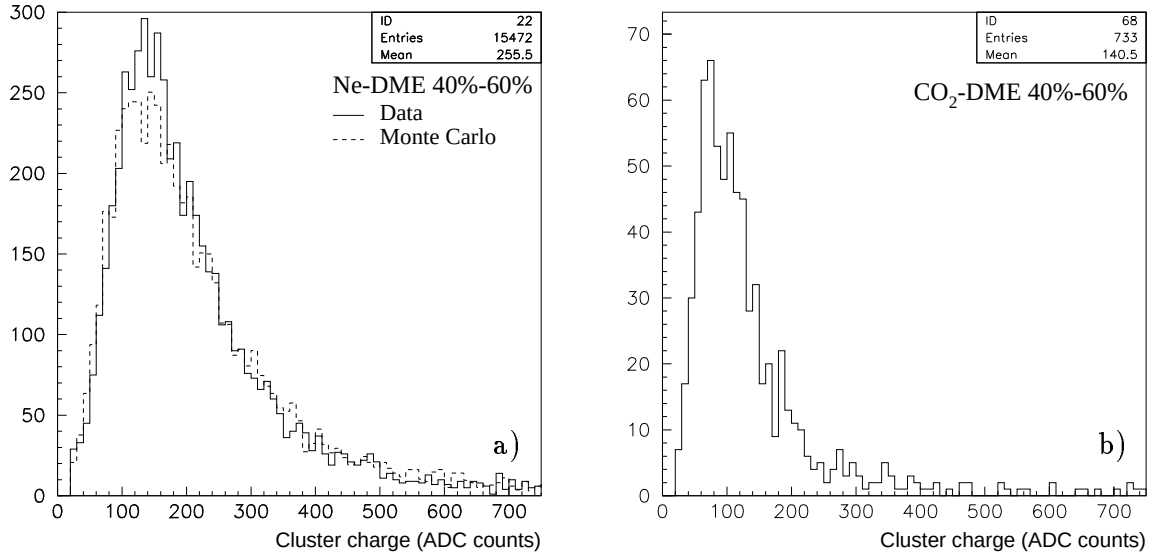

Figure 4.17: a) Cluster charge distribution in Ne-DME 40%-60%, for cosmic particles crossing the detector with $|\alpha| < 3.4^o$. The full line is the measured distribution and the dashed line is the distribution generated with the simulation of the detector response described in section 4.6. b) Cluster charge distribution in CO_2-DME 40%-60% for the same angular range.

The mean collected charge in Ne-DME 20%-80%, 40%-60% and 50%-50% is shown in figure 4.18 as a function of the cathode strip voltage, for a drift voltage of -2200 V. The measurement taken in CO_2-DME 40%-60% at $V_c = -625$ V is also displayed. The signal amplitude exhibits an exponential rise with the cathode strip voltage. Same signal amplitude (125 ADC counts) as in CO_2-DME 40%-60% is reached in Ne-DME mixtures at much lower anode-cathode voltage, 520 to 540 V instead of 625 V. The detector can be operated safely up to cathode voltages yielding three to four times larger pulse height than the maximum attainable signal in CO_2-DME. At identical voltages, the mixture with the highest Ne content provides the largest signal. As the total ionization density decreases with increasing Ne content, the rise in signal amplitude can only be attributed to a greater increase of gas gain, compensating the reduction of ionization.

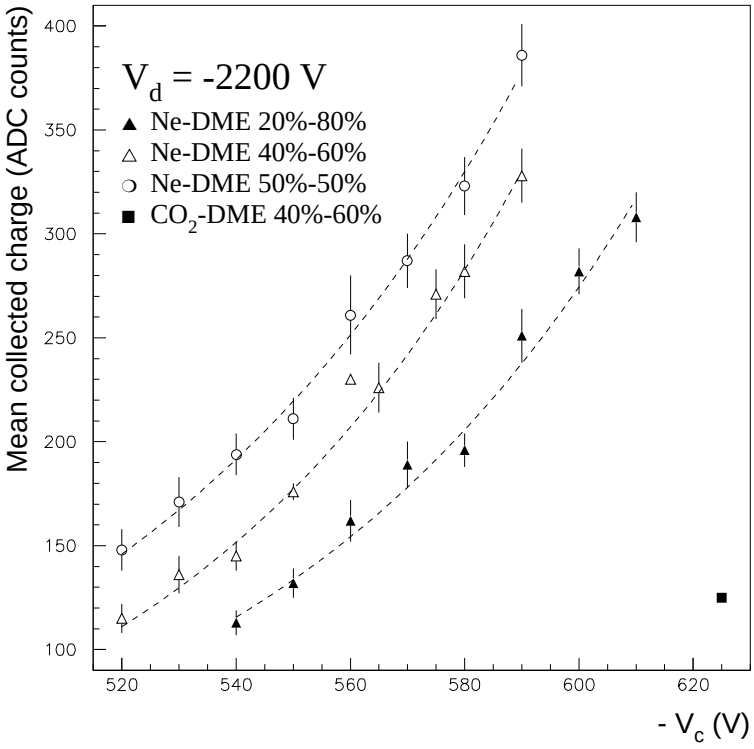

Figure 4.18: Mean collected charge for cosmic rays accepted in the hodoscope, in Ne-DME 20%-80%, 40%-60% and 50%-50%, as a function of cathode strip voltage. The dashed lines are exponential curves. A measurement in CO_2-DME 40%-60% is also given for comparison.

4.5.2 Detection efficiency

As shown in figure 4.19, detection efficiencies above 98% are measured in all mixtures, for a range of cathode voltages exceeding 70 V. This demonstrates that, in all mixtures studied, the gas amplification can be large enough to produce a signal over threshold from the few primary electrons released in the counter (from 9 to 13 primary electrons depending on the mixture). Full detection efficiency is reached at cathode strip voltages as low as 530 V in the mixture with the lowest DME content, as compared to 625 V in CO_2-DME 40%-60%. The plateau curve starts earlier in Ne-DME 50%-50% than in Ne-DME 20%-80%, due to the signal increase with increasing Ne content at constant cathode voltage. The 70 Volts length of the efficiency plateaux provides a good safety margin for long term operation, as a gain drop of a few percent can safely be compensated by an increase of a few volts in cathode voltage. In CO_2-DME 40%-60%, the measurements were stopped at $V_c = -640$ V because of repeated trips. The plateau length is 15 V only.

However, at the LHC it is not recommended to operate at too high signal amplitudes. On one hand, ageing is thought to be an increasing function of the charge accumulated on the strips in the detector lifetime. On the other hand, the dynamic range of the CMS front-end amplifiers is limited to a maximum input signal of a few times 25000 electrons, the average MIP signal in the CMS silicon strip detectors. In figure 4.20, the efficiency values are plotted as a function of the mean collected charge, at the start of the efficiency plateaux, for Ne-DME 20%-80% and Ne-DME 50%-50%. The trend that appears is that for a given efficiency, more pulse height is

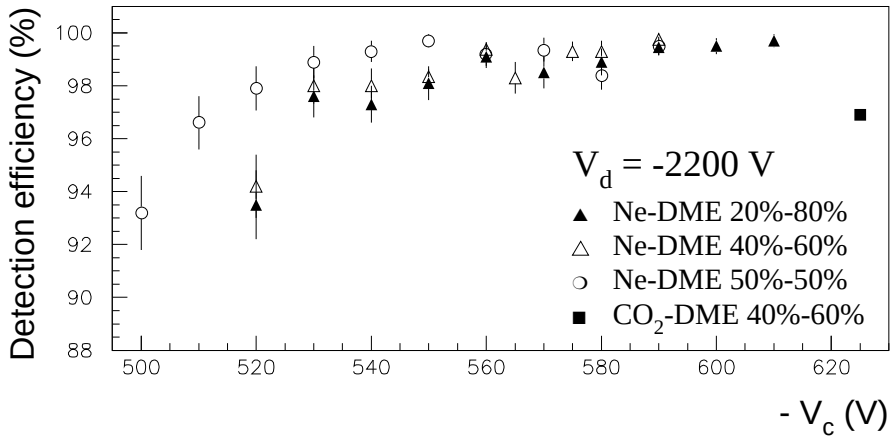

Figure 4.19: Detection efficiency for cosmic rays accepted in the hodoscope, in Ne-DME 20%-80%, 40%-60% and 50%-50%, as a function of cathode strip voltage.

required in gases with a higher Ne content. As will be shown in the Monte Carlo study, this behaviour is due to increased signal fluctuations in mixtures providing less primary ionization.

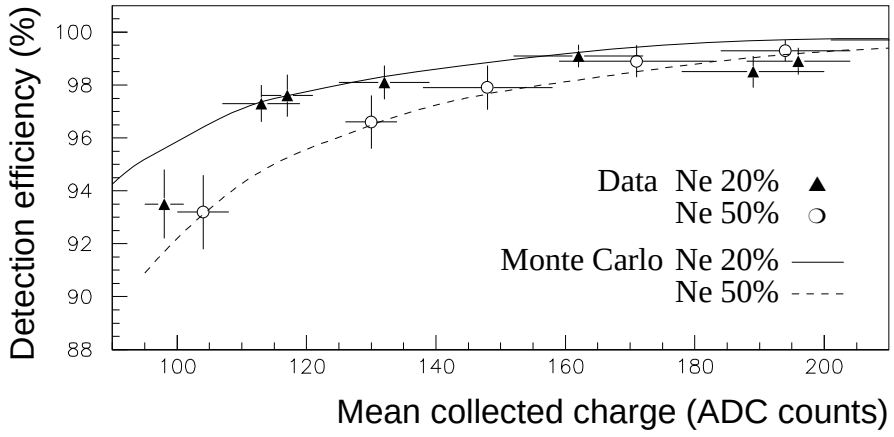

Figure 4.20: Detection efficiency for cosmic rays accepted in the hodoscope, in Ne-DME 20%-80% and 50%-50%, as a function of mean collected charge. The crosses are experimental data and the lines are Monte Carlo estimations.

4.6 Analysis of the MSGC performance with Monte Carlo simulations

In order to understand the behaviour of MSGC's filled with Ne-DME, a Monte Carlo simulation of the detector response was performed. Firstly, it aims to confirm our understanding of the behaviour of the detection efficiency with the proportion of Ne and with the collected charge. Secondly, the diffusion of electrons in the gas is evaluated, by tuning the cluster size of the

simulated data on the measurements. Eventually, the simulation is used to estimate the spatial resolution of the counter, not measured in the present work.

4.6.1 Description of the Monte Carlo program

The MSGC simulation package implemented in the simulation of the CMS detector [92] is well suited for our purposes, as it contains a description of the phenomena relevant for this study, like ionization, diffusion and gas gain. The stochastic processes are described according to the theory explained in chapter 3. The Monte Carlo program was adapted to our experimental setup. Cosmic muons are generated with direction and impact point distributions as measured by the hodoscope. Their momentum is chosen according to the momentum distribution of cosmic rays, and requiring that they traverse the setup. The mean momentum of the accepted muons is 2 GeV/c, and their minimum momentum, 300 MeV/c.

Primary electrons are released along the particle path in the gas, according to a Poisson statistics of mean value $n_P x$, where n_P is the primary ionization density and x is the length of the track inside the detector. For minimum ionizing particles, $n_P \simeq 55$ cm^{-1} in DME and $\simeq 11$ cm^{-1} in Ne. Because most of the accepted muons are faster than minimum ionizing, n_P has to be corrected by the semi-empirical formula [28]:

$$n_P = A_1/\beta^2 \left[\ln(\beta^2\gamma^2) - \beta^2 + A_2\right], \tag{4.4}$$

which depends on the particle velocity β in the same way as the energy loss in the Bethe-Bloch formula. The constants A_1 and A_2, experimentally measured, can be found in reference [28] for various gases. The average primary ionization density for the accepted cosmic rays is about 20% larger than for minimum ionizing particles.

Each primary electron (δ-electron) can escape perpendicularly to the muon track, further ionizing in the gas volume. The δ-ray range is parametrized as in [32]. The probability $w(n)$ that n secondary electrons are emitted along the δ-ray track are described according to formula 3.7. We have estimated the parameters $w(1)$ and κ from our data by tuning the shape of the cluster charge distribution for tracks with $|\alpha| < 3.4^o$. The purpose of this restriction is to minimize the biases which affect the measured signal at larger angles. As α increases, the particle signal is shared between an increasing number of anodes, with less charge per channel. After application of the strip threshold, some hit channels can be discarded, and the measured cluster charge can be reduced. No selection is made on β, as it only affects the signal amplitude through the amount of primary electrons released in the detector, which only changes by 4% in the accepted angular range. The best agreement between the measured and the simulated distributions is shown in figure 4.17. The corresponding values of $w(1)$ and κ are 0.67 and 2.2 respectively.

Primary and secondary electrons drift from their starting point towards the anode plane, while they undergo a transverse displacement with respect to the drift direction, because of diffusion. The precise drift velocity is of no importance in this study: the electron drift time and the APC risetime are short as compared to the duration chosen for the signal integration gate, 600 ns. The length of the transverse displacement is normally distributed, with a standard deviation $\sigma_x = \sigma_T\sqrt{L}$, where σ_T is the transverse diffusion coefficient, and L is the distance from the electron starting point to the electrode plane. The value of σ_T is chosen so as to reproduce the cluster size distribution for tracks with $|\alpha| < 3.4^o$. For such small incident angles, the spread of the primary ionization is limited to a region narrower than one anode pitch. The wider signal dispersion observed in the data is the result of diffusion. Figure 4.21 shows the measured and simulated distributions in Ne-DME 40%-60% and CO_2-DME 40%-60% at a drift field of 6.7 kV/cm. The estimated values of the diffusion coefficient are (166 ± 3) and

(95 ± 10) $\mu m/\sqrt{cm}$ respectively. The excess of large clusters observed in the experimental data are attributed to detector imperfections not simulated in the Monte Carlo program (broken strips, correlated noise).

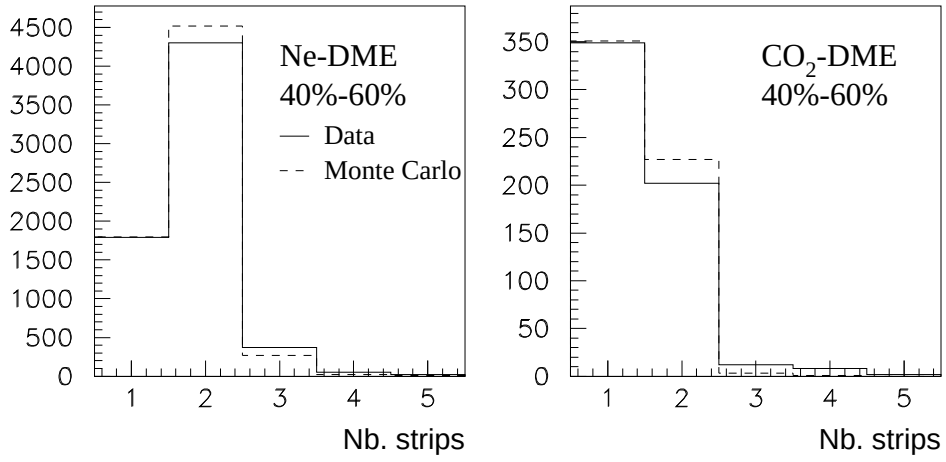

Figure 4.21: Cluster size distributions in Ne-DME 40%-60% and CO_2-DME 40%-60% for cosmic particles crossing the detector with $|\alpha| < 3.4^o$. The full lines are experimental data and the dashed lines are simulated data.

The avalanche development is not simulated. Such a simulation would be too time consuming, and in order to yield a reliable estimation of the gain, it would require the knowledge of the cross-sections of all processes involved in the formation of the avalanche, for which few experimental data exist. Instead, the reduced gas gain $z = K/\bar{K}$ is chosen randomly following a Polya distribution. The average gas gain $\bar{K}$ is adjusted to reproduce the mean value of the experimental cluster charge distribution. The standard deviation of the Polya distribution is taken to be $\sigma = 0.7$ [44]. The cluster charge distribution was not affected when varying σ from 0.6 to 0.8, which covers the range of gain fluctuations theoretically predicted for such gas proportionnal counters as MWPC's, MSGC's or MGC's.

The effect of the capacitive coupling between the electrodes, referred to as "crosstalk", is taken into account in the simulation. Figure 4.22 a) shows a simplified MSGC equivalent circuit. The capacitance between an anode and the block of 16 cathodes to which it is coupled is 6 pF. The total capacitance to ground of the cathode block is about 100 pF. When an avalanche occurs, the detector behaves like a current source which charges up the capacitance of the cathode group. This capacitance discharges through the 16 anodes capacitively coupled to the cathode group, rather than through the high impedance connection to the power supply. Therefore a negative charge equal to $(-1/16)$ of the particle signal is induced on the coupled anodes. The crosstalk fraction was experimentally measured by looking at the pedestal decrease on the channels neighbouring the hit ones (see figure 4.22 b). It was estimated to $(-6 \pm 0.7)\%$, compatible with $(-1/16)$.

In the last step, the electronics response is simulated. The avalanche charge collected during the 600 ns gate of the APC chip is divided by a calibration factor of 250 electrons/ADC count. The electronics noise is described as Gaussian and uncorrelated. The R.M.S. of the simulated noise is equal to the measured value of 4.6 ADC counts.

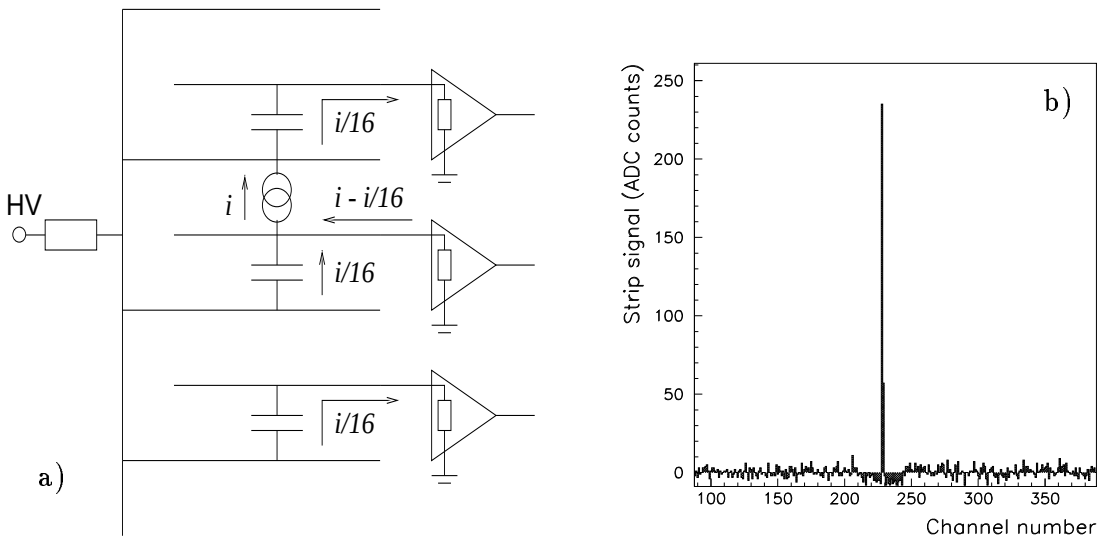

Figure 4.22: a) Simplified MSGC equivalent circuit. The cathode strips are connected in groups of 16 to the HV supply. The anodes are grounded through the preamplifiers. The currents induced by the ionizing particle and by capacitive coupling are shown. b) Strip signals near a particle impact. The pedestal undershoot in the channels capacitively coupled to the hit strips is visible.

4.6.2 Monte Carlo results

Detection efficiency and collected charge

The counter detection efficiency estimated from the Monte Carlo data is calculated in the same way as for the experimental data. In figure 4.20, the efficiency curves as a function of the mean collected charge are compared to the measurements. The simulated curves agree with the experiment within statistical errors. The Monte Carlo confirms that efficiencies above 98% can be reached in all gas mixtures studied, and also that at constant efficiency a higher mean collected charge is needed when the Ne fraction is larger.

This effect is explained by increased fluctuations in the number of primary electrons when the primary ionization density is reduced: $\frac{RMS(n_P x)}{n_P x} \simeq \frac{1}{\sqrt{n_P x}}$. Consequently, the cluster charge distribution broadens with increasing Ne content, as illustrated in figure 4.23. A larger fraction of the simulated signals do not reach the threshold in Ne-rich mixtures. To have the same fraction of the distribution above threshold in Ne-DME 50%-50% as in Ne-DME 20%-80%, the whole distribution has to be pushed towards higher pulse heights. Figure 4.24 summarizes the Monte Carlo results in the form of efficiency contours in a graph where the Ne content is reported on the y-axis and the mean charge on the x-axis.

Diffusion

As explained in paragraph 4.6.1, the transverse diffusion coefficient is adjusted so as to reproduce the cluster size distribution for tracks of small incident angle ($|\alpha| < 3.4^o$). Cluster size measurements have been taken at various drift field intensities and in various mixtures. The values of the diffusion coefficient tuned on the data are shown in figure 4.25, compared to calculations performed by A. Sharma [80] with Magboltz [93], a program of integration of the Boltzmann equation describing the electron transport. The errors are evaluated by changing

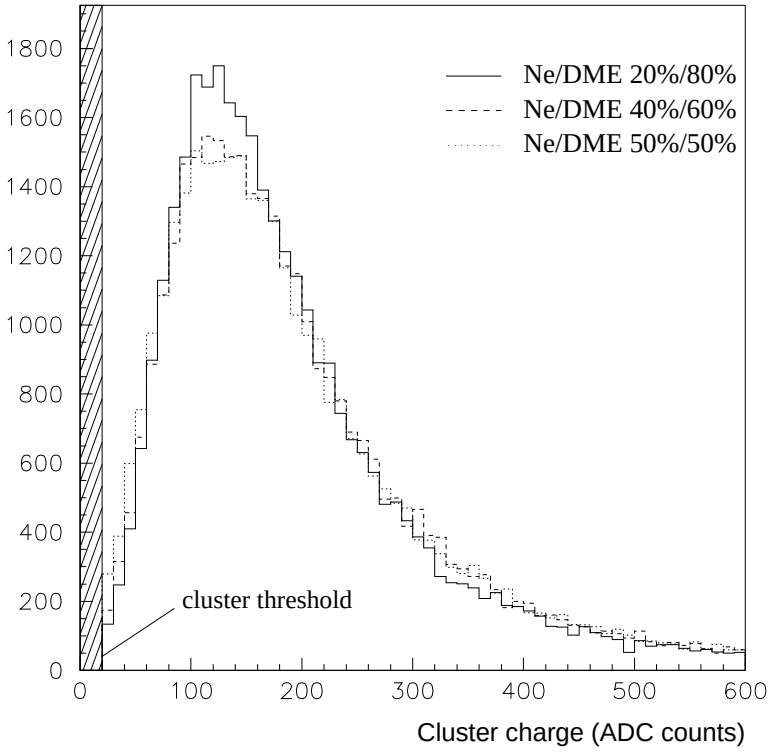

Figure 4.23: Three simulated cluster charge distributions of identical most probable value, in Ne-DME 20%-80% (full line), 40%-60% (dashed) and 50%-50% (dotted).

the diffusion coefficient up to the point where the simulated distribution becomes incompatible with the data. The method used is that, when increasing the diffusion parameter by one standard deviation as compared to the tuned value, the number of clusters of one strip is reduced by its square root. The present estimates are in most cases unprecise to 10 - 20%, but agree qualitatively with the theoretical calculations.

Spatial resolution

When the experimental study of the Ne-DME mixtures started, only two MSGC's were ready to be tested. No sufficiently precise tracking was available to measure the spatial resolution of the prototypes. Instead, the resolution was estimated thanks to the Monte Carlo program. The accuracy of the reconstructed impact point is mostly affected by signal fluctuations and transverse diffusion in the gas. As the simulation is able to reproduce the data in these aspects, it can yield a sensible prediction of the counter spatial resolution.

The impact point position can be calculated in two ways, depending on the readout electronics. With analog readout, like in the present setup, the amplitude of the strip signals can be used to compute the centre of gravity of the cluster. With digital readout, the impact position is taken as the average position of the first and last strip of the cluster. The two algorithms behave differently with α, the angle of incidence in the projection perpendicular to the strips. At normal incidence ($\alpha = 0$), the strip which is closest to the particle track collects the largest charge. The position of this strip gets a larger weight in the determination of the cluster centre of gravity. The analog method performs thus better than the digital method

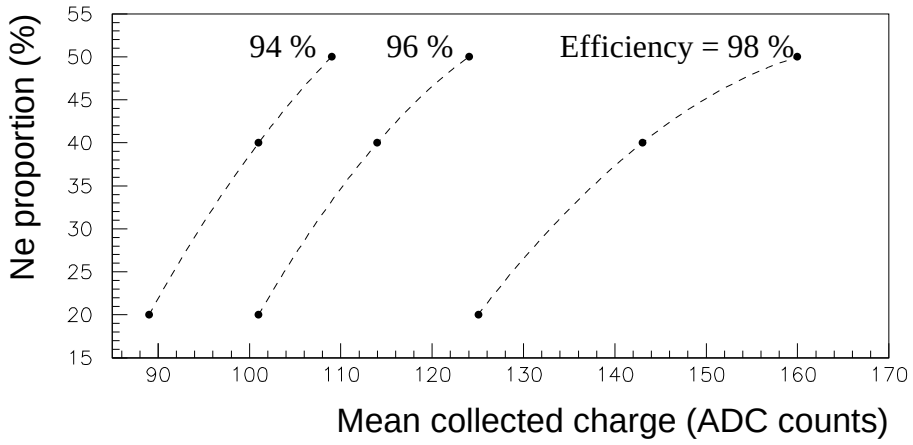

Figure 4.24: Monte Carlo estimates of the detection efficiency for various Ne contents and mean cluster charges.

at normal incidence. When the ionizing particle crosses more than two strips ($\alpha \geq 8^o$ with a 2.7 mm thick gas volume), the number of electrons released over each strip is on average the same. As this number is very small, of the order of 1 primary electron, the strip signals exhibit large fluctuations. Therefore, the digital method, which does not rely on the amplitude of the strip signals, yields better results.

At normal incidence, the spatial accuracy is also affected by diffusion. With analog readout, best performance is obtained when the signal is collected on two strips, so that the charge interpolation can work. With digital readout, the best results can be expected when half of the tracks give rise to a cluster of one strip (the tracks crossing the detector in a 100 μm wide gas column centred on an anode strip), while the others produce a two-strip cluster (the tracks passing in a 100 μm wide gas column in between two anodes). In this case the effective pitch of the counter is reduced to half the anode pitch.

The spatial resolution is evaluated as the standard deviation of the Gaussian curve fitted to the distribution of the distance between the simulated crossing point and the cluster position, reconstructed with the simulated strip signals. Figure 4.26 shows the spatial resolution estimated with the two algorithms as a function of α, for the three gas mixtures studied. An additional curve is shown for Ne-DME 20%-80% with a diffusion coefficient of 170 $\mu\mathrm{m}/\sqrt{\mathrm{cm}}$. This value of the diffusion can be reached by increasing the drift field in the detector from 6.7 kV/cm to 10 kV/cm.

With analog readout, all mixtures yield comparable results. The best resolution for cosmic particles orthogonal to the substrate is evaluated to 30 μm, in Ne-DME 20%-80%, with a 10 kV/cm drift field. Indeed, the signal fluctuations are reduced thanks to the large primary statistics, and the diffusion is large enough to allow good sampling of the charge spread on the strips. This value worsens to 32 μm for particles at the minimum of ionization. For the same mixture, at a lower drift field of 6.7 kV/cm, the diffusion coefficient only amounts to 130 $\mu\mathrm{m}/\sqrt{\mathrm{cm}}$. The charge spread is not sufficient for orthogonal tracks, and the best resolution is thus predicted for an angle α of 2^o. This effect was already seen experimentally in pure DME [94].

With digital readout, the resolution predicted at angles larger than 5^o is also fairly independent of the Ne-DME mixture used. Close to normal incidence, the mixture with the smallest

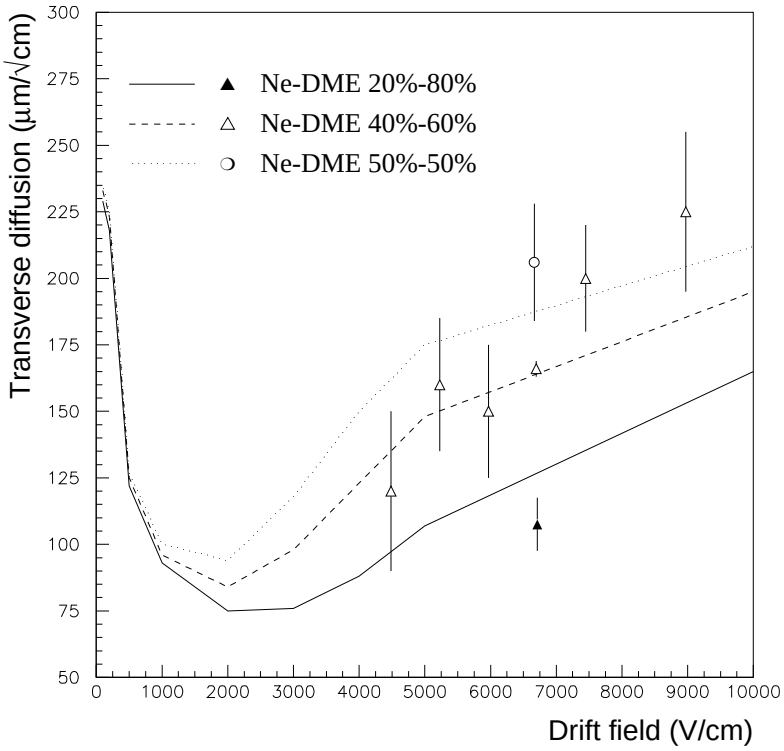

Figure 4.25: Transverse diffusion coefficient as a function of the drift field. The lines are calculations performed by A. Sharma [80] with Magboltz [93] and the points are the present estimates.

diffusion coefficient (Ne-DME 20%-80%, $\sigma_T = 130\ \mu\mathrm{m}/\sqrt{\mathrm{cm}}$) gives the best results, 38 μm. The resolution at $\alpha = 0^o$ varies by 20% between the various simulated conditions. In CMS, analog readout will be used. The intrinsic detector resolution should thus not prevent from reaching the 50 μm resolution required per MSGC layer. Detector alignment will however be a crucial issue, as the position of the 15000 MSGC counters will have to be known with an accuracy of about 30 μm in $R\phi$.

As expected, the digital method performs better for angles larger than 8^o. At 20^o, the resolution estimated with the digital scheme is 140 μm, as compared to 180 μm with the centre of gravity method. These values are compatible with previous experimental results on the angular dependence of the MSGC response [95]. To achieve this performance at 20^o, up to three successive strips without signal must be admitted in a cluster, because the probability of having no signal above threshold on a strip crossed by the incident particle is as large as 20%. The behaviour of the MSGC resolution at large incident angles is an important point, as it affects the reconstruction of low momentum particles in the CMS tracker. Angles around 20^o are reached in the outer detection layer by particles of 2 GeV/c transverse momentum. Optimal track reconstruction would therefore require a flexible clustering algorithm in the MSGC's, with a variable number of successive empty channels and an adequate choice of the method of impact point estimation as a function of the angle α.

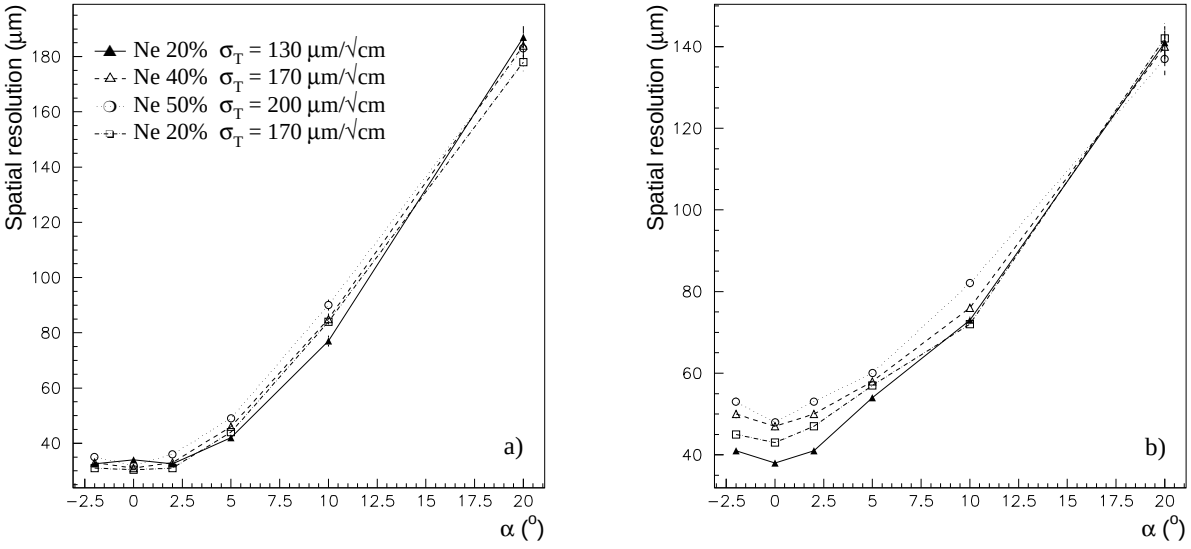

Figure 4.26: Monte Carlo estimations of the spatial resolution as a function of the incident angle α, for analog (a) and digital (b) readout schemes.

4.7 Further developments in gas mixtures for MSGC's

The study of Ne-DME gas mixtures was completed in Antwerp by measurements of drift velocity. As this parameter was found to be hardly sufficient in Ne-DME to achieve the short signal risetime needed at the LHC, triple mixtures of Ne, DME and CO_2 were tried [96]. Figure 4.27 a) shows the drift velocity in Ne-DME 50%-50% and in Ne-DME-CO_2 mixtures. In Ne-DME, the drift velocity saturates at about 55 μm/ns at practical values of the drift field (up to 10 kV/cm). Adding 20% of CO_2 to a mixture with equal parts of Ne and DME increases the drift velocity up to 65 μm/ns at a drift field of 10 kV/cm.

The detection efficiency in these triple mixtures was then measured using the cosmic ray hodoscope. Figure 4.27 b) shows the detection efficiency as a function of the cathode strip voltage in Ne-DME-CO_2 40%-40%-20%. The beginning of the efficiency plateau is shifted by 20 V towards higher voltages as compared to Ne-DME 50%-50%. The plateau also becomes 20 V longer. A 30% lower gain is measured as compared to Ne-DME 50%-50%, which affects the detection efficiency at low voltages, but the counter operation is stabler at high gains. This behaviour is characteristic of a quenching gas like CO_2. No significant change of spatial resolution is expected with Ne-DME-CO_2 40%-40%-20% as compared to Ne-DME 50%-50%. Therefore, provided that no ageing is observed in long-term tests, triple mixtures of Ne, DME and CO_2 are good candidates for use at LHC.

Eventually, it should be noted that DME is a flammable gas, which raises some concerns in terms of safety. Neon, in turn, is much more expensive than argon or helium, with prices around 170 CHF/m^3 for Ne and 5.5 CHF/m^3 for Ar. Adding CO_2 does not help much, as the CO_2 fraction must be kept low to reach high gas gains. He-DME mixtures have been tested, but they yield poorer gain and stability than Ne-DME [96]. The choice of gas mixture seems less limited for high gain devices like a MICROMEGAS or the combination of an MSGC and a GEM foil. These detectors have been successfully operated with cheap non-flammable mixtures, like Ar-CO_2 [68, 84]. However more development work is required in order to study all the aspects of the performance of these counters before they can be used at the LHC.

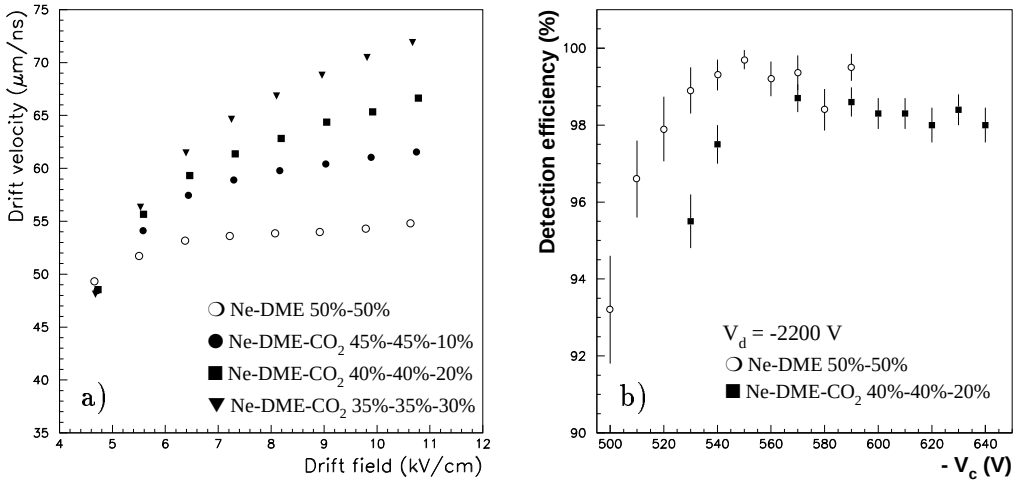

Figure 4.27: a) Drift velocity as a function of the drift field intensity, in Ne-DME 50%-50% and Ne-DME-CO_2 mixtures. b) Detection efficiency for cosmic rays in Ne-DME 50%-50% and Ne-DME-CO_2 40%-40%-20% as a function of cathode strip voltage. [96].

4.8 Conclusions

The studies performed with three MSGC prototypes placed in a cosmic ray hodoscope allowed to test various aspects of the design of the CMS MSGC tracker. The mounting scheme proposed for the forward tracker, in which several MSGC's will be mounted side by side in common ring-shaped gas volumes, was tested with positive results. In cosmic rays, the stability of operation is not degraded by the presence of bare substrate edges at 70 μm distance. The measured detection efficiency is as high as 97.5% and shows no significant drop at the substrate separation, our measurement being sensitive to a dead area corresponding to one dead strip. Further tests with detectors placed side by side are planned. The problem of stability at counting rates comparable to LHC conditions will be adressed in high intensity beam tests. With larger statistics, more accurate measurements of the detection efficiency, together with a measurement of the spatial resolution at the detector junction will be possible. The future prototypes will present a separation in ϕ also for the drift plane.

The choice of an adequate working gas was also studied. Gas mixtures of Ne and DME have provided very good stability of operation at high gas gains. As compared to the best mixture known before our study, CO_2-DME 40%-60%, they allowed high detection efficiency for cosmic rays at much lower cathode strip voltage, and long efficiency plateaux. Detection efficiencies above 98% have been measured for a range of cathode strip voltages exceeding 70 V, in all mixtures studied containing from 20 to 50% of Ne. At fixed cathode strip voltage, the mixture with the highest Ne content yields the highest gain and efficiency. However the small number of primary electrons leads to large signal fluctuations. A larger charge must be collected on the strips to maintain a given efficiency value in Ne-rich mixtures. Therefore a moderate fraction of Ne, smaller than 50%, seems recommended. The spatial resolution of MSGC's filled with Ne-DME mixtures was estimated by Monte Carlo simulations. The best results, 30 μm resolution at normal incidence, are obtained with the centre of gravity algorithm for the mixture with the largest DME content.

Further studies have shown that the drift velocity in Ne-DME mixtures is limited to

55 μm/ns at drift fields up to 10 kV/cm, barely sufficient to meet the speed requirements at the LHC. Therefore triple mixtures of Ne, DME and CO_2 have been tested with encouraging results. Adding 20% of CO_2 to a mixture with equal parts of Ne and DME leads to an increase of drift velocity up to 65 μm/ns at a drift field of 10 kV/cm. The 30% gain drop caused by the addition of 20% of CO_2 is tolerable. The efficiency plateau is shifted by 20 V towards higher cathode strip voltages but becomes 90 V long. These mixtures are thus a step forward in the search for an optimal gas for MSGC's in CMS, provided that no ageing is observed in long-term tests.

Chapter 5

Study of the performance of the CMS tracker

5.1 Introduction

Track reconstruction at full LHC luminosity is a challenging task. Up to hundred tracks of charged particles of transverse momentum higher than 1 GeV/c must be reconstructed per event, in a background of several hundreds of low momentum particles which generate of the order of 10000 hits in the detector elements. Such an environment requires a well designed tracking system: the performance of the tracker must be carefully evaluated for several benchmark physical processes. The LHC environment is also very demanding on the track finding and fitting algorithms, which have to deal with a large number of hit combinations.

The purposes of this chapter are the following. First, we try to understand one of the possible track reconstruction algorithms, and check that the present implementation in the CMS reconstruction program is adequate for track finding and fitting in the CMS tracker. Then, we study the quality of track reconstruction in the CMS tracker with that algorithm, and check that the requirements expressed in the CMS Technical Proposal are fulfilled. We put the emphasis on the features which are relevant for the identification of jets originating from b-quarks with the method of the impact parameter, described in chapter 6.

This work is performed with a detailed simulation of the CMS tracker, described in section 5.2. As a correct track fit requires a good knowledge of the errors on the measured hit coordinates, some time is spent in studying the behaviour of the spatial resolution of the different detector elements with respect to the particle incident angles. The track finding and fitting procedure is explained in section 5.3. In section 5.4, the analysis of the reconstructed tracks is described, and the performance of the CMS tracker is studied for isolated particles and b-jets.

5.2 Simulation of the CMS tracker

The simulation program of the CMS detector, CMSIM, is based on the GEANT simulation package [97]. This software is commonly used in high energy physics to describe the geometry of a detector and to simulate the interactions of particles with the detector material. The user defines the detector structure and sensitive elements, and the program follows the particles step by step, computes the energy lost in interactions with the detector material, generates possible secondary particles resulting from these interactions, and simulates the particle decays if necessary. In the present study, the GEANT parameters are set so as to trace particles down to relatively low energies, 100 keV for electrons and photons, and 1 MeV for muons and

hadrons. Below these cuts the particle range is considered as negligible and all the remaining energy is supposed to be deposited at the stopping point.

The geometry of the tracker that we have simulated is shown in figure 2.8. It corresponds to the version V3 of the tracker design [21]. After simulation of the particle transport through the apparatus, the signals specific to each detector type are simulated in all counters hit by an ionizing particle. The coordinates of the particle crossing points are then computed from these signals. The user can choose between two levels of simulation: hit smearing, or hit digitization and clusterization. In the first option, the hit coordinates are smeared according to Gaussian distributions, the R.M.S. of which are equal to the expected detector resolutions (see table 2.4). In the second option, particle signals and electronics noise are generated on the detector channels, and neighbouring channels above threshold are grouped into clusters.

In the digitization of the solid state detectors, the signal is taken to be proportional to the energy deposited by the particle in the semiconducting material, computed by GEANT. In the digitization of the MSGC's, the Monte Carlo program described in the previous chapter is used. The parameters of the simulation are tuned to the working conditions expected in CMS, as described in section 5.2.1. The version of the CMSIM program that we used is cms111, except for the pixel digitization and clusterization, for which the improved code of version 113 was imported. In order to study the performance of the tracker in the most realistic conditions, all simulations described in this chapter have been performed at the hit digitization and clusterization level.

5.2.1 Digitization of MSGC's in CMSIM

The MSGC Monte Carlo parameters are set to the values foreseen for CMS: the gas mixture is chosen to be DME-Ne 70%-30%, the gas gain is 2100, and the R.M.S. of the noise is set to 1600 e^- according to the specifications of the APV chip for a 10 pF strip capacitance. These conditions correspond to the beginning of the efficiency plateau, for ideal detectors equipped with the APV electronics and filled with that gas mixture. The strip threshold is set to 1.8×1600 e^- and the threshold on the cluster charge is 3.5×1600 e^-. These cuts provide a detection efficiency of 99% for MIP's crossing the detectors at small incident angle, a few degrees apart from the Lorentz angle in the barrel counters, or a few degrees from normal incidence in the forward counters. About 4% of the strips exhibit a noise pulse above the strip threshold. After application of the cluster threshold, 0.1 noise clusters remain per counter per event.

The time response of the APV chip is not simulated. The maximum drift time of a primary electron in the MSGC gas volume is about 55 ns. Convoluted with the 45 ns $RC - CR$ shaping of the APV, it results in a ballistic deficit of 0.7. This reduction factor is introduced in the simulation. Because of fluctuations in the position of the primary ionizations inside the drift space, the MSGC response also has a time jitter corresponding to maximum 2 LHC bunch crossings. This is simulated by piling up twice as many minimum bias events in MSGC's as in silicon strip and pixel detectors. The response of solid state detectors has a much smaller jitter, as all the charge is collected in a few nanoseconds.

Half the detection surface is equipped with double sided detectors, which are simulated as follows. The pitch of the stereo strips is twice the pitch of the $R\phi$ strips. The angle between the strips of the two sides is 50 mrad. The capacitance of the stereo strips is expected to be larger than the capacitance of the anode strips. The noise of the stereo strips is thus assumed to be 2000 e^-, and the signal is expected to decrease by a factor 0.8 as compared to the $R\phi$ side. Therefore the cluster threshold is relaxed to three times the noise, yielding 96% detection efficiency with 0.3 noise clusters per counter per event.

The conditions described above are a compromise between MSGC performance and long term stability, imposed by the performance of the detector components presently available. These conditions would lead to adequate detection efficiency and response speed if the counters were perfect. In real life, a detection efficiency as high as 99% together with an occupation time below 2 LHC bunch crossings is met only at twice higher signal to noise ratio. Several detector components are still being improved in order to reach the required performance in realistic experimental conditions. The use of substrates of better quality and ageing proof materials would allow to operate stably at higher gas gains. Faster gas mixtures, like DME-Ne-CO_2, would lead to faster charge collection, and thus smaller ballistic deficit, higher detection efficiency and smaller time jitter. An amplifier better suited to MSGC's than the present APV would exhibit less noise and less ballistic deficit. The results reported in the next sections should still be regarded as optimistic in the present status of the detector development.

5.2.2 Hit errors in MSGC's

A hit reconstructed in a module of the tracker is defined by its position and error matrix in the local coordinate system of the module. By convention, the local coordinate system (u, v, w) is orthogonal, with its origin at the centre of the counter. The u-axis is perpendicular to the substrate, and the v-axis runs along $R\phi$ at the centre of the module, as shown in figure 5.1. The w-axis is parallel to the beam in the barrel counters, and radial in the forward counters. In MSGC's, the position of the reconstructed hit (RHIT) is determined by the centre of gravity of the cluster formed with adjacent firing strips. Therefore, the natural coordinate system is the strip system, with its axes normal to the strip directions. Simple formulas allow the transformation of the position and error matrix of the reconstructed hit from the strip system to the (u, v, w) system and vice-versa. These formulas can be found in [98].

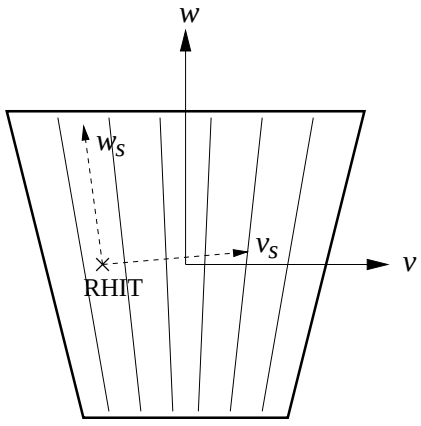

Figure 5.1: Forward single sided MSGC module. The axes (v, w) and (v_s, w_s) of the local and strip coordinate systems are shown.

In the case of single sided detectors, the $R\phi$ coordinate is precisely measured with an accuracy $\sigma_{R\phi}$, while the coordinate along the beam in the barrel or along the radius in the forward part is not measured. The convention is to place the reconstructed hit at the middle of the strips. The error matrix in the strip coordinate system reads:

$$V_{RHIT} = \begin{pmatrix} \sigma^2_{R\phi} & 0 \\ 0 & L^2/12 \end{pmatrix}, \tag{5.1}$$

where L is the detector striplength. In the case of double sided detectors, the error matrix can be written as:

$$V_{RHIT} = \begin{pmatrix} \sigma^2_{R\phi} & V_{12} \\ V_{12} & \sigma^2_{stereo} \end{pmatrix}, \tag{5.2}$$

where σ_{stereo} is the spatial resolution of the stereo side. The covariance term V_{12} is not zero, as will be shown later. In the following paragraphs, the behaviour of the resolutions $\sigma_{R\phi}$, σ_{stereo} and covariance V_{12} with the particle incident angles will be inspected.

Angular dependence of the resolution in the direction perpendicular to the strips

As shown in the previous chapters, the spatial resolution of the MSGC's degrades rapidly when the angle α between the normal to the substrate and the track projected on the plane perpendicular to the strips increases. Because of their bended trajectory, charged particles emerging from the interaction region traverse the counters at an angle α which increases with the distance R to the beam. Table 5.1 gives the values of the deviation from the Lorentz angle α_L as a function of R and of the particle transverse momentum p_T, in the barrel counters. At high p_T (above 20 GeV/c), the deviation is less than 2.2^o at all radii. For particles of $p_T = 1$ GeV/c, the outermost layer is crossed at an angle $|\alpha - \alpha_L|$ of about 50^o.

	R = 0.6 m	0.8 m	1.0 m	1.2 m
p_T = 1 GeV/c	21^o	29^o	37^o	46^o
2	10^o	14^o	17^o	21^o
5	4.1^o	5.5^o	6.9^o	8.3^o
10	2.1^o	2.7^o	3.4^o	4.1^o
20	1.0^o	1.4^o	1.7^o	2.1^o

Table 5.1: Angle of incidence $|\alpha - \alpha_L|$ in the barrel MSGC counters, as a function of the distance to the beam R and of the particle transverse momentum p_T.

Figure 5.2 shows the variation of the MSGC spatial resolution with α in the barrel and forward modules, for $R\phi$ and stereo strips. These results are obtained with the simulation of the MSGC response at the digitization level, in the conditions described in section 5.2.1. The clusters are formed with adjacent strips above threshold. The position of the reconstructed hit is defined as the centre of gravity of the cluster. The curves are slighlty asymmetric with respect to α_L in the barrel counters, and symmetric with respect to the normal to the substrate in the forward counters. The best spatial accuracy for the $R\phi$ side is about 30 μm, at $\alpha = \alpha_L = 14^o$ in the barrel and $\alpha = 0^o$ in the forward part. This result is compatible with the performance of an ideal MSGC of 200 μm readout pitch and 3 mm gas gap, but it is small compared to the 50 μm CMS target resolution per MSGC layer. This comes from the fact that the simulation does not include detector defects, like broken strips, dead electronic channels or mechanical misalignments between counters. The best accuracy for the stereo side is about 70 μm, which leads to a resolution in the w-coordinate of 1.2 mm for high p_T particles.

The spatial resolution at large α is 20% poorer than expected from previous experimental results [11, 95] and from the plots of chapter 4. This is due to the fact that no strip below threshold is accepted in a cluster. We have done so for two reasons. First, the signal to noise ratio in CMS conditions is small, and the number of strips carrying a noise pulse above threshold is large (about 20 per counter per event). The spatial resolution for high p_T particles

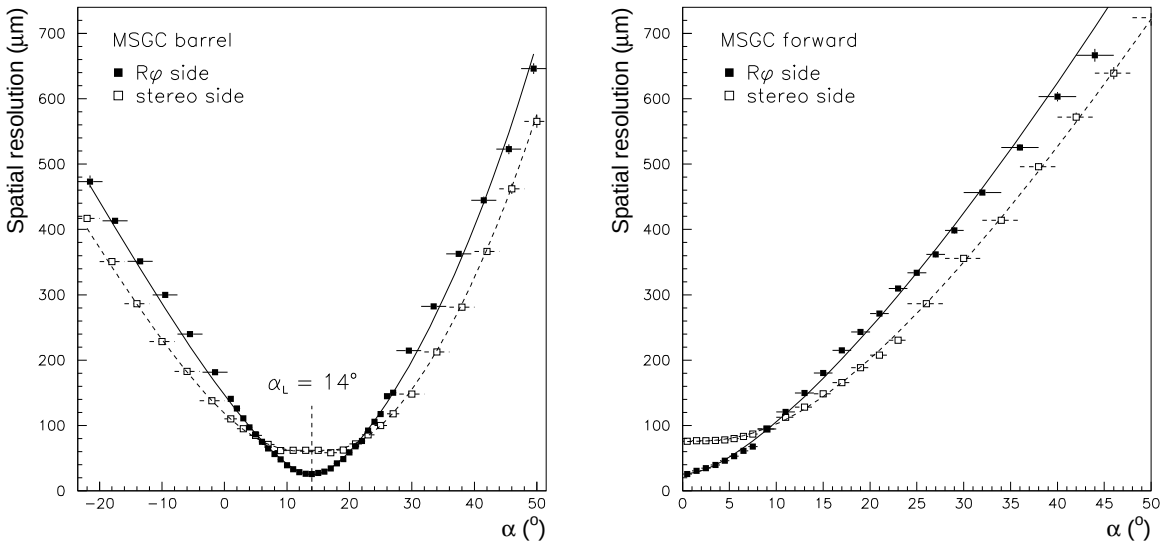

Figure 5.2: Spatial resolution of the MSGC's as a function of the angle of incidence α, from a simulation of the MSGC response at the digitization level in CMS conditions.

will probably be spoiled by noise if a large gap is accepted in a cluster. Second, at high luminosity, we want to avoid merging clusters produced by two different neighbouring tracks.

It should be noted that the worsening of the MSGC resolution with increasing α does not result in a degradation of the tracker momentum resolution, as for low p_T particles the error due to multiple scattering dominates. Formulas 2.13 and 2.15 indicate that for particles of $p_T = 1$ GeV/c the contribution to the momentum resolution due to the error on $R\phi$ would exceed the contribution due to multiple scattering only if the average $R\phi$ resolution would be larger than 1 - 2 mm.

The resolutions used in the track fitting algorithm must correspond to the angle at which the reconstructed track crosses the counter. A routine was thus written which computes the spatial resolution of the $R\phi$ and stereo sides as a function of α. No handy parametrization was found which described the results up to 50° apart from the Lorentz angle. As an example, the resolution of the $R\phi$ side of the barrel counters was parametrized as follows:

$$\sigma\ [\mu\mathrm{m}] = \begin{cases} 24.8\sqrt{1 + x^2(15.5 + 38.7|y| - 26.7y^2)^2} & \text{for } -0.61 < z \leq 0.72 \\ 228 - 620z + 1260z^2 & \text{for } z > 0.72 \\ 278 - 244z + 693z^2 & \text{for } z \leq -0.61 \end{cases} \tag{5.3}$$

with $x = \tan z - \tan \alpha_L$, $y = z - \alpha_L$, $z = \alpha$ in radians.

Angular dependence of the resolutions in the direction parallel to the strips

In the projection parallel to the strips, the angle β with respect to the normal to the substrate is limited to about 50°. This angle of incidence corresponds to the transition between the barrel and the forward part of the tracker for particles emerging from the interaction region. Only a 20% improvement in resolution is seen from $\beta = 0°$ to $\beta = 50°$, due to the increase of the number of primary electrons released above each strip in the detector. This effect can be neglected in the calculation of the hit errors.

Covariance of the reconstructed hits in double sided MSGC's

In double sided MSGC's, the positions of the clusters in the $R\phi$ and stereo sides are correlated. The correlation arises from the fact that the same avalanche is sampled by the two readout sides. If the electron cloud is displaced in one direction with respect to the particle impact, the centres of gravity of the reconstructed clusters are shifted in this direction in both sides.

Figure 5.3 shows the scatter plots of the residuals of the strip coordinates, in double sided barrel MSGC's. The plot to the left is for particles of incident angles $0^o < \alpha - \alpha_L < 3^o$, $\beta = 0^o$, and the plot to the right is for $40^o < \alpha < 50^o$, $45^o < \beta < 55^o$. The equation of the ellipses superimposed on the distributions is:

$$x^2 + y^2 = 1$$

where the variables x and y are defined by:

$$\begin{aligned} \text{residual } R\phi &= \sigma_{R\phi} x, \\ \text{residual stereo} &= \rho\sigma_{stereo} x + \sqrt{1-\rho^2}\sigma_{stereo} y, \\ \rho &= \frac{V_{12}}{\sigma_{R\phi}\sigma_{stereo}}, \end{aligned}$$

with ρ, the correlation coefficient of the strip coordinates. In the hypothesis that the residuals are distributed as two-dimensional Gaussians, the ellipses are equiprobability contours which delimitate a 39% confidence level zone.

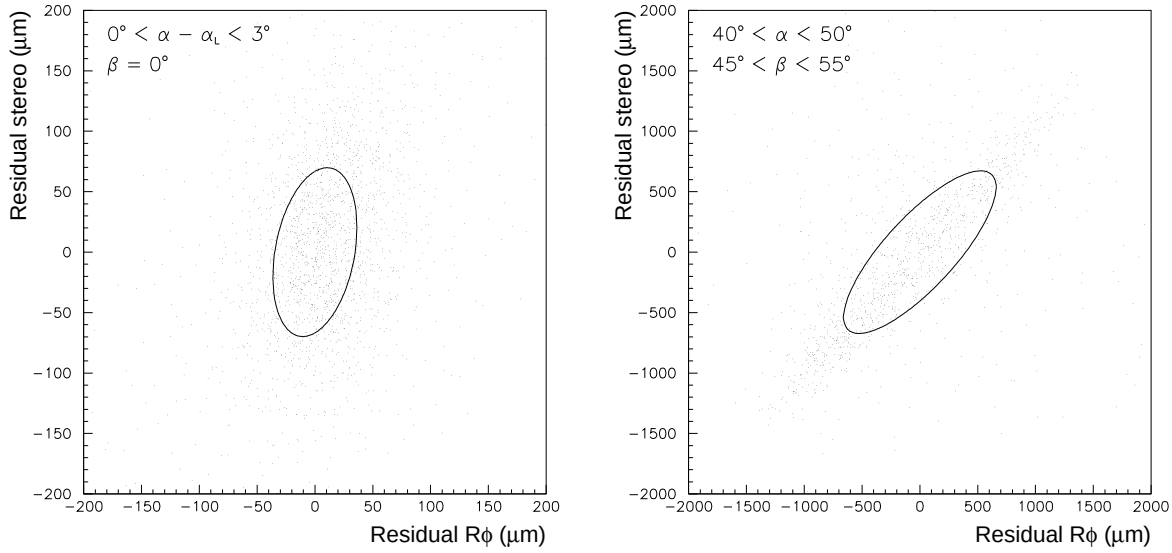

Figure 5.3: Scatter plots of the strip coordinate residuals in double sided barrel MSGC's, for $0^o < \alpha - \alpha_L < 3^o$, $\beta = 0^o$ (left) and $40^o < \alpha < 50^o$, $45^o < \beta < 55^o$ (right). The ellipses are equiprobability contours at 39% confidence level.

The correlation between the strip coordinates is visible from the orientation of the axes of the ellipses, which differ from the axes of the strip coordinate system. For the samples shown, the correlation coefficient ρ equals 0.29 (left plot) and 0.79 (right plot). The error matrix of the strip coordinates in double sided modules is thus not diagonal. Proper treatment of this effect would require to parametrize the correlation coefficient as a function of α and β. This was not

taken into account in the present study, and the strip coordinates are supposed independent in the reconstruction program. The effect of this approximation on the track fitting is discussed briefly in section 5.3.2.

5.2.3 Hit errors in silicon strip and pixel counters

The digitization of the silicon strip and pixel detectors leads to the following results. The average spatial resolutions in $R\phi$ are 14 μm in silicon barrel, 18 μm in silicon forward and 10 μm in pixel counters. In double sided detectors, the coordinate along the beam (along the radius in the forward tracker) is measured with an accuracy of 600 μm in silicon strip counters, 25 μm in pixel barrel and 80 μm in pixel forward modules. No correlation between the strip (pixel) coordinates appeared in the simulation results.

The spatial resolution in solid state detectors can be considered as being independent of the track incident angles. Indeed, these counters are thinner than the MSGC's, 300 μm instead of 3 mm, which reduces the spread of the ionization on the readout electrodes. Moreover, as the counters are close to the interaction region, the angular range is limited in α: up to 20° off Lorentz angle in silicon strip detectors, and 8° in pixel detectors, for particles of $p_T \geq 1$ GeV/c. Figure 5.4 shows the behaviour of the spatial accuracy in barrel solid state modules as a function of α. In barrel silicon strip counters, the resolution is comprised between 8 and 17 μm, with a peak at $\alpha = \alpha_L = 7°$ when all the charge is collected on 1 strip, and optima when the charge is shared by 2 strips. In barrel pixels, the resolution varies from 8 to 14 μm. The range in α is symmetric with respect to 0°, because the barrel pixel counters are not tilted. An asymmetry appears in the resolution curve.

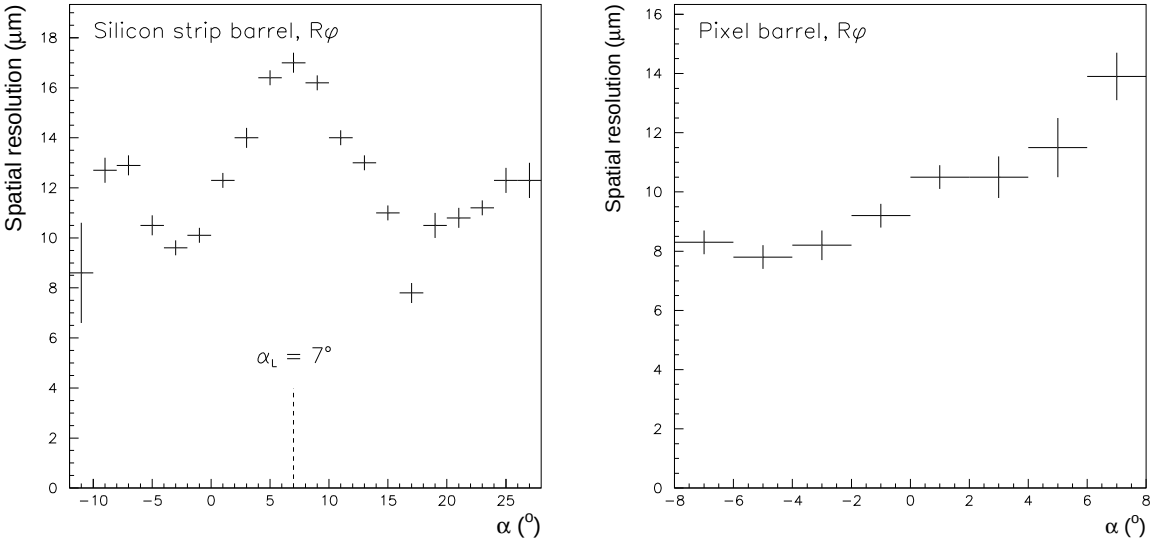

Figure 5.4: Spatial resolution as a function of the incident angle α, in barrel silicon strip and pixel detectors.

5.3 Track finding and fitting in CMS

The purpose of the tracking algorithm in CMS is to find high p_T tracks in a large number of hits, and to measure the track parameters at the vertex in order to study the kinematics of the

event. The first step consists in selecting track candidates, i.e. sets of hits which are likely to form a track. This preselection reduces the number of hit combinations that have to be tested at the track fitting stage, thus saving computation time. The second step consists in fitting a curved trajectory through the selected points, taking into account multiple scattering in the detector materials. It has been shown that recursive algorithms, progressing detection layer per detection layer, are well suited for this purpose. In particular, R. Frühwirth [99] demonstrated that the Kalman filter provides the proper theoretical framework for iterative track fitting in the presence of multiple scattering.

The package that we used for track reconstruction is the CMSIM Local Track Finder (LTF). It comprises a Kalman filter and a hit selector based on the Rigid Template method. The Rigid Template method is described in section 5.3.1. The formalism of the Kalman filter and its implementation in the Local Track Finder are explained in section 5.3.2. In section 5.3.3, we discuss the limitations of the Kalman filter, and how they can be overcome thanks to a method called smoothing.

5.3.1 The Rigid Template method

The Rigid Template method [100] performs hit selection by comparing the hit pattern with predefined three dimensional track roads or templates. A template consists of a list of detector modules or cells, which configuration in space is such that they could be crossed successively by a high p_T track (see figure 5.5). A template is considered as a valid track candidate if a sufficient number of cells contain a reconstructed hit. The LTF requires 3/4 of the cells to be hit, with a minimum of 5 cells.

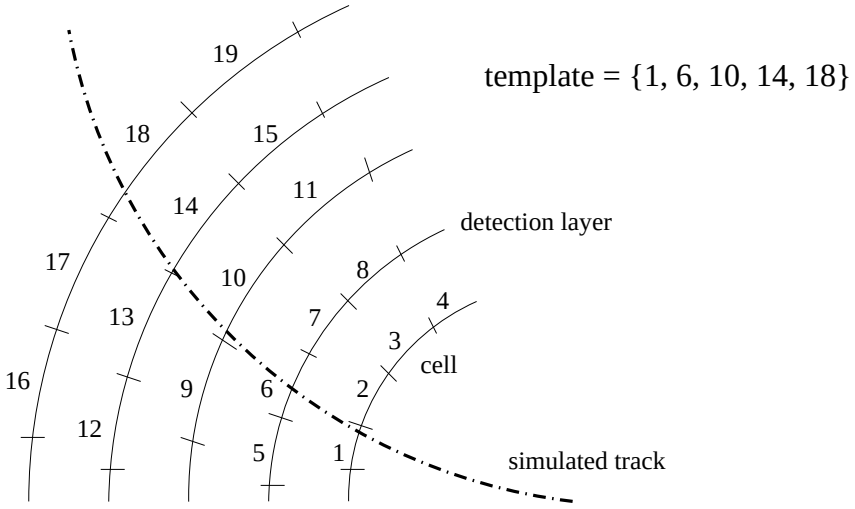

Figure 5.5: Making of a template.

A learning phase is needed in order to create the template data base. A large number of tracks with a direction chosen at random are simulated in order to find all possible cell combinations. A template is stored for each new combination. The template data base for tracks of $p_T \geq 1$ GeV/c requires 10 Gb memory, which renders the use of the Rigid Template method as such prohibitive. Therefore, in the LTF, only the templates which correspond to the tracks of the simulated event are produced. This is of course not possible with real events. However, in jet events, all counters inside the opening cone of the jet are hit. The LTF allows thus to test the reconstruction of tracks inside jets in realistic conditions, because the number

of hit combinations to be tested within the templates is of the same order as in the jet cone in real events.

A few other algorithms, that are able to reconstruct a full event, are tested in the CMS tracking group. These are still in the development phase.

5.3.2 The Kalman filter for track fitting

The Kalman filter is a recursive procedure which allows to estimate the parameters describing the state of a system from a set of measurements. It was introduced in 1960 in the framework of optimal signal filtering in linear systems. A detailed description of the Kalman filter technique can be found in many textbooks [101, 102]. We present here the main equations, following closely references [99] and [103], and focus on its application to track fitting.

The principle is the following. The filter proceeds iteratively, starting from a coarse estimate of the track parameters and including the information of the sucessive detection layers one by one. The track parameters estimated at a given detection layer are propagated to the next layer according to the equations of motion of the charged particle in the external magnetic field, taking into account energy loss in the detector material. Then the information of the hit coordinates measured at that layer is combined to the information of the propagated parameters to provide a new estimate, of better accuracy than the estimate at the previous layer. The weight to be attributed to the measurement and to the propagated parameters in the calculation of the updated parameters is a function of their respective errors. Best precision is reached when all measurements have been included in the estimation.

In the presence of a magnetic field, the trajectory of a particle can be defined at each detection layer by five independent parameters: for example, the particle momentum p, the polar angle complement λ, the azimuthal angle ϕ between the CMS x-axis and the track projected onto the transverse plane, and the two coordinates of the track crossing point in the detection plane. The angle λ is also called the dip angle, as it is the angle at which the track "dips" into the transverse plane. The parameters are grouped into a 5-component state vector, $\mathbf{x} = (p, \lambda, \phi, x, y)$.

Equations of the Kalman filter

Figure 5.6 shows the diagram of a linear system. The evolution of the state vector is described by a linear transformation $\mathbf{F}$ plus a random disturbance $\mathbf{w}$, called the process noise. If the state vector is measured at n points, we have the discrete relation:

$$\mathbf{x}_{k+1} = \mathbf{F}_k \mathbf{x}_k + \mathbf{w}_k, \; k = 1, ...n-1, \tag{5.4}$$

called the evolution equation of the system. The state vector is in general not observed directly. The actual measurements $\mathbf{m}_k$ are linear functions of the state vector such that:

$$\mathbf{m}_k = \mathbf{H}_k \mathbf{x}_k + \boldsymbol{\epsilon}_k, \tag{5.5}$$

where $\boldsymbol{\epsilon}_k$ is the measurement error at point k. By assumption all $\mathbf{w}_k$ and $\boldsymbol{\epsilon}_k$ are independent and have a zero mean value. Their covariance matrices are denoted $\mathbf{Q}_k$ and $\mathbf{V}_k$ respectively. The Kalman filter is the optimal recursive estimator of the state vector of such a system, in the sense that it is unbiased and of minimum variance.

Figure 5.7 shows the interpretation of the above quantities in the framework of tracking. The indices k correspond to the detection layers crossed by the particle, and $\mathbf{x}_k$ is the vector of the track parameters at layer k. The track perturbation between layers k and $k+1$, $\mathbf{w}_k$,

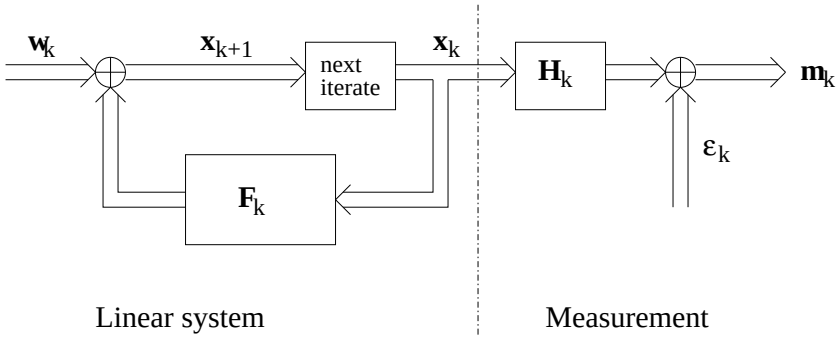

Figure 5.6: Diagram of a linear system.

originates from multiple scattering in the detector material. The detector elements measure the coordinates $\mathbf{m}_k$ of the track crossing points. $\boldsymbol{\epsilon}_k$ is thus a two-component vector representing the residuals of the reconstructed coordinates with respect to the coordinates of the simulated hit. The covariance matrix of the measurement, $\mathbf{V}_k$, corresponds to the hit error matrix defined in section 5.2.2. In a well chosen coordinate system, the matrix $\mathbf{H}_k$ reads:

$$\mathbf{H}_k = \begin{pmatrix} 0 & 0 & 0 & 1 & 0 \\ 0 & 0 & 0 & 0 & 1 \end{pmatrix} \tag{5.6}$$

By solving the equations of motion, the average track parameters at layer $k+1$ can be computed exactly knowing the track parameters at layer k:

$$\mathbf{x}_{k+1} = \mathbf{f}_k(\mathbf{x}_k). \tag{5.7}$$

This operation is called the extrapolation of the track parameters from layer k to layer $k+1$. It is performed by following the particle step by step, taking into account the average energy loss in the detector materials. In contrast with equation 5.4, the track propagator $\mathbf{f}$ is non-linear. In order to apply the concepts of linear filtering to track fitting, the Taylor expansion of the transformation is computed to the first order:

$$f_k(\mathbf{x}_k + \boldsymbol{\Delta}_k) = \mathbf{f}_k(\mathbf{x}_k) + \mathbf{F}_k\boldsymbol{\Delta}_k + \mathcal{O}(\boldsymbol{\Delta}_k^2), \tag{5.8}$$

$$\mathbf{F}_k = \partial\mathbf{f}_k(\mathbf{x}_k)/\partial\mathbf{x}_k. \tag{5.9}$$

This procedure is called an extended Kalman filter. It constitutes the optimal linear estimator of the state vector.

Let us now define the predicted estimate or prediction $\mathbf{x}_k^{k-1}$ as the best estimate of the state vector $\mathbf{x}_k$ at layer k using all measurements up to layer $k-1$. The filtered estimate $\mathbf{x}_k^k$ will be defined as the best estimate using all measurements including the k^{th} measurement. Knowing the filtered estimate $\mathbf{x}_{k-1}^{k-1}$ at layer $k-1$, the prediction at layer k is simply the extrapolation of the filtered estimate at layer $k-1$:

$$\mathbf{x}_k^{k-1} = \mathbf{f}_{k-1}(\mathbf{x}_{k-1}^{k-1}). \tag{5.10}$$

The covariance matrix of the prediction, $\mathbf{C}_k^{k-1}$, is computed by applying the transformation $\mathbf{F}_{k-1}$ to the covariance matrix of the filtered estimate at layer $k-1$, and adding the contribution of multiple scattering:

$$\mathbf{C}_k^{k-1} = \mathbf{F}_{k-1}\mathbf{C}_{k-1}^{k-1}\mathbf{F}_{k-1}^{\mathrm{T}} + \mathbf{Q}_{k-1}, \tag{5.11}$$

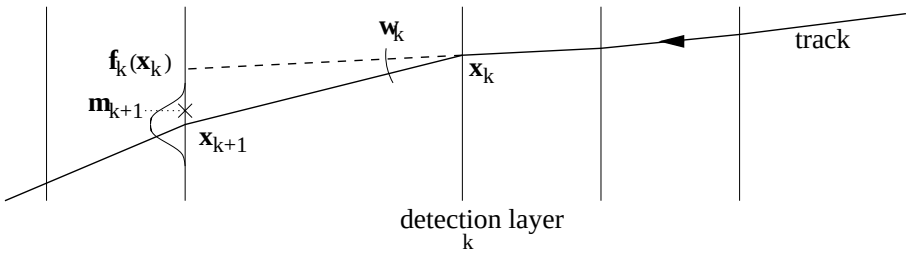

Figure 5.7: Iterative track fitting with the Kalman filter. $\mathbf{x}_k$ is the vector of track parameters at layer k, $\mathbf{f}_k(\mathbf{x}_k)$ are the parameters extrapolated to the next layer, $\mathbf{w}_k$ is the track perturbation due to multiple scattering, and $\mathbf{m}_{k+1}$ is the measurement of the track crossing point performed at layer $k+1$, equal to the hit position plus a normally distributed error.

where $\mathbf{F}_{k-1}^{\mathrm{T}}$ denotes the transpose of $\mathbf{F}_{k-1}$.

We shall now try to find a recursion formula for the filtered state vector. The filtered estimate at layer k is chosen to be a linear combination of the prediction and the measurement at this layer:

$$\mathbf{x}_k^k = \mathbf{M}_k \mathbf{x}_k^{k-1} + \mathbf{N}_k \mathbf{m}_k. \tag{5.12}$$

Requiring $\mathbf{x}_k^k$ to be unbiased leads to the form:

$$\mathbf{x}_k^k = \mathbf{x}_k^{k-1} + \mathbf{K}_k(\mathbf{m}_k - \mathbf{H}_k \mathbf{x}_k^{k-1}), \tag{5.13}$$

where $\mathbf{K}_k$ is called the Kalman gain matrix. The second term of equation 5.13 represents the correction to be applied to the predicted state to obtain the filtered state. This correction is proportional to the difference between the measurement and the prediction, multiplied by the gain matrix. Further, $\mathbf{M}_k = (\mathbf{I} - \mathbf{K}_k\mathbf{H}_k)$ and $\mathbf{N}_k = \mathbf{K}_k$. As the error on the measurement and the error on the prediction are independent, the covariance matrix of the filtered state is:

$$\mathbf{C}_k^k = (\mathbf{I} - \mathbf{K}_k\mathbf{H}_k)\mathbf{C}_k^{k-1}(\mathbf{I} - \mathbf{K}_k\mathbf{H}_k)^{\mathrm{T}} + \mathbf{K}_k\mathbf{V}_k\mathbf{K}_k^{\mathrm{T}}. \tag{5.14}$$

The criterion imposed to determine $\mathbf{K}_k$ is to minimize the sum of the squares of the standard deviations of the filtered parameters:

$$\frac{\partial \mathrm{Tr}(\mathbf{C}_k^k)}{\partial \mathbf{K}_k} = 0, \tag{5.15}$$

where Tr denotes the trace operation. Solving for $\mathbf{K}_k$ yields:

$$\mathbf{K}_k = \mathbf{C}_k^{k-1}\mathbf{H}_k^{\mathrm{T}}(\mathbf{V}_k + \mathbf{H}_k\mathbf{C}_k^{k-1}\mathbf{H}_k^{\mathrm{T}})^{-1} \tag{5.16}$$

$$= \mathbf{C}_k^k\mathbf{H}_k^{\mathrm{T}}\mathbf{V}_k^{-1}. \tag{5.17}$$

The closeness of the measurement and the fitted parameters can be evaluated by the residuals of the prediction:

$$\mathbf{r}_k^{k-1} = \mathbf{m}_k - \mathbf{H}_k\mathbf{x}_k^{k-1}. \tag{5.18}$$

The covariance of the predicted residuals is clearly:

$$\mathbf{R}_k^{k-1} = \mathbf{V}_k + \mathbf{H}_k\mathbf{C}_k^{k-1}\mathbf{H}_k^{\mathrm{T}}, \tag{5.19}$$

and, if the errors are Gaussian, the variable

$$\chi^2_P = \mathbf{r}_k^{k-1\mathrm{T}} (\mathbf{R}_k^{k-1})^{-1} \mathbf{r}_k^{k-1} \tag{5.20}$$

is χ^2-distributed with m degrees of freedom, m being the dimension of the measurement vector. It can be shown that the χ^2 formed with the filtered residuals is equal to the χ^2 formed with the predicted residuals:

$$\mathbf{r}_k^k = \mathbf{m}_k - \mathbf{H}_k \mathbf{x}_k^k, \tag{5.21}$$

$$\chi^2_F = \mathbf{r}_k^{k\mathrm{T}} (\mathbf{R}_k^k)^{-1} \mathbf{r}_k^k = \chi^2_P, \tag{5.22}$$

with the following expression for the covariance of the filtered residuals:

$$\mathbf{R}_k^k = \mathbf{V}_k - \mathbf{H}_k \mathbf{C}_k^k \mathbf{H}_k^{\mathrm{T}}. \tag{5.23}$$

These equations correspond to the gain matrix formalism of the Kalman filter. An equivalent solution, of easier interpretation, is the weighted means formalism, where the filtered estimate is computed as the average between the prediction and the measurement, weighted by the inverse of their errors. It requires the inversion of the 5×5 covariance matrix of the state vector, while the gain matrix method requires the inversion of $m \times m$ matrices. Therefore, when the size of the state vector is larger than the size of the measurement vectors, the gain matrix formalism is usually preferred.

The filtered χ^2 provides a means to test the quality of the association of a hit to a track. In the detectors which measure two coordinates, χ^2_F is $\chi^2(2)$-distributed, and a cut at $\chi^2_{0.99} = 9.21$ keeps 99% of the hits belonging to the track. Thus, hit selection and track fitting are performed detection layer per detection layer, improving the determination of the track parameters with each hit included in the track. Optimal precision is reached after using the information of the n detection layers. Therefore, in order to determine the kinematics of the event at the vertex with optimal accuracy, the filter algorithm proceeds from the tracker outer layers towards the interaction region.

Implementation of the Kalman filter in the Local Track Finder

The propagation of the track parameters and covariance matrix between two detection layers is performed thanks to the GEANE package [104], interfaced with the GEANT description of the tracker geometry. This program also provides the covariance matrices of the multiple Coulomb scattering, $\mathbf{Q}_k$, and the matrices of the linearized transformations, $\mathbf{F}_k$.

The filtering needs to be started with initial values of the state vector and covariance matrix. In the LTF, the initial state vector is obtained by determining a helix on three starting points. Two of the points are chosen among the reconstructed hits of the selected template, and the third point is $(0, 0, z)$, with the z-coordinate left free. In order to obtain a good initial estimate of the track momentum, the first point is chosen in one the two outer cells of the template, and the second point is taken in one of the two mid layers. This method is not a fit, as there are no degrees of freedom: 8 coordinates are used to determine 5 track parameters in a 3-dimensional space. Therefore it does not allow to estimate the errors on the initial state vector. The covariance matrix is initialized with large errors on p, λ and ϕ, about ten times the tracker nominal resolutions, so that the initial values of these parameters get a low weight in the subsequent estimations of the state vector. The initial error matrix of (x, y) is taken as the covariance matrix of the outer starting reconstructed hit.

In each layer, the reconstructed hit closest to the prediction in $R\phi$ is selected. As measurement errors, the values of spatial resolution derived from the detector simulation at the

digitization level are used (see section 5.2). In MSGC's, the hit error is computed at each layer as a function of the predicted value of the incident angle α. If the scattering and hit reconstruction errors are correctly estimated, the filtered chi-squared should be distributed as a $\chi^2(2)$ distribution. As shown in figure 5.8 a), the agreement between the observed and theoretical distributions is poor, for several reasons:

1. at the first three layers of the fit, the knowledge of the state vector covariance matrix is bad. A track segment of four points is required in order to have an estimation of the covariance matrix;

2. half of the detector elements are single sided. The distribution of the residuals of the second coordinate is not Gaussian but uniform;

3. in double sided MSGC's, the correlation between the strip coordinates is not taken into account;

4. there are non-Gaussian tails in the distributions of the residuals of the measured coordinates and of the scattering angles.

The χ^2 cut is tuned so as to reach a track finding efficiency above 97% for single tracks of $p_T \geq 1$ GeV/c in the covered range of η. The cut value is 20.

The filter algorithm is applied to several combinations of starting points inside each template, with a maximum of eight combinations. This allows to find tracks of different particles inside a template, and to choose the best starting combination for each of them. Template cells without a suitable hit are skipped. When four layers had to be left aside, the LTF tries to drop one of the previous retained hits, starting from the latest that has been included. The filter is recomputed from this level on. The tracking stops for a given starting combination when it is not possible to reach the innermost template cell without losing four points or more. Tracks with less than 5 hits are discarded. Eventually, tracks sharing a majority of hits are considered as duplicates, and the shortest one is removed.

5.3.3 Smoothing

In the filtering process, the state vector is known with optimal precision only after the last measurement has been included in the fit. This has some important drawbacks in track reconstruction:

- in the first steps of the filter, the prediction accuracy is poor, and the χ^2 test has a low rejection power for outliers, i.e. hits that do not belong to the track;

- a filter starting from the tracker outer layers yields precise track parameters at the vertex. However one often has to match a track with a calorimeter shower or a muon chamber track segment, reconstructed in an outer detector. This can be done by extrapolating the track parameters from the vertex outwards, but a simple extrapolation is not accurate in the presence of scattering, like for example in the case of a kinked track;

- optimal precision of the estimation of the particle crossing points is desireable at any detection layer of the tracker, to allow precise interalignment of the tracker elements.

For these reasons it is necessary to find an estimator of the track parameters which is optimal all along the particle track. This is called the smoothing problem.

Equations of the smoother

A possible solution to the smoothing problem is to iterate backwards, starting from the filtered estimate at the vertex, and to correct the filtered estimates layer per layer. The smoothed estimate $\mathbf{x}_k^n$ at layer k is calculated as the filtered estimate at that layer plus a correction, proportional to the difference between the smoothed estimate and the prediction at layer $k+1$:

$$\mathbf{x}_k^n = \mathbf{x}_k^k + \mathbf{A}_k(\mathbf{x}_{k+1}^n - \mathbf{x}_{k+1}^k). \tag{5.24}$$

The details of the derivation can be found in reference [102]. The smoother gain matrix $\mathbf{A}_k$ is given by:

$$\mathbf{A}_k = \mathbf{C}_k^k \mathbf{F}_k^{\mathrm{T}} (\mathbf{C}_{k+1}^k)^{-1}. \tag{5.25}$$

The covariance of the smoothed state, the smoothed residuals and the covariance of the smoothed residuals are expressed as:

$$\mathbf{C}_k^n = \mathbf{C}_k^k + \mathbf{A}_k(\mathbf{C}_{k+1}^n - \mathbf{C}_{k+1}^k)\mathbf{A}_k^{\mathrm{T}}, \tag{5.26}$$

$$\mathbf{r}_k^n = \mathbf{m}_k - \mathbf{H}_k \mathbf{x}_k^n, \tag{5.27}$$

$$\mathbf{R}_k^n = \mathbf{V}_k - \mathbf{H}_k \mathbf{C}_k^n \mathbf{H}_k^{\mathrm{T}}. \tag{5.28}$$

If the intermediate covariance and transformation matrices have been stored at the filtering stage, smoothing only involves a few matrix multiplications, and is thus very fast.

It can be shown [99] that the smoothed chi-squared $\chi_S^2 = \mathbf{r}_k^{n\mathrm{T}} (\mathbf{R}_k^n)^{-1} \mathbf{r}_k^n$ formed with the smoothed residuals is more sensitive to wrong hit associations than the filtered chi-squared. When a hit is rejected at the smoothing stage, it can be removed from the fit by an "inverse" Kalman filter:

$$\mathbf{x}_k^{n*} = \mathbf{x}_k^n + \mathbf{K}_k^{n*}(\mathbf{m}_k - \mathbf{H}_k \mathbf{x}_k^n), \tag{5.29}$$

$$\mathbf{K}_k^{n*} = \mathbf{C}_k^n \mathbf{H}_k^{\mathrm{T}} (-\mathbf{V}_k + \mathbf{H}_k \mathbf{C}_k^n \mathbf{H}_k^{\mathrm{T}})^{-1}, \tag{5.30}$$

$$\mathbf{C}_k^{n*} = (\mathbf{I} - \mathbf{K}_k^{n*}\mathbf{H}_k)\mathbf{C}_k^n (\mathbf{I} - \mathbf{K}_k^{n*}\mathbf{H}_k)^{\mathrm{T}} - \mathbf{K}_k^{n*}\mathbf{V}_k\mathbf{K}_k^{n*\mathrm{T}}. \tag{5.31}$$

Formally, this is a step of the filter where the contribution of the rejected measurement is removed from the smoothed estimate by using the hit error matrix with a minus sign. The estimate $\mathbf{x}_k^{n*}$ obtained uses the information of all measurements except $\mathbf{m}_k$. Smoothing may be continued with $\mathbf{x}_k^{n*}$ and $\mathbf{C}_k^{n*}$ instead of $\mathbf{x}_k^n$ and $\mathbf{C}_k^n$, and the estimates $\mathbf{x}_j^n$ with $j < k$ will not be biased by the rejected hit anymore. In the same spirit, when a hit could not be used at layer k at the filtering stage, it can still be included at smoothing, by a normal step of the filter.

However it should be noted that, as the smoothing algorithm proceeds from the vertex outwards, the track parameters at layers $j > k$ and at the vertex will not improve. If the whole track has to be updated, the filter has to be recomputed from layer k inwards, followed by smoothing back over the whole track.

Improvement of the track reconstruction by smoothing

We have implemented the above equations of the smoother in the LTF. To check the improvement of the fit, we have plotted the χ_S^2 distributions in silicon strip and pixel detectors. Figure 5.8 b) and c) show the distributions in double sided and single sided counters. On plot b), a $\chi^2(2)$ curve is superimposed on the distribution. On plot c), the dashed histogram shows the χ^2 distribution expected when one coordinate is normally distributed and the other one is uniform. The agreement between the observed and expected distributions is satisfactory,

although the observed distributions have longer tails due to the non-Gaussian tails of the hit residuals and of the scattering angles. We have also compared the number of crossing points along the track of high p_T particles (p_T = 20 GeV/c) to the number of hits fitted by the filter and by the smoother. On an average of 13.3 simulated hits, the filter keeps 96% of the hits, while the smoother retains 99% of them, with the same χ^2 cut at 20.

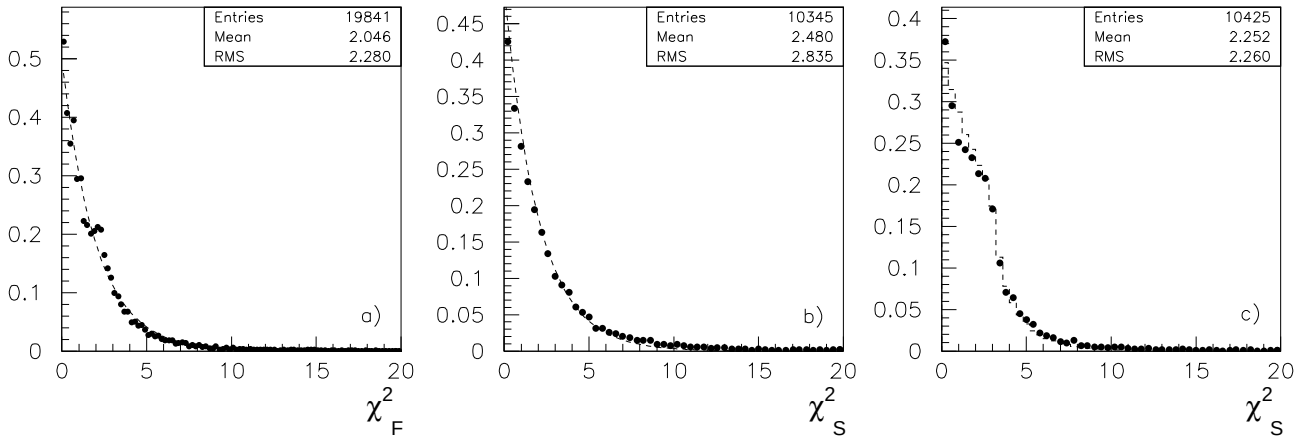

Figure 5.8: a) Distribution of χ^2_F in solid state detectors. Distributions of χ^2_S in double sided (b) and single sided (c) solid state detectors. The dashed curves show the expected theoretical distributions.

Figure 5.9 shows the distribution of the number of outliers in a reconstructed track, after filtering and after smoothing, in b-jet events with pile-up corresponding to full LHC luminosity. The fraction of incorrectly associated hits is already as low as 0.6% at filtering. This shows that the hit density in jets is still low enough, so that the Kalman filter is able to select the hits belonging to a given track. It also indicates that the measurement of the track parameters will not be affected much by outliers. As expected, the test on the smoothed chi-squared allows to reject more outliers with the same χ^2 cut, reducing the fraction of incorrect hit associations down to 0.4%.

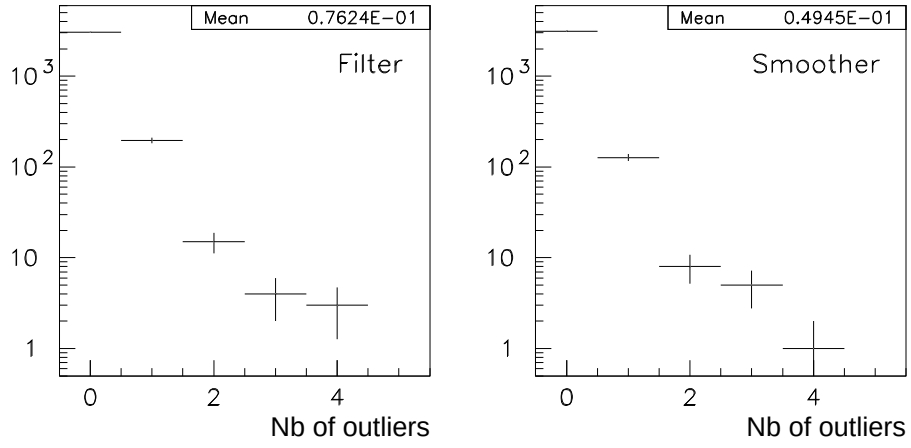

Figure 5.9: Distributions of the number of outliers after filtering and after smoothing, in reconstructed tracks from b-jet events with pile-up corresponding to the full LHC luminosity.

To understand the behaviour of the various track parameter estimators, we have simulated 1000 muons of transverse momentum equal to 5 GeV/c, passing through the forward pixel and silicon strip detectors at $\eta = 2.25$. We have chosen particles of not too high momentum, so that the effect of multiple scattering is still sizeable as compared to the resolution of the detectors. We have compared the track parameters provided by the filter, the smoother and by extrapolation of the parameters from the vertex outwards, to the simulated values at each detection layer.

Figure 5.10 a) shows the R.M.S. of the residual of the momentum as a function of z. The filter starts from the outer layer with a precise estimate of p, given by the initial helix. In the next few steps, the precision of the filtered estimate degrades, because the initial covariance matrix is arbitrary, and so the algorithm does not weight properly the prediction and the measurement. Then, the estimation improves, with best accuracy reached at the innermost detection layer. The smoothed estimate is of constant precision, which shows that the smoother uses at any detection layer the information of all measurements. The curves of momentum resolution for the smoother and for the extrapolation are almost superimposed: in estimating p, extrapolation is almost as good as smoothing. This is because the statistical process which affects the muon momentum, i.e. energy loss, has small fluctuations as compared to the tracker momentum resolution (less than 100 MeV as compared to 300 MeV in this particular case).

Figures 5.10 b) and c) show the same curves for the angles λ and ϕ. Similar comments as for the momentum resolution can be made. The first filtered estimates of λ and ϕ are very unprecise as compared to the estimates at the vertex, particularly in the case of λ. The reason is that at least two stereo hits must be included in the track to determine the track angles accurately. Considering only two detection planes, the accuracy in the dip angle is of the order of the detector spatial resolution in R divided by the distance in z between the detectors, i.e. 50 mrad with two single sided counters, and 0.1 mrad with two double sided counters. The extrapolated track angles are unprecise to about 0.1 mrad at the outermost layer as compared to the smoothed values, due to multiple scattering.

Figure 5.10 d) shows the R.M.S. of the distance in $R\phi$ between the estimated track crossing point and the reconstructed hit. The filtered residuals are the smallest. At filtering, the track is "pulled" towards the measurements: as the error on the predicted state is large, the measurement gets a larger weight in the calculation of the filtered state. At smoothing, the accuracy in $R\phi$ matches the detector resolution. Here we clearly gain in using the smoothing algorithm, because the extrapolated value of $R\phi$ is unprecise to about 100 μm at $z = 240$ cm, due to multiple scattering.

5.3.4 Conclusions of the study of the tracking algorithms

From the study of the tracking algorithms it can be concluded that the Kalman filter is an adequate method to select hits and to fit tracks of charged particles in CMS. It finds 96% of the hits along tracks of high p_T muons. In a dense track environment, like b-jets at high LHC luminosity, the fraction of hits incorrectly associated is only 0.6%. The filter thus provides a precise estimation of the track parameters at the vertex.

In order to obtain a precise estimation of the track parameters in detectors located further outwards, the smoothing algorithm is required. For muons of 20 GeV/c momentum, the accuracy of the smoothed state in $R\phi$ is about 10 μm everywhere along the track. Simple extrapolation of the filtered parameters at the vertex would be unprecise to about 100 μm at the outermost tracker layer, due to multiple scattering. The smoother is also more powerful than the filter in selecting hits. The fraction of hits found is 99%, with a fraction of outliers of 0.4% in b-jet events at high luminosity.

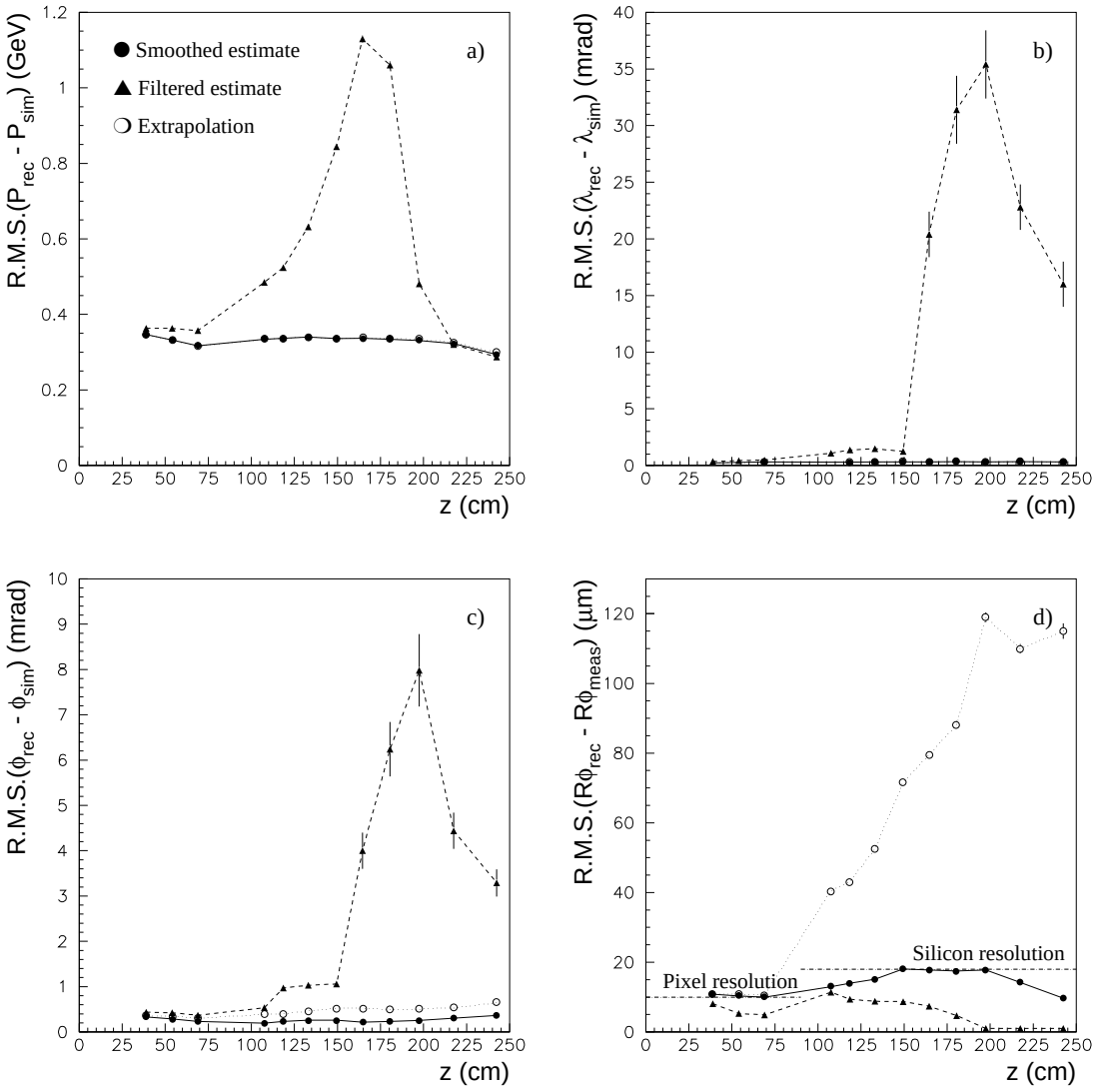

Figure 5.10: Precision of the estimations of the track parameters p, λ, ϕ and $R\phi$, as a function of z, for simulated muons of $p_T = 5$ GeV/c traversing the tracker at $\eta = 2.25$.

The improvement of the track fitting reached by smoothing has been clearly demonstrated. However, as the smoother proceeds from the vertex outwards, it does not improve the estimation of the track parameters at the vertex when an outlier is detected or when a new hit is included. This could be done by a second pass of the filter, starting from the updated detection layer inwards.

5.4 Performance of the CMS tracker

New physics shows up at LHC in two typical event topologies: final states with several isolated leptons, like in the channel $H \rightarrow ZZ^* \rightarrow 4l^{\pm}$, or multijet events, like in heavy flavour physics. The requirements for tracker performance differ in the two cases. To reconstruct the first kind of events, a very high track finding efficiency for isolated tracks is required, in order to find all leptons. The design requirement is a track finding efficiency of 95% in the accepted range of pseudorapidity. In jet events, one often tries to reconstruct a secondary vertex, which requires at least two tracks of the jet to be reconstructed. Lepton isolation tests, as well as the rejection of the background of jets faking isolated leptons, also benefit from a high track finding efficiency inside jets. However, jet events are supposed to be much more demanding on pattern recognition, because of the large number of hit combinations to be tested inside the jet cone. The track finding efficiency requirement is thus relaxed to 90% for tracks within jets.

As a consequence, the tracker performance is usually studied separately for isolated tracks and for jets. Single muons and jets have been simulated with CMSIM and reconstructed with the Local Track Finder. In this section we consider jets produced by the channel $t\bar{t} \rightarrow W^+W^-b\bar{b}$, one of the processes studied in chapter 6 concerning b-tagging. A sample of 900 such events is analysed. The transverse energy of both b-jets is required to exceed 20 GeV, because the reconstruction efficiency of jets in the hadron calorimeter is expected to drop below this value. The simulation of jet events includes a pile-up of 25 minimum bias events on average in solid state detectors and 50 in MSGC's, corresponding to the full LHC luminosity.

5.4.1 Analysis of the reconstructed tracks

After event reconstruction, CMSIM provides a list of simulated and reconstructed tracks with their parameters. In the case of a simulated track, the parameters are given at the vertex where the particle was produced. In the case of a reconstructed track, they are given at the point of closest approach to the beam. In order to compare the simulated and the reconstructed parameters, our analysis program first extrapolates the simulated tracks to the point of closest approach to the beam.

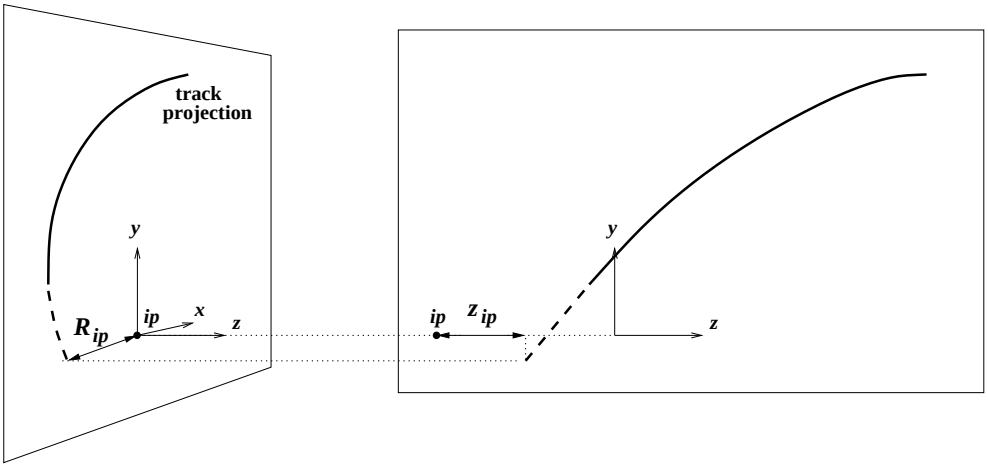

Figure 5.11: Definition of the transverse and longitudinal impact parameters R_{ip} and z_{ip} with respect to the proton interaction point ip.

Apart from the track momentum, dip and azimuthal angles, the most useful track param-

eters for b-tagging studies are the impact parameters with respect to the vertex of the initial proton-proton collision. In general, the transverse impact parameter with respect to a given vertex is defined as the distance of closest approach to that vertex in the transverse plane. The point of closest approach in the transverse plane is called the impact point with respect to that vertex. The transverse impact parameter has a sign: for positively charged particles, it is negative when the vertex is inside the trajectory circle and positive when it is outside, and the opposite for negatively charged particles.

Figure 5.11 illustrates these definitions in the case where the vertex considered is the primary vertex. The transverse impact parameter R_{ip} can be estimated as the distance of closest approach to the beam centre, because the beam transverse dimensions at the interaction point are very small, 15 μm R.M.S. The longitudinal impact parameter, z_{ip}, is the distance in z between the impact point and the primary vertex. As the proton-proton interactions are distributed along the beam axis with a standard deviation of 5.3 cm, the longitudinal impact parameter cannot be estimated without reconstruction of the primary vertex.

Track finding efficiency

The analysis program associates each reconstructed track to the particle which produced most of the hits used in the fit. The ratio of the number of hits used in the fit that have actually been generated by that particle to the total number of hits included in the track is called the hit purity. It is equal to 1 minus the fraction of outliers. Reconstructed tracks with a hit purity lower or equal to 0.5 are rejected.

Then, the quality of the reconstruction is checked with the pulls of the track parameters:

$$Pull(x_i) = \frac{x_i^{rec} - x_i^{sim}}{\sigma(x_i^{rec})}. \tag{5.32}$$

Here x_i^{sim} and x_i^{rec} are the simulated and fitted values of the i^{th} track parameter. The error $\sigma(x_i^{rec})$ is the error on the fitted parameter, i.e. the square root of the corresponding diagonal element of the parameters covariance matrix. Figure 5.12 shows the distributions of the pulls of $1/p$, λ, ϕ, R_{ip} and z_{ip}, for tracks in b-jets. The average values are compatible with zero, showing that the reconstructed parameters are unbiased. The standard deviations of the Gaussian curves fitted to the central part of the distributions are close to 1, indicating that the covariance matrix of the track parameters is correctly estimated. However the distributions exhibit non-Gaussian tails. These are due to reconstruction errors, like the presence of outliers in the tracks, or to physical effects not taken into account in the estimation of the track parameter errors, like non-Gaussian detector residuals or non-Gaussian scattering tails. These effects will be examined in more details further in the text.

A simulated track is considered as found if at least one reconstructed track of purity higher than 0.5 could be associated to it, and if four out of the five track parameter pulls are within the interval $[-5;+5]$. Simulated tracks which traverse less than 6 detection layers are not considered in the estimation of the track finding efficiency.

Ghosts

If more than one reconstructed track satisfies the criteria defined above, the one with the largest number of hits produced by the associated particle is selected. The other tracks are duplicates, and must therefore be regarded as ghosts generated by the track finding algorithm. Tracks with a hit purity below 0.5 are random associations of hits due to different particles, and are thus also counted as ghosts.

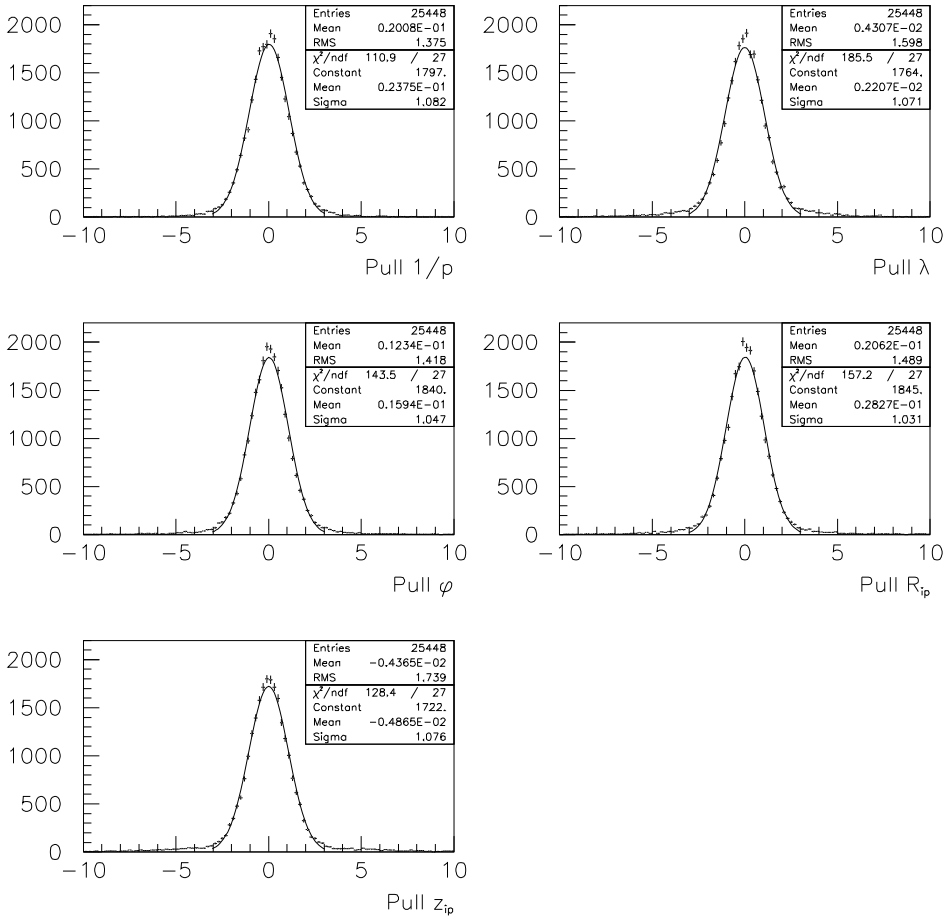

Figure 5.12: Distributions of the pulls of the track parameters $1/p$, λ, ϕ, R_{ip} and z_{ip}, for tracks in b-jets.

Track parameter resolutions

The resolution of a track parameter is estimated as the standard deviation of the Gaussian curve fitted to the distribution of the difference between the reconstructed and the simulated values. The track parameter resolutions are estimated with isolated muon tracks and compared to the results quoted in the Technical Proposal.

5.4.2 Isolated tracks

Track finding efficiency

Table 5.2 gives the track finding efficiency for isolated muons of transverse momentum above 1 GeV/c, at different pseudorapidities between 0 and 2.6. The track finding efficiency is higher than 97% at all transverse momenta and all covered pseudorapidities, with a minimum at $p_T = 1$ GeV/c, $\eta = 0$. This minimum is due to the relatively low detection efficiency of the micro-strip gas counters at large angle of incidence in the projection perpendicular to the strips. The detection efficiency corresponding to the angle at which 1 GeV/c p_T particles cross the first (last) MSGC layer is 96% (92%). This low efficiency is due to the small number of primary

electrons collected per strip. About 3% of the tracks are not reconstructed by the Local Track Finder, which tolerates maximum 3 inefficient layers in total. When η increases, the particle path inside the gas column above each MSGC strip is longer, which leads to an improvement of detection and track finding efficiency.

p_T [GeV/c]	$\eta = 0$	0.7	1.3	1.8	2.25	2.6
1	97%	98%	99%	99%	99%	99%
2	98%	98%	99%	99%	99%	99%
≥ 5	99%	99%	99%	99%	99%	99%

Table 5.2: Track finding efficiency for isolated muons of $p_T \geq 1$ GeV/c, in the pseudorapidity range $0 \leq |\eta| \leq 2.6$. The statistical errors are below 0.5%.

Track parameter resolutions

Figure 5.13 shows the momentum resolution $\Delta p/p$ of isolated muons as a function of the transverse momentum, at three pseudorapidity values ($\eta = 0$, 1.8 and 2.25). The closed marks are the present simulation results, and the open marks show the performance expected with the layout described in the Technical Proposal.

Best results are achieved at $\eta = 0$, where the particle trajectory traverses a small amount of material (0.17 radiation lengths) and has the longest possible lever arm inside the tracker in the transverse plane. The momentum resolution matches the design requirement of $\Delta p/p \simeq 10^{-4} p_T$ (p_T in GeV/c) for transverse momenta above 100 GeV/c, and levels off around 4.10^{-3} below 10 GeV/c. At $\eta = 1.8$, at low momentum, the tracker performance is degraded by multiple scattering in the large thickness of material traversed (0.6 radiation lengths). The momentum resolution levels off at 8.10^{-3} for transverse momenta below 10 GeV/c. At high momenta, the momentum resolution is worse than at $\eta = 0$ because the transverse path inside the tracker has decreased from 1.2 m to 0.9 m. The results however still compare with the required performance at large p_T. At higher pseudorapidity values, the transverse lever arm drops even further, which leads to a drop of momentum resolution. The results for low momentum particles agree with the theoretical multiple scattering limit. The values estimated with the approximative formula 2.15 are $(\Delta p/p)_{m.s.} = 5.10^{-3}$ at $\eta = 0$ and 1.2×10^{-2} at $\eta = 1.8$.

The performance of the tracker geometry studied here is comparable to that of the design described in the Technical Proposal. However, several changes in the tracker geometry have been proposed and the simulation has been improved in many respects since the Technical Proposal, which renders the comparison between the two designs difficult. The tracker total length has decreased from 6 m to 5.5 m, reducing the number of forward MSGC wheels from 14 to 10 on each side. This change results in a reduction of the number of measurement points and of the transverse lever arm for particles emitted in the forward direction, which can explain the 20% poorer momentum resolution of the V3 layout at $\eta = 2.25$. The 20% discrepancy of the curves in the central rapidity region can partly be attributed to the optimistic spatial resolutions used here as compared to the design values used in the Technical Proposal study. These resolutions result from the simulation of ideal detector elements perfectly aligned. Part of the difference at low η could also be due to the additional layer of silicon strip detectors in the barrel part of the V3 layout as compared to the Technical Proposal.

Figure 5.14 a) shows the behaviour of the accuracy in the dip angle, as a function of the muon transverse momentum and pseudorapidity. Best performance is reached in the forward

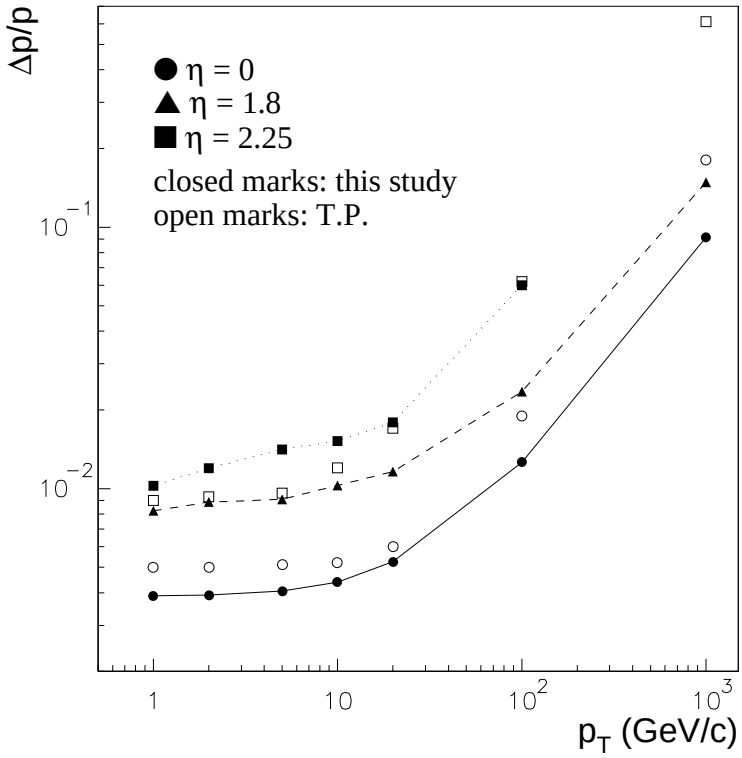

Figure 5.13: Momentum resolution as a function p_T, for various η values. The closed symbols are the present simulation results obtained with the LTF and tracker version V3. The open marks are the performance expected with the layout described in the Technical Proposal.

part of the tracker: 0.3 mrad or better at $\eta \geq 1.8$ for particles of transverse momentum above 10 GeV/c, compared to 0.7 mrad at $\eta = 0$. This is mostly due to the longer lever arm in z, 2.7 m, as compared to the lever arm in R, 1.2 m. Indeed, the error in the dip angle scales with the ratio of the detector resolution in the coarsely measured coordinate (z in the barrel part, R in the forward part) to the distance between the innermost and outermost detection layers traversed by the particle. The resolution in the dip angle at low momentum is degraded by multiple scattering, down to about 1 mrad for particles of $p_T = 1$ GeV/c. According to formula 2.10, the contribution of the error on the dip angle to the momentum resolution is always below 10^{-3}, and can thus be neglected.

Figure 5.14 b) displays the resolution in the azimuthal angle at the impact point with respect to the beam. At very high momenta, the accuracy in ϕ reaches 0.2 mrad or better. The results deteriorate with increasing pseudorapidity, about a factor two worse at the largest pseudorapidity covered as compared to the barrel region. What matters here is the ratio of the detector resolution in $R\phi$ to the track transverse lever arm, and at $\eta = 2.25$ the particle escapes from the tracker at a radius of 0.6 m. The performance rapidly degrades with decreasing transverse momentum. The error dominating at low p_T comes from multiple scattering in the innermost pixel layer. At 1 GeV/c, the contribution of multiple scattering to the angular resolution, estimated from formula 3.9, is of the order of 1 mrad, in agreement with our results.

The accuracy in the transverse impact parameter is shown in figure 5.15 a). This parameter is measured mainly thanks to the pixel detectors, and therefore the asymptotical precision

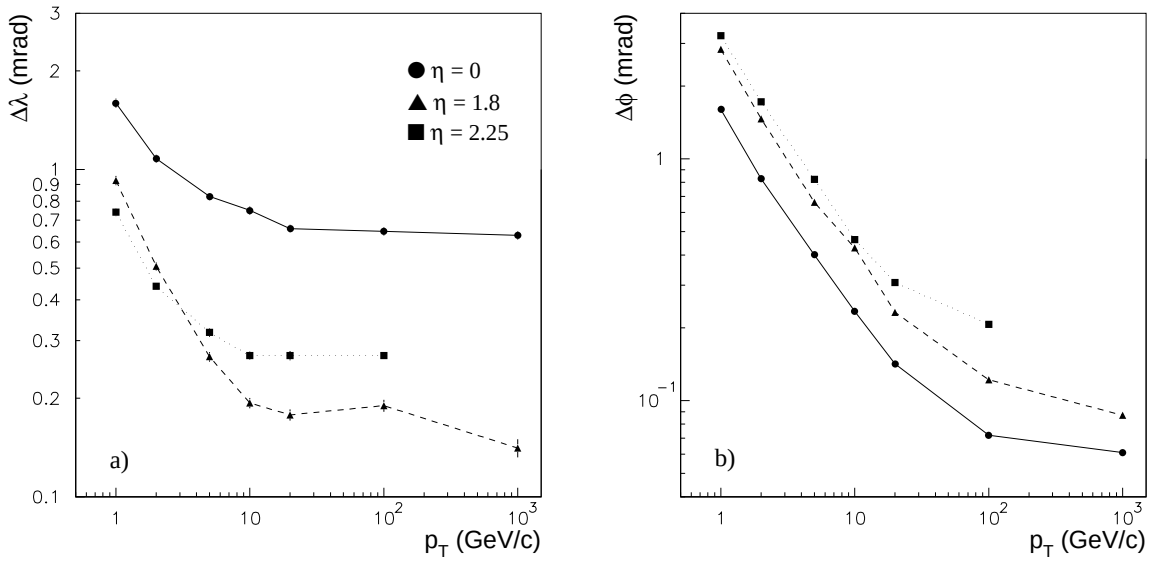

Figure 5.14: a) Resolution in the dip angle as a function of p_T and η. b) Same curves for the azimuthal angle at the impact point.

at high transverse momentum is comparable to the spatial resolution of the pixel counters in $R\phi$, i.e. 10 μm. The degradation of performance with decreasing transverse momentum and increasing pseudorapidity is linked to the deterioration of the measurement of the azimuthal angle: the error in ϕ contributes to the error in the transverse impact parameter by a term of the order of $R_{pxl}\Delta\phi$, where $R_{pxl} = 7.7$ cm is the radius of the innermost pixel layer. This term amounts to about 120 μm at $p_T = 1$ GeV/c, $\eta = 0$. The Technical Proposal results are 50% poorer, which can at least partly be attributed to the worse spatial resolution of the pixel modules considered in the Technical Proposal study.

Similar arguments hold for the longitudinal impact parameter (figure 5.15 b). At low momentum, at $\eta = 0$, the resolution is almost as good as for the transverse impact parameter, because the precisions of the barrel pixel detectors in z and in $R\phi$ are comparable. However the performance does not improve much with the momentum, due to the contribution of the error in the dip angle, which amounts to $R_{pxl}\Delta\lambda$. This contribution is larger than 60 μm at all momenta at $\eta = 0$. In the forward part, the error in the longitudinal impact parameter rises as the tangent of the dip angle times the detector resolution in R. In the forward pixel detectors the radial resolution amounts to 80 μm, and so the resolution in the longitudinal impact parameter is around 200 μm at $\eta = 1.8$, and of the order 400 μm at $\eta = 2.25$.

5.4.3 Tracks in b-jets

We will now describe the results of the track reconstruction in b-jets emitted in $t\bar{t} \rightarrow W^+W^-b\bar{b}$ events. This is the benchmark channel considered in chapter 6 for the evaluation of the b-tagging capability of the CMS tracker. In the simulation of the process, the W bosons are forced to decay into a muon and a neutrino or an electron and a neutrino, so that the only jets produced in these events originate from the hadronization of the b-quarks.

Figure 5.16 a) shows the distribution of the number of charged particles of transverse momentum higher than 1 GeV/c, produced per event inside the pseudorapidity coverage of the tracker. We only consider particles which production vertex is located inside the innermost de-

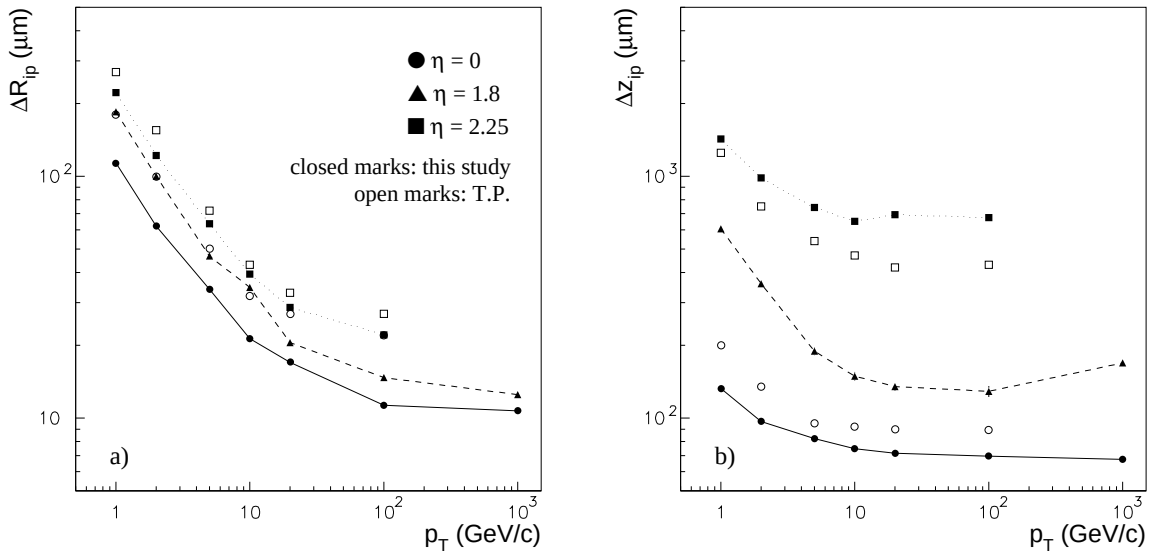

Figure 5.15: a) Resolution in the transverse impact parameter as a function of p_T and η. b) Same curves for the longitudinal impact parameter. The closed symbols are the present results and the open marks are the performances of the Technical Proposal layout.

tection layer: $R \leq 7$ cm, $|z| \leq 38$ cm. This selection retains all tracks from the decay of beauty hadrons, which disintegrate after a few millimeters of flight. The average number of selected particles is 30. On figure 5.16 b), the momentum distribution and type of the charged particles are shown. Most of the particle sample is constituted of pions of transverse momentum of a few GeV/c, coming from the b-jets. Each event contains two isolated charged leptons from the W decays, plus on average one additional lepton from the decay of a hadron in a jet.

Track finding efficiency

Table 5.3 gives the track finding efficiency of charged particles in these events. We distinguish three pseudorapidity regions: the central region, at $|\eta| \leq 1$, the intermediate region, in the range $1 < |\eta| \leq 1.7$, and the forward region, between $1.7 < |\eta| \leq 2.6$. The average track finding efficiency is 87% when applying both selection criteria on the hit purity and on the track parameter pulls. It increases to 92% when no selection is made on the pulls. This shows on one hand that the track finding algorithm is in most cases able to build a track out of the right hits, and on the other hand that the values of the track parameters are sometimes wrong, or that the errors on the parameters are sometimes underestimated.

Possible sources of reconstruction errors are:

- interactions of particles with matter that are not taken into account in the tracking algorithm. Only multiple Coulomb scattering is accounted for in the GEANE package;
- the presence of outliers in the reconstructed tracks, due to the large amount of hits created by the jets and by minimum bias particles.

In order to study the first effect, we have estimated the exclusive track finding efficiency for electrons, muons and pions. In the case of electrons, bremsstrahlung causes large energy losses and kinks in the trajectory. The track finding efficiency averaged in pseudorapidity is as low as 50%. It reaches 70% when no cut is applied on the track parameter pulls. The worst results

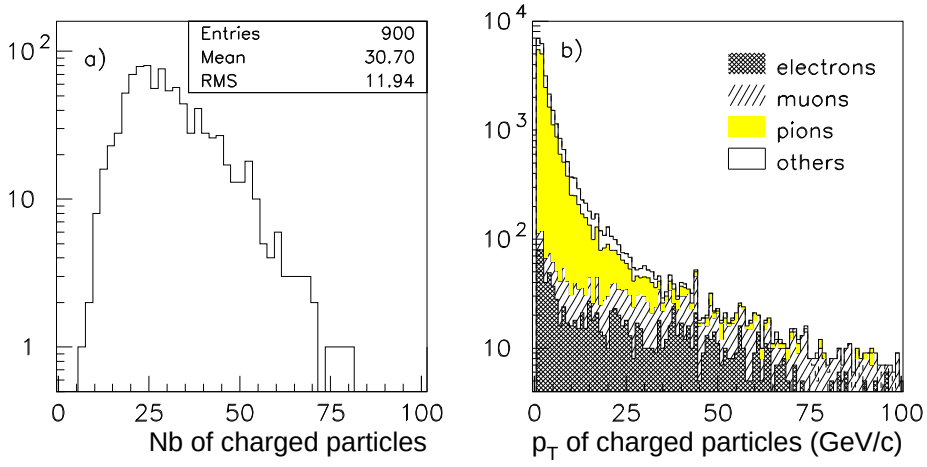

Figure 5.16: a) Distribution of the number of charged particles of transverse momentum higher than 1 GeV/c, produced per $t\bar{t} \rightarrow W^+W^-b\bar{b} \rightarrow l^+l^-\nu\overline{\nu}$ jet jet event inside the pseudorapidity coverage of the tracker. Here l stands for electron or muon. b) Cumulative distribution of the transverse momentum of the different types of charged particles produced in these events.

	$\|\eta\| \leq 1$	$1 < \|\eta\| \leq 1.7$	$1.7 < \|\eta\| \leq 2.6$
all particles	90%	87%	81%
$e^{\pm}$	(58 ± 2)%	(34 ± 2)%	(50 ± 3)%
$\mu^{\pm}$	(96 ± 1)%	(97 ± 1)%	(99 ± 1)%
$\pi^{\pm}$	91%	90%	81%
all but $e^{\pm}$	91%	90%	82%
all but $e^{\pm}$, no mbias	(93 ± 1)%	(93 ± 1)%	(89 ± 1)%
all but $e^{\pm}$, no mbias nor strong interactions	(97 ± 1)%	(97 ± 1)%	(98 ± 1)%

Table 5.3: Track finding efficiency for charged particles in $t\bar{t} \rightarrow W^+W^-b\bar{b}$ events.

are observed in the intermediate and forward rapidity regions, where the material budget is the largest.

As muons are only affected by multiple Coulomb scattering, the average track finding efficiency for muons is high, 97%. This value is only 2% lower than the performance reached for isolated muons in the absence of minimum bias events (see section 5.4.2). Indeed, most of the muons originate from the W decays and are thus separated from the jets. The track finding is only hindered by the presence of minimum bias tracks.

Pions, instead, can experience strong interactions in the detector material. The thickness of the CMS tracker averaged in η is equivalent to about 0.2 nuclear interaction lengths, and thus a hadron has a 20% probability to interact strongly with the nuclei of the material. The track finding efficiency for pions is 8% lower than for muons. The results deteriorate with increasing pseudorapidity. This can partly be explained by the larger amount of material in the intermediate and forward regions. Another possible explanation could be that the distance between two successive detection layers is larger in the forward part of the tracker than in the barrel part. If a pion is scattered at large angle by a strong interaction, the crossing point at the next layer will be at a further distance from the prediction in the forward part than in the

barrel part.

A first conclusion is thus that our algorithm based on GEANE is optimal only for muons. It performs satisfactorily for hadrons, as the probability of a strong interaction in the tracker material is low, about 20%. It is not suited for electrons, as it does not account for bremsstrahlung. A method dedicated to the reconstruction of electron tracks seems mandatory. This technique would first identify the electron, for example by associating a cluster in the electromagnetic calorimeter to a track segment in the outer tracker layers. Then, the track would be reconstructed from the outer layers inwards, checking for kinks correlated with photons detected in the electromagnetic calorimeter.

We have then estimated the effect of minimum bias events on the tracking algorithm. The table gives the track finding efficiency for all particles except electrons, with and without minimum bias events superimposed on top of the $t\bar{t}$ events. The performance of the reconstruction is 92% on average without event pile up, as compared to 89% in the situation corresponding to the full LHC luminosity. The bias introduced by the presence of outliers is thus small, as could be foreseen from the high purity of the reconstructed tracks (see section 5.3.3).

Eventually, to confirm our understanding of the reconstruction results, we have simulated 50 $t\bar{t}$ events without minimum bias events and with the simulation of strong interactions switched off in GEANT. Charged hadrons then behave like muons. A track finding efficiency very close to the performance obtained for isolated muons is reached, i.e. 97% for all particles but electrons. The remaining efficiency loss of 2% could be an effect of the high the track density in the jets. However this effect is small, probably because these jets are not very collimated. The average distance in ϕ between tracks of transverse momentum above 1 GeV/c is 0.1 rad. The corresponding distance in $R\phi$ between two hits is of the order of 1 cm in the pixel detectors, of the order of 5 cm in the silicon strip counters, and about 10 cm in the MSGC's. The spatial resolutions of the detectors and the precision of the estimation of the track crossing points during Kalman filtering are much better than the hit separation, which permits easy hit selection.

The average track finding efficiency of 89% can be regarded as satisfactory as compared to the required value of 90%. However one should consider that some physical and systematic effects are missing in the simulation: full simulation of the response of the readout electronics, dead channels, detector misalignments, possible additional backgrounds due to low energy particles or material activation, etc. Moreover, the Local Track Finder is partly guided by the simulated tracks for the building of the templates. The Kalman filter is initialized with a rather precise estimate of the track parameters, and therefore the number of hit combinations to be tested is reduced and the hit selection is facilitated. The same performance is probably achievable with a more realistic track finder, but much more hit combinations will have to be tested.

Ghosts

About 0.1 ghost track is generated per event. The average momentum of the ghosts is 2 GeV/c. The average number of hits along a fake track is 6, as compared to 12 - 13 for real tracks. Rejecting reconstructed tracks with 6 hits or less would reduce the number of ghosts by a factor two while reducing the track finding efficiency by 1%. Such a cut is not adequate if the reconstruction of vertices displaced by several tens of centimetres with respect to the interaction point is required, like for example in the reconstruction of short lived kaons.

Transverse impact parameter resolution in b-jets

The method of b-jet identification described in the next chapter relies on the detection of particles, produced in the beauty hadron decay chain, which transverse impact parameter is significantly greater than zero in absolute value. The significance of the transverse impact parameter, s_{ip}, is defined as the ratio of the transverse impact parameter to its error ΔR_{ip}.

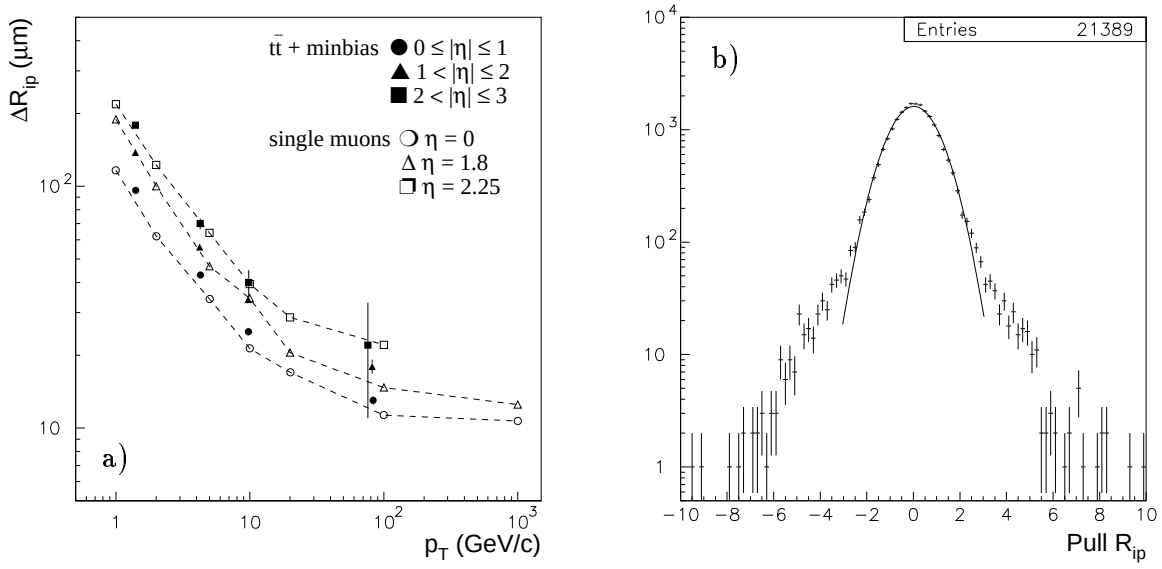

Figure 5.17: a) Transverse impact parameter resolution as a function of p_T and η for tracks in $t\bar{t}$ events with high luminosity pile up, compared to the performance for isolated muons. b) Distribution of the transverse impact parameter pull for tracks reconstructed in $t\bar{t}$ events with high luminosity pile up. The full line is a Gaussian curve fitted to the central part of the distribution.

The impact parameter resolution for tracks in b-jets thus determines the b-tagging capability of the CMS tracker. We have seen that the track fitting algorithm can be expected to yield optimal results only for muon tracks. As most of the particles in b-jets are hadrons, a check of the impact parameter resolution for such particles is necessary. Figure 5.17 a) shows the transverse impact parameter resolution of the CMS tracker for tracks in b-jets at high LHC luminosity, compared to the performance for isolated muons. Results very close to the resolution for single muons are obtained. The discrepancy between the impact parameter resolution averaged over the rapidity range $0 \leq |\eta| \leq 1$ and the resolution for single muons at $\eta = 0$ is a consequence of the degradation of the impact parameter resolution with increasing η.

The sample of tracks with a significant transverse impact parameter is contaminated by tracks for which the impact parameter error is underestimated. Incorrect estimation of the impact parameter error occurs when the track has a kink, when it contains an outlier, or when the detector spatial resolutions are incorrectly estimated. The fraction of tracks with an underestimated impact parameter error thus determines the contribution of reconstruction errors to the b-jet mistagging rate (see chapter 6). It can be evaluated by studying the distribution of the transverse impact parameter pull. This variable is distributed as a standard Gaussian when the error on the transverse impact parameter is correctly estimated. Figure 5.17 b) shows that, in b-jet events, 6% of the tracks have a R_{ip} pull larger than 3 in absolute value, as compared to the 0.3% expected for a standard Gaussian distribution. In chapter 6 we shall see that this

number is small enough so that the contribution of reconstruction errors to the b-jet mistagging rate is small as compared to the contribution due to the kinematics of the background jets.

5.5 Conclusions

We have investigated the performance of the CMS tracker in reconstructing the tracks of isolated particles and of particles in jets. This work was performed with a detailed simulation of the detector response, up to the level of the signals induced by the particles on the electronics channels, including the generation of electronics noise.

In such a study it is difficult to disentangle the intrinsic detector performance from the performance of the reconstruction algorithm. We therefore had a close look at one of the possible track finding and fitting algorithms, based on the Kalman filter. We have first evaluated the spatial resolutions resulting from the simulation of the tracker elements, and we have introduced the values obtained in the fit formulas. We have then compared the behaviour of the Kalman filter algorithm and of an improved algorithm including smoothing, that we have implemented in the reconstruction program.

The Kalman filter was shown to be able to retain 96% of the hits along the tracks of particles of transverse momentum above 1 GeV/c. At full LHC luminosity the fraction of outliers was estimated to less than 1%. However, as the algorithm proceeds from the outer tracker layers towards the interaction region, the estimation of the track parameters is optimal only at the vertex of production of the particles. The smoothing algorithm proceeds from the vertex outwards and corrects the estimation of the filter, detection layer per detection layer. It yields an optimal estimation of the track parameters at any layer, as well as in the detectors located outside the tracker. It is more powerful in selecting the hits belonging to a given track than the filter algorithm: we have found that 99% of the hits could be kept, with only 0.4% of outliers at high luminosity. The smoother will also be helpful in aligning the different tracker elements, and in associating tracks with showers in the calorimeters.

The track finding efficiency was then evaluated for isolated muons and for tracks inside b-jets from $t\bar{t}$ events. The simulation of $t\bar{t}$ events included a pile up of minimum bias events corresponding to the full LHC luminosity. The track finding efficiency is above 97% for isolated muons of transverse momentum above 1 GeV/c, in the range of pseudorapidity $|\eta| \leq 2.6$. In b-jets, for all particles except electrons, the average track finding efficiency amounts to 89%. Most of the particles in b-jets are indeed hadrons, some of which experience strong interactions in the tracker material. In the case of electrons, the track finding efficiency drops to 50% because of bremsstrahlung in the detector material. Ghost tracks are generated at the level of 0.1 ghost per b-jet event. These results are close to the requirements expressed in the Technical Proposal of CMS, except for electrons.

The track parameter resolutions achieved with the tracker version V3 have been investigated. The results are comparable to the figures given in the Technical Proposal. The momentum resolution is compatible with the requirement $\Delta p/p \simeq 10^{-4} p_T$ (p_T in GeV/c) at high transverse momentum in the pseudorapidity range $|\eta| \leq 1.8$. At larger η, the momentum resolution degrades because of the reduction of the lever arm in the transverse plane. The resolution in the transverse impact parameter tends to 10 μm at $\eta = 0$ for high momentum particles. This result is compatible with the value expected with a pixel detector of 10 μm resolution in $R\phi$, but it is twice better than the result quoted in the Technical Proposal. This is due partly to the fact that detector misalignments have not been taken into account in the present study, and partly to the worse detector resolutions considered in the Technical Proposal study.

Multiple scattering limits the tracker performance for low momentum particles. The mo-

mentum resolution levels off to about 1% at low p_T. The transverse impact parameter resolution exceeds 100 μm at $p_T = 1$ GeV/c. The p_T value below which the track parameter errors are dominated by the contribution of multiple scattering is about 10 - 20 GeV/c. This value is high compared to the minimum transverse momentum that we intend to measure in CMS (around 1 GeV/c). The CMS tracker is thus probably not optimal for the study of low energy processes, like for example in B-physics. The large amount of material present in the tracker also renders the reconstruction of electron tracks very difficult, and is responsible of the loss of about 8% of the hadron tracks. These losses can partly be recovered by accounting for bremsstrahlung and strong interactions during track reconstruction, but this is certainly not straightforward. These are strong indications that the CMS tracker is already too thick in the present design. The amount of material in the tracker should definitely be kept to a minimum, below the present level if possible.

Eventually, it should be kept in mind that, although we have used the most complete simulation and reconstruction programs presently available, this study is not yet completely realistic. First of all the performance of the tracker should be studied with a global track finding algorithm capable of treating a full LHC event. The problem of pattern recognition was partly avoided here by using the Local Track Finder. Secondly, the values of detector resolutions used in our study are too optimistic, because misalignments between counters were not taken into account. Important effects like a loss of detection efficiency or an increase of the event pile up could also appear when introducing a detailed description of the front-end electronics in the simulation of the detector response. These aspects certainly deserve systematic studies in order to make sure that the tracker behaviour in realistic conditions of operation is understood and under control.

Chapter 6

Tagging of b-jets with the CMS tracker

6.1 Introduction

This chapter investigates the potential of the CMS tracker in identifying b-jets at high LHC luminosity. Preliminary studies performed with a parametrized simulation of the tracker performance have shown that an average b-tagging efficiency around 50% could be expected for b-jets of several tens of GeV, with a mistagging probability around 12% for c-jets and below 3% for jets from lighter partons [105]. The results of this study have been used since to evaluate the potential of CMS in detecting supersymmetric particles [106, 107]. A good sensitivity can be expected if the tracker b-tagging performance is as good as foreseen from parametrized simulations.

However the visibility of some SUSY signals seems to be quite dependent of the actual value of the b-tagging efficiency [106]. It is therefore important to evaluate the b-tagging capability of the CMS tracker in realistic detector operating conditions. This is one of the aims of our work. The study is performed with a detailed simulation of the detectors and a realistic track reconstruction program. We shall try to identify the physical and instrumental aspects determining the CMS tracker b-tagging capability, and check if the expected performance is achieved.

Our method of b-jet identification relies on the selection of particles likely to be produced in the beauty hadron decay chain. Because of the noticeable lifetime of beauty hadrons, typically 1 to 1.6 ps, it is natural to select particles with a certain impact parameter with respect to the proton collision point. Figure 6.1 illustrates a possible decay process of a B^+ meson. The tracks of the long-lived charged particles produced in the B^+ decay chain (the K^-, π^+ and charged lepton in the figure) can be reconstructed, and their transverse impact parameter with respect to the primary vertex, of the order of a few hundreds of micrometers, can be measured. The b-jet selection technique based on the impact parameter measurement is simple and is expected to yield high tagging efficiencies. It does not provide the optimum b-tagging results, as it does not use all the detector information available. However it permits a test of the intrinsic b-tagging capability of the CMS tracker, which is in any case related to the accuracy of the impact parameter measurement.

The method of evaluation of the CMS tracker b-tagging performance is explained in section 6.2. This section also describes some discriminating variables that allow to select b-jets. In section 6.3 we describe how the cuts to be applied on the discriminating variables are chosen, and mention the tagging efficiency and background rejection achieved. In section 6.4 the different effects that influence the b-tagging performance are discussed. Eventually, the results obtained in this study are compared to results from other groups, and possible ways of improving the CMS b-tagging capability are considered.

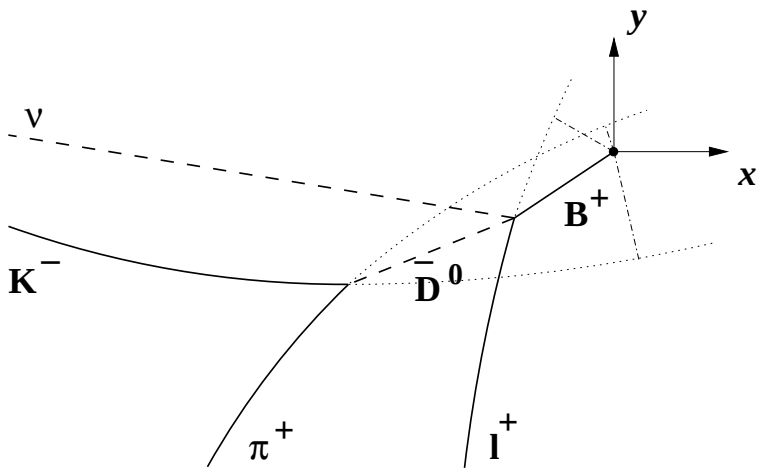

Figure 6.1: A possible decay chain of a B^+ meson. The flight path of charged particles is drawn in solid lines, that of neutral particles in dashed lines. The tracks of charged particles are extrapolated to the beam crossing point (dotted lines) and the dash-dotted lines show their transverse impact parameter.

6.2 Method

The b-tagging efficiency is estimated for b-jets produced in a particular process, $t\bar{t} \rightarrow W^+W^-b\bar{b}$. This process was chosen because its kinematics is characteristic of events involving b-quarks which are of interest at the LHC. It indeed features a heavy particle decaying into a b-quark of large transverse momentum.

The contamination of jets from light partons is estimated with events of comparable signature, i.e. the production of a W boson in association with a light parton (a quark u, d, s or c or a gluon) of large transverse momentum. Light parton jets can incorrectly be tagged as b-jets for several reasons. Some are physical: firstly, an additional $b\bar{b}$ pair can be emitted in the initial p-p collision. This occurs in about 3% of $W + q, g$ events. Secondly, long-lived particles containing no b-quark can be created during the hadronization of the initial parton. Strange particles like K^0_S mesons and Λ^0 baryons are copiously produced,[1] but as their lifetime is much larger than that of beauty hadrons, of the order of 100 ps, part of them can be rejected by applying an upper cut on the transverse impact parameter. Mistaggings are more likely to occur with c-jets, as charmed and beauty hadrons have comparable lifetimes, with typical values of 0.4 - 1 ps and 1 - 1.6 ps respectively.

Other sources of background are due to detector effects, such as interactions of particles with the tracker material and errors in track reconstruction. Photons can convert into an e^+e^- pair and leave two tracks of potentially large impact parameter. Kinked tracks or tracks containing outliers can exhibit an artificial impact parameter, as explained in chapter 5.

Our estimation of the CMS tracker b-tagging capability proceeds as follows. First we simulate the kinematics of the signal and background channels described above. We then simulate the response of the CMS hadron calorimeter and tracker, and reconstruct energy clusters and tracks. The b-tagging algorithm then selects tracks likely to be produced in the decay chain of a beauty hadron and groups them in b-jet candidates. These are finally matched to calorimeter clusters. The b-tagging efficiency of the tracker, E, is then defined as the fraction of b-jets

[1] The pair production rates during hadronization are significant only for quarks lighter than the c-quark. Their relative values are $u : d : s : c \sim 1 : 1 : \frac{1}{3} : 10^{-11}$.

reconstructed in the calorimeter that could be associated to a b-jet candidate. The mistagging rate, M, is defined as the fraction of light parton jets that were associated to a b-jet candidate.

6.2.1 Simulation of the event kinematics

The event kinematics was simulated with the PYTHIA event generator [108]. Samples of 1730 $t\bar{t}$ events, 1900 $W + c$ events and 1850 $W + u, d, s, g$ events were generated. To separate the contribution of the different backgrounds and study the intrinsic performance of the tracker, we require no b-quark in the $W + c$ sample and no b- nor c-quark in the $W + u, d, s, g$ sample. This selection rejects about 3% of $W + c$ events and 20% of $W + u, d, s, g$ events. We also force the W's to decay into a final state of minimum track multiplicity (eν_e or $\mu\nu_\mu$) to save computation time.

6.2.2 Hadron calorimeter simulation

The CMS hadron calorimeter simulation interfaced with CMSIM is still in development. We have therefore preferred to rely on the LUCELL routine provided with PYTHIA. This routine permits a rough simulation of the calorimetry, and provides a simple jet reconstruction routine in line with what is currently used in the study of high-p_T collider events.

LUCELL takes as input the calorimeter coverage, segmentation and energy thresholds. It adds up the energy deposited in each calorimeter cell by any particle but neutrinos. The cells containing a transverse energy $E_T = E \sin\theta$ exceeding a certain "seed" threshold are used as jet initiators. All cells in a cone of a given aperture $\Delta R_{cell} = \sqrt{\Delta\eta^2 + \Delta\phi^2}$ around the seed cell are included in the jet provided that the transverse energy contained exceeds a low threshold. Jets of total transverse energy above a third "jet" threshold are retained. The input values derived from the CMS HCAL design are the following: a coverage up to $|\eta| = 3$, a segmentation of 0.087 in η and ϕ, a seed threshold of 5 GeV, a cone aperture of 5 cells around the seed cell ($\Delta R_{cell} = 5 \times 0.087$), a low threshold of 1 GeV and a jet threshold of 20 GeV.

An event is retained only if the initial parton (or both b-quarks in the case of $t\bar{t}$ events) gives rise to a detectable energy cluster in the calorimeter. The direction of the initial parton is requested to fall into the reconstruction cone of one of the jets. Figure 6.2 a) shows the distributions of the parton jet transverse energy in the different samples. As the top quark is very heavy, the b-quarks are emitted with a large transverse momentum, hence the larger average transverse energy of b-jets as compared to jets from W + light parton events (80 GeV as compared to 50 GeV).

6.2.3 Tracker simulation

The tracker response is simulated with CMSIM, including the digitization and clusterization of the particle signals in the detector elements. A pile up of minimum bias events corresponding to the full LHC luminosity is superimposed on top of the simulated events. Track reconstruction is performed with the CMSIM Local Track Finder (cf. chapter 5 for more details).

6.2.4 Reconstruction of b-jet candidates in the tracker

After event simulation and reconstruction, tracks satisfying a set of kinematical criteria are selected. The discriminating variables considered are the transverse impact parameter, the significance of the transverse impact parameter $s_{ip} = R_{ip}/\Delta R_{ip}$ and the transverse momentum. The distributions of the transverse impact parameter of the charged particles simulated are

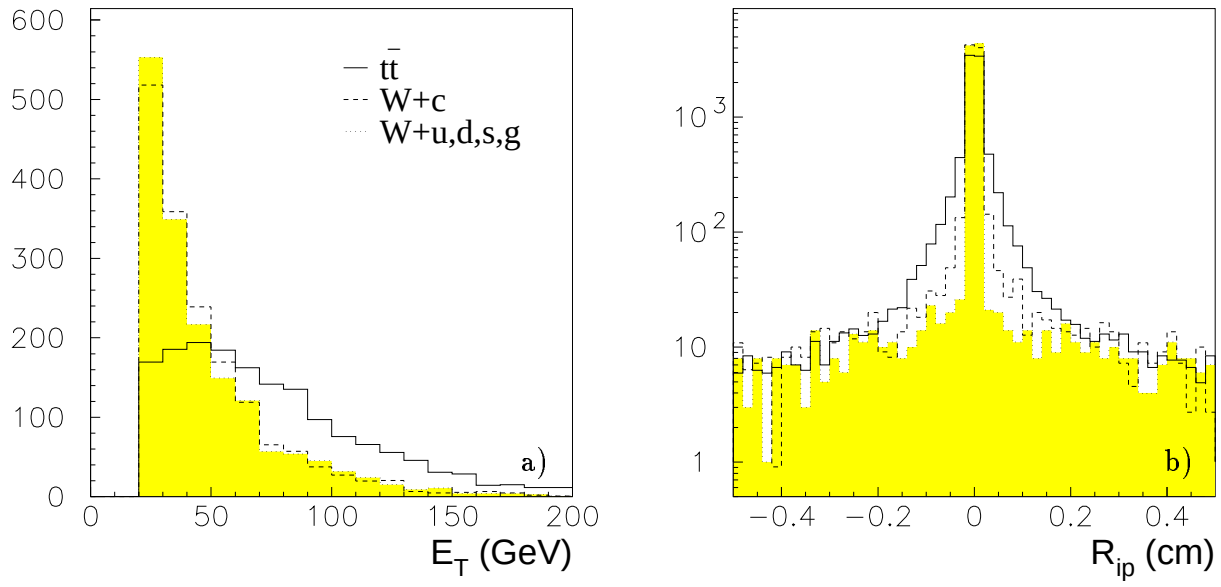

Figure 6.2: a) Distributions of the parton jet transverse energy in $t\bar{t}$, $W + c$ and $W + u, d, s, g$ events. b) Distributions of the transverse impact parameter of the charged particles simulated.

shown in figure 6.2 b) for the three event samples studied. The histograms are normalized to the same number of entries. The fraction of particles with a non-zero impact parameter is the largest in the $t\bar{t}$ sample. The $W + c$ sample also shows an excess of particles produced at displaced vertices, as compared to the $W + u, d, s, g$ sample. This excess is smaller than in the case of b-jets because on one hand the lifetime of charmed hadrons is smaller than that of beauty hadrons, and on the other hand the most probable decay processes of beauty hadrons lead to a charmed particle plus a few other charged or neutral particles. The three samples contain however the same fraction of tracks with a large transverse impact parameter ($|R_{ip}| \geq 2$ mm). These originate mainly from the decay of light long-lived particles (K^0_S, Λ^0,...) and from photon conversions in the tracker material.

Because of the finite detector resolution, a non-zero transverse impact parameter is not necessarily detected. To determine if a reconstructed track is compatible with the primary vertex or not, we use the significance of the transverse impact parameter. The distributions of this variable for the different event samples are shown in figure 6.3 a). The fraction of tracks in the tails of the distribution is the largest in the $t\bar{t}$ event sample.

As their transverse energy is larger than that of light parton jets, the jets from the $t\bar{t}$ sample are likely to contain particles of higher transverse momentum. Figure 6.3 b) shows the p_T distributions for tracks satisfying the criterion $|s_{ip}| \geq 3$. The average p_T is slightly higher in $t\bar{t}$ events, 6.5 GeV/c compared to 4 GeV/c in $W + u, d, s, g$ events. However a large overlap exists, for all variables considered, between the distributions observed in signal and background events. The tagging algorithm will thus be a trade-off between b-tagging efficiency and rate of mistags. The values of the cuts to be applied on the discriminating variables will be determined in section 6.3.

The tracks passing the selection criteria are then grouped together into b-jet candidates. The first jet is built around the track of largest transverse momentum among the selected ones. All selected tracks in a cone of aperture ΔR_{track} around the track of largest p_T are included in the jet. The jet is retained as a valid b-jet candidate if the number of tracks grouped together

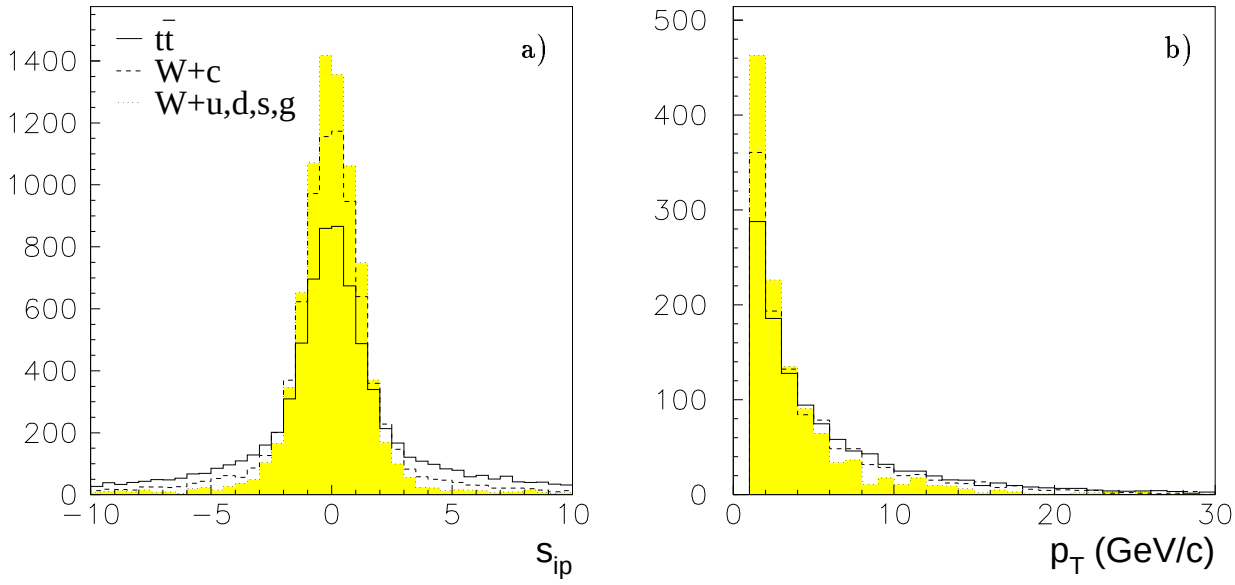

Figure 6.3: a) Distributions of the significance of the reconstructed transverse impact parameter for charged particles in $t\bar{t}$, $W + c$ and $W + u, d, s, g$ events. b) Distributions of the transverse momentum for tracks satisfying the criterion $|s_{ip}| \geq 3$.

exceeds a minimum value. The next jets are reconstructed in the same way using the selected tracks not yet included in a valid b-jet candidate. Figure 6.4 a) shows the distributions of the angle ΔR between the track of largest p_T and the auxiliairy tracks. As the distributions are almost identical in the three event samples, no large background rejection can be achieved by applying a cut on ΔR. A large cone aperture is chosen in order to maximize the tagging efficiency ($\Delta R_{track} = 0.7$).

The distributions of the b-jet candidate track multiplicity are shown in figure 6.4 b). The average multiplicity is the largest in $t\bar{t}$ events. However it is difficult to take advantage of this variable, as it is discrete and as there is an important overlap between the distributions. Requiring 3 tracks in b-jet candidates instead of 2 results in a large loss of b-tagging efficiency, about 20%.

6.2.5 Matching of b-jet candidates with calorimeter clusters

For each b-jet candidate, the direction of the jet is estimated by adding the momenta of the selected particles. A jet reconstructed in the calorimeter is finally tagged as b-jet if the direction of one of the b-jet candidates is in a cone of aperture $\Delta R_{track} = 0.5$ around its axis.

6.3 Optimization of the b-tagging algorithm

Several combinations of selection criteria are tried, so as to reach a b-tagging efficiency around 50% while minimizing the mistagging rate from u, d, s, g-jets. The contamination from c-jets is studied separately, as it is likely to be dominated by event kinematics and not by the tracker performance. We first apply a lower cut on the significance of the transverse impact parameter. This criterion is then combined to either an upper cut on the transverse impact parameter, a lower cut on the particle p_T or a lower cut on the b-jet candidate track multiplicity. The

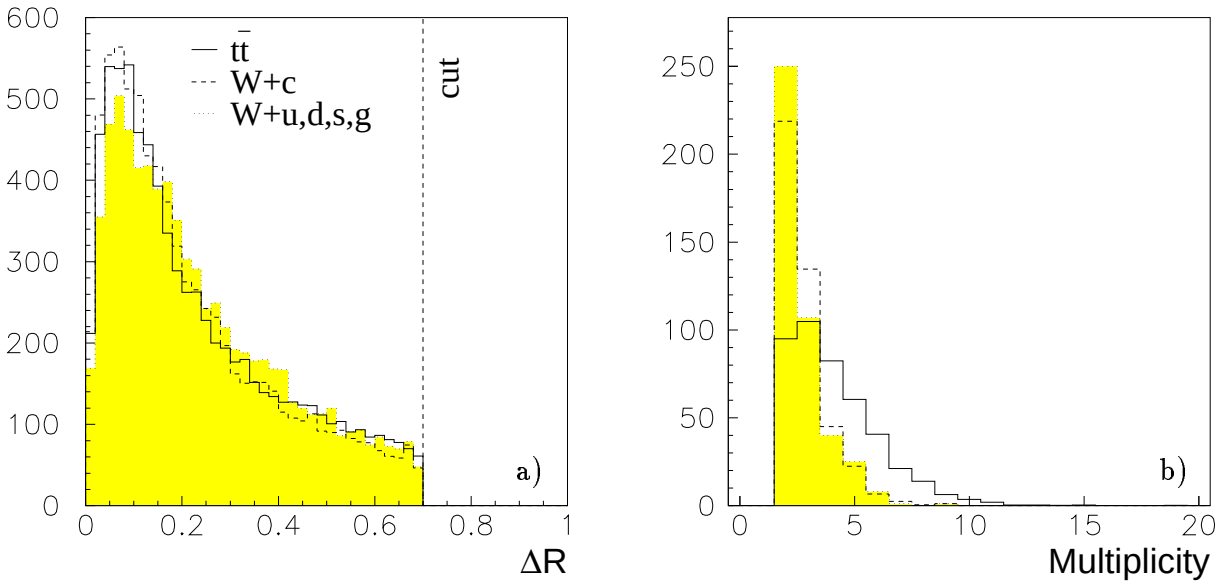

Figure 6.4: a) Distributions of the angle ΔR between the selected track of largest p_T and the auxiliairy tracks in b-jet candidates. b) Distributions of the b-jet candidate track multiplicity.

cut values are varied up to the point where the signal to background ratio E/M is maximum, provided that the tagging efficiency is still above 50%.

Figure 6.5 a) shows the dependence of the tagging efficiency, mistagging rate and signal to background ratio as a function of the cut applied on the transverse impact parameter significance. The mistagging rate first drops rapidly with increasing cut values, then the decrease is slower for cuts higher than 3. The tagging efficiency decreases steadily when the significance required increases. The signal to background ratio first rises rapidly, then levels off and shows no significant improvement at cut values above 3. The optimal selection criterion is thus $|s_{ip}| \geq 3$, corresponding to a b-tagging efficiency of $(75 \pm 0.7)\%$ with a mistagging rate of $(23 \pm 1)\%$ for $W + u, d, s, g$ events.

Figure 6.5 b) shows the performance of the b-tagging algorithm when applying an additional cut on the transverse impact parameter. As explained earlier this criterion is effective against the background from strange hadrons and photon conversions. While the b-tagging efficiency is slowly decreasing with decreasing R_{ip} cut, a steep increase of the E/M ratio is observed, down to a cut at $|R_{ip}| \leq 0.8$ mm. More severe cuts do not lead to a significant improvement of the E/M ratio but cause a drop of the tagging efficiency.

Table 6.1 summarizes the results obtained by cutting on the transverse momentum of the particles or on the multiplicity of the b-jet candidates, in addition to the cut on the impact parameter significance. These criteria are less selective than a cut on the transverse impact parameter. The values of E/M ratio obtained are, at the same tagging efficiency, lower than the values achieved with a cut on the transverse impact parameter. We therefore propose the following algorithm:

- $|s_{ip}|$ of reconstructed tracks ≥ 3;
- $|R_{ip}|$ of reconstructed tracks ≤ 0.8 mm;
- p_T of reconstructed tracks ≥ 1 GeV/c;

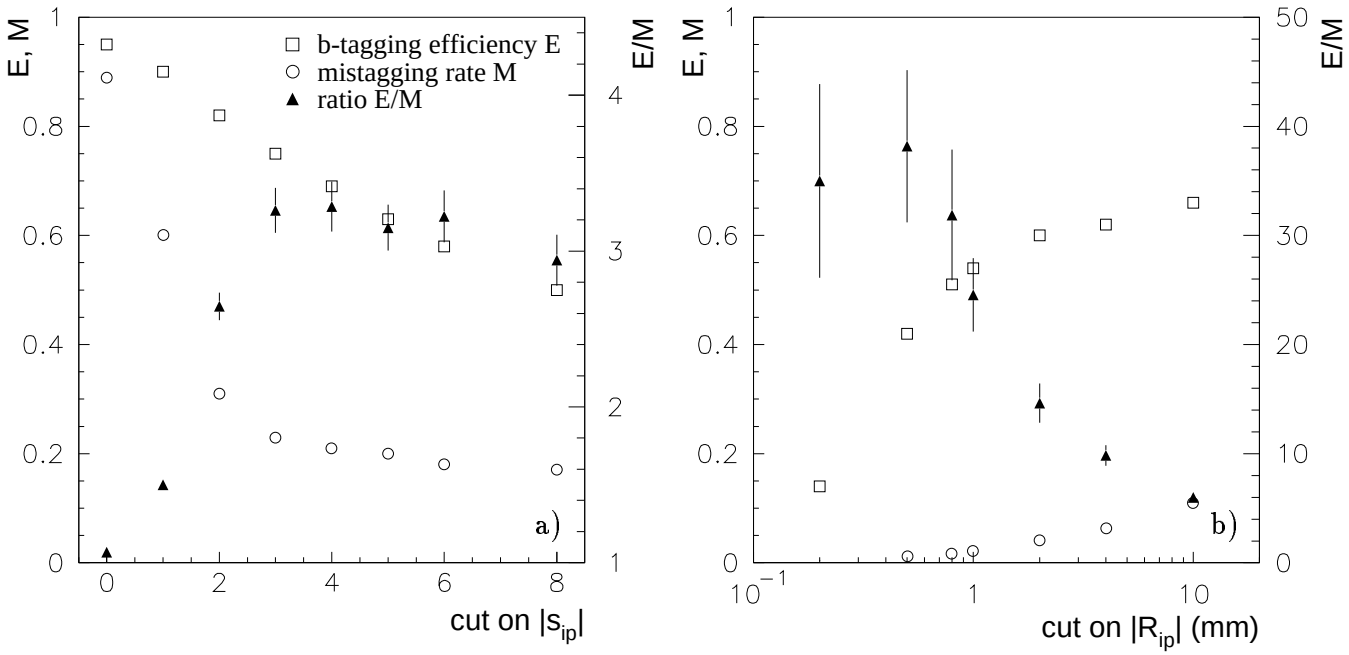

Figure 6.5: a) Curves of the b-tagging efficiency E, mistagging rate for u, d, s, g-jets M and their ratio E/M, as a function of the cut on the significance of the transverse impact parameter. b) Curves of E, M and E/M obtained when cutting on the transverse impact parameter, after selection of tracks with a $|s_{ip}| \geq 3$.

- multiplicity of b-jet candidates ≥ 2;

with the following results: a b-tagging efficiency of $(51 \pm 0.8)\%$ for b-jets from $t\bar{t}$ events, a mistagging rate of $(1.6 \pm 0.3)\%$ for jets from light partons in $W + u, d, s, g$ events, and a fraction of c-jets incorrectly identified as b-jets of $(12 \pm 0.7)\%$ in $W + c$ events.

6.4 Discussion

We shall now try to separate the contributions of the different effects influencing the b-tagging performance of the CMS tracker. To evaluate the contribution of the event kinematics we have estimated the tagging efficiency and mistagging rate that would be obtained with an ideal detector. These numbers are estimated by applying the tagging algorithm to the simulated tracks contained in the tracker acceptance. In the absence of knowledge of the primary vertex position, we assume that the transverse impact parameter is known with an accuracy of 15 μm, i.e. the natural dispersion of the transverse impact parameter with respect to $(0, 0)$ due to the beam transverse dimensions. With this uncertainty we compute a transverse impact parameter significance for the simulated tracks.

Figure 6.6 shows the dependence of the tagging efficiency with the b-jet transverse energy and pseudorapidity. The open marks indicate the ideal tracker performance, determined by event kinematics and tracker acceptance. The closed marks show the results obtained after track reconstruction. A tagging efficiency of $(77 \pm 0.7)\%$, averaged in η and E_T, is obtained as maximum performance as compared to the $(51 \pm 0.8)\%$ obtained after track reconstruction. An increase of the tagging efficiency is noticed with increasing jet transverse energy, as well as

cut on p_T			
p_T (GeV/c) $\geq$	E (%)	M (%)	E/M
1	75 ± 0.7	23 ± 1	3.3 ± 0.15
2	64 ± 0.8	13 ± 0.8	4.9 ± 0.3
4	44 ± 0.8	4.4 ± 0.5	10 ± 1
cut on the multiplicity			
multiplicity $\geq$	E (%)	M (%)	E/M
2	75 ± 0.7	23 ± 1	3.3 ± 0.15
3	59 ± 0.8	11 ± 0.7	5.4 ± 0.3
4	42 ± 0.8	4.3 ± 0.5	9.8 ± 1.1

Table 6.1: b-tagging efficiency E, mistagging rate for u, d, s, g-jets M and ratio E/M, achieved by applying cuts on the transverse momentum of the particles and on the multiplicity of the b-jet candidates, after a 3σ cut on the transverse impact parameter.

a decrease of tagging efficiency with increasing jet pseudorapidity.

6.4.1 Dependence of the tagging efficiency on η and E_T

The drop of tagging efficiency at $|\eta| \geq 2.5$ is an effect of the tracker coverage, which extends up to $|\eta| = 2.6$. The slow decrease of performance with increasing $|\eta|$, observed in reconstructed events, is mainly due to the deterioration of the transverse impact parameter resolution. As discussed in the previous chapter the degradation of ΔR_{ip} with increasing η is related to the increase of the amount of material traversed. At low momentum, $\Delta R_{ip} \simeq R_{pxl}\Delta\phi$, where the error in the azimuthal angle is dominated by the contribution of multiple scattering in the innermost pixel counters.

The increase of tagging efficiency with increasing jet transverse energy is due to the combined effects of a rise of the average particle transverse momentum, a decrease of the transverse impact parameter dispersion, an improvement of the transverse impact parameter significance and an increase of the b-jet multiplicity, as illustrated in figure 6.7. The increase of the particle p_T results in an improvement of the impact parameter resolution. This improvement is such that, even if high energy jets are more collimated, the significance of the transverse impact parameter improves with E_T.

6.4.2 Influence of event kinematics and reconstruction errors

The tagging efficiency results can be decomposed as follows: among the 77% of b-jets that can be identified on the basis of their kinematics, 49% can still be identified after reconstruction and 28% cannot be identified anymore. Among the 23% of b-jets with an unfavourable kinematics, 2% could be identified after reconstruction, and 21% were rejected.

The efficiency loss due to event reconstruction is thus 26%. The main reason is the finite impact parameter resolution of the tracker. As shown in figure 6.7 the average transverse momentum of the selected particles is between 5 and 13 GeV/c, depending on the jet transverse energy. The average R_{ip} resolution in this p_T range is around 40 μm (see figure 5.17). This resolution should be compared to typical values of the transverse impact parameter for particles produced in the beauty hadron decay chain, given by the R.M.S. of the transverse impact parameter of the selected particles, about 400 μm. Requiring $|s_{ip}| = |R_{ip}/\Delta R_{ip}| \geq 3$ thus

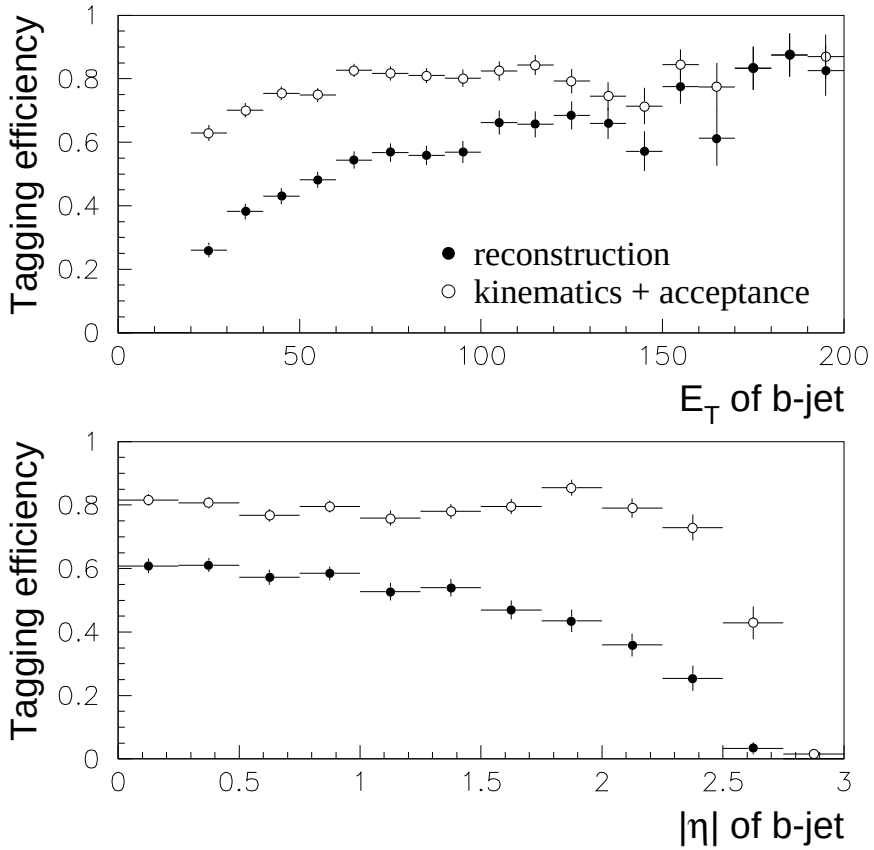

Figure 6.6: Tagging efficiency as a function of the b-jet transverse energy (upper plot) and pseudorapidity (lower plot). The closed marks show the results obtained after event simulation and reconstruction and the open marks show the kinematical and acceptance limit.

rejects a non-negligible fraction of the particles from beauty hadron decays. This fraction is estimated to 25%. A second cause of tagging inefficiency is the limited track finding efficiency for particles in b-jets. This results in an additional loss of 11% of the useful tracks.

The b-tagging capability of the CMS tracker could thus be improved by improving the impact parameter resolution and increasing the track finding efficiency. In the case of a well designed pixel detector containing a minimum amount of material, the only way to improve ΔR_{ip} is to reduce the radius of the inner pixel layer. This is not possible at high luminosity, because below $R_{pxl} = 7.7$ cm the counters would be exposed to an excessive radiation dose. At low luminosity a pixel layer located at 4 cm from the beam pipe is foreseen. Possible ways of improving the track finding efficiency have already been mentioned in the previous chapter, like the use of algorithms accounting for strong interactions and bremsstrahlung. Writing such algorithms will however not be easy. The alternative would be to design the tracker with significantly less material.

In order to study the influence of event kinematics and track reconstruction on the mistagging rate from u, d, s, g-jets, we have estimated the fraction of such jets that would be b-tagged by an ideal detector, and the fraction that would be rejected by an ideal detector but are actually b-tagged because of reconstruction errors. These numbers are noted M_s and M_r respectively. The real mistagging rate is lower than $M_s + M_r$, as only a small fraction fraction of

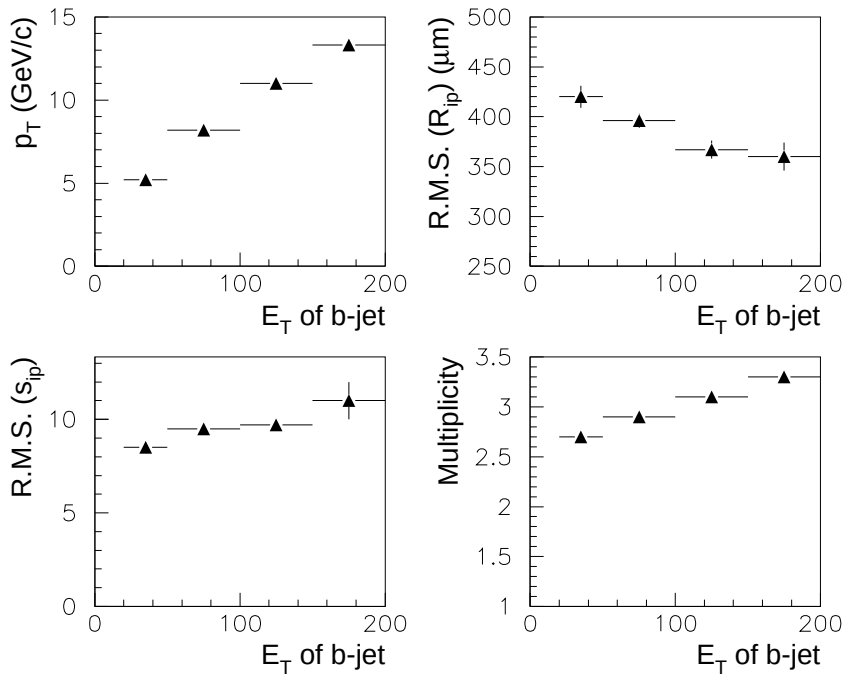

Figure 6.7: Average p_T, R.M.S. of the transverse impact parameter, R.M.S. of the transverse impact parameter significance and average multiplicity of tracks in b-jet candidates, as a function of the b-jet transverse energy.

M_s is b-tagged after reconstruction.

Figure 6.8 shows the behaviour of M_s and M_r as a function of the cut applied on the transverse impact parameter, after application of a cut at $|s_{ip}| \geq 3$. The curves show that the wrong tags due to the event kinematics dominate up to mistagging rates of about 3%, then the two sources of tagging errors become comparable. Reconstruction errors have a small effect, probably because particular care was taken in order to obtain a statistically correct track fit. By statistically correct we mean that the detector resolutions were carefully estimated and multiple scattering in the tracker material was properly taken into account. This results in a correct estimation of the track parameter errors and a small amount of tracks in the non-Gaussian tails of the transverse impact parameter pull distribution. It can be concluded that, with a tagging algorithm based on the impact parameter measurement and with a good track fit, the event physics is the most important source of mistags.

As mentioned earlier, a large fraction of tagging errors comes from K^0_S and Λ^0 decays and photon conversions. These particles could be identified by reconstructing their decay or conversion vertex, which could improve the background rejection. In addition, the b-tagging efficiency could be increased by using also the longitudinal impact parameter, but this would require the reconstruction of the position of the primary proton-proton interaction along the beam. These possibilities were not considered, by lack of a vertex reconstruction program.

6.4.3 Influence of impact parameter and pixel resolutions

The dependence of the tagging results on the impact parameter resolution can be estimated from figure 6.5. It is indeed almost equivalent to require a twice larger impact parameter significance as to estimate the tagging performance with a twice worse impact parameter resolution. With

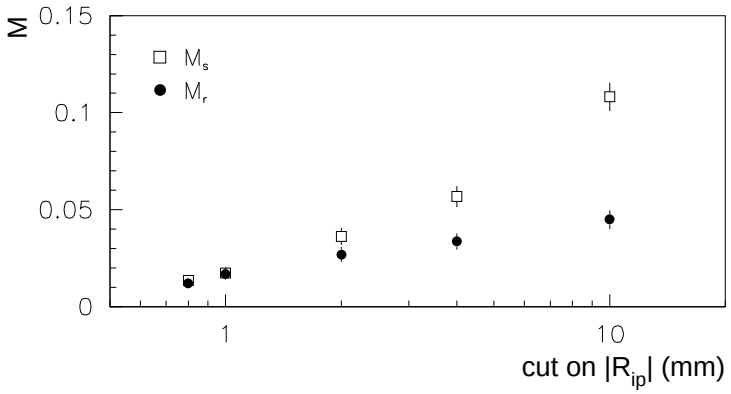

Figure 6.8: Fractions of u, d, s, g-jets that are b-tagged on the basis of their kinematics (M_s) and that would be rejected on the basis of the kinematics but are actually tagged because of reconstruction errors (M_r), as a function of the cut on the transverse impact parameter, after application of a cut at $|s_{ip}| \geq 3$.

an impact parameter resolution two times larger than nominal and a cut at 3 on the significance we can expect a tagging efficiency of 78% of the nominal value without a significant change of background rejection. After application of a cut on the transverse impact parameter, the b-tagging efficiency drops to about 40% if the mistagging rate from u, d, s, g-jets has to be kept below 2%. This is about the minimum performance required for some SUSY studies [106].

The 40 μm average transverse impact parameter resolution expected for particles in b-jets is dominated by the contribution of multiple scattering. The pixel $R\phi$-resolution should therefore have a relatively small influence on the b-tagging performance, at least in the high luminosity configuration of the vertex detector. Degrading the pixel resolution from 10 to 20 μm would result in an increase of the impact parameter resolution by 7 μm, according to reference [109]. This would lead to a loss of tagging efficiency of a few percent.

6.5 Conclusions and comparison with previous results

We have estimated the b-tagging capability of the CMS tracker at high LHC luminosity with the help of a detailed simulation of the detector response and with a realistic track reconstruction algorithm as described in chapter 5. The b-tagging efficiency was evaluated for b-jets produced in top decays. The mistagging probability was estimated for jets from u, d, s-quarks and gluons as well as for c-jets.

The b-tagging algorithm studied consists in cuts applied on a set of four discriminating variables: the transverse impact parameter significance, the transverse impact parameter, the particle transverse momentum and the multiplicity of the jet. A b-tagging efficiency of $(51 \pm 0.8)\%$ was achieved, with a mistagging probability of $(1.6 \pm 0.3)\%$ for u, d, s, g-jets and of $(12 \pm 0.7)\%$ for c-jets. The tagging algorithm chosen is the following:

- $|s_{ip}|$ of reconstructed tracks ≥ 3;
- $|R_{ip}|$ of reconstructed tracks ≤ 0.8 mm;
- p_T of reconstructed tracks ≥ 1 GeV/c;
- multiplicity of b-jet candidates ≥ 2;

This performance is in close agreement with the results obtained with a preliminary analysis based on a parametrized impact parameter resolution. Our study thus fully confirms these results.

We have then estimated the contributions of the different sources of inefficiency and mistagging. The tagging efficiency that would be reached on the basis of the event kinematics alone is close to 80%. The inefficiency due to track reconstruction is thus about 30%, mainly due to the finite transverse impact parameter resolution, around 40 μm, and to the limited track finding efficiency, 89%, for tracks inside the b-jets simulated. The transverse impact parameter resolution is dominated by the uncertainty in the track azimuthal angle, due to multiple scattering in the vertex detector. The only way of improving it is to reduce the radius of the inner pixel layer, as foreseen in the low luminosity layout of the CMS vertex detector. Possible ways of improving the track finding efficiency have already been proposed in chapter 5. However a large increase of track finding efficiency is unlikely.

Besides, we have evaluated the decrease of tagging efficiency that can be expected if the impact parameter resolution becomes two times worse than nominal. It is estimated to 1/5 of the nominal value. The possibility of improving the tagging efficiency by using also the longitudinal impact parameter remains to be studied. This idea was not tried by lack of a primary vertex reconstruction program.

The tagging errors due to the physics of the background events dominate those due to reconstruction errors. This is because the track fitting algorithm provides a good estimation of the transverse impact parameter error, as shown by the small fraction of tracks in the non-Gaussian tails of the transverse impact parameter pull distribution. The majority of the tagging errors is attributed to strange particle decays and photon conversions, producing secondary particles with a large impact parameter with respect to the primary vertex. These sources of background can probably be reduced with the help of a secondary vertex reconstruction algorithm and a cut on the parent particle flight path.

Studies of b-jet identification have been performed by many groups. In ATLAS, the performance of a simple algorithm based on the impact parameter measurement was compared to that of a probabilistic method originally introduced by the ALEPH collaboration [110]. In this method the probability of containing a long-lived particle is computed for each reconstructed jet. This probability is higher in the case of b-jets, which permits their selection. The benchmark process studied is the decay of a 100 GeV/c^2 Higgs into a $q\overline{q}$ or a gg pair. The results, obtained with a detailed simulation of the ATLAS tracker, are similar for the two methods: 50% b-tagging efficiency, 11% mistagging rate for c-jets and 2.2% for u, d, s, g jets [111].

A note from the DELPHI collaboration [112] describes a statistical method of accumulating the discriminating power of several variables into a single tagging variable. This method is optimal in the sense that, if the discriminating variables are independent, a cut on the tagging variable provides the best background rejection for a given efficiency value, and using more variables can only improve the results. The author of this note also lists a few kinematical variables not related to the b-hadron lifetime that can help improving the background rejection. These methods, as well as selection techniques based on neural networks, are likely to permit an improvement of the CMS b-tagging performance. However we could show that a simple algorithm relying on the precision of the tracker impact parameter measurement already allows efficient b-jet selection and strong background suppression.

Chapter 7

Conclusions

In this thesis we have contributed to the study of the central tracker of the Compact Muon Solenoid (CMS). CMS is one of the two general purpose particle detectors that will be installed at the LHC, the future proton-proton collider of CERN. It is designed for a wide range of physics studies, and optimized for the discovery of the Higgs boson in the mass range from 85 GeV/c^2 to 1 TeV/c^2 that will not be covered by LEP experiments. These studies will be made possible by the unprecedented proton interaction energy and luminosity of the LHC, 14 TeV and 10^{34} cm^{-2}s^{-1}. They also require detectors capable of measuring the energy and momentum of energetic particles (p_T up to a few TeV/c) with a high precision in a background of the order of 1000 low energy particles emitted every 25 ns into the detectors.

We have first participated to the development of Micro-Strip Gas Counters (MSGC). Such detectors will equip the outer layers of the CMS tracker. The MSGC tracker is requested to measure seven points on average along the tracks of high momentum particles, with a detection efficiency close to 100% and an accuracy of about 50 μm in $R\phi$. The Belgian experimental groups of high energy physics contribute to the design and construction of the endcap MSGC disks. They have proposed a layout in which the counters will be mounted side by side at less than 100 μm distance in a common gas volume. This layout minimizes the dead space between counters and the amount of material inside the tracker.

To verify the feasibility of this design we have tested a prototype made of two pieces of MSGC substrates assembled at 70 μm distance. This counter was placed in a cosmic ray hodoscope together with two reference MSGC's. We have checked the uniformity of the detection efficiency for minimum ionizing particles across the prototype surface and the stability of operation. A uniform detection efficiency of 97.5% was measured, with no significant loss at the substrate separation. The range of cathode strip voltages at which full detection efficiency is measured, called the efficiency plateau length, is as large as for the reference chambers, showing the good stability of operation of the prototype. These tests validate the mounting scheme proposed for the endcap MSGC's.

We have then contributed to the study of gas mixtures suited for MSGC operation at the LHC. When this work started, no gas mixture known was fulfilling all the requirements. The best mixture identified at that time, CO_2-DME 40%-60%, delivers enough ionization in a 3 mm thick MSGC gas gap to permit efficient detection of minimum ionizing particles, and allows fast electron collection as needed in order to limit the pile up of signals from different LHC bunch crossings. However it requires high working voltages to get enough gas gain, and does not provide a long efficiency plateau. The energy released in case of spark is thus large, which can damage the electrodes, and the stability margin between the working voltage and the breakdown point is small.

Ne-DME mixtures, instead, deliver high gas gains at low voltages. We could show that, in

spite of the low amount of ionization produced in Ne, these high gains lead to full detection efficiency at cathode strip voltages 100 V below the beginning of the efficiency plateau in CO_2-DME 40%-60%. In addition the plateau is 70 V long, which permits operation well below the breakdown point. Later on, triple mixtures of Ne, DME and CO_2 were tried. Adding CO_2 increases the electron drift velocity, from 55 μm/ns in Ne-DME 50%-50% to 65 μm/ns in Ne-DME-CO_2 40%-40%-20% at a 10 kV/cm drift field. The beginning of the efficiency plateau is shifted by 20 V towards higher voltages, but the plateau becomes 90 V long. Therefore, Ne-DME-CO_2 mixtures are a good choice of gas filling for MSGC operation at the LHC, provided that no detector ageing is observed in long-term irradiation tests.

MSGC's have demonstrated a level of performance meeting the requirements of high luminosity experiments in almost all respects: detection efficiency, spatial resolution, rate capability, response speed as well as stability of operation of small scale prototypes. Present research and development concentrate on the mass production of the counters and reliability studies of large scale systems. It has not been fully proven yet that a large MSGC system will survive during ten years at the LHC in realistic conditions of operation. In this respect, recently introduced detectors like the GEM or the MICROMEGAS are of particular interest, as they are expected to be less sensitive to sparks and ageing than MSGC's. However these technologies are less mature and additional development studies are required before they can be used at the LHC.

We have then investigated the performance of the CMS central tracking system. The CMS tracker is requested to reconstruct tracks of charged particles with an efficiency of 95% for isolated tracks and 90% for particles in jets. It should allow to measure their transverse momentum with an accuracy $\Delta p/p \simeq 10^{-4} p_T$ (p_T in GeV/c) at transverse momenta above 100 GeV/c, and their transverse impact parameter with a precision much better than 100 μm. The tracker performance was evaluated with the help of a detailed detector simulation based on the GEANT program. The detector response is simulated up to the level of the signals induced by the particles on the electronics channels (signal digitization).

We have first studied a track finding and fitting algorithm based on the Kalman filter. In order to obtain a statistically correct fit and a reliable estimation of the track parameters and their errors, detector resolutions and multiple scattering in the detector material must properly be taken into account. We have therefore introduced a parametrization of the dependence of the MSGC spatial resolution with the particle incident angle. The MSGC resolution varies between 30 μm and about 1 mm in the relevant range of incident angles for particles of $p_T \geq$ 1 GeV/c. Multiple scattering is accounted for by GEANE, a program interfaced with the GEANT description of the detector. The Kalman filter was shown to be able to perform hit selection effectively: a reconstructed track contains on average 96% of the hits produced by the corresponding simulated particle. The fraction of incorrect hit associations is 0.6% in a dense hit environment like b-jets at high LHC luminosity. The track parameters estimated by the Kalman filter are unbiased and their errors are correctly evaluated, as shown by the distributions of the track parameter pulls.

The filter algorithm provides an optimal estimation of the track parameters only at the particle production vertex. The smoothing algorithm, which corrects the estimation of the filter in detectors located further outwards, leads to an optimal knowledge of the particle trajectory at any point. It therefore permits better hit selection than the filter: 99% of the hits are retrieved, with a fraction of outliers of 0.4%. It also permits better association of particle trajectories reconstructed in the tracker with showers measured in the calorimeters and track segments reconstructed in the muon chambers.

The performance of the tracker version V3 estimated from our study is as follows:

- a track finding efficiency above 97% for isolated muons,

- a track finding efficiency of 89% for particles in b-jets at high luminosity, except for electrons, for which it only amounts to 50%,
- a number of ghost tracks around 0.1 per event at high luminosity,
- a momentum resolution meeting the requirement at high p_T in the pseudorapidity range $|\eta| \leq 1.8$,
- a momentum resolution of 1% or better below $p_T = 10$ GeV/c,
- a transverse impact parameter resolution of about 10 μm at high p_T, degrading to 100 - 200 μm at $p_T = 1$ GeV/c.

The track finding efficiency and track parameter resolutions are thus satisfactory for muons and hadrons.

The track finding inefficiency is mainly due to interactions of particles with the tracker material. Strong interactions are responsible for the loss of 8% of the hadron tracks, and bremsstrahlung renders the reconstruction of electron tracks very difficult. The track parameter resolutions are dominated by the contribution of multiple scattering at transverse momenta below 10 - 20 GeV/c. This value is high compared to the minimum transverse momentum that we intend to measure in CMS (about 0.7 GeV/c). Designing the tracker with significantly less material would allow to increase the track finding efficiency for hadrons and electrons, and to improve the track parameter resolutions for low momentum particles. In any case a dedicated electron track reconstruction algorithm has to be developed, possibly including the information of the electromagnetic calorimeter.

Some factors were not taken into account in the simulation, like detector misalignments or a detailed description of the front-end electronics response. Our study, although performed with the most complete simulation and reconstruction programs available, is therefore not yet completely realistic. In addition, the problem of pattern recognition has not been fully addressed here, as the track finding algorithm used proceeds in a rather narrow region around the simulated tracks, i.e. the templates of the Local Track Finder. To our knowledge pattern recognition is an open problem. Several algorithms are under test in the CMS collaboration, but none has shown a decisive superiority in track finding efficiency or reconstruction speed. Many other techniques could still be tried, like neural networks for example.

Eventually, we have estimated the potential of the CMS tracker in identifying b-jets. The b-tagging algorithm used relies on the precise measurement of the transverse impact parameter provided by the tracker. The beauty hadron decay products can be distinguished from particles emitted in light parton jets by their transverse impact parameter, which amounts typically to a few hundreds of micrometers. We have simulated and reconstructed 1730 $t\bar{t} \rightarrow W^+W^-b\bar{b}$ signal events, and 1900 $W + c$ and 1850 $W + u, d, s, g$ background events. The simulation was performed at the signal digitization level and includes an event pile up corresponding to the full LHC luminosity. Track reconstruction was done with the track finding and fitting algorithms described above.

A b-tagging efficiency of (51 ± 0.8)% was reached, with a mistagging probability of (1.6 ± 0.3)% for u, d, s, g-jets and of (12 ± 0.7)% for c-jets. The tagging algorithm chosen is the following:

- significance $|s_{ip}| = |R_{ip}/\Delta R_{ip}|$ of reconstructed tracks ≥ 3;
- $|R_{ip}|$ of reconstructed tracks ≤ 0.8 mm;
- p_T of reconstructed tracks ≥ 1 GeV/c;

- multiplicity of b-jet candidates ≥ 2;

The performance achieved is in close agreement with the results of preliminary studies based on a parametrized impact parameter resolution.

We have shown that the 50% tagging efficiency loss was due for 20% to the kinematics of the events, and for 30% to the limited impact parameter resolution and track finding efficiency of the tracker. An improved tagging efficiency is expected with the low luminosity layout of the pixel detector, which will provide a more precise measurement of the impact parameter. We have also demonstrated that, down to mistagging rates of a few percent, the physics of the background jets is the dominant source of tagging errors, well above the contribution of track reconstruction errors.

Possible ways of improving the CMS b-tagging performance have been pointed out. The reconstruction of the proton interaction vertex would allow to use the longitudinal impact parameter as additional discriminating variable. The background from long-lived particles and photon conversions could be reduced by reconstructing the secondary vertices and cutting on the parent particle flight path. More sophisticated tagging algorithms should also be tried. These would allow to combine the discriminating power of several variables in an optimal way.

In this work we have had the opportunity to study different aspects of the CMS tracker performance. The results indicate that the tracker should work as required, except for electrons. In several occasions the large amount of material in the tracker was pointed out as the main cause of performance limitation. It is worth stressing again the importance of keeping the tracker thickness as small as possible, below the level of the V3 layout if possible.

Bibliography

[1] The LHC study group, *The Large Hadron Collider, Conceptual Design*, CERN/AC/95-05, 1995.

[2] D. Denegri, *Standard Model physics at the LHC (pp collisions)*, Proc. ECFA workshop for LHC, Aachen 1990, CERN 90-10, Eds. G. Jarlskog and D. Rein, vol. I, p. 56.

[3] UA4/2 collaboration, *Predictions on the total cross-section and real part at LHC and SSC*, Phys. Lett. **B315** (1993) 503.

[4] D.H. Perkins, *Introduction to High Energy Physics*, Third edition, Addison-Wesley, 1987.

[5] F. Englert and R. Brout, Phys. Rev. Lett. **13** (1964) 321.

[6] P.W. Higgs, Phys. Rev. **145** (1966) 1156.

[7] V. Ruhlmann-Kleider, *Search for Higgs bosons at LEP200*, to be published in Proc. XXXIIIrd Rencontres de Moriond, 1998.

[8] The LEP working group for Higgs boson searches, *Lower bound for the Standard Model Higgs boson mass from combining the results of the four LEP experiments*, CERN-EP/98-046, 1998.

[9] M. Spira, *QCD effects in Higgs physics*, CERN-TH/97-68, 1997.

[10] ATLAS Collaboration, *Technical Proposal*, CERN/LHCC 94-43, 1994.

[11] CMS Collaboration, *Technical Proposal*, CERN/LHCC 94-38, 1994.

[12] D.P. Roy, *Higgs and SUSY searches at LHC*, TIFR/TH/98-08, 1998, and references therein.

[13] Particle data group, Phys. Rev. **D54** (1996) 1.

[14] F. Abe et al., Phys. Rev. Lett. **74** (1995) 2626.

[15] L. Wolfenstein, *Parametrization of the Kobayashi-Maskawa matrix*, Phys. Rev. Lett. **51** (1983) 1945.

[16] CMS Collaboration, *The Muon Project*, CERN/LHCC 97-32, 1997.

[17] CMS Collaboration, *The Electromagnetic Calorimeter Project*, CERN/LHCC 97-33, 1997.

[18] CMS Collaboration, *The Hadron Calorimeter Project*, CERN/LHCC 97-31, 1997.

[19] R.L. Gluckstern, *Uncertainties in track momentum and direction, due to multiple scattering and measurement errors*, Nucl. Instr. and Meth. **24** (1963) 381.

[20] W. Blum, L. Rolandi, *Particle detection with drift chambers*, Accelerator Physics, Springer-Verlag, 1994.

[21] CMS Tracker Layout Optimization Group, *V3 CMS tracker layout - Detector break-up*, CMS NOTE 1996/013 (1996).

[22] A. Oed, Nucl. Instr. and Meth. **A263** (1988) 351.

[23] CMS Collaboration, *The Tracker Project*, CERN/LHCC 98-6, 1998.

[24] The original paper is: L.D. Landau, *On the energy loss of fast particles by ionization*, *J. Phys. USSR* **8** (1944) 201.
See also: U. Fano, *Penetration of protons, alpha particles, and mesons*, Ann. Rev. Nucl. Part. Sci. **13** (1963) 1.

[25] V.A. Chechin, V.C. Ermilova, *The ionization loss distribution at very small absorber thickness*, Nucl. Instr. and Meth. **136** (1976) 551.

[26] V.C. Ermilova et al., *Fluctuations and the most probable values of relativistic charged particle energy loss in thin gas layers*, Nucl. Instr. and Meth. **145** (1977) 555.

[27] J.H. Cobb et al., *The ionization loss of relativistic charged particles in thin gas samples and its use for particle identification*, Nucl. Instr. and Meth. **133** (1976) 315.

[28] A.V. Zarubin, *Properties of wire chamber gases*, Nucl. Instr. and Meth. **A283** (1989) 409.

[29] R. Bouclier et al., *Recent developments of the multidrift tube*, Nucl. Instr. and Meth. **A283** (1989) 509.

[30] H. Fischle et al., *Experimental determination of ionization cluster size distributions in counting gases*, Nucl. Instr. and Meth. **A301** (1991) 202.

[31] M. Geijsberts et al., *Tests of the performance of different gas mixtures in MSGC's*, Nucl. Instr. and Meth. **A313** (1992) 377.

[32] F. Sauli, *Principles of operation of multiwire proportional and drift chambers*, CERN report 77-09 (1977).

[33] E.B. Wagner et al., *Time-of-flight investigations of electron transport in some atomic and molecular gases*, J. Chem. Phys. **47** (1967) 3138.

[34] J.H. Parker et al., *Theory of electron diffusion parallel to electric fields*, Phys. Rev. **181** (1969) 290.

[35] A. Peisert, F. Sauli, *Drift and diffusion of electrons in gases: a compilation*, CERN report 84-08 (1984).

[36] P. Rice-Evans, *Spark, streamer, proportional and drift chambers*, Richelieu, 1974.

[37] J.A. Kadyk, *Wire chamber ageing*, Nucl. Instr. and Meth. **A300** (1991) 436.

[38] M. Jibaly et al., *Some results on the ageing of wire chambers with dimethylether*, Nucl. Instr. and Meth. **A273** (1988) 161.

[39] S.C. Curran et al., *Phil. Mag.* **40** (1949) 929.

[40] J. Byrne, Proc. Roy. Soc. **A 66** (1962) 33.

[41] A. Lansiart, J.P. Morucci, *J. Phys. Radium* **23** (1962) 102A, suppl. no 6.

[42] G.D. Alkhazov, *Statistics of electron avalanches and ultimate resolution of proportional counters*, Nucl. Instr. and Meth. **89** (1970) 155.

[43] G.D. Alkhazov, *Mean value and variance of gas amplification in proportional counters*, Nucl. Instr. and Meth. **75** (1969) 161.

[44] R. Bellazzini, M. A. Spezziga *Electric field, avalanche growth and signal development in Micro-Strip Gas Chamber and Micro-Gap chamber*, La Rivista del Nuovo Cimento **vol.17** (1994) n^{o}12.

[45] R. Horisberger, D. Pitzl, *A novel readout chip for silicon strip detectors with analog pipeline and digitally controlled analog signal processing*, Nucl. Instr. and Meth. **A326** (1993) 92.

[46] M. Raymond et al., *The APV6 readout chip for CMS microstrip detectors*, Imperial College note IC/HEP/97-10, 3rd Workshop on Electronics for LHC Experiments, London, 1997.

[47] F.G. Sciacca, *Impact of fast shaping at the front-end on signals from micro-strip gas chambers*, CMS NOTE 1997/105 (1997).

[48] F. Angelini et al., *Study of the bunch crossing identification at LHC using micro-strip gas chambers*, Nucl. Instr. and Meth. **A368** (1996) 345.

[49] G. Charpak et al., Nucl. Instr. and Meth. **62** (1968) 262.

[50] F. Angelini et al., *The Micro-Gap Chamber*, Nucl. Instr. and Meth. **A335** (1993) 69.

[51] F. Angelini et al., *Results from the first use of MSGC's in a high energy physics experiment*, Nucl. Instr. and Meth. **A315** (1992) 21.

[52] M.K. Ballintijn et al., *Results from the MSGC tracker at SMC*, Nucl. Phys. **B** (Proc. Suppl.) **44** (1995) 268.

[53] J. Blouw et al., *Operational experience with the large microstrip gas tracker of HERMES*, Proc. Int. Workshop on MSGC's, Lyon, 1995, Eds. D. Contardo and F. Sauli.

[54] V. Zhukov et al., *A curved micro-strip gas counter for synchrotron radiation time resolved SAXS/WAXS experiments*, Nucl. Instr. and Meth. **A392** (1997) 83.

[55] R. Bellazzini et al., *The MicroGap Chamber as a polarimeter for X-ray astronomy*, Proc. Int. Workshop on MSGC's, Lyon, 1995, Eds. D. Contardo and F. Sauli.

[56] E.B. Babichev et al., *High pressure multiwire proportional and gas microstrip chambers for medical radiology*, Nucl. Instr. and Meth. **A360** (1995) 271.

[57] *Development of MSGC's for radiation detection and tracking at high rates*, final status report of the RD-28 collaboration, CERN/LHCC 96-18, LDRB Status Report/RD-28 (1996).

[58] R. Bouclier et al., *Some factors affecting the lifetime of Micro-Strip Gas Chambers operated at high rates in laboratory conditions*, Proc. Int. Workshop on MSGC's, Lyon, 1995, Eds. D. Contardo and F. Sauli.

[59] J.T.M. Baines et al., *Work at RAL on the ageing properties of gas microstrip detectors*, Proc. Int. Workshop on MSGC's, Lyon, 1995, Eds. D. Contardo and F. Sauli.

[60] I.P. Duerdoth et al., *Lifetime characteristics of an MSGC with thin, high resistivity substrate*, Proc. Int. Workshop on MSGC's, Lyon, 1995, Eds. D. Contardo and F. Sauli.

[61] R. Bouclier et al., *Development of microstrip gas chambers on thin plastic supports*, Nucl. Instr. and Meth. **A315** (1992) 521.

[62] R. Bouclier et al., *Development of MSGC's for high rate operation*, Nucl. Instr. and Meth. **A367** (1995) 168.

[63] R. Bouclier et al., *High rate operation of micro-strip gas chambers*, Proc. IEEE Nuclear Science Symposium, San Fransisco, Oct. 21-28, 1995.

[64] B. Boimska et al., *Progress with diamond over-coated microstrip gas chambers*, Nucl. Instr. and Meth. **A404** (1998) 57.

[65] M.R. Bishai et al., *Plastic MSGC's with two-sided readout*, Proc. Int. Workshop on MSGC's, Legnaro, 1994, Eds. G. Della Mea and F. Sauli.

[66] J.J. Florent et al., *The electrostatic field in microstrip chambers and its influence on detector performance*, Nucl. Instr. and Meth. **A329** (1993) 125.

[67] V. Peskov et al., *Feedback and breakdowns in microstrip gas counters*, Nucl. Instr. and Meth. **A397** (1997) 243.

[68] R. Bouclier et al., *The Gas Electron Multiplier*, CERN-PPE-96-177, 1996 IEEE Nuclear Science Symposium and Medical Imaging Conference, Anaheim, CA, 3-9 Nov 1996.

[69] R. Bellazzini et al., *Technique for the characterization of discharges in micro-strip gas chambers*, INFN PI/AE 97/01, 1997.

[70] D. Abbaneo et al., *Recent beam tests of CMS MSGC tracker prototypes*, CMS Conference Report 1998/012, submitted for publication in Nucl. Instr. and Meth.

[71] W. Beaumont et al., *MSGC test with fast neutrons*, CMS NOTE 1998/014 (1998).

[72] F. Angelini et al., *A large area micro-gap chamber with two-dimensional small angle stereo read-out for the CMS central tracker*, Proc. Int. Workshop on MSGC's, Lyon, 1995, Eds. D. Contardo and F. Sauli.

[73] J.E. Bateman, J.F. Conolly et al., *The experimental characterization of gas microstrip detectors III. Lifetime Characteristics* RAL-94-114 (1994).

[74] F.D. van den Berg et al., *Gas gain stability of MSGC's operating at high rate*, NIKHEF/97-014 (1997).

[75] B. Boimska et al., *Noise in MSGC with resistive strips*, CMS TN/95-203 (1995).

[76] R. Bouclier et al., *Optimization of design and beam test of MSGC's*, Nucl. Instr. and Meth. **A367** (1995) 163.

[77] J. Schmitz, *Results on Monte Carlo simulation of a microstrip gas counter*, Nucl. Instr. and Meth. **A323** (1992) 638.

[78] *ATLAS MSGC*, ATLAS internal note INDET-NO-076 (1994).

[79] R. Bouclier et al., *Results of wire chamber ageing tests with CH_4- and DME-based gas mixtures*, Nucl. Instr. and Meth. **A346** (1994) 114.

[80] A. Sharma, private communication.

[81] F. Angelini et al., *A large area, high gain micro-gap counter*, Nucl. Instr. and Meth. **A362** (1995) 273.

[82] O. Bouhali et al., *Operation of MSGC's with Ne-DME gas mixtures*, Nucl. Instr. and Meth. **A378** (1996) 432.

[83] F. Angelini et al., *Behaviour of MSGC's in strong magnetic field*, Nucl. Instr. and Meth. **A343** (1994) 441.

[84] Y. Giomataris et al., *MICROMEGAS: a high granularity position sensitive gaseous detector for high particle flux environments*, Nucl. Instr. and Meth. **A376** (1996) 29.

[85] J. Buytaert et al., *The forward muon detector of the DELPHI experiment at LEP*, Nucl. Instr. and Meth. **A310** (1991) 596.

[86] F. Stichelbaut, *La détection des muons dans l'expérience DELPHI et son rôle dans l'étude de l'interaction $e^+e^- \rightarrow \mu^+\mu^-$*, thèse de doctorat, Université Libre de Bruxelles, 1993.

[87] The APC controller was designed by F. Hartjes, NIKHEF-H, according to specifications mentioned in [45].

[88] CERN EP-Electronics note 90-01.

[89] CERN UA1 Technical Note 90-01.

[90] O. Bouhali, *The calibration of the IIHE hodoscope*, IIHE internal note, 1997.

[91] T. Todorov, *Simulation of avalanche development in MSGC/MGC detectors*, Proc. Int. Workshop on MSGC's, Lyon, 1995, Eds. D. Contardo and F. Sauli.

[92] F. Angelini, A. Toropin, *MSGC simulation program for CMS software*, CMS TN/94-280 (1994).

[93] S.F. Biagi, Nucl. Instr. and Meth. **A283** (1989) 716.

[94] F. Angelini et al., *Development of a very large area microstrip gas chamber for the CMS central tracking system*, Nucl. Instr. and Meth. **A360** (1995) 22.

[95] F.D. v.d.Berg et al., *Experimental study of inclined particle tracks in microstrip gas counters*, Nucl. Instr. and Meth. **A349** (1994) 438.

[96] O. Bouhali et al., *Operation of MSGC's with DME-based mixtures*, to be published in Nucl. Instr. and Meth.

[97] R. Brun et al., *GEANT, Detector description and simulation tool*, CERN program library W5013 (1994).

[98] V. Karimäki, *Hit covariances in strip detector simulation and reconstruction*, CMS TN/95-170 (1995).

[99] R. Frühwirth, *Application of Kalman filtering to track and vertex fitting*, Nucl. Instr. and Meth. **A262** (1987) 444.

[100] N. Stepanov, A. Khanov, *Towards the fast trackfinder algorithm for the CMS tracker*, CMS TN/94-181 (1994).

[101] P.E. Caines, *Linear stochastic systems*, Wiley (1988).

[102] A. Gelb et al., *Applied optimal estimation*, M.I.T. Press, Cambridge (1974).

[103] E.J. Wolin et al., *Covariance matrices for track fitting with the Kalman filter*, Nucl. Instr. and Meth. **A329** (1993) 493.

[104] V. Innocente et al., *GEANE - Average Tracking and Error Propagation Package*, CERN writeup W5013 (1994).

[105] R. Kinnunen, D. Denegri, *B-tagging with impact parameter in the CMS tracker*, CMS TN/96-045 (1996).

[106] S. Abdullin, D. Denegri, *On the possibility to observe $h \rightarrow b\bar{b}$ with $S/B \sim 1$ in SUSY (mSUGRA), and implications for tracker and HCAL*, CMS NOTE 1997/070 (1997).

[107] S. Lehti et al., *Study of h, H, $A \rightarrow \tau\tau \rightarrow e\mu$ in the CMS detector*, CMS NOTE 1998/019 (1998).

[108] T. Sjöstrand, *PYTHIA 5.7 and JETSET 7.4, Physics and Manual*, CERN TH/93-7112, Comp. Phys. Comm. **82** (1994), 74.

[109] V. Karimäki, *Parametrization of the impact parameter resolution*, CMS TN/96-047 (1996).

[110] ALEPH Collaboration, *A precise measurement of $\Gamma_{Z\rightarrow b\bar{b}}/\Gamma_{Z\rightarrow hadrons}$*, Phys. Lett. **B313** (1993) 535.

[111] L. Vacavant, *Etiquetage des quarks b par un détecteur à pixels dans l'expérience ATLAS auprès du LHC*, thèse de doctorat, Université de la Méditerrannée, Aix-Marseille II (1997).

[112] G. Borisov, *Combined b-tagging*, DELPHI Note 97-94 PHYS 716 (1997).

Acknowledgements

Tout d'abord je tiens à remercier le Professeur Jean Sacton pour m'avoir accueilli dans son laboratoire, dans un premier temps pour mon Travail de Fin d'Etudes, et ensuite pour ma thèse.

Je remercie ensuite chaleureusement Catherine Vander Velde pour m'avoir proposé ce sujet de thèse et pour avoir accepté de me diriger durant ces cinq années. Je dois beaucoup à son expérience, son esprit critique, ses encouragements et son sens de l'organisation. Merci également d'avoir relu avec attention le texte de cette thèse et d'avoir soulevé les imprécisions et erreurs qu'il contenait.

Je voudrais associer à ces remerciements le Professeur Stefaan Tavernier, qui avait dirigé mon Travail de Fin d'Etudes et m'avait ensuite suggéré de faire une thèse. Je n'oublie pas mon oncle Léon Etienne, qui a en grande partie suscité mon intérêt pour la physique des particules.

Mes remerciements vont ensuite au Professeur Walter Van Doninck, avec qui la physique a été intéressante et amusante à partir de tôt le matin jusque tard le soir, parfois même très tard autour d'une table bien garnie et avec un bon verre de vin. I am also very grateful to Fred Udo, who always provided me with precious help, fruitful suggestions and remarks. Thanks also to Fred Hartjes for his priceless support.

Je suis également très reconnaissant envers Valeri Zhukov, qui a donné l'impulsion initiale à mon travail expérimental. Un gros boost, en fait. J'ai aussi beaucoup apprécié le travail en équipe avec Othmane Bouhali. Je voudrais ici le saluer, ainsi que sa famille. Merci aussi à Jacqueline Stefanescu, grâce à qui la chasse aux bugs dans les dédales des programmes de simulation a été moins pénible.

Je suis très obligé envers Daniel Bertrand, qui a accepté de relire mon chapitre sur la reconstruction de traces, ainsi qu'envers Gaston Wilquet, pour les nombreux problèmes de statistique qu'il m'a aidé à résoudre.

Among the people from the CMS collaboration, I would like to thank first Professor Ronaldo Bellazini and his team for their friendly welcome during beam tests. I have learned a lot about MSGC's with them. Anna Peisert also gave me the opportunity to work close to the detectors and gain some experience in hardware.

Among the CMS software team, Martti Pimiä provided me with constant support and good advice. Veikko Karimäki always expressed interest for my code developments and carefully checked the routines I wrote. Alessandra Caner convinced me to join the CMS tracker optimization group for some time. Thanks to her help, as well as with the numerous explanations of Sasha Khanov and Nikita Stepanov, I could progress rapidly in understanding track reconstruction. Many thanks also to Ritva Kinnunen, who kindly gave me her Pythia programs.

J'ai également eu le plaisir de travailler avec Teddy Todorov au CERN et à Strasbourg. Merci à Teddy de m'avoir initié, avec un enthousiasme communicatif, à la programmation orientée objet. J'espère que ca tient toujours, pour l'escalade du Mont Blanc... Je tiens aussi à remercier Walter Geist, qui s'est chargé des aspects logistiques et administratifs de mon premier séjour à l'Institut de Recherches Subatomiques de Strasbourg. Grâce à Jean-Marie Brom, cette

expérience pourra sans doute se renouveler l'année prochaine. Je lui suis très redevable de sa confiance et de son soutien. Il faut également que je salue mon confrère Pascal Pralavorio, qui en ce temps-là m'offrit le gîte. Ce fut cool de sa part.

J'ai enfin eu la chance de faire ma thèse annexe à l'Institut d'Aéronomie Spatiale de Belgique avec l'équipe du Professeur Paul Simon. Je tiens à remercier le Professeur Paul Simon pour avoir accepté de superviser ce travail. Grâce à Jean-Christopher Lambert, j'ai pu approcher les problèmes de la chimie et de la dynamique de la couche d'ozone. Je suis aussi redevable à José Granville d'avoir extrait les fichiers de données et visualisé les résultats. Merci également à tous deux pour les nombreuses discussions que nous avons eues.

Il y a encore beaucoup de monde que je voudrais remercier ou simplement saluer. Tout d'abord les copains doctorants, avec par ordre de taille approximatif Jordi, Stan, Bart, Tom, Laurent, Joëlle, Barbara, Arkadi, Francesca, Ruru, Kathy, Redouane, Kim, Isabelle, Liu Xuan et tous les autres. Merci particulièrement à Patrick pour m'avoir révélé les mystères du filtre de Kalman, à Muriel et Véronique pour l'organisation des marches du dimanche, à Véronique encore pour le rock acro, à Peter pour le support Macintosh et à Patrio pour le stage de 4.70.

Merci ensuite à Luc Van Lancker ainsi qu'à Etienne Lievens pour leur aide lors de la construction et l'installation des dispositifs expérimentaux. Je serais impardonnable si j'oubliais l'aide de Monique Garnier, Danielle Peymans et Myriam Pins lors de l'écriture des nombreux rapports, autant que celle de Josée pour les photocopies et travaux de reliure. Merci également à Denis Johnson et à John Wickens pour les nombreuses corrections d'anglais.

Merci enfin à ma famille, pour des raisons qu'il n'est pas nécessaire d'expliquer.